Site 1256[1]

Expedition 335 Scientists[2]

Chapter contents

Introduction

This chapter presents descriptions and measurements on cores and other samples retrieved during Integrated Ocean Drilling Program (IODP) Expedition 335 to Hole 1256D. The background and objectives of Expedition 335 are described in detail in **"Background and geological setting"** and **"Scientific objectives"** both in the "Expedition 335 summary" chapter (Expedition 335 Scientists, 2012a), and expedition operations are documented in **"Operations"** in the "Expedition 335 summary" chapter (Expedition 335 Scientists, 2012a).

The following sections report observations and measurements made on cores from the plutonic section recovered during IODP Expedition 312, as well as material recovered during Expedition 335 (Fig. **F1**). Here we summarize what was recovered as cores and as other nonstandard geological samples from the numerous hole-clearing and fishing runs during Expedition 335. These materials were described by the Shipboard Scientific Party and archived at the IODP Gulf Coast Repository.

Redescription of Expedition 312 Cores 312-1256D-202R through 234R

The archive and working halves of Cores 312-1256D-202R through 234R (1372.8–1507.1 meters below seafloor [mbsf]) from the lower part of the granoblastic dikes to the bottom of the hole at 1507.1 mbsf, including the plutonic section of Hole 1256D (Fig. **F2**) (Teagle, Alt, Umino, Miyashita, Banerjee, Wilson, and the Expedition 309/312 Scientists, 2006), were shipped to the R/V *JOIDES Resolution* prior to Expedition 335. These cores were made available to the science party for the purpose of familiarization with the recovered plutonic section of Hole 1256D and to establish and test description protocols during the transit to Site 1256. The scientists also developed the DESClogik interface for the capture of plutonic rock descriptions for the first time since the introduction of the LIMS database (see **"Information architecture"** in the "Methods" chapter [Expedition 335 Scientists, 2012b]). The long duration of operations required to open Hole 1256D to its full depth at the beginning of Expedition 335 (~16 days; see **"Operations"** in the "Expedition 335 summary" chapter [Expedition 335 Scientists, 2012a]) provided sufficient time for the Shipboard Scientific Party to completely redescribe these cores. This was actually much more time than was available to the shipboard scien-

[1]Expedition 335 Scientists, 2012. Site 1256. *In* Teagle, D.A.H., Ildefonse, B., Blum, P., and the Expedition 335 Scientists, *Proc. IODP,* 335: Tokyo (Integrated Ocean Drilling Program Management International, Inc.). doi:10.2204/iodp.proc.335.103.2012
[2]**Expedition 335 Scientists' addresses.**

tists at the end of Expedition 312. Discrete measurements (paleomagnetism and physical properties) were also performed. These observations and measurements were uploaded to the LIMS database and are presented together with descriptions and measurements of the new material recovered during Expedition 335. No Expedition 312 shipboard thin sections were available onboard the *JOIDES Resolution* to complete new descriptions, but Expedition 312 thin section descriptions were also uploaded to the LIMS database. Expedition 335 scientists supplemented their core descriptions through the use of a series of personal thin sections from Expedition 312 cores brought aboard by Expedition 335 science party members.

Material recovered during Expedition 335

Four cores were taken during Expedition 335 (Cores 335-1256D-235R through 238R) (see Table **T4** in the "Expedition 335 summary" chapter [Expedition 335 Scientists, 2012a]) immediately following the ~16 day reopening of the 922 mbsf interval of Hole 1256D at the beginning of the expedition (see **"Operations"** in the "Expedition 335 summary" chapter [Expedition 335 Scientists, 2012a]). This period of coring lasted only 36 h before the C9 coring bit (Run 9) stopped making progress in the hole and was retrieved completely destroyed (Fig. **F3**), initiating the second long period of remediation for the remainder of Expedition 335. Thirteen subsequent drilling, milling, and fishing runs were required to retrieve metallic junk from the bottom of the hole. Twelve of these runs provided large amounts of cuttings (from fine-grained sand to several centimeter–sized pebbles and chips) and cobbles (Table **T1**). Expedition 335 activities in Hole 1256D concluded with a campaign of cementing operations that were directly preceded by the cutting of a final core (335-1256D-239R).

During several fishing runs, large amounts (up to several hundreds of kilograms) of fine-grained cuttings were recovered, in particular in the bit sub of the fishing magnet (Run 10) and in the bottom-hole assembly (BHA) during the two reverse circulation junk basket Runs 12 and 13 (Table **T1**). Six shipboard grain-mount thin sections were prepared from the fine-grained cuttings from external junk baskets (EXJBs) on Runs 11 and 12 and from the sand-filled drilling collars of the Run 12 BHA. These grain-mounts were point counted and the grains identified to establish the origin of the fine-grained cuttings (Table **T2;** Fig. **F4**). The cuttings contain fragments of three main rock types recovered in Hole 1256D (basaltic lava, granoblastic basalt, and gabbro), indicating that cuttings from the entire hole are present. Basaltic lavas make up ~36% of the grains. These basaltic cuttings are likely to have been progressively accumulating in the hole since the beginning of drilling of Hole 1256D during Ocean Drilling Program (ODP) Leg 206. Granoblastic basalt makes up the largest proportion of the grains (49%), indicating also that coring (including several hours with a destroyed bit), subsequent drilling, and fishing operations during Expedition 335 near the bottom of the hole contributed significantly to the accumulation of these cuttings in the hole. Once the hole was clear of the basaltic sand that filled the BHA during Runs 12 and 13, most of the cuttings and cobbles recovered were granoblastic basalt and gabbroic rocks (Table **T3**). This material was described, measured, and analyzed following the same standard procedure (except for measurements in core reference frame) as those used for describing cores (see **"Core handling and core flow"** in the "Methods" chapter [Expedition 335 Scientists, 2012b]), and the results are reported in the following sections.

To facilitate description and discussion of the crustal stratigraphy at Site 1256 and to assist in the interpretation of cores and junk basket materials recovered during Expedition 335, we present an updated lithostratigraphy of Hole 1256D showing the major divisions (Fig. **F1**; see Table **T5** in the "Expedition 335 summary" chapter [Expedition 335 Scientists, 2012a]). The only major change to the lithostratigraphy presented at the end of IODP Expedition 309/312 is the differentiation of Dike Screens 1 and 2. Figure **F5** shows the progress in Hole 1256D over four scientific ocean drilling expeditions. The lack of gradient in the Expedition 335 segment reflects the dominance of hole opening and remediation during the expedition.

Igneous petrology

Hole 1256D was deepened from 1507.1 to 1521.6 mbsf during Expedition 335. The first core was Core 335-1256D-235R, which continues the numerical sequence from Expedition 312 (Core 312-1256D-234R). Lithologic units (Table **T4;** Fig. **F6**) were defined based on criteria observable in hand specimen, including mineralogy, texture, and grain size (see **"Igneous petrology"** in the "Methods" chapter [Expedition 335 Scientists, 2012b]). The principal objective of the unit designations was to ensure that individual cooling and/or intrusive units are recognized and retrievable from the database. One new unit was identified during Expedition 335 (Unit 1256D-96). In addition, rocks drilled during Expedition 312 were redescribed.

The material recovered from the junk baskets during many of the cleaning and fishing runs (Runs 11–15

and 17–22), in addition to sand and gravel, contained cuttings, gravel, and cobbles (up to 20 cm × 10 cm × 11 cm, or 4.5 kg) (Tables T5, T6). For each run, material larger than ~1 cm was grouped by lithology and texture and subsequently weighed. Rocks of special interest were given a letter code (e.g., Sample 335-1256D-Run13-RCJB-Rock A; see Table T1 in the "Methods" chapter [Expedition 335 Scientists, 2012b]) and formally described using the procedures for core description.

Redescription of plutonic section recovered during Expedition 312

During Expedition 335, the plutonic section recovered during Expedition 312 was redescribed; the updated igneous stratigraphy is listed in Table T4 and illustrated in Figure F6. The new descriptions followed the original unit and subunit structure (Teagle, Alt, Umino, Miyashita, Banerjee, Wilson, and the Expedition 309/312 Scientists, 2006), and the Expedition 312 and 335 unit boundaries agreed, with two exceptions. The first exception is the definition of a new subunit (Unit 1256D-88B), which comprises a crosscutting coarse-grained oxide gabbro. The second change is in the lower part of Unit 1256D-88 and in Unit 1256D-89 (as defined during Expedition 312), where the Expedition 335 Igneous Petrology team identified significant olivine. As a result, the Unit 1256D-88/89 boundary was moved from 1450.80 mbsf (Section 335-1256D-223R-2, 0 cm) to 1439.66 mbsf (Section 335-1256D-221R-1, 6 cm), where the first olivine gabbro (olivine ≥ 5%) occurs, to create a single unit of olivine gabbro (Unit 1256D-89). Within this unit, two series of olivine gabbro were recognized (Unit 1256D-89A, 11.8 m thick, and Unit 1256D-89C, 2.8 m thick) that range from olivine poor at the top to olivine rich at the base (Figs. F6, F7). The two subunits are separated by a sharp modal contact, where the olivine mode drops abruptly from ~20% to 2% (Fig. F8). Below the olivine-rich (~20%) base of the second olivine gabbro series (Unit 1256D-89C), a single piece of relatively olivine poor (~4%) gabbro was recovered (Section 312-1256D-224R-1). Because of the significant drop in olivine content, this was designated as a separate subunit (1256D-89D). Unit 1256D-89B, which comprises two ~15 cm intervals of intrusive oxide gabbro and oxide quartz diorite at 1451.2 and 1451.6 mbsf, was retained from Expedition 312.

The modal mineralogy and textures of the Expedition 312 plutonic rocks were also redescribed during Expedition 335. The only significant difference in modal mineralogy is the recognition during Expedition 335 of large amounts of olivine, leading to the definition of olivine gabbro Units 1256D-89A and 89C, as described above. In addition, there are slight differences in oxide and orthopyroxene modes, with estimates made for these phases during Expedition 335 generally higher than those made during Expedition 312. Gabbro 2 is principally made up of two units (1256D-92A and 1256D-93), which were identified as orthopyroxene-bearing gabbro during Expedition 312. However, the orthopyroxene estimates made during Expedition 335 exceeded 5% (Fig. F7), and these units, and Gabbro 2 in general, have been renamed gabbronorite. The modal estimates made during Expedition 335 are in good agreement with the thin section modes described during Expedition 312, particularly with respect to the higher olivine (Unit 1256D-89) and orthopyroxene (Gabbro 2; Units 1256D-92A and 1256D-93) contents.

Texturally, many of the gabbros were described during Expedition 312 as being poikilitic. Although some oikocrysts were recognized by the Expedition 335 Igneous Petrology team, the gabbros were deemed to be predominantly subophitic.

Cores recovered during Expedition 335

The four cores recovered during Expedition 335 (Cores 335-1256D-235R, 236R, 238R, and 239R) comprise predominantly fine grained aphyric basalt with granoblastic textures. The degree of recrystallization is variable, ranging from strong (in which plagioclase generally retains lath shapes) to complete. This textural variation is the basis for dividing Unit 1256D-96 into Units 96A (strongly granoblastic) and 96B (completely granoblastic) (Table T4).

Unit 1256D-96A

In Unit 1256D-96A, plagioclase forms an isotropic framework of lath-shaped crystals (as long as 1 mm), which is interpreted as relict intergranular texture (Fig. F9A). The interstices between the plagioclase laths are filled with equant to prismatic clinopyroxene and orthopyroxene, along with roundish oxide grains. There are numerous ~1–30 µm inclusions of Fe-Ti oxide within both types of pyroxene.

Unit 1256D-96B

The granoblastic basalts of Unit 1256D-96B are characterized by complete recrystallization of the matrix but contain relics of former lath-shaped plagioclase microphenocrysts, as long as 2 mm, that have survived the granoblastic overprint (Fig. F9B). Bands of elongated, ~50 µm sized clinopyroxene, orthopyroxene, and oxide grains in the core of these former microphenocrysts are interpreted as metamorphosed groundmass or glass inclusions originally in the cen-

tral part of the microphenocrysts. Such inclusions are commonly present within (micro)phenocrysts within unmetamorphosed basalt and dolerites higher up in the hole (e.g., figs. F207 and F212 in Expedition 309/312 Scientists, 2006).

Unit 1256D-96C

Three pieces of leucocratic rock were recovered, which together define Unit 1256D-96C. The first (Section 335-1256D-235R-1 [Piece 5]) comprises oxide quartz diorite with a centimeter-wide tonalite vein (Fig. F10). The contact relationships with the granoblastic basalt were not recovered. Microscopic observations show that the contact between both leucocratic rocks is sutured. The tonalite is fine grained and granular, with clinopyroxene as the principal mafic phase, and 2% Fe-Ti oxides. A 3 mm grain of euhedral, primary magmatic amphibole associated with clinopyroxene suggests high water activities during the formation of this rock (Fig. F11). Apatite and zircon are accessory phases, forming needles as long as 1 mm. Many of the quartz grains host abundant fluid inclusions.

The oxide quartz diorite hosting the tonalite vein is fine grained and granular, with clinopyroxene and amphibole as mafic phases. Clinopyroxene shows marked twinning, contains many oxide inclusions, and ranges from a prismatic to a poikilitic habit, enclosing plagioclase. Amphiboles, although strongly altered, can still be recognized as a primary magmatic phase by their euhedral (Fig. F12) and poikilitic habits. Locally, amphibole is associated with apatite, titanite, zircon, and Fe-Ti oxides, representing typical late-stage igneous assemblages. Plagioclase is strongly zoned, and some crystals show relict cores.

The second piece (Section 335-1256D-235R-1 [Piece 7]; Fig. F10) is fine-grained, granular, oxide-rich (±10%) quartz diorite. The contact relationships with the granoblastic basalt were not recovered.

The third leucocratic rock (within Section 335-1256D-236R-1 [Piece 1]) is in sharp planar contact with cryptocrystalline granoblastic basalt. It is a strongly altered, microcrystalline, granular rock composed of dusty altered plagioclase intergrown with aggregates of fibrous to prismatic needlelike actinolite (Fig. F13). The extinction angles of the plagioclase vary between 0° and 20°, consistent with a high albite component (<40 mol% An). Given its high proportion of plagioclase (85%), this rock has been classified as albitite. Former small ilmenite grains have been converted to "leucoxene" (mixture of ilmenite, titanite, and other ilmenite replacement phases). Minor epidote is present, locally occurring as poikiloblasts enclosing granular plagioclase. Matrix plagioclase is granular, with a similar texture as the granoblastic basalt, and relict plagioclase microphenocrysts occur locally. The absence of quartz, the relict granoblastic texture, and the presence of relict microphenocrysts suggest that this rock is a strongly altered granoblastic basalt.

Unit 1256D-96D

Some of the granoblastic basalt (Section 335-1256D-239R-1 [Pieces 5, 7, and 10]) contains small (<3 cm × 1.5 cm) irregular patches of oxide diorite (Fig. F14), and these have been designated as Unit 1256D-96D. The contact between the oxide gabbro and granoblastic basalt ranges from sutured to gradational and is irregular. The oxide gabbro is medium grained and equigranular, has a granular texture, and contains ~7% Fe-Ti oxides, as well as subhedral, elongate amphibole crystals (~10%).

Rocks recovered during cleaning operations in Hole 1256D

A range of rock types was recovered during hole cleaning and fishing operation Runs 11–15 and 17–22 (Tables T5, T6). These are described below in order of abundance (by weight).

Granoblastic basalt

By far the most abundant rock type (95.3 wt%; Table T5) recovered is cryptocrystalline to fine-grained (<0.1–0.5 mm), generally aphyric basalt with a distinct granoblastic texture. Although all samples have granoblastic textures, the degree of recrystallization varies, with strongly granoblastic rocks dominant (92.9 wt%) over completely granoblastic (7.1 wt%) rocks.

Although the granoblastic basalts recovered during the cleaning operations are strongly recrystallized, some primary magmatic features are preserved. Sample 335-1256D-Run12-RCJB-Rock S has a sharp, planar, apparently igneous contact between a light-colored, cryptocrystalline, completely granular, plagioclase phyric domain and a darker, fine-grained, strongly granular and aphyric domain (Fig. F15). This is interpreted as a dike/dike contact. Although the fine-grained basalt does not show any significant variation in mineralogy and grain size, the cryptocrystalline basalt displays a 1 mm wide zone parallel to the contact, where the grain size is slightly smaller and the modal composition is slightly different from the interior of this domain (more clino- and orthopyroxene; less plagioclase and Fe-Ti oxide). This contact is therefore interpreted as a chilled margin of the cryptocrystalline plagioclase-

phyric basalt against the fine-grained aphyric basalt, now granoblastically overprinted. A second magmatic feature preserved in some samples is plagioclase phenocrysts. The cores of these phenocrysts are commonly preserved, whereas the rims are recrystallized along with the granoblastic matrix. The contact between the relict cores and the recrystallized rims is commonly marked by granular crystals of clinopyroxene and Fe-Ti oxides. A higher extinction angle in the cores (Fig. F16) relative to the rims suggests that the cores have higher anorthite contents (following the Michel-Levy method). In addition, an increase in extinction angle throughout the rim suggests that the rims are reversely zoned. Similar reverse zoning is present in plagioclase within the granoblastic matrix, suggesting that the reverse zoning is metamorphic in origin.

Intrusions in the granoblastic basalt

Approximately half of the described granoblastic basalts contain a minor amount of evolved plutonic material. These evolved rocks occur in two styles: (1) igneous veins and dikelets and (2) igneous patches. The igneous patches are as large as 5 cm × 3 cm and are composed of oxide gabbro, diorite, and tonalite (Fig. F17). Some of the patches show elongate crystals growing inward from the contact with the granoblastic basalt, indicating that they are intrusive. Others, however, have more gradational contacts, and these may be either intrusions or segregations.

The plutonic patches, dikelets, and veins are generally medium grained and granular, and grain size distributions range from equigranular to seriate and poikilitic. Their magmatic textures (lack of recrystallization, subhedral to euhedral shapes of several phases, and poikilitic textures) contrast strongly with the granoblastic textures of the host rocks. Fe-Ti oxide contents are variable, ranging from 2% to 20%. Locally, the veins are observed to be offshoots of the igneous patches (Figs. F17, F18) and dikelets (Fig. F19). This observation indicates that the igneous veins, dikelets, and patches form part of the same network and could mark a single generation of intrusion of evolved melts into the granoblastic basalt. The igneous textures of the intrusive rocks demonstrate that intrusion occurred after the granoblastic recrystallization of the host rock. However, the latter was still hot during intrusion, as indicated by the sutured contacts and the diffuse impregnation of the granoblastic basalts by the veins (see below).

Thin section observations provide constraints on the nature and crystallization histories of the magmatic patches. Sample 335-1256D-Run11-EXJB (Thin Section 13) (Fig. F18) is a medium-grained quartz diorite with relatively high amounts of clinopyroxene and green to brownish hornblende as primary mafic minerals (both 27%); the oxide content is about 2%. Hornblende grows around clinopyroxene, implying a crystallization order of clinopyroxene before amphibole. The presence of zircon documents the highly evolved nature of the melt that crystallized this rock. Toward the contact with the granoblastic basalt, a ~2 mm wide zone is developed where the grain size of the quartz diorite decreases and a higher degree of alteration is recorded. The contact between both lithologies is sutured. Another magmatic patch (in Sample 335-1256D-Run13-RCJB-Rock A; Thin Section 31) is an oxide-rich (8%), fine-grained tonalite (Fig. F20). The primary mafic minerals are remarkably fresh clinopyroxene (20% of the primary mode) and green to brownish hornblende (17% of the primary mode). Similar to Sample 335-1256D-Run11-EXJB (Thin Section 13), prismatic clinopyroxenes are enclosed by amphibole. The abundance of quartz (30%), as well as the presence of several grains of apatite and zircon, implies that this tonalite patch crystallized from a highly evolved melt.

The igneous veins (~1–2 mm wide) and dikelets (<1.5 cm wide) are composed of oxide gabbro to quartz diorite. Contacts between the veins and the granoblastic basalt range from planar to irregular but are invariably sutured. Similar to the igneous patches, the association within the igneous veins of green to brownish hornblende—some of which overgrew pyroxene—quartz, Fe-Ti oxide, and the local occurrence of zircon and apatite points to an evolved melt composition. However, compared with the igneous patches, the veins contain a higher content of mafic minerals (as much as 83% in Sample 335-1256D-Run12-RCJB-Rock B), commonly including granular orthopyroxene (as much as 25% in Sample 335-1256D-Run12-RCJB-Rock D) (Fig. F21A). In addition, there are several textural differences. First, some of the veins contain clinopyroxene oikocrysts enclosing either granoblastic clinopyroxene and orthopyroxene (Sample 335-1256D-Run19-RCJB-Rock C) or plagioclase (Sample 335-1256D-Run12-RCJB-Rock D; Fig. F21B), and others (Samples 335-1256D-Run12-RCJB-Rock B and 335-1256D-Run12-RCJB-Rock J) contain plagioclase oikocrysts that enclose granular clinopyroxene (Fig. F21C). Second, one diorite dikelet (in Sample 335-1256D-Run19-RCJB-Rock C; Figs. F19, F22) has a fine-grained marginal facies containing relics of granoblastic pyroxenes. Third, many plagioclase grains, both granular matrix grains and chadacrysts, contain inclusions of micrometer-sized pyroxene (Fig. F21D). This is common in recrystallized plagioclase within the granoblastic basalt (see above). Overall, the abundance of mafic minerals

(particularly granular orthopyroxene), the poikilitic texture, and the granular pyroxene inclusions suggest that the veins are impregnations of the granoblastic matrix by evolved melts, resulting in a hybrid rock composed of relict granoblastic matrix material (orthopyroxene and clinopyroxene chadacrysts; plagioclase with inclusions) and magmatic grains (plagioclase and clinopyroxene oikocrysts, amphibole, zircon, and apatite).

Gabbroic rocks

Gabbroic rocks form 2.9 wt% of the material recovered (Table T5). They have variable modes, ranging from disseminated oxide gabbro to orthopyroxene-bearing olivine gabbro. Irrespective of composition, the gabbroic rocks are medium grained, with grain size ranging from 0.5 to 7 mm (average = 3 mm). The grain size distribution ranges from seriate to equigranular. Oxide contents are generally low (0.5%–2%).

The disseminated oxide gabbro, recovered predominantly as 1–5 cm platy chips during Run 11, has two textural domains, being subophitic in the finer grained parts and granular in the coarser grained parts (Fig. F23). In thin section, clinopyroxene shows symplectite-like intergrowth with a second clinopyroxene toward the rim (Fig. F24), perhaps due to a high-temperature reaction related to interaction between clinopyroxene and a melt. Similar features were observed in Gabbro 1 cores recovered during Expedition 312 (see "Gabbro 1: Units 1256D-81 through 89" in Expedition 309/312 Scientists, 2006; Koepke et al., 2011). Locally, amphibole forms a coherent interstitial network, suggesting it is of primary magmatic origin. It may contain fragments of relict clinopyroxene and locally replaces clinopyroxene, suggesting it formed by reaction. Thus, both clinopyroxene and amphibole record late-stage reaction of the gabbro with a melt; the presence of primary amphibole suggests this melt may have been hydrous.

The disseminated oxide olivine gabbronorite, recovered as chips during Run 11, has a subophitic to granular texture. In thin section (Sample 335-U1256D-Run11-EXJB; Thin Section 29), it contains 15% olivine with prismatic habit, which is in part enclosed by orthopyroxene. Olivine contains micrometer-sized wormy exsolutions, probably of Fe-Ti oxides (Fig. F25), which were also found in Gabbro 1 olivine (Sample 335(312)-1256D-223R-2, 65–67 cm [Piece 3]; Thin Section 1) during Expedition 335. Similar features were described in olivine from the Rum layered intrusion and explained as a result of reaction resulting from an increase in the oxidation state of the rock ("oxidation exsolution"; Nitsan, 1974). Clinopyroxene and orthopyroxene are prismatic and locally intergrown subophitically with plagioclase. The enclosed plagioclase is elongate and locally encloses trains of small clinopyroxene crystals (now altered to actinolite), suggestive of fast crystal growth. Similar features were observed in Gabbro 1 during Expedition 312. Green to brownish green amphibole locally forms an interstitial network, which is commonly associated with millimeter-sized oxide grains, implying a primary magmatic origin.

The disseminated oxide orthopyroxene-bearing olivine gabbro, recovered as a single, ~1 kg block (Sample 335-1256D-Run20-Rock C; Fig. F26), is medium grained, equigranular, and has a uniform subophitic texture. Microscopic features of this rock are very similar to the olivine gabbronorite described above (Sample 335-U1256D-Run11-EXJB; Thin Section 29), except that the orthopyroxene content is much lower (2%). Plagioclase forms a granular framework of tabular to elongated crystals, locally intergrown subophitically with clusters of anhedral clinopyroxene. Plagioclase commonly displays patchy zoning as a result of the presence of dusty ghost cores. Green to brownish hornblende locally formed interstitially. Olivine contains different types of inclusions: micrometer-sized wormy exsolutions of probably Fe-Ti oxides, trails of micrometer-sized Fe-Ti oxides, and ~100 µm sized roundish inclusions, some with radiating cracks, which may represent former melt inclusions (now filled with alteration products).

Basalt

Basaltic lava forms 1.3 wt% of the rocks recovered during cleaning and fishing (Table T5). The lava is aphyric and glassy to fine grained, and some pieces show an intersertal texture (Fig. F27). Although generally aphyric, some pieces contain <1% microphenocrysts of plagioclase and clinopyroxene.

Leucocratic rocks

Most runs recovered generally small (<5 cm) pieces of leucocratic rocks (0.3 wt% of the total recovery) (Table T5; Fig. F28). The leucocratic rocks have differing proportions of mafic minerals (5%–20%) but are all characterized by cryptocrystalline to fine grain size (typically ~0.1 mm), granular textures, and dominance of Fe-Ti oxides over mafic phases. Hence, they are grouped into one lithologic unit. A few pieces contain planar and sutured contacts between the leucocratic rocks and the granoblastic basalt, and one piece preserves a gradational contact between the two. In addition, two pieces (Sample 335-1256D-Run20-RCJB-Rocks D and E) contain contacts be-

tween leucocratic rocks and coarse-grained diorite, the latter being intrusive.

Microscopic observations show that the leucocratic rocks are very similar to the albitite recovered in Section 335-1256D-236R-1; like this sample (Thin Section 4), they are characterized by pervasive alteration, which has resulted in a dusty, cloudy appearance with a very low grade of crystallinity (Fig. F29A). They also consist mostly of plagioclase (85%–95%) and secondary minerals (greenish actinolite to hornblende, poikiloblastic epidote, secondary diopside, and titanite/oxide associations) and contain relict plagioclase microphenocrysts. In addition, the distribution and the shape of oxides in these rocks (Fig. F29B) are very similar to those observed in the granoblastic dikes. Hence, like part of Section 335-1256D-236R-1 (Piece 1), these leucocratic rocks are interpreted as strongly altered granoblastic basalt.

(Oxide) diorite

Discrete pieces of diorite form a very small component (0.09 wt%) of the recovered rocks (Table T5). The diorite is generally medium grained, although some coarse-grained diorite occurs (Fig. F28C). It is equigranular with a granular texture and is characterized by the presence of subhedral to euhedral, elongate amphibole crystals, similar to the diorite dikelet that crosscuts the granoblastic basalt (Sample 335-1256D-Run19-RCJB-Rock C). The oxide content ranges from 1% to 7%.

Discussion

Origin of junk basket material

Several features of the recovered material provide constraints on its origin and significance. The basalt shows typical textures (e.g., intersertal) and alteration (e.g., celadonite and smectite) of basalt recovered from the extrusive section of Hole 1256D and is likely derived from the upper part of the hole. In contrast, many of the granoblastic basalt and gabbro pieces are chips, some as thin as 0.5 mm, suggesting they were broken off of the borehole wall by the bit during drilling, reaming, and fishing runs. Some of these gabbros (Sample 335-1256D-Run11-EXJB; Thin Section 12) are similar to rocks recovered during Expedition 312; they are characterized by finer grained subophitic to poikilitic gabbro domains and coarser grained oxide gabbro domains, the same domains that predominate in Gabbro 1 (Koepke et al., 2011). However, many other gabbros (including the large olivine gabbro block) are unlike those recovered during Expedition 312 in that they are characterized by relatively simple, single igneous domain textures, in contrast to Gabbro 1 and Gabbro 2. In addition, their clinopyroxene is unusually dark in color, giving the rock a distinct black-and-white appearance. These observations suggest that many of the recovered gabbros represent a unit that was not previously recovered in Hole 1256D. Hence, it is most likely that, with the exception of the basalt and some of the gabbro chips recovered during Run 11, most of the material recovered from the junk baskets originates from near the bottom of the hole, below the section recovered during Expedition 312 (1507 mbsf) (Teagle, Alt, Umino, Miyashita, Banerjee, Wilson, and the Expedition 309/312 Scientists, 2006).

Igneous geology of rocks recovered during Expedition 335

The rocks recovered during Expedition 335 represent a ~15 m interval of the transition zone from the upper to the lower crust. Several observations constrain the igneous geology of this interval. First is the relative abundance of the different rock types, with granoblastic basalts forming the vast majority of the rocks recovered. The second observation is that the mineralogy, granoblastic texture, and preservation of dike/dike contacts and phenocrysts suggest that the granoblastic basalts are sheeted dikes that have been recrystallized. The peak metamorphic assemblage of orthopyroxene-clinopyroxene-plagioclase without amphibole in the granoblastic basalts suggests recrystallization occurred at granulite facies temperatures. The third observation is that the granoblastic basalts have been intruded by a series of small-scale patches, veins, and dikelets of evolved rocks (predominantly oxide diorite and tonalite). In addition, numerous chips and a single block of gabbroic rock were recovered, the contact relationships of which cannot be established unambiguously. However, because most gabbroic rocks do not resemble gabbroic rocks recovered during Expedition 312 (see **"Origin of junk basket material"**), it is likely that least some of the gabbroic rocks occur intercalated with the granoblastic basalt, perhaps forming small intrusions. Although we cannot constrain the maximum size of the intrusions, the relatively low percentage of intrusive rocks in the junk basket material suggests that the plutonic rocks did not form large intrusive bodies. Rather, they are likely restricted to small (tens of centimeters?) bodies.

Overall, a picture emerges of a section of metamorphosed granoblastic sheeted dikes that underwent small-scale intrusion by both gabbroic and evolved plutonic rocks. This section is very similar to the dike screen recovered between Gabbro 1 and Gabbro 2 during Expedition 312 at 1458.9–1483.1 mbsf (Tea-

gle, Alt, Umino, Miyashita, Banerjee, Wilson, and the Expedition 309/312 Scientists, 2006).

Geochemistry

During Expedition 335, whole-rock chemical analyses were performed on three granoblastic basalts from Cores 335-1256D-235R through 238R and on one basalt, five granoblastic basalts, and two gabbroic rocks retrieved during junk basket runs. These samples are representative of the rock types recovered from Hole 1256D during Expedition 335. They were chosen from the least altered parts of the core and rock samples, as far as possible from hydrothermal veins and magmatic intrusions, in order to obtain the best estimate of primary compositions. Where possible, a thin section was taken next to the geochemistry sample for detailed petrographic characterization (see **"Igneous petrology"** and **"Alteration and metamorphism"** for thin section petrographic description). The 11 rock samples were analyzed for major and trace element concentrations and H_2O and CO_2 contents following standard shipboard procedures (see **"Geochemistry"** in the "Methods" chapter [Expedition 335 Scientists, 2012b]). Table **T7** lists the geochemical analyses collected during Expedition 335.

Basalt

Sample 335-1256D-Run02-EXJB, a basalt, was retrieved from Hole 1256D at a maximum depth of 923 mbsf, during junk basket Run 2. The sample was prepared from roughly 1 cm size gravel, by careful separation of the gravel from the sand that constituted most of the junk basket material. No thin section was taken.

Sample 335-1256D-Run02-EXJB is characterized by a loss on ignition (LOI) of 1.22 wt%, H_2O of 2.6 wt%, and CO_2 of 0.12 wt%. These values suggest that this sample has been altered and are the highest H_2O and CO_2 measured during Expedition 335. As illustrated in Figure **F30,** LOI and H_2O in all measured samples are positively correlated, although the measured H_2O is significantly higher than LOI values. LOI slightly underestimates the total volatile content because of the conversion of Fe^{2+} to Fe^{3+} during heating of the sample powders to 1020°C (see **"Geochemistry"** in the "Methods" chapter [Expedition 335 Scientists, 2012b]). However, this cannot be the sole explanation for this difference. During Expedition 335, the unresolved overlap of the water peak with sulfur in gas chromatography leads to a systematic 20%–30% overestimate of water contents in standards (see **"Geochemistry"** in the "Methods" chapter [Expedition 335 Scientists, 2012b]) and to a large uncertainty in the actual water content of the measured samples. Indeed, the measured water content in Sample 335-1256D-Run02-EXJB is significantly higher than published H_2O values for Hole 1256D samples (H_2O from 0.58 to 1.65 wt% in variably altered basalt; Shilobreeva et al., 2011). The water measurements are therefore considered as qualitative and will not be further discussed.

The measured CO_2 concentration in Sample 335-1256D-Run02-EXJB (0.116 wt%) is higher than other samples measured during Expedition 335 (0.03–0.07 wt%) (Fig. **F30**). This slightly higher value does not correlate with higher Ca and Sr contents compared to Site 1256 basalts or to Expedition 335 samples, which would indicate the presence of carbonate minerals in this altered sample. It is, however, in the same range of values as the basalt that constitutes the upper volcanic section of Hole 1256D (0.05–0.25 wt%; Shilobreeva et al., 2011). This suggests some variability in the CO_2 content in the volcanic section.

Sample 335-1256D-Run02-EXJB overlaps in major and trace element composition with the basalt sampled in the volcanic section of Hole 1256D (above 1004 mbsf) (Figs. **F31, F32, F33**). It has a typical mid-ocean-ridge basalt (MORB) tholeiite composition with SiO_2 concentrations of 50.4 wt%, (Na_2O + K_2O) of 2.91 wt%, Mg# (cationic Mg/(Mg + Fe) ratio with all Fe as Fe^{2+}) of 58, and relatively low trace element contents (e.g., Zr = 77 ppm, Y = 32 ppm, and Sr = 88 ppm). However, Sample 335-1256D-Run02-EXJB is distinguished by low concentrations of CaO and Zn and higher concentrations of Ba (24 ppm) relative to the previously analyzed Hole 1256D basalts at a given MgO concentration. These differences suggest slight albitization of plagioclase (Ca loss and Na gain) associated with the circulation of hydrothermal fluids (leaching of Zn and transport of fluid mobile elements such as Ba). Similar chemical variations were previously observed in the lower part of the volcanic section and are associated with low-temperature alteration of basalt and precipitation of hydrous minerals (Wilson, Teagle, Acton, et al., 2003; Teagle, Alt, Umino, Miyashita, Banerjee, Wilson, and the Expedition 309/312 Scientists, 2006; Alt et al., 2010). The lack of a thin section does not allow confirmation of this interpretation for Sample 335-1256D-Run02-EXJB. However, these similarities in composition lead us to suggest that Basalt 335-1256D-Run02-EXJB is derived from the lower part of the drilled volcanic section at Hole 1256D.

Granoblastic basalts

The granoblastic basalts have LOI of –0.369 to 0.273 wt% and H_2O of 0.54 to 1.2 wt%, and their CO_2 contents vary between 0.01 and 0.048 wt% (Fig. F30). The small to negative LOI, together with the low CO_2 contents, shows that these rocks were not heavily affected by late alteration processes.

The cored granoblastic basalts and the junk basket samples overlap in composition. They have 7.2–8.7 wt% MgO, 48.5–50.8 wt% SiO_2, 13.9–15.1 wt% Al_2O_3, 9.7–12.4 wt% FeO, and 11.4–12.3 wt% CaO (Fig. F31). As illustrated in Figures F32 and F33, they have relatively homogeneous compositions in most minor (e.g., Sc = 47–51 ppm) and trace (e.g., Ba = 9–12 ppm; Sr = 71–82 ppm; Y = 19–33 ppm) elements and Zr (31–58 ppm). Only Cr shows more variable concentrations, ranging from 88 to 165 ppm. These concentrations do not follow the trend of other data; they are interpreted as evidence of variable amounts of a minor Cr-rich phase.

The samples analyzed overlap in composition with those of the sheeted dike complex and of the granoblastic dikes previously sampled in Hole 1256D, which span the entire range of composition of the basalt that composes the volcanic section. Similar to the dikes sampled during previous expeditions (Teagle, Alt, Umino, Miyashita, Banerjee, Wilson, and the Expedition 309/312 Scientists, 2006), the composition of the granoblastic basalts sampled during Expedition 335 is consistent with fractionation of the MORB melts, which formed the entire section of oceanic crust sampled by Hole 1256D.

Two of the junk basket samples, 335-1256D-Run12-RCJB-Rock B and 335-1256D-Run19-RCJB-Rock C, are distinguished by slightly higher FeO (13.3–14.2 wt%) and lower CaO (9.6–10.2 wt%) and Ca# (cationic Ca/(Ca + Na) = 66–69) compared to other Expedition 335 granoblastic basalts (FeO = 9.7–12.3 wt%; CaO = 11.4–12.3 wt%; Ca# = 72–75) and Hole 1256D granoblastic dikes (Fig. F31). Sample 335-1256D-Run12-RCJB-Rock B also has the highest TiO_2 (1.6 wt%) and V (480 ppm) concentrations. Higher oxide modal contents could explain the variations of FeO, TiO_2, and V (see Thin sections in "Core descriptions") but not the lower values of Ca#. Samples 335-1256D-Run12-RCJB-Rock B and 335-1256D-Run19-RCJB-Rock C are both crosscut by dioritic hornblende–rich veins. Although Expedition 335 shipboard analyses were carried out on material collected as far as possible from those veins, samples may have been contaminated by these more evolved melts. This process is generally associated with an increase in incompatible trace element concentrations, but we do not observe significant changes of the minor and trace element concentrations in these samples. Another possible explanation of these slight differences in composition is a higher degree of interaction with hydrothermal fluids in these samples compared to the other granoblastic basalts sampled during Expedition 335. This process would have led to albitization of the plagioclase. This explanation is consistent with the higher LOI of these two samples, the highest of the granoblastic basalts sampled during Expedition 335. Petrographic description of the thin section does not provide supporting evidence for this interpretation, although both samples show some degree of hydration. Further constraints (e.g., in situ chemical analyses) will require shore-based studies.

A common characteristic of the granoblastic basalts sampled during Expedition 335 is their depleted Cu, Zn, Zr, and Y compositions compared to those of previously sampled basaltic samples in Hole 1256D. These elements plot at the low concentration end of the field of composition of the granoblastic dikes and sheeted dikes (Figs. F32, F33). These variations in composition appear correlated to depth and will be discussed later in this section (see "Downhole chemical variations").

Gabbroic rocks

Two gabbroic rocks were analyzed during Expedition 335: Sample 335-1256D-Run11-EXJB, an olivine gabbronorite, and Sample 335-1256D-Run20-RCJB-Rock C, an olivine gabbro. They were retrieved from Hole 1256D during junk basket runs. Compared to granoblastic basalts, both samples overlap in composition for CO_2 (0.035–0.07 wt%) but have high LOI values (0.815–1.16 wt%), which are most likely related to secondary alteration mineral assemblages observed in these samples (chlorite and minor smectite; see Thin sections in "Core descriptions") and imply that they were more affected by hydrothermal alteration compared to the neighboring granoblastic basalts (see "Alteration and metamorphism").

The analyzed gabbros have relatively high concentrations of MgO (11.21–12.24 wt%), Cr (450–750 ppm), and Ni (230–350 ppm) and low concentrations of trace elements such as TiO_2 (0.69–0.72 wt%) and Y (16 ppm) compared to granoblastic basalts (Figs. F31, F32, F33, F34). In contrast with Gabbro 1 and Gabbro 2 from Expedition 312, Expedition 335 gabbroic rocks are quite distinct from the granoblastic basalts with respect to trace elements. They overlap in composition with gabbros sampled in other oceanic environments, and their compositions are consistent with formation as cumulates from a parental MORB melt. Their relatively high Mg# (70–72)

and distinctly high Ni (230–350 ppm) reflect the slight variations in modal olivine in the samples.

As illustrated in Figure **F34**, Expedition 335 gabbroic rocks overlap in composition with the least evolved gabbros previously sampled in Hole 1256D. These gabbros were found only in the Gabbro 1 interval. This characteristic could be used to infer the origin of the junk basket samples as being in the Gabbro 1 interval. All less evolved gabbros in Hole 1256D are characterized by the presence of olivine. Olivine was also described during Expedition 335 (see **"Igneous petrology"**) in the samples from the Gabbro 2 interval, but these samples were not analyzed. Therefore, existing geochemical data cannot rule out an origin of the two analyzed gabbroic rocks from this interval or even from below.

Downhole chemical variations

The lower part of Hole 1256D, below 1340 mbsf, is characterized by strong chemical variations with, for example, Mg# ranging from 42 to 72 ppm and Zr from 23 to 117 ppm (Fig. **F35**). These changes in composition mainly reflect the changes in rock types from the low-Mg#, trace element–rich sheeted and granoblastic dikes and dike screens to the higher Mg# and trace element–depleted gabbroic rocks of Gabbro 1 and Gabbro 2. However, there are significant depth-dependent trace element variations in the granoblastic basalts.

There is a general downhole trend of decreasing incompatible element contents (i.e., Zr and, to a lesser extent, Y) in the granoblastic basalts, with Zr ranging from 73 to 110 ppm above Gabbro 1, from 47 to 86 ppm in Dike Screen 1, and from 15 to 58 ppm in Dike Screen 2 (Fig. **F35**). At a smaller scale, granoblastic basalts sampled within Dike Screens 1 and 2 define a trend of increasing Zr with depth, with the lowest Zr values always found in the upper part of the dike screens. This pattern is particularly marked at the bottom of Hole 1256D, where the most depleted granoblastic basalts (15 ppm Zr; Yamasaki et al., 2009) were sampled at 1502 mbsf, just below Gabbro 2. Expedition 335 samples show increasing Zr contents from ~30 ppm at 1507–1512 mbsf to 58 ppm in Sample 335-U1256D-238R-1W, 15–17 cm, at 1518 mbsf. These downhole variations in incompatible element contents are illustrated by changes in Zr/Y; the most depleted samples from below Gabbro 2 have low Zr/Y (~1.5) compared to the sheeted dikes and granoblastic dikes above Gabbro 1 (Zr/Y = 2–3). Zr and Y are generally considered as not being affected by alteration and can be used as indicators of magmatic processes. The relative depletion of the more incompatible Zr relative to Y is commonly interpreted as evidence of partial melting. The observed variations can be explained either by changes of composition or degree of partial melting at the source or as evidence for local remelting of the granoblastic basalts. Because no petrologic or chemical observations support a change within the mantle source, we favor local remelting of the granoblastic basalts. We interpret the systematic depletion observed in the granoblastic basalts just below both Gabbro 1 and Gabbro 2 as evidence of small degrees of partial melting, probably caused by the gabbroic intrusions into the partially hydrated dikes. The degree of partial melting is probably minor, as the effects on the major element compositions of the dikes are undetectable. However, partial melting appears to modify the incompatible element composition of the granoblastic basalts over significant distances: 10 m below Gabbro 1 and at least 18 m below Gabbro 2. This implies a perturbation of the local thermal conditions over a significant time period.

We also observe lower Zn and Cu compositions in the granoblastic basalts cored at the bottom of Hole 1256 compared to the sheeted dikes and granoblastic dikes sampled above Gabbro 1 (Fig. **F35**). These elements are commonly mobilized during hydrothermal alteration. Below Gabbro 2, granoblastic basalts have Cu and Zn contents of 20–47 and 25–47 ppm, respectively, compared to 50–100 ppm for Cu and 50–150 ppm for Zn in the granoblastic dikes and sheeted dikes in the upper part of the borehole. A general decrease in Cu and Zn contents was also observed in the lower part of the sheeted dike complex in Hole 504B (Alt et al., 1996). These elements are remobilized during high-temperature hydrothermal alteration (>350°C), which leaches Cu and Zn out of the rock (e.g., Alt et al., 1996). At the bottom of Hole 1256D, this process appears to affect mostly (only?) the granoblastic basalts. Hole 1256D gabbros do not show evidence of Cu and Zn depletion compared to other gabbroic suites: for example, Hole 1256D gabbroic rocks have Zn of 25–73 ppm compared to 10–70 ppm Zn in the gabbros and olivine gabbros sampled at Atlantis Massif (30°N Mid-Atlantic Ridge; Godard et al., 2009). They also have relatively high concentrations of these elements compared to the neighboring granoblastic basalts. This may imply that the injection of Gabbro 1 and Gabbro 2 occurred during or after this stage of high-temperature hydrothermal alteration. Although this hypothesis is consistent with the remelting process suggested to explain Zr/Y downhole variations, it cannot be conclusively demonstrated with the available shipboard data.

Most of the material sampled during Expedition 335 was recovered during junk basket runs, with no direct indication of their original depth. However, all of the

granoblastic basalt samples are depleted in Zr, Y, Cu, and Zn with low Zr/Y, similar to those of Dike Screen 2 (i.e., below 1497.5 mbsf). Therefore, the geochemistry of the granoblastic basalts sampled by the junk basket Runs 12–20 provides evidence that they come from the bottom of the borehole (at the Gabbro 2 lower interface and below) rather than from shallower levels. Although the gabbro geochemistry does not provide similarly strong indicators, gabbros sampled with the Expedition 335 junk baskets are also most likely derived from the same interval from the bottom of Hole 1256D below Gabbro 2.

Alteration and metamorphism

Summary of Expedition 312 results

Alteration of the plutonic section cored during Expedition 312 was reexamined during Expedition 335 by visual observation of the archive section halves, with estimations of secondary mineral abundances and primary mineral alteration in hand specimen calibrated by examination of thin sections and aided by previously published works (Teagle, Alt, Umino, Miyashita, Banerjee, Wilson, and the Expedition 309/312 Scientists, 2006; Koepke et al., 2008; France et al., 2009; Alt et al., 2010). These observations are recorded in the Expedition 335 alteration log and vein and halo log (see DESCLOGIK_WORKBOOKS _335(312) in DESCRIPTIONS in **"Supplementary material"**). The rocks display pervasive alteration as well as localized alteration effects. These are divided into

- Pervasive background alteration,
- Localized alteration patches,
- Recrystallized granoblastic basalt and recrystallized domains (xenoliths),
- Secondary mineral veins, and
- Alteration halos along veins.

Figure **F36** summarizes the distribution of alteration textures and recrystallized domains (xenoliths) versus depth in the plutonic section, and Figure **F37** summarizes the overall distribution of secondary minerals versus depth.

The alteration history of the plutonic section penetrated during Expedition 312 involves hydrothermal alteration of sheeted dikes in a mid-ocean-ridge axial hydrothermal system, intrusion of gabbro bodies into hydrothermally altered sheeted dikes, and contact metamorphism of the intruded dikes, followed by crystallization of the gabbros, cooling, injection of late-stage dikes, and hydrothermal alteration of gabbro and early and late-stage dikes, with superimposition of greenschist-grade alteration on previously metamorphosed dikes (Teagle, Alt, Umino, Miyashita, Banerjee, Wilson, and the Expedition 309/312 Scientists, 2006; Koepke et al., 2008; France et al., 2009; Alt et al., 2010).

Background alteration

Coarser grained (gabbroic) and finer grained (dikes) rocks exhibit pervasive background alteration (Fig. **F38**). Gabbroic rocks are typically dark gray and moderately (10%–50%) altered but range from highly to completely altered locally. More intense alteration is commonly associated with coarser grained areas, igneous contacts, and leucocratic rocks.

Figure **F39** shows the major mineralogy of primary phase replacement in the background alteration. Olivine is partially to totally altered to smectitic phyllosilicates ± red Fe oxyhydroxide, talc, and magnetite, with local outer rims of pale blue-green and colorless amphibole and minor chlorite. Clinopyroxene is typically moderately altered to green amphibole with common small (~1–10 µm) inclusions of magnetite. Slightly altered clinopyroxenes have clear cores that give way outward to dusty corroded rims and then amphibole replacement and overgrowth. Brown amphibole occurs locally in interstitial areas and as patches within clinopyroxene and may be of late igneous origin. Plagioclase is generally less altered than clinopyroxene and is partially altered to secondary plagioclase (albite), amphibole, chlorite, prehnite, laumontite, and epidote. Orthopyroxene, where present, is partially altered to smectitic phyllosilicates and green and colorless amphibole. Titanomagnetite exhibits ilmenite exsolution lamellae and is typically partially to highly replaced by titanite. Recrystallized igneous sulfide globules are common in interstitial areas and as inclusions in plagioclase and rarely in amphibole replacing clinopyroxene.

The last pieces of core recovered during Expedition 312 (Section 312-1256D-234R-1 [Pieces 4–8]) are dark greenish gray, with clinopyroxene altered to dusty clinopyroxene, amphibole, chlorite, and secondary plagioclase. The presence of primary intergranular igneous texture and the absence of granoblastic recrystallization indicate that the core represents a late dike.

Alteration patches

Alteration patches are zones that are more intensely altered than the background alteration and are typically 50%–90% altered (average = 60%) (Fig. **F40**). The patches range from <1 to >3 cm across and range from round to irregular, elongate, and network shaped. Most of the gabbros exhibit patchy altera-

tion, averaging ~8% of the recovered gabbro cores, but patches are more abundant in Gabbro 1, where they commonly form interconnected networks in the uppermost 5 m. Patches range from dark to light gray or green to white for more felsic patches (Fig. F41). Secondary mineralogy of the patches is generally similar to background alteration (Fig. F42), but patches can locally contain abundant epidote.

Recrystallized basalts and recrystallized domains

The dike screens consist of fine-grained basalts that are strongly to completely recrystallized to granoblastic assemblages of clinopyroxene, plagioclase, orthopyroxene, ilmenite, and magnetite ± olivine. Fragments of these recrystallized rocks are incorporated into the gabbro units (Fig. F36). These fragments are xenoliths or stoped blocks of recrystallized dike rock, may be variably resorbed by the magma, and are referred to here as recrystallized domains. These domains are strongly to completely recrystallized to granoblastic assemblages as in the recrystallized dikes. They range from centimeter-scale streaks and areas to several centimeter–sized angular blocks and are most common near the margins of Gabbro 2. Recrystallized domains exhibit slight to locally strong postrecrystallization hydrous alteration to amphibole, albite, and smectite.

Veins and vein-related alteration halos

The gabbros average 10 veins/m recovered core, compared to ~35 veins/m in the sheeted dikes (Figs. F43, F44, F45). Among the earliest generation of veins are green amphibole veins with diffuse boundaries. These veins are narrow (<0.1 mm) and are defined by amphibole replacement of clinopyroxene in a narrow (1–2 mm) amphibole-rich halo in the wall rock. These veins are cut by discrete 0.5–1 mm green amphibole veins that also have amphibole alteration halos. Also early are narrow (typically ~1 mm but as wide as 5 mm) quartz ± amphibole ± plagioclase veins. In some cases these veins may be hydrothermal in origin, but in others they are related to late magmatic fluids (Alt et al., 2010). Veins of epidote, quartz, and prehnite, with intensely altered chloritic margins, are present locally. Relationships are not always clear in hand specimen, but these veins cut or fill centers of earlier amphibole veins (Teagle, Alt, Umino, Miyashita, Banerjee, Wilson, and the Expedition 309/312 Scientists, 2006; Alt et al., 2010).

The dike screens contain ~15–30 veins/m, most with halos. The first generation of post-contact metamorphic veins is wispy <0.1 mm amphibole veins, with diffuse 1–2 mm amphibole-rich halos. These veins are cut by later amphibole veins bounded by actinolite-rich alteration halos. Later chlorite-actinolite, quartz-chlorite, and quartz veins with 1–2 mm chloritic margins cut the earlier veins.

Expedition 335 Sections 335-1256D-235R-1 through 239R-1

Sections 335-1256D-235R-1 through 239R-1 comprise dark gray, fine-grained, recrystallized basalt and are essentially identical to the granoblastic basalts from Dike Screen 2 in the Expedition 312 plutonic section. Also present are local pieces of coarser grained plutonic material. Similar recrystallized basalt in the junk baskets (see **"Expedition 335 junk baskets,"** below) retains chilled contacts and textures of brecciated dike margins and most likely came from near the bottom of the hole, indicating that Expedition 335 cores and junk basket samples are part of a dike screen within the plutonic section, most likely Dike Screen 2.

Granoblastic basalts

The dike screens are recrystallized material consisting of fine-grained to very fine grained basalt recrystallized to granoblastic assemblages of clinopyroxene, orthopyroxene, plagioclase, magnetite, ilmenite, and rare brown hornblende and quartz. These rocks are essentially identical to similar rocks described from the Expedition 312 plutonic section (Teagle, Alt, Umino, Miyashita, Banerjee, Wilson, and the Expedition 309/312 Scientists, 2006; Koepke et al., 2008; Alt et al., 2010) and exhibit a similar degree of recrystallization (Figs. F46, F47). The rocks are completely recrystallized mineralogically but exhibit variable degrees of development of granoblastic textures and concomitant loss of original igneous textures (Fig. F48). The degree of development of granular texture ranges from partial to complete and is highly variable from one sample to another (Fig. F47). Several factors influenced recrystallization, including initial grain size, the type and extent of hydrous alteration of the protolith, and the temperature and duration of reheating.

Magnetite and ilmenite occur as equant, discrete grains, and ilmenite is also present as segregations or lamellae within magnetite in some samples. Local 100–200 µm wide veins of orthopyroxene are present and probably represent preexisting hydrothermal veins in the protolith that were subsequently recrystallized during contact metamorphism (Fig. F48C).

Sulfide minerals, including pyrite, chalcopyrite, and pyrrhotite, are present in trace amounts. Sulfides, which may be recrystallized igneous grains or preex-

isiting secondary sulfides that were recrystallized during contact metamorphism, occur in interstitial areas and as tiny inclusions in plagioclase and rarely in clinopyroxene and appear adjacent to orthopyroxene veins. Sulfide minerals that are likely related to post-contact metamorphism hydrothermal alteration occur along grain boundaries, in coronae around and in amphibole replacing clinopyroxene and orthopyroxene, and disseminated outside alteration halos along amphibole veins.

The recrystallized basalts are generally only slightly altered by subsequent hydrous alteration but are locally moderately to highly altered (e.g., Samples 335-1256D-236R-1, 0–4 cm, and 238R-1, 13–15 cm). Clinopyroxene is variably altered to amphibole plus variable but minor amounts of magnetite and to local chlorite (Fig. F49). Orthopyroxene is partly altered to amphibole and local talc and smectite. Plagioclase is less altered than pyroxenes but is slightly altered to actinolite, secondary plagioclase, clays, and local chlorite veinlets and to rare epidote, prehnite, zoisite, and quartz. Ilmenite is variably replaced by titanite.

Sample 335-1256D-236R-1, 0–4 cm, contains a contact between fine-grained felsic material and typical granoblastic basalt. The felsic material is highly altered, with pyroxene replaced by amphibole, magnetite, and chlorite. Plagioclase is altered to secondary plagioclase and minor chlorite and clays. Magnetite is altered to titanite. Also present are poikiloblasts of epidote. Alteration of granoblastic material is generally more intense around intrusions (Fig. F49B).

Veins and halos

The most common veins contain amphibole (actinolite and/or hornblende) and range from ~10 µm to 1.5 mm wide (Figs. F50, F51, F52). Small (~10 µm) veins of amphibole (predominantly actinolite) are common throughout most thin sections. A characteristic of these tiny amphibole veins is that clinopyroxene and in some cases plagioclase are replaced by amphibole where cut by the veins. Larger amphibole veins (as wide as 0.5 mm) display ~1–5 mm wide amphibole-rich alteration halos in the wall rock, where clinopyroxene and orthopyroxene are replaced by amphibole (Fig. F51). In some cases, the larger amphibole veins also contain chlorite and titanite. In some samples, the ~10 µm actinolite veins cut across the larger amphibole veins. Sample 335-1256D-236R-1, 0–4 cm, contains a 300–400 µm wide vein of actinolite + epidote + chlorite that grades into a 500 µm wide vein lined with chlorite and filled with prehnite enclosing needles of actinolite (Fig. F52B). This vein cuts across and offsets a contact between felsic and granoblastic materials in this sample. Quartz + amphibole is present in a 1–2 mm wide vein in Section 335-1256D-235R-1 (Piece 6). Carbonate is present with quartz in a 1 mm wide vein along the edge of Sample 335-1256D-236R-1, 31–32 cm.

Coarse-grained material

Only limited coarse-grained material was recovered in the Expedition 335 cores. This material (e.g., Sample 335-1256D-235R-1, 23–35 cm [Piece 5]) consists of foliated diorite hosting a leucocratic tonalite vein that is in turn cut by an amphibole vein (Fig. F53). The background consists of moderately altered foliated diorite, where amphibole replaces clinopyroxene and igneous amphibole. Plagioclase appears cloudy and is altered to secondary plagioclase, chlorite, and rare epidote and zeolite. Quartz and apatite are also present. Titanomagnetite is highly altered to titanite. The main part of the section consists of a leucocratic magmatic vein that is similarly moderately altered to amphibole and plagioclase, but plagioclase is more cloudy and altered than in the host rock. A ~1 mm vein is present in the central part of the leucocratic vein and is composed of amphibole + quartz + epidote + plagioclase + magnetite. A 3 mm clot of epidote is present in one area of the vein.

Expedition 335 junk baskets

Rock samples were recovered in junk basket Runs 11–22. The rocks are mainly pebbles to cobbles of fine-grained basalt recrystallized to granoblastic assemblages. Also present are fine-grained platy fragments exhibiting granoblastic recrystallization; coarser grained fragments of olivine gabbronorite, oxide gabbro, and quartz diorite; and dark gray to black fine-grained basalt fragments.

The dark gray to black basalt fragments have igneous textures of basalt lava, and smectite coating fracture surfaces on one piece was identified by X-ray diffraction. These observations are consistent with these samples falling to the bottom of the hole from the volcanic section.

Volcanic basalt aside, the rocks in the junk baskets are similar to those recovered from the lower granoblastic dikes and dike screens during Expedition 312. The rocks are mainly granoblastic basalts, including dike margins (see below), with local small (0.1–3 cm) intrusions of coarse-grained gabbro and more differentiated material. The lithology, angularity, and large size (>10 cm) of many blocks in the junk baskets suggest that the majority of this material fell into the hole from the lowermost ~10 m of the hole. These rocks thus provide a greater sampling and fur-

ther view of the rocks from these depths than a single one-dimensional drill core.

Recrystallization of granoblastic basalts

The main lithology from the junk baskets consists of basalt recrystallized to granoblastic assemblages of clinopyroxene, orthopyroxene, plagioclase, magnetite, ilmenite, and rare brown hornblende and quartz. These are essentially identical to the granoblastic basalts cored in Dike Screens 1 and 2 during Expeditions 312 and 335. Clinopyroxene and orthopyroxene are totally recrystallized and contain common round magnetite inclusions. Magnetite and ilmenite are completely recrystallized and are present as equant, discrete mineral grains or as domains of one mineral within the other. Sulfide minerals (pyrite, chalcopyrite, and pyrrhotite) are present in interstitial areas, in coronas around pyroxenes, as inclusions in plagioclase, and, rarely, in clinopyroxene and orthopyroxene. Linear trails or bands (tens to ~100 µm wide) of orthopyroxene and plagioclase or orthopyroxene and clinopyroxene are present locally (e.g., in Sample 335-1256D-Run11-EXJB-J1) and are probably recrystallized hydrothermal veins.

Orthopyroxene veins (100–200 µm wide), similar to those in the Expedition 335 cores, are present in several samples from the junk baskets (e.g., Figs. **F48C, F49C, F50A**). These orthopyroxene veins are commonly interconnected, similar to the hydrothermal vein networks present in some upper dike samples from Expedition 312 (Teagle, Alt, Umino, Miyashita, Banerjee, Wilson, and the Expedition 309/312 Scientists, 2006; Alt et al., 2010).

Sample 335-1256D-Run12-RCJB-Rock S consists of a fine-grained dike chilled against a relatively coarser grained dike (Fig. **F54**). The entire sample is recrystallized to a granoblastic assemblage, and later fine amphibole veins cut across the contact and both dikes. Local 0.5 mm thick plagioclase-rich banding in the chilled margin may represent previous hydrothermal veins or possibly relate to flow structures and alteration of the chilled margin protolith. Aggregates of sulfide minerals (as large as 250 µm of pyrite, chalcopyrite, pyrrhotite, ± magnetite) are common in the chilled margin and in the plagioclase-rich bands and may be recrystallized hydrothermal grains.

Two samples (335-1256D-Run12-RCJB-Rock Q and 335-1256D-Run14-EXJB-Foliated) exhibit granoblastic recrystallization but also display a 1–10 mm banded texture. The bands comprise plagioclase-rich, orthopyroxene-rich, and oxide-rich zones. Sample 335-1256D-Run14-EXJB-Foliated comprises recrystallized breccia (Fig. **F55**). Angular 5–10 mm clasts consist of granoblastic plagioclase with minor clinopyroxene, orthopyroxene, magnetite, and ilmenite. The protolith of this material was probably altered fine-grained chilled margin material. The matrix is orthopyroxene rich, with minor clinopyroxene, plagioclase, and oxides, and forms ~5 mm wide bands separating the plagioclase-rich clasts. The orthopyroxene-rich material likely recrystallized from hydrothermal minerals (e.g., amphibole and chlorite) veining and cementing the breccia protolith. More typical granoblastic material forms one end of the thin section, and the other consists of coarser grained orthopyroxene- and plagioclase-rich granoblastic material with typical magnetite and ilmenite and with abundant intergrown pyrite, chalcopyrite, pyrrhotite, and magnetite. The texture and abundance of sulfide minerals are similar to those in mineralized dike margins from shallower in the Expedition 309/312 dike sections (e.g., figs. F61 and F62 in Expedition 309/312 Scientists, 2006; Alt et al., 2010). Other samples (335-1256D-Run12-RCJB-Rock C and 335-1256D-Run12-RCJB-Rock T) exhibit less distinct compositional banding, which may be related to intense prerecrystallization hydrothermal veining and alteration of the protoliths.

Rocks from Sample 335-1256D-Run11-EXJB comprise equant to platy basalt fragments, 1–3 cm thick by as much as 7 cm × 10 cm across. Several samples have stepped edges defined by veins and fractures. Aside from a few stray basalt fragments from the volcanic section, these rocks are recrystallized to granoblastic assemblages with slight later hydrous alteration and amphibole veins, as described above. Some samples consist of several centimeter–sized platy fragments of extremely fine grained, hard, microcrystalline material (possibly basaltic). The abundance of veins and fractures and the platy morphology of most of these rocks suggest two possibilities: (1) there is a highly fractured and veined interval in the wall rock at approximately this depth or (2) this material may be typical granoblastic dike material at this site, which has low recovery because the abundant fractures cause the rock to break up and be ground up during drilling.

Postrecrystallization alteration of granoblastic basalt

The granoblastic rocks typically exhibit at most only slight alteration (generally <15%) to hydrous minerals, mainly amphibole (Figs. **F45, F46**). Clinopyroxene is locally partly altered to amphibole, orthopyroxene is variably altered to amphibole and local talc and smectite, and plagioclase is locally slightly altered to trace chlorite and actinolite and to secondary plagioclase and clays (likely smectite). Fe-Ti oxides are partly altered to titanite. The granoblastic

rocks are more highly altered in 1 mm wide alteration halos along amphibole veins. Clinopyroxene and orthopyroxene in these alteration halos are highly to completely replaced by amphibole, whereas plagioclase is generally unaltered or may be slightly altered to actinolite and trace chlorite. Sulfide minerals (pyrite, pyrrhotite, and minor chalcopyrite) are locally common in minor amounts disseminated in the wall rock along amphibole veins. In some cases, the granoblastic rocks are more altered where associated with intrusions of coarser grained rock (Fig. **F49B**). For example, Sample 335-1256D-Run11-EXJB-J6 contains diorite intruding granoblastic rock, and the host rock is highly altered, with clinopyroxene highly altered to amphibole.

The granoblastic material sampled by the junk baskets contains common hydrothermal veins, the most common being filled with amphibole (actinolite and/or hornblende). Amphibole veins range from ~10 µm to 1 mm in width. The most abundant veins occur as tiny cracks filled with amphibole, but the distinguishing characteristic is the presence of amphibole replacing clinopyroxene and orthopyroxene that are cut by the tiny cracks (Fig. **F50**). These micrometer-sized actinolite veins cut recrystallized (granoblastic) veins and mixed amphibole-chlorite veins. The larger amphibole veins have 1 mm wide (rarely as wide as 4 mm) amphibole-rich alteration halos. Chlorite and rarely later prehnite are also present in veins. The density of veins is variable, but vein nets occur in several samples (e.g., in Sample 335-1256D-Run12-RCJB-Rock F). Epidote and quartz are present in three veins in Sample 335-1256D-Run11-EXJB, as 1.5–2 mm wide veins of quartz + epidote ± chlorite and in a 0.4 mm vein of quartz + amphibole + epidote.

Alteration of coarser grained lithologies

Gabbro is present as coarser grained fragments of amphibole-rich oxide-gabbronorite in Samples 335-1256D-Run11-EXJB-J5 and 335-1256D-Run11-EXJB-TS#29 as a centimeter-scale intrusion into a granoblastic host (Sample 335-1256D-Run12-RCJB-Rock B) and as equant to elongate and irregular intrusions linked by amphibole veins in large cobbles in Sample 335-1256D-Run14-FTJB. Similar coarse-grained intrusions are present in some small fragments (e.g., Sample 335-1256D-Run13-RCJB). Clinopyroxene is highly altered to amphibole plus minor magnetite and chlorite (Fig. **F56**). Plagioclase in the gabbroic rocks is partly altered to secondary plagioclase and minor amphibole, chlorite, clay, prehnite, and epidote. Sulfide minerals (chalcopyrite and pyrrhotite) are locally common in interstitial areas as inclusions in ilmenite and plagioclase, intergrown with amphibole, and in tiny veinlets. Ilmenite-magnetite is altered to titanite. Olivine is abundant in Sample 335-1256D-Run11-EXJB and is altered to magnetite, talc, amphibole, chlorite, and smectite in coronitic textures. Rare smectite associated with iron oxide in hand specimens (Sample 335-1256D-Run14-EXJB) indicates the presence of altered olivine or orthopyroxene.

Oxide-rich quartz-diorite is present locally as 0.5–2 cm wide intrusions (patches and veins; Samples 335-1256D-Run11-EXJB-J6 and 335-1256D-Run13-RCJB-Rock A). A few coarse-grained leucocratic veins and pebbles, cuttings and pebbles of tonalite, and a coarse-grained quartz diorite pebble are present in Samples 335-1256D-Run13-RCJB, 335-1256D-Run14-EXJB, and 335-1256D-Run17-BSJB. These felsic rocks are highly altered, with plagioclase highly altered to secondary plagioclase, minor chlorite, epidote, and local prehnite and quartz. Clinopyroxene and primary amphibole are highly altered to amphibole + magnetite, and minor orthopyroxene is replaced by talc and smectite. Fe-Ti oxides are slightly altered to titanite. Interstitial quartz contains needles of actinolite. Zircon, apatite, and rare biotite are also present.

Thin section observations reveal that some pebbles of leucocratic material are plagioclase rich (>90%), consisting of granular plagioclase with minor Fe-Ti oxide, apatite, and clay and local larger crystals of phenocryst-like plagioclase. The unusual textures and mineralogy suggest that these rocks may be metasomatized dikes.

Veins within the coarser grained lithologies are rare. In thin section these are only observed where coarse material intrudes granoblastic material, with amphibole veins that extend through the granoblastic host rock and cut across the coarser grained intrusive material.

Expedition 335 rocks

The cores and rocks recovered during Expeditions 312 and 335 sample the transition from sheeted dikes to the gabbroic section of oceanic crust. The dikes underwent hydrothermal alteration in a mid-ocean-ridge hydrothermal system at the spreading axis, at temperatures reaching >400°C, and with fluid compositions similar to those of black smokers venting at the seafloor (Alt et al., 2010). The hydrothermally altered dikes were then intruded by the two gabbro bodies cored during Expedition 312 and underwent contact metamorphism at temperatures of ~900°–1000°C, with the degree of recrystallization influenced by the effects of prior hydrothermal alteration (Teagle, Alt, Umino, Miyashita, Banerjee, Wil-

son, and the Expedition 309/312 Scientists, 2006; Koepke et al., 2008; France et al., 2009; Alt et al., 2010). Crystallization of the gabbro bodies and cooling of the gabbros and recrystallized dikes allowed penetration of fluids and hydrothermal alteration of the rocks, with formation of amphibole veins and later retrograde minerals (actinolite, quartz, epidote, chlorite, prehnite, and late smectite and iron oxyhydroxides).

The granoblastic dikes represent the conductive boundary layer between mafic magma and the overlying hydrothermal system, and the rocks from Hole 1256D are similar to those observed in ophiolites and elsewhere in oceanic crust (e.g., Gillis, 2008; France et al., 2009). The granoblastic basalts sampled beneath Gabbro 2 during Expedition 312 are part of a dike screen within the transition from sheeted dikes to gabbros. The rocks are more strongly recrystallized than Dike Screen 1 and similar to the granoblastic dikes above the gabbros.

Structural geology

The following observations were made on cores from Hole 1256D recovered during Expedition 312 between 1406.1 and 1507.1 mbsf (core), as well as cores (between 1507.1 and 1521.6 mbsf) and cuttings and cobbles from the lower part of the hole recovered during Expedition 335. Gabbroic and basaltic rocks with granoblastic textures (referred to hereafter as "plutonic rocks") display structures of magmatic, alteration, and metamorphic origins (Fig. **F57**). Structures occur both within granoblastic dikes and gabbroic rocks. All planar orientations are recorded as dip direction (000–360) and dip (0°–90°).

Reevaluation of macroscopic structures in the Hole 1256D plutonic section

We redescribed structures observed in the Expedition 312 plutonic cores to ensure consistency in the description for Hole 1256D plutonic rocks, following techniques and methods used to describe and document structures reported in **"Structural geology"** in the "Methods" chapter (Expedition 335 Scientists, 2012b).

The Hole 1256D plutonic section drilled during Expedition 312 (1406.1–1507.1 mbsf) comprises two gabbro units (Gabbro 1 and Gabbro 2) and basaltic rocks interpreted to be dike screens with granoblastic texture (Teagle, Alt, Umino, Miyashita, Banerjee, Wilson, and the Expedition 309/312 Scientists, 2006; Koepke et al., 2008). Observations were made and structural orientation measured on the archive section halves of Sections 312-1256D-213R-1 through 234R-1. The newly obtained results were compared with previous structural logs recorded during Expedition 312 (see STRUCTURE_LOGS_312_335 in DESCRIPTIONS in **"Supplementary material"**). Where discrepancies were found between the new observations and the Expedition 312 structure logs, further analyses were made on the archive section halves. The structure data log for the Expedition 312 plutonic section was revised to generate a coherent data set for the Hole 1256D plutonic section (see STRUCTURE_LOGS_312_335 in DESCRIPTIONS in **"Supplementary material"**).

In general, newly made observations and measurements were consistent with the Expedition 312 structural descriptions. Noticeable changes or additions are

- Orientations of newly identified internal boundaries in Gabbro 1 and Gabbro 2 (see **"Igneous petrology"**);
- Two-dimensional quantitative estimates of shape-preferred orientation (SPO) on oriented pieces of Gabbro 1; and
- Relogged brittle structures introducing the concept of subhorizontal irregular fractures (SIFs).

All structural observations were incorporated to generate the Structural synthesis column (Fig. **F58**). We also attempted to restore orientations of important structures into the geographic reference frame using available paleomagnetic data (see **"Structural geology"** in the "Methods" chapter [Expedition 335 Scientists, 2012b]) (see STRUCTURE_LOGS_312_335 in DESCRIPTIONS in **"Supplementary material"**). It must be noted that significant uncertainties in the reliability of reorientation of *individual* structures are likely, relating to assumptions made in the reorientation process. However, spatial coherence within different classes of reoriented data (e.g., fractures) suggests that the *distributions* of reoriented data provide first-order insights into primary structural trends in the geographic reference frame.

Some important new observations and reinterpretations of Expedition 312 cores made during Expedition 335 include the following:

- The tentative reoriented azimuths of the contact between sheeted Dike Screen 1 and Gabbro 2 and the internal contact between Units 81 and 82 of Gabbro 1 suggest that these units are steeply dipping toward the west-southwest (i.e., toward the spreading ridge). Other igneous contacts of minor igneous veins display moderate dips in various directions (Fig. **F59**).
- Veins in the Expedition 312 cores are variably oriented but are generally clustered into two popula-

tions (Fig. F60). One population is steeply dipping and the other is shallowly dipping; both have similar northwest–southeast strikes and dip mainly to the southwest (Fig. F61). Dark green veins tend to have steeper dips.

- The concept of SIFs was introduced to try to constrain drilling-induced fractures. Downhole fracture density is variable, with boundary zones between the gabbros and granoblastic dikes displaying higher fracture densities.
- Gabbro 1 consists of three distinct zones marked by different magnetic susceptibility and SPO of leucocratic patches. The distribution of plagioclase-rich patches in Gabbro 1 is consistent with porous melt flow through a crystal mush.

Structural measurements

During the redescription of Expedition 312 cores, a few mistakes in structural measurements and one computational error were identified in the previous structural logs. The error occurred with the computation program that translates two apparent dip and direction measurements to dip and dip direction of a planar structure, which was systematically used throughout Expedition 312. The mistakes were corrected in the revised structural data log (see STRUCTURE_LOGS_312_335 in DESCRIPTIONS in "Supplementary material") and uploaded into DESClogik.

Igneous contacts

Igneous contacts measured range from boundaries between units to magmatic veins (see "Igneous petrology" for discussion). The orientation of each contact was measured and recorded in the igneous petrology workbook on the Contacts tab. In the Expedition 312 core there are four major contacts in the plutonic section, where only two occur in oriented core pieces. The only geographically reoriented contact is the upper boundary of Gabbro 2 (Fig. F58). The upper boundary of Gabbro 1 was observed in an oriented piece, but no stable principal component of remanence was obtained; hence this boundary cannot be reoriented. The lower contact of Gabbro 1 was not recovered. The lower contact of Gabbro 2 was recovered, but the piece is not oriented.

The geographically reorientated azimuth of the contact between Dike Screen 1 and Gabbro 2 is 76°/255 on average (n = 3). The geographically reoriented azimuth of the internal contact between Units 81 and 82 in Gabbro 1 is 69°/237 (n = 1). The orientations of the preserved contacts suggest that they steeply dip toward the west-southwest (i.e., toward the spreading ridge). Other igneous contacts of minor igneous veins dip moderately to various directions (Fig. F59).

There are 10 oriented contacts between units within Gabbros 1 and 2 and within Dike Screen 1 (unit/unit contacts), which vary in orientation. Contacts range in dip from 15° to 72°, with the majority of the dips lying between 15° and 45° (n = 9). Contacts between magmatic veins and their host rocks are usually planar and sharp.

Magmatic and crystal-plastic fabrics

Magmatic fabrics, such as magmatic banding or textural banding, were remeasured. No major change was made in the description of Expedition 312, and data were uploaded into DESClogik, together with information from two-dimensional SPO analysis (see "Quantitative estimation of shape-preferred orientation of Gabbro 1"). Crystal-plastic fabrics (see STRUCTURE_SKETCHES_335 in DESCRIPTIONS in "Supplementary material") were reexamined, but detailed observation was not possible without the shipboard thin sections.

Quantitative estimation of shape-preferred orientation of Gabbro 1

The macroscopic fabric of gabbros in the plutonic section of Hole 1256D is overall isotropic, and in order to detect any possible downhole variation in magmatic fabric, we used an image analysis method to quantify SPO (Launeau et al., 1990) (see "Structural geology" in the "Methods" chapter [Expedition 335 Scientists, 2012b]). SPO was measured on zones with leucocratic patches from Gabbro 1 in the interval from 1410.9 to 1452.5 mbsf (Figs. F62, F63, F64). These leucocratic zones correspond to plagioclase-rich patches and clusters and are defined, for image analysis, by a digital threshold number > 60 on the grayscale image.

Gabbro 1 was separated into three zones based on variations in magnetic susceptibility and in the percentage of leucocratic patches. The modal percentage of leucocratic patches in Zone 1 of Gabbro 1, from 1410.9 to 1416.2 mbsf, is relatively large: 8.4% ± 3.2% (Fig. F64). Zones 2 and 3 of Gabbro 1, from 1416.2 to 1452.5 mbsf, show smaller and fewer disseminated leucocratic clusters that account for 3.3% ± 2.3% of the rock. At 1422.47 mbsf (Sample 312-1256D-217R-1, 87–92 cm [Piece 21]), a plagioclase-rich zone shows a higher percentage of leucocratic clusters (20.6%) characterized by euhedral plagioclase grains. These variations suggest that Gabbro 1 may consist of three distinct petrological units: Zone

1 is defined by larger and more abundant leucocratic patches than Zones 2 and 3. All zones are characterized by a broad upward increase in percentage of leucocratic patches. Zone 2 is defined by a statistically higher average SPO shape ratio (1.044) than Zone 2 (1.032) and Zone 1 (1.016). The boundaries between zones were determined independently of petrological units, yet these limits correspond to the Unit 1256D-85/86A and 89A/89C boundaries (Fig. F58). SPO provides important information on internal boundaries in Gabbro 1. The leucocratic patches, characterized by a lower anorthite content measured in plagioclase grains compared to groundmass plagioclase (Koepke et al., 2008), are interpreted as late-stage felsic melts. The increase in percentage of these leucocratic patches toward the top of Gabbro 1 most likely reflects the accumulation and upward movement of felsic melts that typically have a lower density than the surrounding crystal mush.

The SPO shape ratio of the leucocratic patches is overall very small and confirms the macroscopically isotropic fabric of Gabbro 1 (Fig. F64). The shape ratio varies between 1.001 and 1.140, corresponding to SPO shape ratio ranks between 0 and 1 (isotropic to weak; average ≈ 1.030). The most anisotropic intervals of Gabbro 1 are 1417–1420 and 1443–1452 mbsf. These two intervals correspond to the lower part of Zone 1 and the lower part of Zone 3, respectively. Elsewhere, the SPO shape ratio is < 1.050, corresponding to an SPO shape ratio rank of 0. Overall, the shape ratio shows a weak negative correlation with the percentage of leucocratic patches (Fig. F65). The interpretation of this correlation remains speculative because the SPO shape ratio is overall very small (average = 1.030) and because SPO analysis was performed in two dimensions only. One possible explanation would be that some compaction took place in the magmatic crystal mush before complete solidification. This mechanism would explain why shape ratios are larger toward the base of Zones 1 and 3.

Most of the steeply dipping leucocratic zones occur in Zone 1 of Gabbro 1 between 1410.9 and 1419.0 mbsf. However, this zone also exhibits 20% of gently dipping zones, which gives the rock a reticulated fabric with intertwined steep and shallow fabrics (Fig. F63). Zone 3 of Gabbro 1, between 1445 and 1452 mbsf, is characterized by great variation of SPO orientation. This variation could be explained by incipient segregation of plagioclase-rich melt through a weakly organized crystal mush (Fig. F66).

Vein orientation

Several veins measured in Expedition 312 cores seem to have a systematic distribution in orientation. Several core pieces were tentatively geographically reoriented based on paleomagnetic data (see **"Structural geology"** in the "Methods" chapter [Expedition 335 Scientists, 2012b]). All of the geographically reoriented veins were plotted in a stereonet (Fig. F60B). They have variable orientations but generally form two populations. One population is steeply dipping (>60°) and the other is shallowly dipping (<30°), and both have similar northwest–southeast strikes. This is mirrored in Figure F60A, where all dips, reoriented or not, show the dip distribution of various types of veins (grouped by color). Dark green veins tend to have steeper dips.

Geographically reoriented data were used to plot several rose diagrams to show the vein strikes in the three major units: Gabbro 1, Dike Screen 1, and Gabbro 2 (Fig. F61). Veins in Gabbro 1 and Gabbro 2 have similar bulk orientations, with some scatter. Veins in Dike Screen 1 have northwest–southeast orientations, slightly different from those in the gabbro units. The vein azimuth is plotted using the right-hand rule, so dip direction is always to the right of the strike direction. Most veins, therefore, would strike northwest–southeast and dip toward the southwest.

Brittle deformation

Macroscopic brittle structures are present in all core sections. The majority of brittle features were classified as SIFs (see **"Structural geology"** in the "Methods" chapter [Expedition 335 Scientists, 2012b]). SIFs are mostly exhibited on piece end surfaces, and it is unclear whether these fractures are drilling induced or whether they reflect a preexisting plane of weakness in the rocks. High densities of SIFs near the upper contact between the granoblastic dikes and Gabbro 1 may correlate with closely spaced subhorizontal features observed in Formation MicroScanner (FMS) images (see Teagle, Alt, Umino, Miyashita, Banerjee, Wilson, and the Expedition 309/312 Scientists, 2006) and therefore are not drilling induced. Several nonmineralized steeply dipping fractures were also observed. The distribution of fracture orientations is bimodal, with a common occurrence of dip angles near 20° and a higher frequency of dip angles between 70° and 90° (Fig. F67). The majority of geographically reoriented steep fractures tend to dip to the southwest.

No semibrittle features or fault structures were identified from macroscopic observations. Fractures other than SIFs tend to be steeply dipping. Many of these steep open fractures have mineralized surfaces, indicating places where the rock has broken along a vein. Small confined joints or cracks that do not fully penetrate the core pieces are very common in

the granoblastic dikes and are also present but less common in the gabbros. Unoriented pieces of cuttings and cobbles from the hole also contain some small irregular joints. These tend to be very fine and have irregular and splayed morphologies. Gabbro 2 contains some intervals of recovered gravel-sized pieces that may represent rocks with a very high fracture density.

Downhole fracture intensity is variable, with the zones between the gabbro and granoblastic dikes having higher fracture densities (Fig. F68). For instance, the high fracture densities seen in the intervals near 1410 and 1460 mbsf and just above 1500 mbsf are all associated with major lithological boundaries. The highest occurrence of SIFs is near the top of Gabbro 1, which is reflected in the small size of recovered pieces. Non-SIF brittle features appear to be slightly more abundant in gabbro than in granoblastic material.

Expedition 335 plutonic section

The following observations were made on cores (1507.1–1521.6 mbsf), cuttings, and cobbles recovered during Expedition 335. The recovered material mostly consists of aphyric basalt with a granoblastic texture with minor amounts of dioritic rocks and olivine gabbros. Observations were made on the archive section halves of Sections 312-1256D-235R-1 through 239R-1, and structural measurements were done on oriented pieces (see STRUCTURE _SKETCHES_335 in DESCRIPTIONS in **"Supplementary material"**). During Expedition 335, numerous cuttings and cobbles were recovered that carry important information about the crosscutting relationships of several types of veins. Details specific to structural features were illustrated with comments and sketches (see STRUCTURE _SKETCHES_335 in DESCRIPTIONS in **"Supplementary material"**). Structural orientations were measured on large cobbles, with respect to arbitrarily chosen *x*-, *y*-, and *z*-axes. Cubes for magnetic measurements were sampled from the same cobbles using the same reference frame to reorient the measured structures. Thin sections were made from cores, cuttings, and cobbles to confirm macroscopic descriptions of structures and to characterize the microstructures (see STRUCTURE_SKETCHES _335 in DESCRIPTIONS in **"Supplementary material"**). Important structural observations are as follows:

- Vein crosscutting relationships indicate that magmatic veins and orthopyroxene veins occurred first and were followed by actinolite needle veins, anhedral hornblende veins, and thin, black anhedral actinolite(-chlorite) veins, in that order.
- The irregular shapes of quartz-bearing magmatic veins and pyroxene veins that were cut by amphibole veins with alteration halos illustrate the interplay between magmatic, metamorphic, fluid flow, and brittle deformation processes.

Gabbros

Overall, gabbros display equilibrated magmatic microstructures. Samples of olivine gabbronorite sampled during Runs 11 and 20 display a magmatic isotropic fabric characterized by equant granular microstructure, subrounded grains, and lobate grain boundaries (Sample 335-U1256D-Run 11-EXJB; Thin Section 29). Olivine and pyroxenes are systematically surrounded by abundant small grains of oxides (Fig. F69). The large difference in grain size between these grains and magmatic phases such as olivine, pyroxene, and plagioclase indicates that these oxides are not primary but, to the contrary, result from alteration. Microstructures indicative of crystal-plastic deformation are very rare and limited, when present, to tapered twins in plagioclase.

Basaltic granoblastic dikes

Basaltic dikes are host rocks to Gabbro 1 and Gabbro 2, and within tens of meters above, below, and in between contacts, they display equilibrated and equigranular microstructures, referred to as granoblastic (Teagle, Alt, Umino, Miyashita, Banerjee, Wilson, and the Expedition 309/312 Scientists, 2006; Dziony et al., 2008). These microstructures, characteristic of high-grade static metamorphism, have been attributed to the thermal overprint caused by emplacement and cooling of relatively large gabbro bodies (Teagle, Alt, Umino, Miyashita, Banerjee, Wilson, and the Expedition 309/312 Scientists, 2006; Koepke et al., 2008). Recrystallization is pervasive and affects all parts of the basaltic dikes, including narrow pyroxene domains interpreted as recrystallized hydrothermal veins (Koepke et al., 2008; France et al., 2009). Overall, magmatic structures have been extensively overprinted (Fig. F70). However, in several samples, magmatic foliation marked by recrystallized plagioclase laths may persist (Fig. F71). Rare relics of plastic deformation can also be observed in a few large plagioclase grains (Sample 335-1256D-235R-1, 11–12 cm; Thin Section 2). One recrystallized medium-grained sample displays strong banding and plagioclase foliation (Sample 335-1256D-Run12-RCJB-Rock Q; Thin Section 25) (Fig. F71).

Magmatic veins

A 15 mm thick magmatic leucocratic vein of quartz diorite (Section 335-U1256D-235R-1, 23–25 cm

[Piece 5]; Thin Section 3) cuts through granoblastic dikes at 1507.34 mbsf. The quartz-diorite displays a magmatic microstructure with lobate grain boundaries along plagioclase/quartz contacts. Quartz shows weak undulose extinction.

Vein crosscutting relationships

There are several types of veins in the Expedition 335 cores, cuttings, and cobbles. In this section, the relationships between different vein types and especially their crosscutting relationships are discussed. The five main vein types are

1. Magmatic veins defined by plagioclase and pyroxene ± amphibole ± quartz;
2. Pyroxene veins defined by orthopyroxene or clinopyroxene ± plagioclase;
3. Amphibole veins defined by green actinolite intergrown needles;
4. Black amphibole veins defined by anhedral, diffuse actinolite (±chlorite) crystals; and
5. Green to colorless amphibole veins defined by anhedral, diffuse hornblende crystals.

(See **"Veins and vein-related alteration halos"** in "Alteration.")

Several thin sections exemplify different crosscutting relationships between veins: Samples 335-1256D-Run12-RCJB-Rock B (Thin Section 21; Fig. **F72**), 335-1256D-Run12-RCJB-Rock C (Thin Section 22; Fig. **F73**), and 335-1256D-238R-1, 24 cm (Thin Section 6; Fig. **F74**). The crosscutting relationships depicted in Sample 335-1256D-Run12-RCJB-Rock B (Thin Section 21) indicate the following sequence: orthopyroxene and magmatic veins occurred first, then the actinolite needle veins, and last the smaller anhedral, diffuse actinolite veins. The crosscutting relationships exhibited in Sample 335-1256D-Run12-RCJB-Rock C (Thin Section 22) indicate diffuse background alteration occurred before coherent actinolite veins formed. Actinolite veins were then cut by thin, black actinolite veins. The crosscutting relationships in Sample 335-1256D-238R-1, 24 cm (Thin Section 6), indicate the following sequence: the larger actinolite needle vein came first, then the anhedral hornblende vein, and all are crosscut by the conjugate black, anhedral actinolite veins.

Brittle structure

Piece sizes in the recovered cores were typically <10 cm. There is a common occurrence of SIFs, and several nonmineralized steeply dipping fractures were observed. Fracture density is essentially uniform in the recovered intervals. Section 335-1256D-236R-1 contains brittle structures. In this section, Piece 1, 0–5.5 cm, contains an igneous contact that is crosscut by a small fault with ~2 mm of offset (Fig. **F75**). This piece also contains evidence of deformation (possibly submagmatic fractures) in the alteration halo around the contact. The random orientation of prehnite and chlorite along the fault surface suggests that this mineralization postdates faulting. A lower interval in the same core (Sample 236R-1, 43–68 cm) contains a set of shear veins with an uncertain amount of offset. In nonmineralized steeply dipping fractures, slickensides in the form of chlorite lineations on the fracture surfaces of the shear veins indicate that the motion of shearing is approximately parallel to the strike of the vein (Fig. **F76**).

Paleomagnetism

The primary goal of paleomagnetic studies is to quantify the structure, direction, and intensity of natural remanent magnetizations (NRMs) in the different rock types that make up the lower oceanic crust and to use these data to provide insights into crustal accretion, deformation, and the source of marine magnetic anomalies. In addition, magnetic fabric analysis can provide valuable information on the degree and direction of weak preferred alignments of mineral phases, leading to improved understanding of magmatic and tectonic processes. Because of low recovery during Expedition 335, the majority of data discussed here were acquired from analyses conducted on samples taken from Expedition 312 section halves (predominantly from Gabbro 1 and Gabbro 2 lithostratigraphic units). Discrete samples prepared from these legacy core section halves during Expedition 335 are curated with the prefix 335(312).

Remanence data

Continuous measurements

The lack of significant recovery of archive section halves resulted in an exceptionally limited number of continuous remanence measurements during Expedition 335.

In order to assess the effectiveness of the 2G superconducting rock magnetometer (SRM) inline demagnetizing coils in recovering characteristic remanent magnetizations (ChRMs) from core sections affected by drilling-induced magnetization, prior to analysis of Expedition 335 cores a number of archive section halves from Expedition 312 were subjected to stepwise alternating field (AF) demagnetization from 40 mT up to a maximum peak field of 80 mT. These sections had previously been subjected to stepwise AF treatment up to 40 mT during Expedition 312, but no stable endpoint component was reached by this

level of demagnetization. A typical result of this two-stage demagnetization process is illustrated in Figure F77A. The initial treatment to 40 mT was effective in removing most of the steeply inclined drilling-induced remanent magnetization (DIRM) in the sample, resulting in a great circle path trending toward shallower inclinations. However, treatment at higher fields reverses this trend and the remanence migrates to a near-vertical direction by 80 mT. To confirm that this was not the result of incorrect processing and amalgamation of data collected during different expeditions by different operators, the corresponding (previously undemagnetized) working section half was subjected to stepwise AF treatment from 0 to 80 mT. Results are shown in Figure F77B and again exhibit a hairpin-shaped trajectory that migrates to vertical inclinations at high fields.

These experiments demonstrate that the SRM inline AF demagnetizing coils generate a spurious, strong anhysteretic remanent magnetization along the *z*-axis of the system at fields >40–50 mT (which is often insufficient to isolate non-DIRM components in hard rock samples). This may result from the presence of a residual magnetic field directed along the *z*-axis in the region of the coils as a result of the less effective magnetic shielding along this direction. However, the measured field at the position of the z-coil was only ~30 nT during these experiments. Alternatively, it may indicate a problem with the AF waveform produced by this coil. Until this instrumental problem is resolved, demagnetization data from the SRM system must be treated with caution.

Because only section half pieces >10 cm in length may be reliably measured using the SRM system because of artifacts arising from edge effects within 5 cm of the ends of core pieces (see "Paleomagnetism" in the "Methods" chapter [Expedition 335 Scientists, 2012b]), only one archive section half piece recovered during Expedition 335 was suitable for analysis. Results are shown in Figure F78 (note that demagnetization data above 60 mT are omitted, as they are contaminated by instrument-induced anhysteretic remanence). This sample of granoblastic dikes from Dike Screen 2 near the current base of Hole 1256D does not exhibit the near-vertical DIRM component ubiquitous in previous recovered samples (see "Discrete samples" below), suggesting that a change in operating procedure since Expedition 312 (most likely the use of nonmagnetic core barrels) may have reduced DIRM acquisition. The ChRM component of this sample has an inclination of +30°. Although data from a single sample cannot be interpreted with any confidence, we note that this inclination is indistinguishable from the overall mean inclination calculated from discrete samples downhole from the top of Gabbro 1 (see "Discrete samples," below).

Discrete samples

Given the very limited recovery of oriented core pieces during Expedition 335, shipboard experiments on discrete samples were conducted principally on a suite of 11 minicube samples cut from Expedition 312 working section halves within Gabbro 1 and Gabbro 2. These samples were subject to AF or thermal demagnetization, with six samples being pretreated with two runs of low-temperature demagnetization (LTD) in order to remove a significant proportion of the ubiquitous DIRM encountered in all previous drilling phases at the site. These shipboard data were augmented by unpublished shore-based data provided by R. Anma and D. Wilson derived from demagnetization of discrete samples performed subsequent to Expedition 312. A total of 53 samples measured by R. Anma were treated with standard AF demagnetization, with anisotropy of magnetic susceptibility determined for a subset of 22 samples. A total of 19 samples measured by D. Wilson were split into 2 subsamples: one half minicube was subject to AF demagnetization, the other to thermal demagnetization (following initial AF demagnetization to a maximum field of 10 mT to reduce DIRM). Data from the AF demagnetized half minicubes show evidence of laboratory-induced anhysteretic remanence prior to isolation of the characteristic remanence and are not discussed further. Principal component analysis of data from the combined suite of 83 samples was conducted during Expedition 335 to provide consistency and insights into remanence structure and directions through Gabbro 1, Dike Screen 1, and Gabbro 2. However, only demagnetization data from the 11 specimens measured during Expedition 335 are presented in detail here (Figs. F79, F80; Tables T8, T9), although results of principal component analysis of the combined sample set are represented graphically in summary figures.

Orthogonal vector plots of demagnetization data (Figs. F79, F80) reveal a range of magnetic components in samples from Gabbro 1 and Gabbro 2. A low-stability, steeply inclined component is evident in all samples and is interpreted as a DIRM. This component dominates the vector difference sum (VDS; i.e., the sum of the vectors removed at each demagnetization step, representing the total magnetization present in a sample; Tauxe, 2010; Gee et al., 1993), contributing on average 66% of the VDS (with a range of 18%–91%). The dominance of the DIRM component results in a distribution of NRM directions for all samples that is clustered around

steep inclinations (Figs. F81, F82), whereas principal component analysis demonstrates that the DIRM is tightly clustered around near-vertical inclinations.

Six samples were subjected to two cycles of LTD (Merrill, 1970; Dunlop, 2003; Yu et al., 2003) to determine whether the DIRM could be successfully reduced by this treatment prior to subsequent AF or thermal demagnetization. The first cycle of LTD was found to remove (on average) 52% of the NRM, with the component removed having inclinations ranging from +78° to +86° (Table T8). Hence, a single cycle of LTD is demonstrably successful in removing a significant proportion of the drilling-induced magnetization in these rocks. The second LTD cycle only removed an additional 5% of the NRM (on average). Data from adjacent samples in Section 335(312)-1256D-222R-2W in igneous Unit 89 in Gabbro 1 (Fig. F80A) illustrate improvements in the resolution of low unblocking temperature components resulting from LTD. The sample at 44 cm in this section was not pretreated with LTD cycles and exhibits a steep but nonlinear demagnetization path until a ChRM component of moderate inclination is isolated between 560° and 600°C. In contrast, the sample at 47 cm exhibits a large, vertical DIRM component that is removed by two LTD cycles and thermal demagnetization at 100°C. Magnetization then jumps to a shallower inclination by 200°C and thereafter exhibits a ChRM that is linear between 450° and 600°C. LTD treatment has therefore improved separation of the DIRM and ChRM in these samples. The jump in magnetization direction between 100° and 200°C in Sample 335(312)-1256D-222R-2W, 47 cm, suggests that a non-DIRM-related, low-unblocking temperature component may be present in these rocks (possibly representing a thermoviscous component acquired in the present-day field at elevated temperatures). Further experiments with more closely spaced temperature steps are required to better define this component.

Following removal of the DIRM component, principal component analysis identifies linear components (with maximum angular deviations < 10°) trending toward the origin in 63 of 83 samples analyzed. These components are typically isolated above 35 mT or 540°C and are considered to represent the ChRM of the samples. Maximum unblocking temperatures of 580°–600°C are consistent with remanence being carried by magnetite. The dispersion in ChRM declinations (Fig. F81C) reflects the lack of azimuthal control on the orientation of IODP cores. ChRMs have moderate inclinations (Figs. F81C, F82) with a mean of +30.7° (α_{95} = 3.3°, k = 30.0, and n = 63; Arason and Levi, 2010). There is no significant difference between the mean inclinations for Gabbro 1 and Gabbro 2 (+31.6° and 29.9°, respectively), although sample dispersion is slightly higher in Gabbro 1 (k = 17.9, α_{95} = 6.5°, and n = 29 and k = 59.3, α_{95} = 3.7°, and n = 26, respectively). ChRM inclinations for the granoblastic rocks of Dike Screen 1 are indistinguishable from the overall mean of the section, but the number of samples in this lithostratigraphic unit marked by low core recovery is too small to allow calculation of a separate, statistically meaningful mean inclination.

The overall mean inclination of the section (Fig. F82) is significantly steeper than that expected for the paleoposition of Site 1256, which restores to an equatorial paleolatitude in the Miocene (Wilson, Teagle, Acton, et al., 2003). Similar anomalous inclinations were observed in shipboard analyses during Expedition 312 (Teagle, Alt, Umino, Miyashita, Banerjee, Wilson, and the Expedition 309/312 Scientists, 2006). Potential explanations for the origin of the moderately inclined observed inclinations are discussed below.

Multicomponent remanence in gabbroic rocks from Hole 1256D

In addition to DIRM and ChRM components, thermal demagnetization of Sample 335(312)-1256D-231R-1W, 115 cm, provides evidence for acquisition of remanence during at least two geomagnetic polarity chrons. This sample exhibits a high-stability remanence component with a positive inclination that is unblocked from 500° to 600°C and forms a linear ChRM above 550°C (Fig. F80B). In addition, this sample shows a well-defined negatively inclined component removed at temperatures from 200° to 450°C. These components are nearly antipodal, strongly suggesting that remanence was acquired in different geomagnetic polarity periods. However, without independent reorientation of the core piece and recovery of original declinations, it is impossible to define the original polarity of each component. In addition, a significant jump in remanence direction between 100° and 200°C may indicate the presence of a third low-unblocking temperature positive inclination component, although more closely spaced demagnetization steps would be required to test this inference. Similar low-unblocking temperature components may also be present in Samples 335(312)-1256D-222R-2W, 47 cm, and 231R-3W, 114 cm (Fig. F80).

Sample 335(312)-1256D-231R-1W, 115 cm, represents the first multicomponent (excluding DIRM overprints) gabbroic sample reported in Hole 1256D. Similar multicomponent, multipolarity remanences have been seen previously in lower crustal rocks re-

covered by drilling in slow spreading rate crust along the Mid-Atlantic Ridge. Meurer and Gee (2002) reported three components of different polarities in gabbros from the Mid-Atlantic Ridge Kane Fracture Zone (MARK) area sampled during ODP Leg 153 and interpreted these as components acquired across the Jaramillo Subchron and the Matuyama and Brunhes Chrons during protracted construction of the lower crust by intrusion of thin sills. Morris et al. (2009) reported three component remanences from gabbros recovered from the footwall of Atlantis Massif sampled during IODP Expedition 304/305 and showed that these resulted from prolonged cooling of the section across the polarity reversals either side of the Jaramillo Subchron. In both cases, data provide constraints on the thermal history of the sampled sections. Further sampling and detailed thermal demagnetization and rock magnetic experiments are now required in order to understand the distribution, origin, and geological significance of multicomponent remanences within Hole 1256D gabbros.

Origin of moderately inclined remanence components

Characteristic components of magnetization throughout the studied interval of Hole 1256D have inclinations that are significantly steeper than the expected subhorizontal direction, with an overall mean inclination of +30.7°. The cause of these anomalous inclinations is difficult to establish with certainty, but a number of potential contributing factors are discussed and assessed below.

Drilling-induced artifacts

As noted previously, the majority of samples analyzed have a significant, near-vertical DIRM component. Principal component analysis identifies a clear linear component decaying to the origin in most samples once this DIRM is removed by low-field/low-temperature demagnetization. However, these final ChRM components potentially could be biased toward positive inclinations if a residual DIRM persists to higher treatment levels. This explanation has previously been invoked to explain anomalously steep inclinations in Hole 1256D (Teagle, Alt, Umino, Miyashita, Banerjee, Wilson, and the Expedition 309/312 Scientists, 2006). Simple forward modeling of superimposed natural and drilling-induced remanence components indicates that significant steepening of linear ChRM components requires near-complete overlap of the high treatment level parts of the coercivity/unblocking temperature spectra of the natural and drilling-induced components. The degree of bias also depends on the relative intensities of DIRM and ChRM. Assuming that the DIRM is carried by multidomain magnetite grains and the stable ChRM by finer, (pseudo)single domain grains (Allerton et al., 1995), overlap sufficient to produce linear ChRMs biased by +30° is unlikely.

Several additional aspects of the paleomagnetic data set analyzed during Expedition 335 also suggest that contamination by DIRM cannot fully explain the observed anomalous inclinations:

- There is no relationship between the strength of DIRM and ChRM inclination, as illustrated by plotting the ratio of the intensity of the DIRM and the vector difference sum of the demagnetization path (DIRM/VDS) against the inclination of the ChRM for discrete samples from core sections from the top of Gabbro 1 to the bottom of Hole 1256D (Fig. **F83**). High values of DIRM/VDS indicate a remanence dominated by the drilling-induced component. No significant correlation is seen, and indeed the five lowest ChRM inclinations occur in samples where the DIRM forms >65% of the VDS. There is a similar lack of correlation of ChRM inclination with low-field magnetic susceptibility, a parameter that directly reflects the concentration of coarse, multidomain magnetite grains that are more susceptible to acquiring a DIRM.
- Nearly antipodal components of magnetizations are observed in Sample 335(312)-1256D-231R-1W, 115 cm. Significant contamination of the remanence in this sample by a persistent downward-directed DIRM overprint should steepen the downward-directed natural component and pull the upward-directed component to a shallower inclination. The difference in inclinations between these components (Table **T8**) does not match this scenario and cannot be explained by a DIRM-related bias.
- The single result obtained from an archive section half recovered during Expedition 335 using a nonmagnetic core barrel does not exhibit a subvertical DIRM component (Fig. **F78**) and yet has a ChRM of 30° (i.e., indistinguishable from the overall mean inclination calculated from discrete samples).
- Detailed previous studies of the geometry of DIRMs in ODP core sections have documented a pronounced radial DIRM component in addition to the dominant subvertical component. In particular, experiments conducted during Leg 206 on a suite of samples cut from a whole-round basaltic core piece from Hole 1256D demonstrated that DIRM results in a bias of working section half

remanences toward southerly declinations in the core reference frame (i.e., toward the center of the core section). This bias is not observed in the distribution of ChRM components in discrete samples cut from working section halves (Fig. **F81C**), where (if anything) there is a predominance of ChRMs in the northern hemisphere.

In conclusion, contamination of ChRM components by residual DIRM extending to high demagnetization levels may partially contribute to anomalously steep inclinations but seems unlikely to fully account for the total apparent steepening of 30° inferred from comparison of observed inclinations with a geocentric axial dipolar reference inclination.

Present-day overprint

The International Geomagnetic Reference Field (IGRF) at Site 1256 (calculated using the IGRF.py program of Tauxe, 2010) is as follows: declination = 004°, inclination = 30.9°, and intensity = 33,666 nT. The IGRF inclination is close to the mean inclination of the section. However, the presence of multipolarity remanence in Sample 335(312)-1256D-231R-1W, 115 cm, is difficult to reconcile with a complete overprint by a present-day field component in these rocks. In addition, the estimated ambient temperature of the section prior to drilling (even if held constant for 15 m.y.) would result in maximum laboratory unblocking temperatures of only ~250°–300°C for ideal magnetite-hosted remanence (Tauxe, 2010), compared to maximum observed unblocking temperatures of >540°.

Nondipole fields/inadequate sampling of paleosecular variation

Inclinations are anomalous compared to an expected direction calculated from a geocentric axial dipolar (GAD) field. Modeling of geomagnetic field data covering the last 5 m.y. demonstrates that nondipolar field contributions may be persistent on geological timescales (e.g., Gubbins and Kelly, 1993; Kelly and Gubbins, 1997). Additional information on nondipole components may be derived from analysis of the skewness of marine magnetic anomalies (Gee and Kent, 2007). Results for the Galapagos Ridge region for the last 1 m.y. (Schneider, 1988) suggest an inclination anomaly of –3.4° (deviation from a GAD value). It is not known whether an anomalous geometry of the geomagnetic field persisted over the equatorial Pacific region at 15 Ma, but in any case it would be unlikely to result in more than a few degrees deviation in inclination from the GAD value.

An alternative source of anomalous inclination would be inadequate sampling of paleosecular variation (PSV) of the geomagnetic field by the suite of discrete samples. Statistical field models allow prediction of the variability of field directions due to PSV at Site 1256. Figure **F84** shows the distribution of vector endpoints calculated from 1000 realizations of the statistical field model TK03.GAD of Tauxe and Kent (2004), calculated for a normal polarity field only for clarity. At equatorial latitudes there is a pronounced north–south elongation in the distribution of field directions, most evident when data are presented after rotation of the GAD direction to the vertical. Interpretation of observed paleomagnetic data by comparison with GAD reference directions relies on sufficient sampling of PSV, assuming that the long-term geomagnetic field has a GAD geometry. This is typically achieved by combining data from rocks that acquired their remanence over time periods on the order of 10^5 y or more. It is generally assumed that cooling rates in lower crustal gabbros are sufficiently slow to adequately average PSV (Gee and Kent, 2007), and this is clearly the case in intervals containing multipolarity remanences. Hence, anomalous inclinations are unlikely to result from systematic undersampling of PSV.

Tectonic rotation

Tectonic tilting of the section after remanence acquisition is capable of producing significant changes in magnetization direction, but it is critically dependent on the orientation of the tilt axis relative to the initial remanence direction. Ridge-parallel tilt axes are likely to dominate at a spreading axis. Reconstruction of the geometry of the East Pacific Rise in the Miocene suggests a ridge orientation of 340°, with Site 1256 located very close to the Equator (Wilson, Teagle, Acton, et al., 2003). The effect of rotation around this axis on originally horizontal remanences of normal and reversed polarity is illustrated in Figure **F85.** This geometry would require unrealistic amounts of tilting to account for substantial changes in inclination but may contribute part of the observed inclination steepening. The orientation of sheeted dikes in Hole 1256D has been determined independently by Tominaga et al. (2009). The average dip and dip direction of inferred dike contacts observed on FMS images is 79° ± 8° and 053° ± 23°, suggesting a maximum permissible tilt of ~20° (down to the southwest), assuming that dikes were emplaced vertically. Tilting of this magnitude around a ridge-parallel axis would rotate initially horizontal reversed/normal polarity remanences to inclinations of ±5°–10°, respectively. Rotation around alternative axes at higher angles to the initial remanence declination would be more effective at

producing the observed moderate inclinations but are unlikely in this tectonic setting.

Remanence deflection due to significant anisotropy

Pronounced magnetic anisotropy in a rock (resulting from a preferred orientation of minerals) can produce a deflection of remanences away from the ambient geomagnetic field direction at the time of magnetization (Stephenson et al., 1986; Potter, 2004). Anisotropy of magnetic susceptibility (AMS) fabrics in the sampled rocks are quite weak (1%–3% anisotropy; see **"Magnetic fabric"**). However, AMS includes contributions from both remanence-carrying and nonremanence-carrying minerals. A given AMS fabric may not, therefore, accurately reflect the orientation distribution of the remanence-carrying phases in the rock and hence provides a poor measure of the potential amount of remanence deflection. This can only be effectively quantified using the anisotropy of remanence (usually by determination of the anisotropy of anhysteretic remanence [AARM]; Potter, 2004). The degree of remanence anisotropy is usually much more pronounced than that of AMS (Stephenson et al., 1986). AARM fabrics in lower crustal gabbros from Atlantis Massif have been shown to potentially result in up to ~15° of remanence deflection in some samples (J.S. Gee, pers. comm., 2007).

Reoriented AMS ellipsoids in gabbros in Hole 1256D have maximum principal axes that broadly trend north–south (see **"Magnetic fabric"**). Hence, if remanence anisotropy and AMS ellipsoids are similarly oriented, significant deflection of remanence away from the ambient geomagnetic field direction is potentially possible and may partially account for observed anomalously steep inclinations. AARM analysis will therefore form a focus of postcruise research on these rocks.

Magnetic susceptibility, NRM intensity, and Königsberger ratio

In mafic igneous rocks, low-field magnetic susceptibility (k) is principally controlled by the volume concentration of magnetite. Discrete samples from Gabbro 1, Dike Screen 1, and Gabbro 2 have a mean susceptibility of 39.7×10^{-3} SI (range = 5.8×10^{-3} to 116×10^{-3} SI) and a mean NRM intensity of 5.7 A/m (range = 4.4–15.5 A/m). NRM variability is also controlled by variations in magnetite content but may be influenced by variability in the magnitude of DIRM. The relation of NRM intensity and susceptibility is expressed by the Königsberger ratio, Q, which is defined as the ratio of remanent to induced magnetization in a rock (where induced magnetization equals the product of k (SI) and the geomagnetic field strength in A/m). Values of $Q > 1$ indicate that remanence dominates the magnetization of a rock unit.

Figure **F86** shows a log-log plot of NRM intensity against k, together with lines of equal Q calculated for a field of 27 A/m. The majority of samples plot close to $Q = 10$. This, combined with high NRM intensities, suggests that this section may contribute a significant fraction to observed magnetic anomalies (as noted previously by Teagle, Alt, Umino, Miyashita, Banerjee, Wilson, and the Expedition 309/312 Scientists, 2006). However, caution is required in the interpretation of Q ratios calculated for these samples, as NRM intensities may be artificially increased by drilling-induced magnetization. A full discussion of modeling of marine magnetic anomalies in the region around Site 1256 is provided by Wilson (1996).

Magnetic fabric

AMS was determined for all discrete samples prepared during Expedition 335, and results are summarized in Table **T9.** Additional data were provided by R. Anma from analysis of discrete samples requested after Expedition 312. In both cases, measurements were conducted using an AGICO Kappabridge, ensuring consistency within the data. Combined results for Gabbro 1 and Gabbro 2 are summarized in Figure **F87.** Most susceptibility tensors are weakly to moderately anisotropic ($P' < 1.09$ [mean = 1.03], where P' is the corrected anisotropy degree) (Jelinek, 1981). There is a range of ellipsoid shapes from strongly oblate to strongly prolate. In the core reference frame there is no coherent arrangement of maximum and minimum principal axes, reflecting the lack of primary azimuthal control on the orientation of core pieces. In order to compare the orientations of magnetic fabrics from different samples, some common reference frame is required. Under the assumption that the stable ChRM for each sample approximates the time-averaged geomagnetic field direction at the site at the time of accretion, magnetic fabric data have been restored to a common reference frame by a simple vertical axis rotation that restores the ChRM declination to 000°. This correction is not dependent on the indeterminate polarity of the ChRM, as AMS principal axes are bidirectional, but does ignore the natural variability in remanence directions that may arise from secular variation. After correction, AMS principal axes become more coherently organized, with maximum axes forming two north–south oriented clusters and minimum axes forming a girdle distribution that trends east–west. Separating samples with prolate

and oblate fabrics results in improved clustering of maximum/minimum axes for prolate/oblate ellipsoids, respectively.

AMS maximum axes represent the magnetic lineation, and their preferred orientation is normally interpreted as a proxy for magmatic flow/emplacement directions in igneous rocks (Tarling and Hrouda, 1993). The north–south alignment of maximum axes in gabbros of Hole 1256D is broadly aligned with the presumed orientation of the East Pacific Rise and suggests a component of ridge-parallel fabric development during crystallization of these rocks. Similar ridge-parallel magnetic lineations have been reported in lower crustal gabbros of the Troodos ophiolite by Abelson et al. (2001), where it is inferred to reflect redistribution of melt toward a spreading segment end.

Physical properties

During Expedition 335, we carried out shipboard physical property measurements to investigate the physical characteristics of rocks recovered from 1372.80 to 1521.6 mbsf in Hole 1256D. We conducted physical property measurements on three groups of rock samples: legacy core from Expedition 312, Expedition 335 core, and non-core material collected during Expedition 335. We conducted the following measurements:

- Analyses using the multisensor core loggers on Expedition 312 archive section halves (Sections 312-1256D-202R-1A through 234R-1A) and Expedition 335 whole-round sections and section halves (Sections 335-1256D-235R-1 through 238R-1);
- Thermal conductivity measurements of archive section half pieces from Expeditions 312 and 335, as well as non-core material from Expedition 335;
- Measurements of discrete cube samples (~8 cm^3) from Expeditions 312 and 335 for *P*-wave velocity, density, and porosity; and
- Magnetic susceptibility measurements of non-core material from Expedition 335.

Multisensor core logger data

Expedition 312 cores revisited

At the beginning of Expedition 335, we remeasured Expedition 312 archive section halves with the Whole-Round Multisensor Logger (WRMSL), Natural Gamma Radiation Logger (NGRL), and Section Half Multisensor Logger (SHMSL) (see **"Physical properties"** in the "Methods" chapter [Expedition 335 Scientists, 2012b]). Although both the WRMSL and NGRL are calibrated for whole-round sections, these section-half measurements qualitatively indicate the downhole trend of properties. Measurements were made at a higher resolution than during Expedition 312. For presentation and comparison to the measurements made on whole-round sections during Expeditions 312 and 335, measurements on the archive halves have been scaled.

Overall, remeasured and processed Expedition 312 archive section half data reveal significant variations in physical properties within Gabbros 1 and 2. Data from the granoblastic dike intervals between 1406 and 1507 mbsf appear relatively uniform, given the limited recovery (Fig. **F88**).

Within the gabbro units, the largest peaks in multisensor core logger data correspond to the occurrence of evolved intrusions of diorite, oxide diorite, and oxide quartz diorite (see **"Igneous petrology"**). The highest WRMSL magnetic susceptibility value was >15,000 instrument units (IU), observed in an oxide-rich vein in interval 335-1256D-230R-1, 48–60 cm. Peaks in natural gamma radiation (NGR) appear to be associated with the occurrence of narrow intrusions of evolved dioritic rock, and NGR data are broadly consistent with the concentrations and general geochemical trends in K, U, and Th analyzed from Hole 1256D (Fig. **F89**) (Gao et al., 2009; Neo et al., 2009; Yamazaki et al., 2009). High counts associated with evolved dioritic rocks do not always correspond to high concentrations in all three radiogenic elements. Although in the upper part of Gabbro 1 oxide quartz diorites are enriched in K, U, and Th, at the base of Gabbro 2 (1494–1495 mbsf) dioritic intrusions have no corresponding peak in the K window.

Variations within the gabbros are most clearly seen in magnetic susceptibility and color reflectance data, with minor variations in NGRL counts and gamma ray attenuation (GRA) density. Magnetic susceptibility and color reflectance data are interpreted to be relatively sensitive to the oxide and olivine content of rocks. At the top of Gabbro 1 (1410–1420 mbsf), b* (red–green value) and magnetic susceptibility decrease downhole, whereas a* (blue–yellow value) increases; this observation may correspond to decreasing oxide and/or olivine content. Similarly, at the base of Gabbro 1 (1430–1455 mbsf), as olivine mode increases downhole, b* values increase (Fig. **F90**) and L* values decrease.

Similar observations can be made at the top of Gabbro 2 (1482.5–1486 mbsf); very high magnetic susceptibility values (>15,000) correspond to an oxide vein, but the oxide gabbro host rocks also have relatively high magnetic susceptibility. Magnetic suscep-

tibility then decreases downhole as lithology changes to disseminated oxide gabbros and then gabbronorite, together with a coincident increase in L* and a* reflectance values and a decrease in b* values and NGR counts. The lower section of Gabbro 2 (1488–1495 mbsf) shows more complicated trends in physical properties that may reflect minor changes in the concentrations of oxides in the disseminated oxide gabbronorites. At a broad scale, magnetic susceptibility and b* reflectance values initially decrease downhole from 1488 to 1491 mbsf before increasing toward the base of Gabbro 2. In contrast, L* and a* reflectance values show the opposite trend. A similar trend in magnetic susceptibility and b* values is also observed at the base of Gabbro 2, where a small decrease in olivine mode corresponds with a decrease in b* values and magnetic susceptibility. These observations suggest that color reflectance data can be used for gabbroic rock samples to evaluate relative modal changes in composition.

Expedition 335 shipboard results

During Expedition 335, we measured four whole-round and archive-half core sections recovered while deepening Hole 1256D, as well as non-core material that was obtained during the cleaning of the hole. Pieces in Sections 335-1256D-235R-1 and 236R-1 were too short to be measured with the NGRL. Section 335-1256D-237R-1 was empty. The three pieces in Section 335-1256D-238R-1 are also too small to obtain any reliable signals from both the WRMSL and NGR (a total length of <20 cm). Core from Section 335-1256D-239R-1 was analyzed using all instruments.

Overall, GRA density values are surprisingly low (maximum = ~2.2 g/cm^3) for Sections 335-1256D-235R-1 and 236R-1 (Fig. **F88**), although measurements of the standard water sample were still within ~1.5% of its certified value. These values are probably related to the relatively small core diameter of the recovered pieces, typically <50 mm. A correction has been applied to these cores as described above to allow comparison of filtered data with those acquired on Expedition 312 cores.

Both whole-round magnetic susceptibility and point magnetic susceptibility (MSPOINT) data show generally high magnetic susceptibility values consistent with observations from granoblastic basalt in Expedition 312 cores and from the non-core material (see **"Expedition 335 non-core material"** in "Compressional wave velocity"). The highest observed magnetic susceptibility and GRA density values are observed in interval 332-1256D-235R-1, 22–24 cm (Piece 5), which hosts a tonalite dike. Whether the peak in magnetic susceptibility reflects the tonalite dike or the altered host rock is unclear. In contrast, MSPOINT data display a low value over the same piece, although there may have been poor sensor contact, as the piece is small (~2.5 cm).

Thermal conductivity

Expedition 312 cores revisited

Thermal conductivity was measured on a total of nine archive section half pieces (Table **T10**). The results of these measurements complement the Expedition 312 data (Fig. **F91**). We tentatively interpret an increase in thermal conductivity downhole in Gabbro 1 to be linked to a corresponding increase in olivine mode (see **"Igneous petrology"**), whereas the uniform thermal conductivity of Gabbro 2 appears to be broadly consistent with the more uniform mineralogy of Gabbro 2.

Expedition 335 shipboard results

Thermal conductivity was measured on Section 335-1256D-235R-1 (Piece 1), on a 12 cm long piece of dolerite ~5 cm in diameter (Table **T11**). Tests were conducted to assess the spatial response curve for the half-space thermal conductivity probe, as, given the low recovery, we considered measuring small pieces of core. Measurements were made at different positions across and along the core piece to determine the edge effect of the measurements to each piece (Fig. **F92**). Results were within the reported 2% instrument accuracy of measurements made at the center of the core until the center of the detector was within 15 mm of the edge of the sample. Although this length scale is likely to be dependent on the conductivity of the core (the average is 2.27 W/[m·K] for measurements away from piece edges) and the heating power applied (3 W/m), the results suggest that robust measurements can be obtained from relatively small core pieces. This inference is consistent with the estimated characteristic length scale (l) of thermal conduction of ~8 mm for the experiment, where the characteristic length scale is derived from the equation for the diffusion of heat:

$$l = (kt/\rho c_p)^{1/2},$$

assuming a thermal conductivity (k) of 2.3 W/(m·K), a period of heating (t) of 80 s, a density (ρ) of 2.9 g/cm^3, and specific heat capacity (c_p) of 900 J/(kg·K). For low-porosity mafic rocks, these results appear to indicate that robust thermal conductivity measurements might be attained on half cores with a radius of >15 mm and a length of >30 mm, although further tests are required to refine minimum reliable piece size.

Thermal conductivity of Expedition 335 non-core material

Thermal conductivity measurements were made on two slabs cut from Samples 335-1256D-Run12-RCJB-Rock C and 335-1256D-Run13-RCJB-Rock B (Table T10). Both samples were granoblastic basalts; Sample RCJB-Rock C is a granoblastic basalt cut by several alteration veins, whereas Sample RCJB-Rock B is a uniform, unaltered granoblastic basalt. Both samples yielded thermal conductivities consistent with measurements of cored granoblastic basalt (2.2–2.3 W/[m·K]).

Thermal conductivity measurements were also made to assess the anisotropy of thermal conductivity due to the veins in Sample 335-1256D-Run12-RCJB-Rock C (Fig. F93). As the angle between the needle probe and the veins increased, the observed thermal conductivity also increased (from 2.21 to 2.23 W/[m·K]), consistent with greater thermal conduction to the veins (1% anisotropy).

Discrete sample measurements

We measured a total of 11 cubes, which were shared with the Paleomagnetism group, in order to (1) compare data acquired during Expedition 335 to that acquired with a different instrument during Expedition 312 and (2) to complement and add to the existing downhole sample data.

Compressional wave velocity

Expedition 312 cores revisited

Compressional wave velocity (V_P) was measured on 11 seawater-saturated hard rock samples from gabbroic sections of the Expedition 312 cores (Table T12).

V_P measurements were initially made on cubes using Expedition 312 protocols; however, we found that variations in the surface saturation of the minicubes had a dramatic effect on velocity values, resulting in differences of as much as 900 m/s (~15%) for measurements on a single cube (see the "Methods" chapter [Expedition 335 Scientists, 2012b]). To obtain more reliable, reproducible values, we developed a new approach for measuring velocities in which minicubes are submerged in a seawater bath during measurement (see "Physical properties" in the "Methods" chapter [Expedition 335 Scientists, 2012b]). This procedure led to considerably more stable results.

Velocity measurements using the seawater bath were obtained for four minicubes that had undergone AF demagnetization by the Paleomagnetism group and so were available for repeated measurements. The remaining seven cubes were not reanalyzed using the seawater bath because they had already undergone high-temperature (as high as 600°C) demagnetization, and so the measured V_P may no longer have been representative.

V_P measurements on four gabbro minicubes submerged in the seawater bath range from 6200 to 6800 m/s with standard deviations for each measurements on the order of ~40 m/s (Table T12). In contrast, measurements made on seven minicubes without the seawater bath range between 4922 and 6017 with standard deviations for each direction of 160 m/s. Measurements made without the seawater bath are interpreted to underestimate velocity, with scatter attributed to variations in the coupling between the sample and sensor for each reading.

V_P measurements on the minicubes in three orthogonal directions vary by <2% for each sample, which is insignificant, given they are less than instrumental error. Hence the samples do not display a well-pronounced anisotropy in V_P as might be expected from the isotropic nature of both granoblastic basalt and the Gabbro 1 and 2 recovered. For samples measured using the seawater bath, averaging the velocities measured in each orthogonal direction yields sample average velocities for three of the gabbro cubes analyzed that lie in the range from 6694 to 6759 m/s; the remaining cube has a lower velocity of 6298 ± 170 m/s.

Velocity measurements with the seawater bath are markedly higher than those obtained during Expedition 312 on samples from the same intervals (Fig. F94). We suggest that the seawater bath provides more reliable results and that V_P values for gabbros in Hole 1256D may be higher than reported during Expedition 312. We note that the velocities are generally >6500 m/s, match shore-based measurements between 1440 and 1460 mbsf (Violay et al., 2010; Gilbert and Salisbury, 2011), and are consistent with the downhole sonic log (~6800 m/s) (Guerin et al., 2008). Although measured velocities are >6500 m/s and consistent with seismic Layer 3, an interpretation that the Layer 2/3 boundary has been reached is premature, as the velocities also lie at the upper range of Layer 2 values (see also discussion in Gilbert and Salisbury, 2011).

Expedition 335 non-core material

Two minicubes were cut from each of the granoblastic basalt slabs that were used for thermal conductivity measurements (Samples 335-1256D-Run12-RCJB-Rock C and 335-1256D-Run13-RCJB-Rock B). Density, porosity, and V_P were measured for each cube. Prior to cutting, V_P was also measured perpen-

dicular to the cut faces of the slab from Sample 335-1256D-Run13-RCJB-Rock B. These latter measurements were made without the seawater bath because of sample size. Average V_P for the slab was 6123 ± 20 m/s (1σ error). For the four minicube samples, V_P ranged from 6610 ± 22 to 6907 ± 21 m/s. These velocities are higher than values measured during Expedition 312 because of the improved surface saturation of samples measured using the seawater bath (see the **"Methods"** chapter [Expedition 335 Scientists, 2012b]) (Fig. **F94;** Table **T12**), an inference consistent with the observation that V_P measured in the *z*-direction of minicubes using the seawater bath is ~300 m/s greater than measurements made on the slab without the seawater bath. The velocities of these granoblastic basalts are generally higher than those of gabbros.

Moisture and density

Expedition 312 cores revisited

Density and porosity results for the 11 minicubes are directly comparable to the results obtained during Expedition 312 (Table **T12;** Fig. **F95**). Bulk density values increase slightly with depth from ~2.9 to 3.0 gm/cm^3 over the interval from 1400 to 1507 mbsf, whereas porosity decreases from ~2% to 0.5%. These observations are consistent with the general trend of increasing V_P over the same interval. Superimposed on this apparent trend is variation associated with lithology; in particular, porosity and V_P vary more in Gabbro 1 than within the granoblastic basalts and Gabbro 2, an observation that is consistent with the comparably more heterogeneous texture and mineralogy of Gabbro 1.

Expedition 335 non-core material

Density and porosity results for the four minicubes analyzed from non-core material appear to continue the downhole trends observed for samples from rocks recovered during Expedition 312. Bulk densities of 3.01–3.07 g/cm^3 are among the highest observed in Hole 1256D, whereas porosities of 0.4%–0.8% continue the decreasing trend in porosity downhole.

Magnetic susceptibility of Expedition 335 non-core material

Unoriented samples recovered during operations to clear Hole 1256D were not analyzed using the logging tracks; however, we measured magnetic susceptibility using a portable Bartington MS2F probe on all large samples from the reverse circulation junk basket (RCJB) runs and on representative samples (approximately >5 cm^3) from EXJBs on Runs 11 and 14.

Histograms of magnetic susceptibility indicate that rock samples from Run12 and Run13 have a high susceptibility [mean = (5580 ± 200) × 10^{-5} SI; 95% confidence] (Fig. **F96**). Separating the data by lithology shows that data are dominated by results for the granoblastic basalts [mean = (6190 ± 200) × 10^{-5} SI; 95% confidence], which show relatively consistent magnetic susceptibilities. This observation contrasts with the broader distribution but generally lower magnetic susceptibility of the gabbroic samples [mean = (3010 ± 450) × 10^{-5} SI; 95% confidence limit]. These results agree with previous measurements of magnetic susceptibility of gabbros and granoblastic basalts in Hole 1256D (Teagle, Alt, Umino, Miyashita, Banerjee, Wilson, and the Expedition 309/312 Scientists, 2006).

Downhole logging

Complete logging programs had been run in Hole 1256D during previous expeditions above ~1420 mbsf, and logging operations during Expedition 335 were designed to focus mostly on the deepest section of the hole. Another objective was to record a full caliper log over the entire hole, both to assess the results of the cementing operations earlier in the expedition and to help plan the final cementing to stabilize Hole 1256D for future expeditions.

A predrilling temperature log and water-sampling temperature probe (WSTP) geochemical sampling were originally scheduled but did not occur because of the hole obstruction at ~920 mbsf. Temperature sondes were included in every tool string scheduled to estimate the thermal rebound of the hole.

Operations

At the end of the run of the magnetic fishing tool (bit Run 22), the hole was displaced with 200 bbl of freshwater to decrease the resistivity contrast between the borehole fluid and the formation below ~1250 mbsf, where formation resistivity was known to exceed 10,000 Ωm. After recovering the magnetic fishing tool, a logging bit was run to 3864.3 mbrf (218.9 mbsf), ~50 m above the casing shoe, to ensure that the longest tool string would be able to exit the pipe while still fully inside the casing. Preparations for logging on the rig floor started at 2000 h on 26 May 2011 (times in local time, Universal Time Coordinated [UTC] – 6). Table **T13** provides complete details on the sequence and timing of events during the logging operations.

First deployment: triple combo

Shortly after exiting the casing, the tool string was stopped at 4000 mbrf to continue the ongoing evaluation of the wireline heave compensator (WHC). The chosen configuration reduced tool motion by ~50% from surface heave. After completion of WHC testing, logging down resumed at 5000 ft/h. It was stopped at 5100 mbrf to calibrate the High-Resolution Laterolog Array (HRLA) resistivity tool for in situ temperature. Calibration was performed while the tool was lowered to a total depth of 5165 mbrf (1520 mbsf), indicating that no fill had accumulated at the bottom of the hole.

After starting logging upward at 900 ft/h, the caliper of the Hostile Environment Litho-Density Sonde (HLDS) did not open immediately and the first caliper reading was only at ~5132 mbrf (1487 mbsf). Considering the position of the caliper in the tool string, ~12 m of caliper reading was missed. It was decided not to attempt a routine repeat pass, to avoid the risk of not being able to open the caliper a second time and not be able to record a complete profile of the hole size.

At a depth of 4850 mbrf (1205 mbsf), the logging speed was increased to 3600 ft/h to complete the caliper log.

The uplog was completed after entering the bit, and the tools were brought back to the surface without incident. However, the Modular Temperature Tool (MTT) started showing erratic readings at the end of the uplog. Because temperature measurements provided by the Enhanced Digital Telemetry Cartridge (EDTC) were in good agreement with the MTT, it was decided not to run the MTT on the second tool string.

During rig-down, it was observed that the three bowsprings of one of the centralizers were worn out, and the three springs were replaced with new ones. Unlike the replaced springs, the new ones had an inside rubber padding designed to prevent erosion.

Second deployment: FMS-sonic

After running into the hole, the tool could not be lowered below 3885 mbrf. With the bit at 3864 mbrf, it was assumed that the hold was at the newly refurbished upper centralizer and the tools were brought back to the surface. No sign of any damage was observed, and it was decided that the new springs were just stiff and that we should be able to go through. As a precautionary measure, one of the springs of the lower centralizer that was also showing signs of wear was also replaced at this time.

This second attempt was stopped at the same depth, and after more attempts within safe operating parameters, we were not able to make any progress or retrieve the tool. After ~90 min without progress, it was decided to use the Kinley fishing set to recover the tool string.

The procedure was performed very efficiently by the rig crew. After crimping the wire to secure the tools, cutting the wireline, and then recovering it, the drill string was pulled out of the hole, and all logging tools were safely recovered. When the tools arrived at the rig floor, it was confirmed that the upper centralizer was jammed in the fishing landing sub. The rubber padding under the new centralizer bowsprings had made the centralizer too wide to go through. The lower centralizer with only one new spring was able to go through without any trouble, but the upper one with three new springs was too wide, indicating the narrow margin for error. The last logging tools were rigged down at 1130 h on 28 May 2011.

Data quality

The hole size in Figure F97 shows that the bottom was significantly enlarged after the several weeks and bit runs dedicated to cleaning the hole. The hole is irregular in the new section logged below ~1400 mbsf, and the low density and high porosity readings below this depth are a direct consequence of the hole size and the inability of the tool sensors to make proper contact with the formation. As in the several shallower intervals with large hole diameter, density log values are systematically much lower than measurements made on core samples below 1400 mbsf. The decoupling (i.e., offset) between the shallow and deep resistivity logs below this depth is also a consequence of hole size. However, the deep resistivity measurement should not be affected by hole size.

The comparison between the hole sizes during Expeditions 312 and 335 in Figure F98 shows that the hole has changed little after 5 y and despite working the hole for several weeks before logging. Hole enlargements are indicated in the same intervals and have similar extents. This is confirmed by the very good repeatability between the different logs for both expeditions.

The only significant difference between the two sets of logs is in the gamma ray log between ~920 and ~960 mbsf, suggesting that the cement used includes radioactive nuclides detected by the gamma ray sensor. This is shown more clearly in Figure F99, where differences between the two holes are illustrated by showing intervals of hole enlargement and hole reduction between the two expeditions. Intervals where hole size has decreased, presumably because

of the cement emplaced when the bit was at ~960 mbsf, mostly coincide with higher gamma ray readings during Expedition 335. The largest difference in the gamma ray logs is between 925 and 934 mbsf, where the hole was the largest and presumably the largest volume of cement was deposited. The increase in hole size above 920 mbsf is probably the result of several days spent trying to pass this depth. The cement reduced the hole size and its roughness between 930 and 970 mbsf, eliminating asperities and allowing the many smooth reentries following the cementing.

In addition to density and porosity measurements in the enlarged hole, the other questionable data are the large temperature excursions recorded by the MTT during the uplog in several places above 850 mbsf (Fig. **F97**). These excursions were neither recorded on the downlog nor by the EDTC temperature sensor during any of the passes and are likely related to episodic tool failures and not indicative of any borehole fluid temperature anomalies. They were removed from the other figures in this chapter to avoid any erroneous interpretation.

Logging results

Figure **F100** shows data recorded in the deeper section of the hole. To compensate for the lack of reliable density and porosity logs in the enlarged hole, we used the relationship defined by Archie (1942) to estimate porosity from the deep resistivity log. For the fluid resistivity necessary in this relationship, we used the fluid resistivity measurement provided by the HRLA. The value used for the tortuosity coefficient (a = 1) and the cementation coefficient (m = 2) in this relationship are generic values (Becker, 1985) that seem appropriate to provide a reasonable agreement with the core measurement. We then used the average grain density measured on core samples for a log-derived continuous density profile from the porosity calculated from the resistivity.

One of the most significant observations in the newly recorded data is a decrease in resistivity with depth, starting within Gabbro 1 (~1420 mbsf) and becoming more noticeable in the deeper dike screens and Gabbro 2. As a resistivity increase with depth was expected in the plutonic section based on the shallower trend and previous observations, these lower resistivity values suggest that the deepest section might be fractured, possibly part of a fault, which could explain some of the difficulties encountered while coring. However, these resistivity values are in the same range as higher in the sheeted dikes complex and could be representative of the actual electric properties of the dike screens.

The ~5 m interval immediately above the lower resistivity trend (1410–1415 mbsf) defines a sharp interval with lower resistivity and higher gamma ray that could encompass a quartz-rich oxide diorite and several occurrences of evolved plutonic rocks observed in Core 312-1256D-214R (Expedition 309/312 Scientists, 2006). The lower resistivity and increased gamma ray in this interval are likely related to higher intensities of alteration observed in these rocks.

Temperature logs

The comparison between the temperature logs recorded by the two temperature tools during Expedition 335 and the temperatures measured during previous expeditions in Hole 1256D (Fig. **F101**) shows similar trends as the borehole fluid recovers from the disturbance of drilling operations. The maximum temperature recorded (80°C) is well below the predicted equilibrium temperature and shows that the tools were not at risk from excessive temperature.

Several excursions to lower temperatures, in particular around 925 mbsf and at 1060 mbsf, at the top of the sheeted dike complex, coincide with intervals with lower resistivity, indicating more permeable intervals where the formation might have been invaded by drilling fluid and is consequently recovering more slowly from the drilling process. However, the larger hole diameter in these intervals could contribute to the slower thermal rebound. A kick at ~1300 mbsf, also observed during Expedition 312, coincides with lower resistivity and is probably also associated with fluid exchange with the formation. These anomalies will be the object of numerical modeling, which, in combination with other logs, should provide estimates of the permeability in these intervals.

Core section image analysis

During Expedition 335, external surfaces of the three vertically oriented pieces recovered from Cores 335-1256D-235R and 236R were imaged and merged to synthetic unrolled 360° images (Figs. **F102, F103**). Because the pieces are small and recovery was very low, there is little hope of successfully identifying true orientation by matching these images to logging images.

Underway geophysics

While transiting between Costa Rica and Site 1256 during Expedition 335, we collected echo sounder data over most of 860 km of trackline and magne-

tometer data over most of 730 km of trackline away from shipping lanes. The profile covers the early record of spreading between the Cocos and Pacific plates. Magnetic and bathymetric data were also collected on the transit from Site 1256 to Panama.

References

Abelson, M., Baer, G., and Agnon, A., 2001. Evidence from gabbro of the Troodos ophiolite for lateral magma transport along a slow-spreading mid-ocean ridge. *Nature (London, U. K.),* 409(6816):72–75. **doi:10.1038/35051058**

Agar, S.M., Casey, J.F., and Kempton, P.D., 1997. Textural, geochemical, and isotopic variations in gabbroic shear zones from the MARK area. *In* Karson, J.A., Cannat, M., Miller, D.J., and Elthon, D. (Eds.), *Proc. ODP, Sci. Results,* 153: College Station, TX (Ocean Drilling Program), 99–121. **doi:10.2973/odp.proc.sr.153.007.1997**

Allerton, S., Pariso, J.E., Stokking, L.B., and McClelland, E., 1995. Origin of the natural remanent magnetism of sheeted dikes in Hole 504B cored during Legs 137 and 140. *In* Erzinger, J., Becker, K., Dick, H.J.B., and Stokking, L.B. (Eds.), *Proc. ODP, Sci. Results,* 137/140: College Station, TX (Ocean Drilling Program), 263–270. **doi:10.2973/odp.proc.sr.137140.030.1995**

Alt, J.C., Laverne, C., Coggon, R.M., Teagle, D.A.H., Banerjee, N.R., Morgan, S., Smith-Duque, C.E., Harris, M., and Galli, L., 2010. Subsurface structure of a submarine hydrothermal system in ocean crust formed at the East Pacific Rise, ODP/IODP Site 1256. *Geochem., Geophys., Geosyst.*, 11:Q10010. **doi:10.1029/2010GC003144**

Alt, J.C., Laverne, C., Vanko, D.A., Tartarotti, P., Teagle, D.A.H., Bach, W., Zuleger, E., Erzinger, J., Honnorez, J., Pezard, P.A., Becker, K., Salisbury, M.H., and Wilkens, R.H., 1996. Hydrothermal alteration of a section of upper oceanic crust in the eastern equatorial Pacific: a synthesis of results from Site 504 (DSDP Legs 69, 70, and 83, and ODP Legs 111, 137, 140, and 148.) *In* Alt, J.C., Kinoshita, H., Stokking, L.B., and Michael, P.J. (Eds.), *Proc. ODP, Sci. Results,* 148: College Station, TX (Ocean Drilling Program), 417–434. **doi:10.2973/odp.proc.sr.148.159.1996**

Arason, P., and Levi, S., 2010. Maximum likelihood solution for inclination-only data in paleomagnetism. *Geophys. J. Int.,* 182(2):753–771. **doi:10.1111/j.1365-246X.2010.04671.x**

Archie, G.E., 1942. The electrical resistivity log as an aid in determining some reservoir characteristics. *J. Pet. Technol.,* 5:1–8.

Becker, K., 1985. Large-scale electrical resistivity and bulk porosity of the oceanic crust, Deep Sea Drilling Project Hole 504B, Costa Rica Rift. *In* Anderson, R.N., Honnorez, J., Becker, K., et al., *Init. Repts. DSDP,* 83: Washington, DC (U.S. Govt. Printing Office), 419–427. **doi:10.2973/dsdp.proc.83.124.1985**

Dick, H.J.B., Natland, J.H., Miller, D.J., et al., 1999. *Proc. ODP, Init. Repts.,* 176: College Station, TX (Ocean Drilling Program). **doi:10.2973/odp.proc.ir.176.1999**

Dunlop, D.J., 2003. Stepwise and continuous low-temperature demagnetization. *Geophys. Res. Lett.,* 30(11):1582. **doi:10.1029/2003GL017268**

Dziony, W., Koepke, J., and Holtz, F., 2008. Data report: petrography and phase analyses in lavas and dikes from Hole 1256D (ODP Leg 206 and IODP Expedition 309, East Pacific Rise). *In* Teagle, D.A.H., Alt, J.C., Umino, S., Miyashita, S., Banerjee, N.R., Wilson, D.S., and the Expedition 309/312 Scientists, *Proc. IODP,* 309/312: College Station, TX (Integrated Ocean Drilling Program Management International, Inc.). **doi:10.2204/iodp.proc.309312.201.2008**

Expedition 309/312 Scientists, 2006. Site 1256. *In* Teagle, D.A.H., Alt, J.C., Umino, S., Miyashita, S., Banerjee, N.R., Wilson, D.S., and the Expedition 309/312 Scientists. *Proc. IODP,* 309/312: Washington, DC (Integrated Ocean Drilling Program Management International, Inc.). **doi:10.2204/iodp.proc.309312.103.2006**

France, L., Ildefonse, B., and Koepke, J., 2009. Interactions between magma and the hydrothermal system in the Oman ophiolite and in IODP Hole 1256D: fossilisation of dynamic melt lens at fast spreading ridges. *Geochem., Geophys., Geosyst.,* 10(10):Q10O19. **doi:10.1029/2009GC002652**

Gao, Y., Huang, J., and Casey, J.F., 2009. Data report: trace element geochemistry of oceanic crust formed at superfast-spreading ridge, Hole 1256D. *In* Teagle, D.A.H., Alt, J.C., Umino, S., Miyashita, S., Banerjee, N.R., Wilson, D.S., and the Expedition 309/312 Scientists, *Proc. IODP,* 309/ 312: Washington, DC (Integrated Ocean Drilling Program Management International, Inc.). **doi:10.2204/iodp.proc.309312.202.2009**

Gee, J., Staudigel, H., Tauxe, L., Pick, T., and Gallet, Y., 1993. Magnetization of the La Palma Seamount Series: implications for seamount paleopoles. *J. Geophys. Res., [Solid Earth],* 98(B7):11743–11767. **doi:10.1029/93JB00932**

Gee, J.S., and Kent, D.V., 2007. Source of oceanic magnetic anomalies and the geomagnetic polarity timescale. *In* Kono, M. (Ed.), *Treatise on Geophysics: Geomagnetism* (Vol. 5): Amsterdam (Elsevier), 455–507.

Gilbert, L.A., and Salisbury, M.H., 2011. Oceanic crustal velocities from laboratory and logging measurements of Integrated Ocean Drilling Program Hole 1256D. *Geochem., Geophys., Geosyst.,* 12:Q09001. **doi:10.1029/2011GC003750**

Gillis, K.M., 2008. The roof of an axial magma chamber: a hornfelsic heat exchanger. *Geology,* 36(4):299–302. **doi:10.1130/G24590A.1**

Godard, M., Awaji, S., Hansen, H., Hellebrand, E., Brunelli, D., Johnson, K., Yamasaki, T., Maeda, J., Abratis, M., Christie, D., Kato, Y., Mariet, C., and Rosner, M., 2009. Geochemistry of a long in-situ section of intrusive slow-spread oceanic lithosphere: results from IODP Site

U1309 (Atlantis Massif, 30°N Mid-Atlantic-Ridge). *Earth Planet. Sci. Lett.,* 279(1–2):110–122. doi:10.1016/j.epsl.2008.12.034

Gubbins, D., and Kelly, P., 1993. Persistent patterns in the geomagnetic field over the past 2.5 Myr. *Nature (London, U. K.),* 365(6449):829–832. doi:10.1038/365829a0

Guerin, G., Goldberg, D.S., and Iturrino, G.J., 2008. Velocity and attenuation in young oceanic crust: new downhole log results from DSDP/ODP/IODP Holes 504B and 1256D. *Geochem., Geophys., Geosyst.,* 9(12):Q12014. doi:10.1029/2008GC002203

Jelinek, V., 1981. Characterization of the magnetic fabric of rocks. *Tectonophysics,* 79(3–4):T63–T67. doi:10.1016/0040-1951(81)90110-4

Kelly, P., and Gubbins, D., 1997. The geomagnetic field over the past 5 million years. *Geophys. J. Int.,* 128(2):315–330. doi:10.1111/j.1365-246X.1997.tb01557.x

Koepke, J., Christie, D.M., Dziony, W., Holtz, F., Lattard, D., Maclennan, J., Park, S., Scheibner, B., Yamasaki, T., and Yamazaki, S., 2008. Petrography of the dike–gabbro transition at IDOP Site 1256 (equatorial Pacific): the evolution of the granoblastic dikes. *Geochem., Geophys., Geosyst.,* 9(7):Q07O09. doi:10.1029/2008GC001939

Koepke, J., France, L., Müller, T., Faure, F., Goetze, N., Dziony, W., and Ildefonse, B., 2011. Gabbros from IODP Site 1256, equatorial Pacific: insight into axial magma chamber processes at fast spreading ocean ridges. *Geochem., Geophys., Geosyst.,* 12(9):Q09014. doi:10.1029/2011GC003655

Launeau, P., Archanjo, C.J., Picard, D., Arbaret, L., and Robin, P.-Y., 2010. Two- and three-dimensional shape fabric analysis by the intercept method in grey levels. *Tectonophysics,* 492(1–4):230–239. doi:10.1016/j.tecto.2010.06.005

Merrill, R.T., 1970. Low-temperature treatments of magnetite and magnetite-bearing rocks. *J. Geophys. Res., [Solid Earth],* 75(17):3343–3349. doi:10.1029/JB075i017p03343

Meurer, W.P., and Gee, J., 2002. Evidence for the protracted construction of slow-spread oceanic crust by small magmatic injections. *Earth Planet. Sci. Lett.,* 201(1):45–55. doi:10.1016/S0012-821X(02)00660-X

Morris, A., Gee, J.S., Pressling, N., John, B.E., MacLeod, C.J., Grimes, C.B., and Searle, R.C., 2009. Footwall rotation in an oceanic core complex quantified using reoriented Integrated Ocean Drilling Program core samples. *Earth Planet. Sci. Lett.,* 287(1–2):217–228. doi:10.1016/j.epsl.2009.08.007

Neo, N., Yamazaki, S., and Miyashita, S., 2009. Data report: bulk rock compositions of samples from the IODP Expedition 309/312 sample pool, ODP Hole 1256D. *In* Teagle, D.A.H., Alt, J.C., Umino, S., Miyashita, S., Banerjee, N.R., Wilson, D.S., and the Expedition 309/312 Scientists, *Proc. IODP,* 309/312: Washington, DC (Integrated Ocean Drilling Program Management International, Inc.). doi:10.2204/iodp.proc.309312.204.2009

Nitsan, U., 1974. Stability field of olivine with respect to oxidation and reduction. *J. Geophys. Res., [Solid Earth],* 79(5):706–711. doi:10.1029/JB079i005p00706

Potter, D.K., 2004. A comparison of anisotropy of magnetic remanence methods—a user's guide for application to palaeomagnetism and magnetic fabric studies. *In* Martín-Hernández, F., Lüneburg, C.M., Aubourg, C., and Jackson, M. (Eds.), *Magnetic Fabric: Methods and Applications*. Geol. Soc. Spec. Publ., 238(1):21–35. doi:10.1144/GSL.SP.2004.238.01.03

Schneider, D.A., 1988. An estimate of the long-term nondipole field from marine magnetic anomalies. *Geophys. Res. Lett.,* 15(10):1105–1108. doi:10.1029/GL015i010p01105

Shilobreeva, S., Martinez, I., Busigny, V., Agrinier, P., and Laverne, C., 2011. Insights into C and H storage in the altered oceanic crust: results from ODP/IODP Hole 1256D. *Geochim. Cosmochim. Acta,* 75(9):2237–2255. doi:10.1016/j.gca.2010.11.027

Stephenson, A., Sadikun, S., and Potter, D.K., 1986. A theoretical and experimental comparison of the anisotropies of magnetic susceptibility and remanence in rocks and minerals. *Geophys. J. Int.,* 84(1):185–200. doi:10.1111/j.1365-246X.1986.tb04351.x

Tarling, D.H., and Hrouda, F., 1993. *The Magnetic Anisotropy of Rocks:* London (Chapman and Hall).

Tauxe, L., 2010. *Essentials of Paleomagnetism:* La Jolla, California (Univ. California Press). http://www.ucpress.edu/book.php?isbn=9780520260313

Tauxe, L., and Kent, D.V., 2004. A simplified statistical model for the geomagnetic field and the detection of shallow bias in paleomagnetic inclinations: was the ancient magnetic field dipolar? *Geophys. Monogr.,* 145:101–115.

Teagle, D.A.H., Alt, J.C., Umino, S., Miyashita, S., Banerjee, N.R., Wilson, D.S., and the Expedition 309/312 Scientists, 2006. *Proc. IODP,* 309/312: Washington, DC (Integrated Ocean Drilling Program Management International, Inc.). doi:10.2204/iodp.proc.309312.2006

Tominaga, M., Teagle, D.A.H., Alt, J.C., and Umino, S., 2009. Determination of volcanostratigraphy of the oceanic crust formed at superfast spreading ridge: electrofacies analyses of ODP/IOPD Hole 1256D. *Geochem., Geophys., Geosyst.,* 10(1):Q01003. doi:10.1029/2008GC002143

Violay, M., Pezard, P.A., Ildefonse, B., Belghoul, A., and Laverne, C., 2010. Petrophysical properties of the root zone of sheeted dikes in the ocean crust: a case study from Hole ODP/IODP 1256D, eastern equatorial Pacific. *Tectonophysics,* 493(1–2):139–152. doi:10.1016/j.tecto.2010.07.013

Wilson, D.S., 1996. Fastest known spreading on the Miocene Cocos–Pacific plate boundary. *Geophys. Res. Lett.,* 23(21):3003–3006. doi:10.1029/96GL02893

Wilson, D.S., Teagle, D.A.H., Acton, G.D., et al., 2003. *Proc. ODP, Init. Repts.,* 206: College Station, TX (Ocean Drilling Program). doi:10.2973/odp.proc.ir.206.2003

Yamazaki, S., Neo, N., and Miyashita, S., 2009. Data report: whole-rock major and trace elements and mineral compositions of the sheeted dike–gabbro transition in ODP Hole 1256D. *In* Teagle, D.A.H., Alt, J.C., Umino, S., Miyashita, S., Banerjee, N.R., Wilson, D.S., and the

Expedition 309/312 Scientists, *Proc. IODP,* 309/312: Washington, DC (Integrated Ocean Drilling Program Management International, Inc.). **doi:10.2204/iodp.proc.309312.203.2009**

Yu, Y., Dunlop, D.J., and Özdemir, Ö., 2003. On the resolution of multivectorial remanences. *Earth Planet. Sci. Lett.,* 208(1–2):13–26. **doi:10.1016/S0012-821X(02)01149-4**

Publication: 3 June 2012
MS 335-103

Figure F1. Stratigraphic column for Hole 1256D at the end of Expedition 335, showing the major and minor lithologic divisions of the upper oceanic crust.

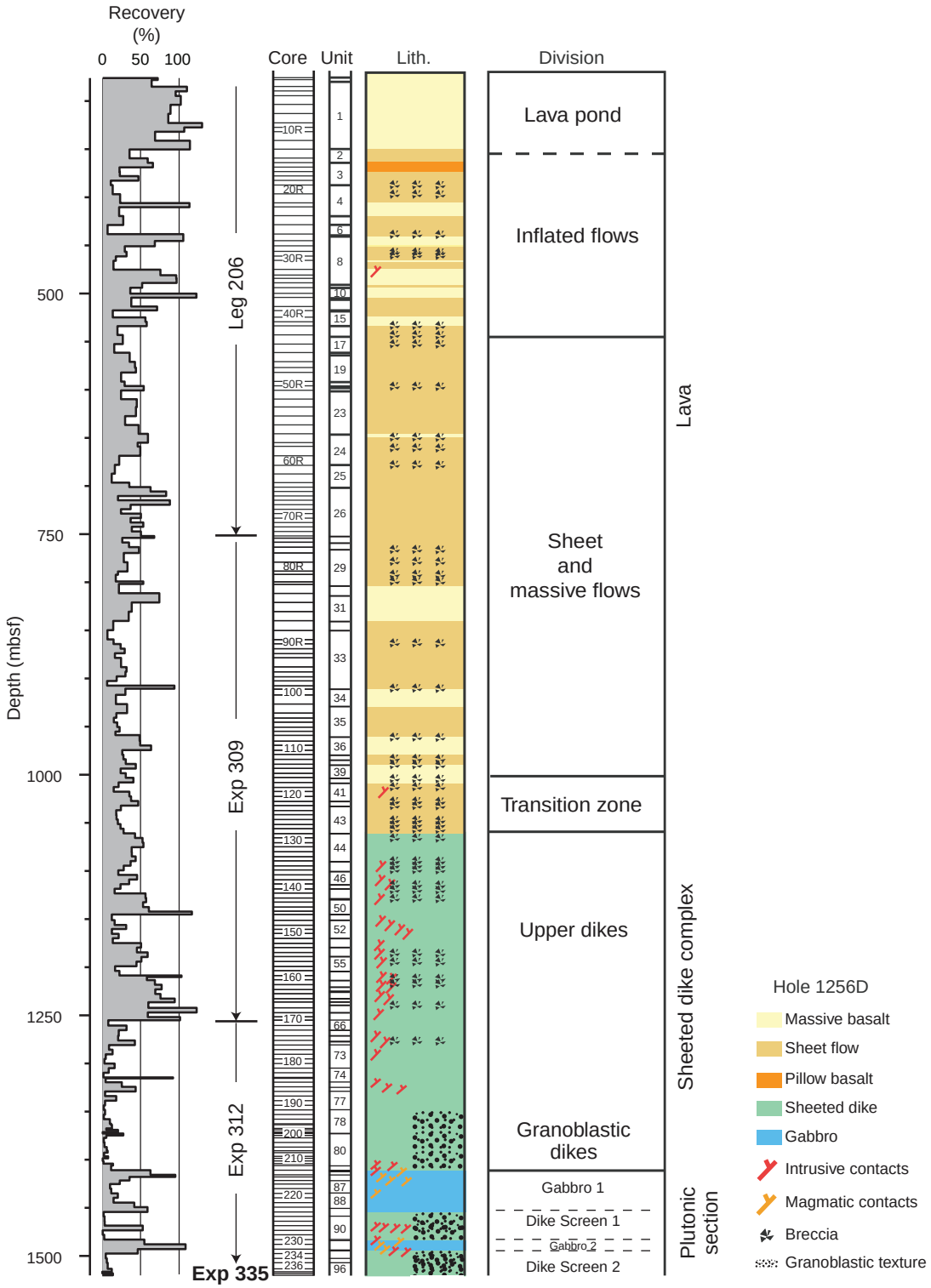

Figure F2. Age map of the Cocos plate and corresponding regions of the Pacific and Nazca plates. Isochrons at 5 m.y. intervals have been converted from magnetic anomaly identifications according to the timescale of Cande and Kent (1995). Selected DSDP and ODP sites that reached basement are indicated by circles. The wide spacing of the 10 to 20 Ma isochrons to the south reflects the extremely fast (200–220 mm/y) full spreading rate. FZ = fracture zone.

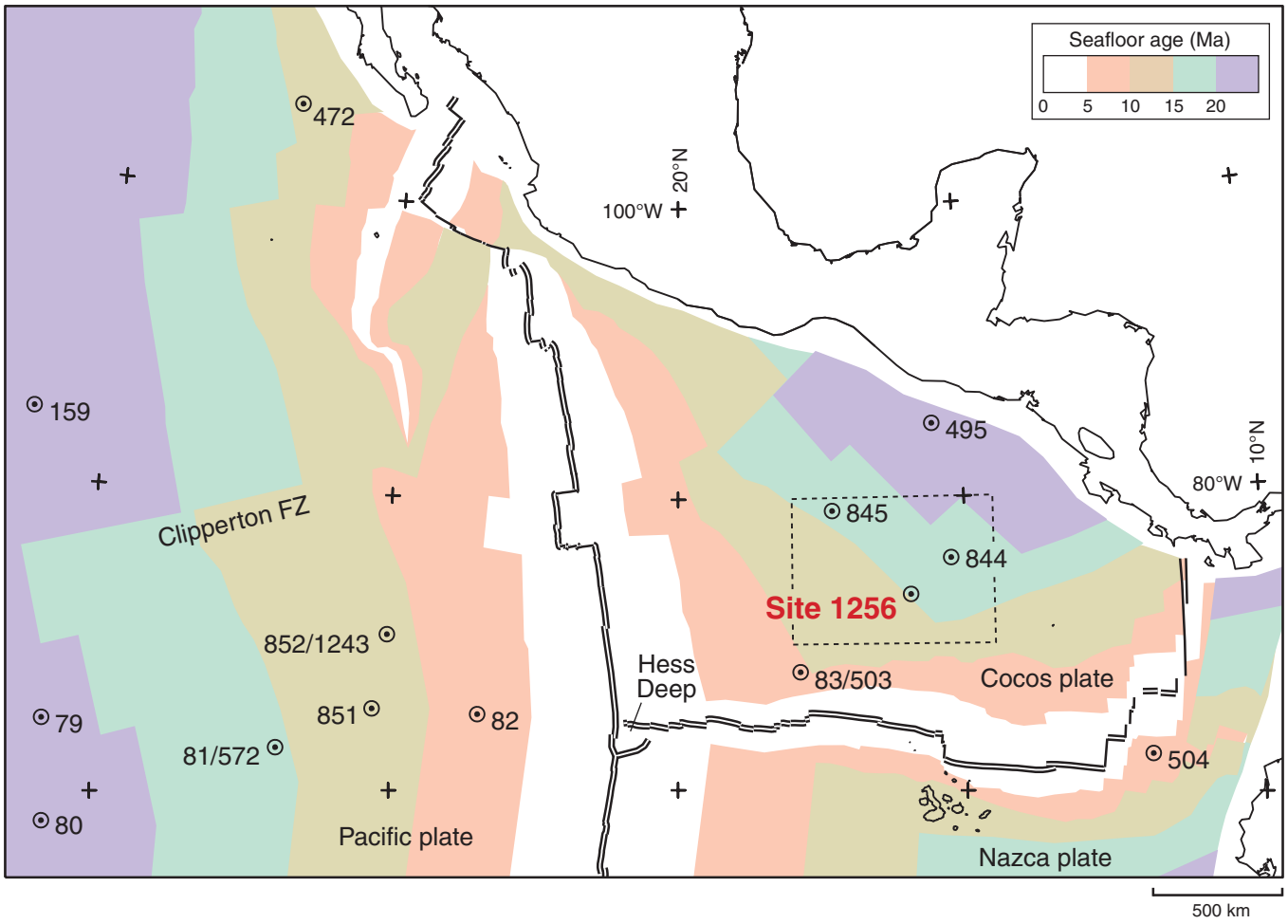

Figure F3. Photographs of various coring, drilling, fishing, and milling tools used during Expedition 335, illustrating some of the multiple operation events reported in "Operations" in the "Expedition 335 summary" chapter. **A.** Smith 9 inch F9 tricone bit used for Run 1 to work the obstruction between 920 and 925 mbsf; teeth were not worn, and much of the work was on the outside faces. **B.** Reed 9 inch tricone bit (IADC Type 517) used for Run 2. Note the more aggressive cutting structure of this bit compared to the first one. Again, after working the obstructed interval between 920 and 923 mbsf, the cones underwent very little damage, except for a couple of missing teeth. **C.** After Runs 3–5, dedicated to working further and cementing the interval between 882 and 922 mbsf, this 9 inch Atlas HP61 tricone bit was used during Run 6 to drill through cement and again work the obstructed interval at 922–923 mbsf. It returned in good condition with no appreciable shirttail wear, with all teeth intact and exhibiting very little wear. **D.** One of the two external junk baskets (EXJBs) run together with the tricone of E during Run 6; the two EXJBs returned basalt fine-grained cuttings and pebbles. (Continued on next 10 pages.)

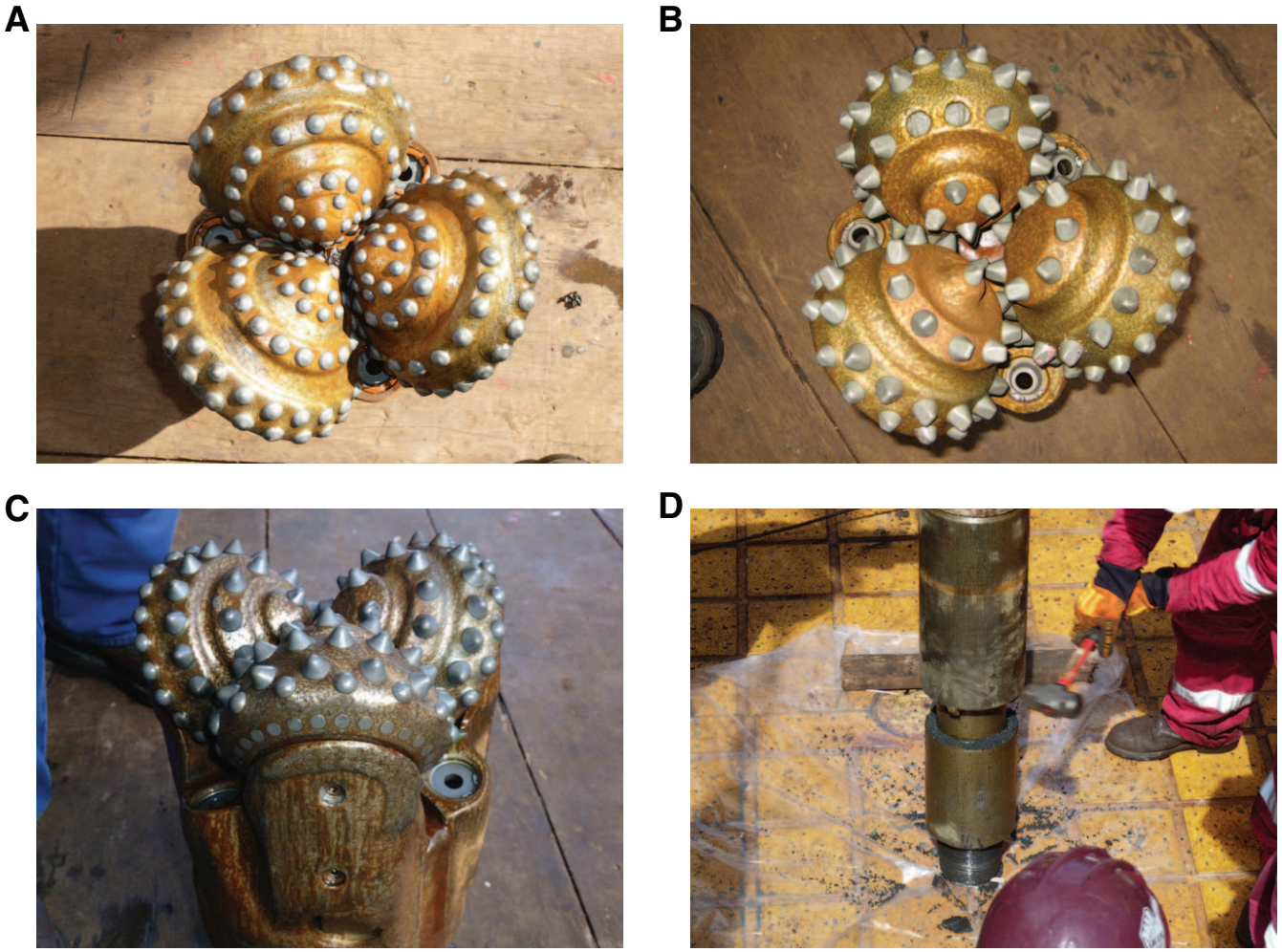

Figure F3 (continued). E. Smith 9 inch tricone bit used for Run 7 to successfully clear the obstructed interval at 922–923 mbsf and work several ledges before reaching the bottom of the hole on the morning of 1 May. The bit was slightly out of gauge after 32.8 h of use. **F.** The worn core catcher used during Run 9, the first coring run of Expedition 335. As drilling continued for ~10 h with a destroyed bit (G, H), the core catcher was in contact with metal/junk and/or rocks; it is ~1 cm shorter than the new core catcher on the right. **G, H.** Remains of the Ulterra C9 rotary core barrel coring bit used during Run 9. The bit was probably used for ~10 h after it disintegrated, which resulted in this spectacularly abraded and sculptured bit ("Stumpy"), something never seen before by the drillers. (Continued on next page.)

Figure F3 (continued). I. The 9 inch Bowen fishing magnet used for Run 10. **J.** The fishing magnet could not be deployed all the way to the bottom of the hole, as increased pump pressure indicated loss of circulation at ~1434 mbsf. When back on the rig floor, 4 m of fine-grained cuttings were found inside the bit sub and the two junk baskets. This marked the beginning of a series of fishing runs, which eventually cleared the hole of a massive amount of fine-grained sandlike cuttings. **K.** The fishing magnet recovered a limited amount of small-sized metallic debris mixed with fine basaltic grains. **L.** One of the EXJBs used for Run 11 in conjunction with an Atlas 9 inch HP61 tricone bit. (Continued on next page.)

I

J

K

L

Figure F3 (continued). M. The junk baskets used for Run 11 recovered fine-grained cuttings to large pieces of rock, mostly granoblastic basalt, and some small gabbro chips. **N.** Bowen 9.75 inch reverse circulation junk basket (RCJB) used for Runs 12 and 13. Once reverse circulation is activated (S), water flows outside the tool through the jets visible in N and returns upward through the center of the tool, where a large junk catcher retains the fished material (O). **O.** Bottom of the Bowen RCJB, showing its hard-facing structure and the junk catcher spring fingers inside. **P.** The entire bottom-hole assembly (BHA) used for Run 12, up to the top drill collar, returned completely filled with several hundreds of kilograms of fine-grained cuttings. (Continued on next page.)

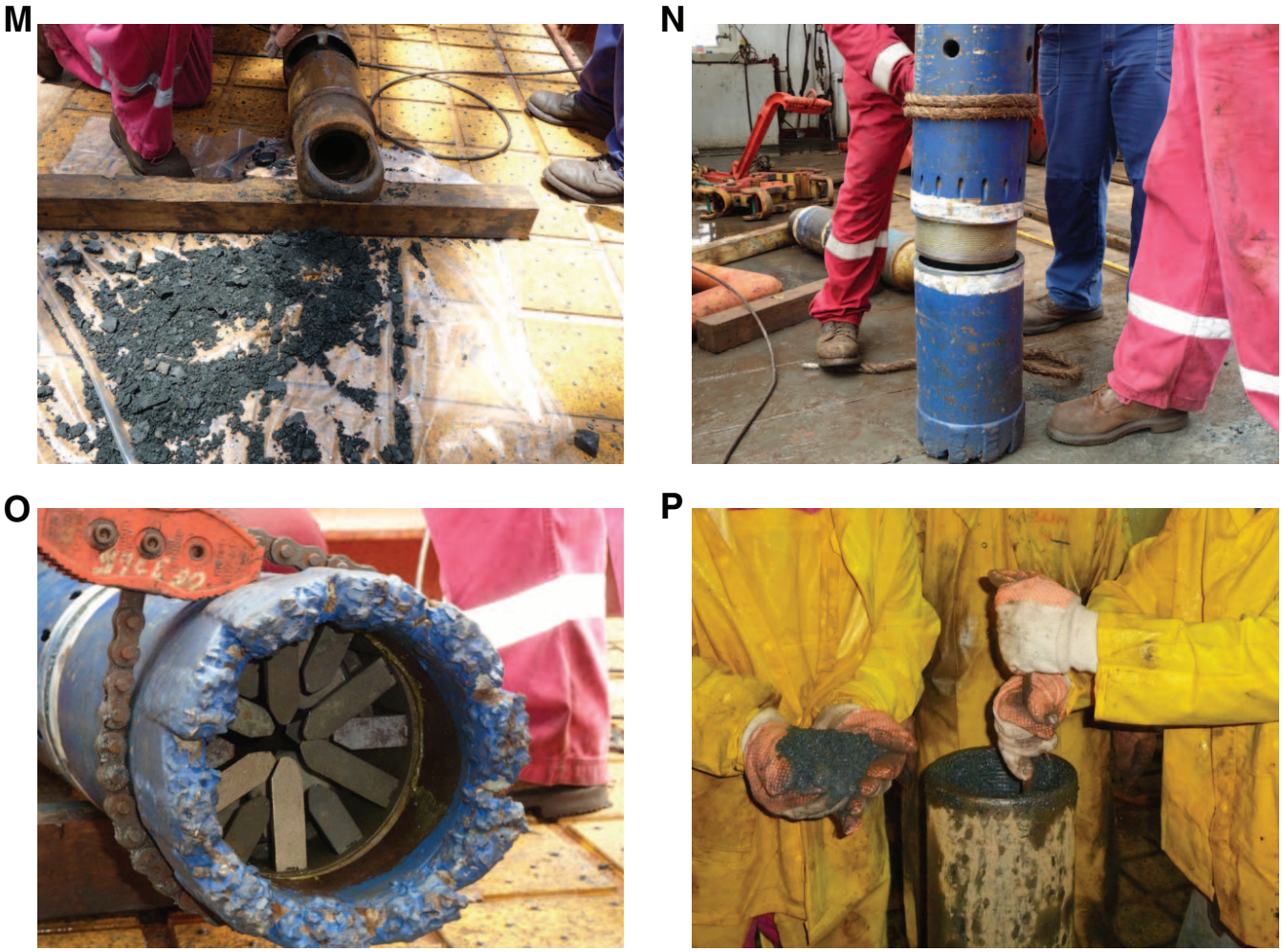

Figure F3 (continued). Q, R. The RCJB returned from Run 12 completely filled with packed cuttings and ~20 kg of rock samples, mostly granoblastic basalt. Note the heavily worn hard-facing structure of the tool after going through ~2.5 m of fill at the bottom of the hole. **S.** Top of the Bowen RCJB, showing the stainless steel ball dropped from the rig floor to activate reverse circulation by plugging the central throat and diverging fluid flow to the jets that are visible on the outside face of the tool in N. **T.** The second RCJB run (13) also returned a BHA packed by fine-grained cuttings and granoblastic basalt pebbles and large cobbles. (Continued on next page.)

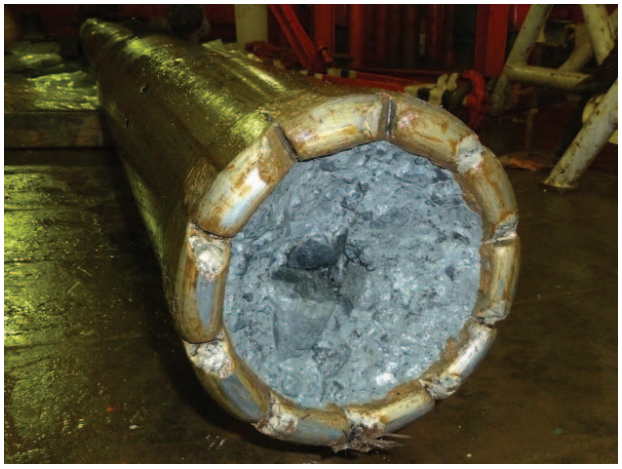

Figure F3 (continued). U. Bottom of the Homco 9.75 inch flow-through junk basket (FTJB) used for Run 14. **V.** The FTJB (Run 14) returned to the rig floor with a completely worn hard-facing structure, all fingers (but one) of the lowermost row of the junk catcher missing, and two large cobbles of granoblastic basalt. **W.** The Smith hard formation 9 inch 7JS tricone bit used in Run 15 to work the lowermost 2–3 m of the hole returned to the rig floor with cone bearings still tight and no worn teeth. The bit was severely under gauge (0.4 inches) with some shirttail wear and minor junk damage on its body (Y), indicating that the lowermost portion of the hole was under gauge. **X.** EXJB used during Run 15, showing significant damage on the edge of one of its pockets. (Continued on next page.)

U

V

W

X

Figure F3 (continued). Y. Under gauge and worn Smith tricone bit used for Run 15 (W). **Z, AA.** 9 inch Smith FH3VPS tricone bit used for Run 16. This more armored bit (compare with the previous one in Y) was more efficient to ream and clean the undergauge bottom of the hole. It returned in gauge to the rig floor, and six large teeth were missing. **BB.** Heavily worn and undergauge 9 inch flat-bottomed milling tool used for Run 17. This tool worked at the bottom of the hole for 12 h; its final (terminal) state indicates the very abrasive nature of metal debris and/or rocks at the bottom of the hole and an undergauge lowermost portion (tens of centimeters) of the hole. Note for comparison the hard-facing structure of the next milling tool (DD) on the right side of the picture. (Continued on next page.)

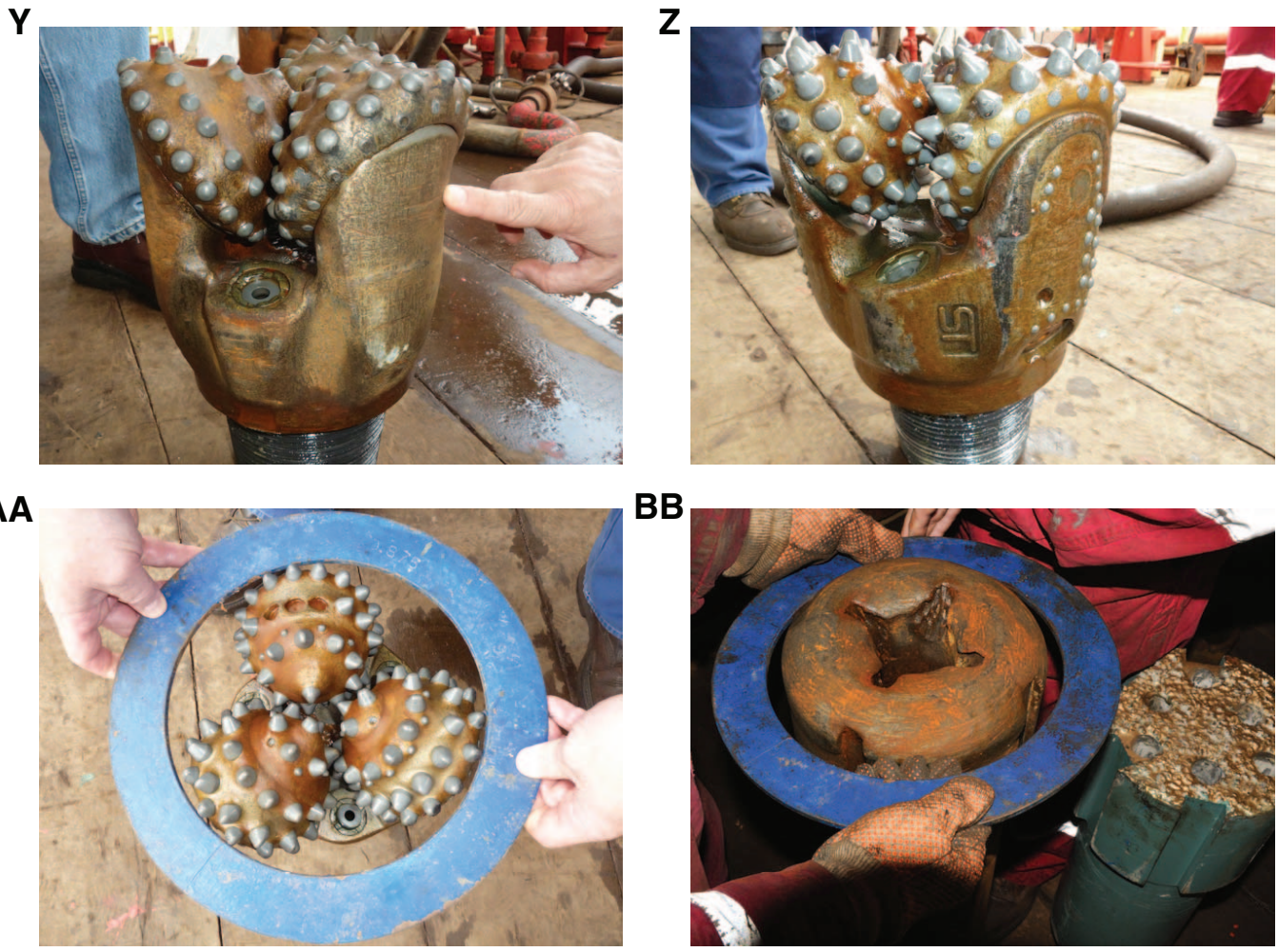

Figure F3 (continued). CC. Damaged bit sub junk basket (BSJB) used for Run 17, probably caused by granoblastic basalt angular blocks falling down the borehole walls while milling at the bottom. **DD.** 9 inch flat-bottomed milling tool used for Run 18. Note the hard-facing structure of the bottom of the tool. **EE.** The BSJB used for Run 18 returned with a damaged pocket, probably due to rock(s) detached from the borehole wall (CC). **FF.** 9 inch flat-bottomed milling tool used for Run 18, after working 6 h at the bottom of the hole. The abrasive surface (note the difference with DD) was eroded away and some external junk damage noted on the side of the tool and the crossover sub directly above the milling tool. (Continued on next page.)

CC

DD

EE

FF

Figure F3 (continued). GG. Bottom of the Bowen RCJB used for Runs 19 through 21. Note the spring fingers of the catching structure inside the tool. **HH.** The RCJB was deployed in Runs 19 through 21 with two EXJBs and one BSJB. This picture shows the junk basket tower being assembled on the rig floor. **II.** The RCJB on its return to the rig floor after Run 19 recovered four large cobbles of granoblastic basalt and rock pebbles. **JJ.** Jets on the outside of the RCJB, just above the tool bit. These grooves in the metallic body of the tool were formed by high-pressure water flow when reverse circulation was activated at the bottom of the hole (compare with the new tool in N). The picture was taken at the end of Run 20 (i.e., after a total of four runs for this tool). (Continued on next page.)

GG

HH

II

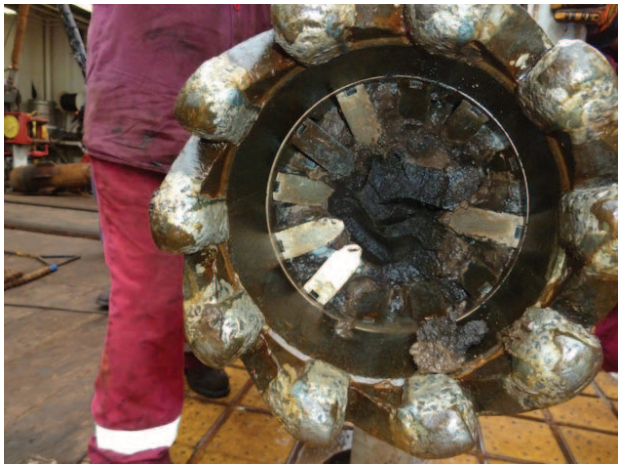

JJ

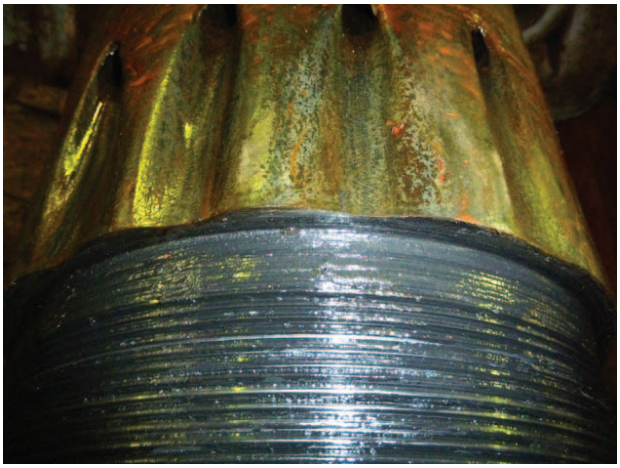

Figure F3 (continued). KK. Bowen fishing magnet tool, at the end of Run 22, with very little metal debris, although the tool tagged the bottom of the hole. **LL.** Damaged bowsprings of the upper centralizer of the logging tools after running the first (triple combo) logging run (Run 23). **MM.** The bowsprings were replaced by new, slightly thicker ones, which caused the Formation MicroScanner-sonic tool to be stuck in the logging BHA at the start of the second logging run. This picture shows the bowsprings stuck in the landing saver sub during the recovery of the tool. **NN.** Ulterra RCB C-9 bit used for the last run of Expedition 335 (24), for coring and then cementing the lowermost 10 m of the hole and the interval between 910 and 940 mbsf. (Continued on next page.)

KK

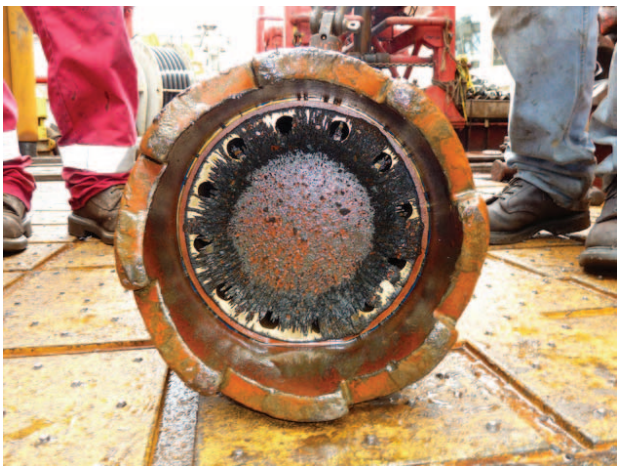

LL

MM

NN

Figure F3 (continued). OO. The C9 bit used for Run 24 (NN) returned to the rig floor in relatively good condition and nearly in gauge. It cored for ~2.5 h. **PP.** Worn outward faces of the cones, one missing tooth, and a small crack that started to propagate in the welding of the cone leg (see bottom right, close to the jet). **QQ.** Small marks on the outward facing structure of the Run 24 C9 bit, likely caused by hard, abrasive granoblastic basalt. Note the difference with the next picture. **RR.** For comparison with QQ, this picture shows the partly broken bit from Expedition 312 (missing cones), heavily damaged and cut by metal junk.

OO

PP

QQ

RR

Figure F4. Photographs (plane-polarized light) of thin sections made after fine-grain cuttings from fishing Runs 11 and 12 (field of view = ~35 mm) and histograms of the counted grains in these six thin sections (see Table T2), Expedition 335.

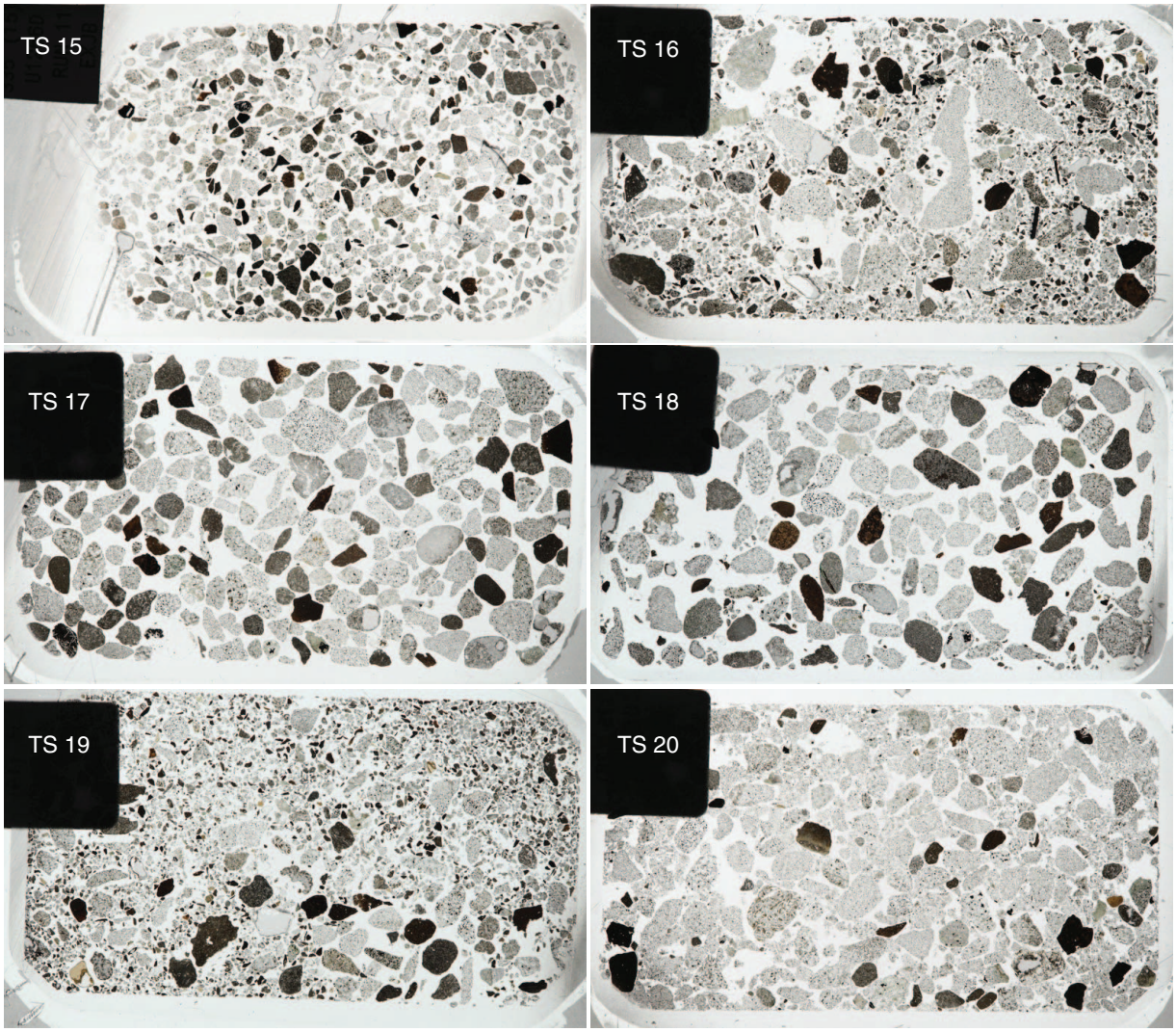

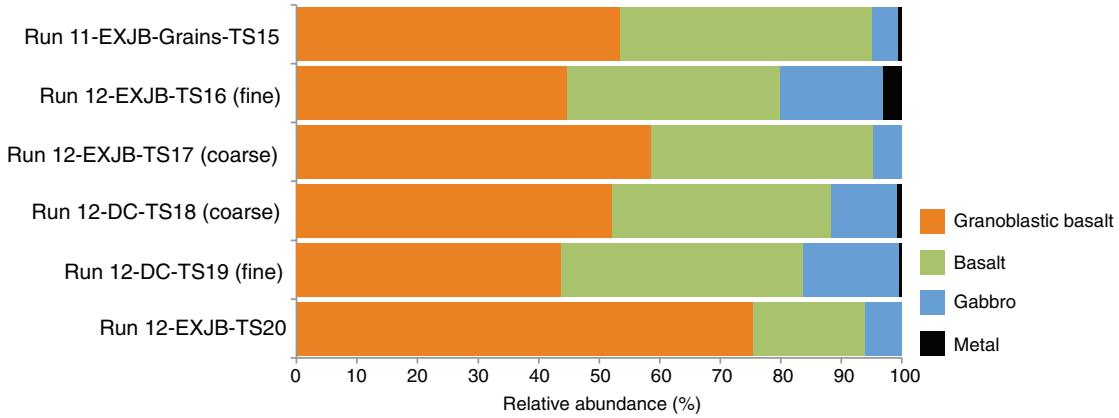

Figure F5. Plot showing the progressive deepening of Hole 1256D over four scientific ocean drilling cruises and the division of time on site into casing, coring, downhole logging, and hole remediation activities.

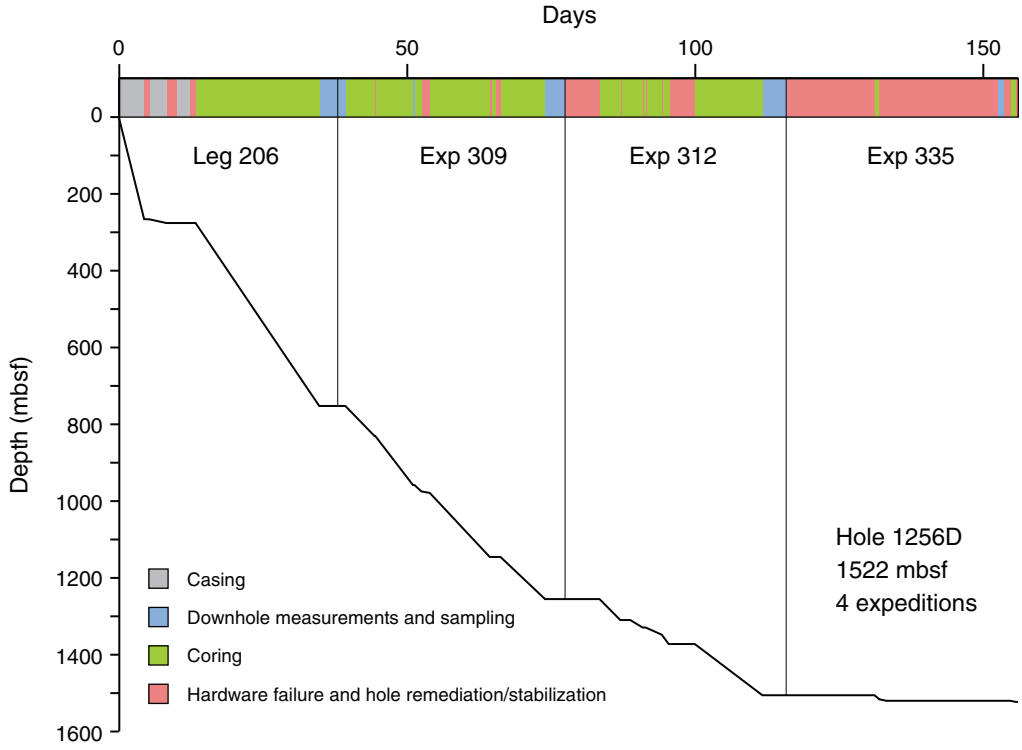

Figure F6. Igneous stratigraphy of the plutonic section recovered during Expeditions 312 and 335, following (re-)description by Expedition 335 igneous petrologists.

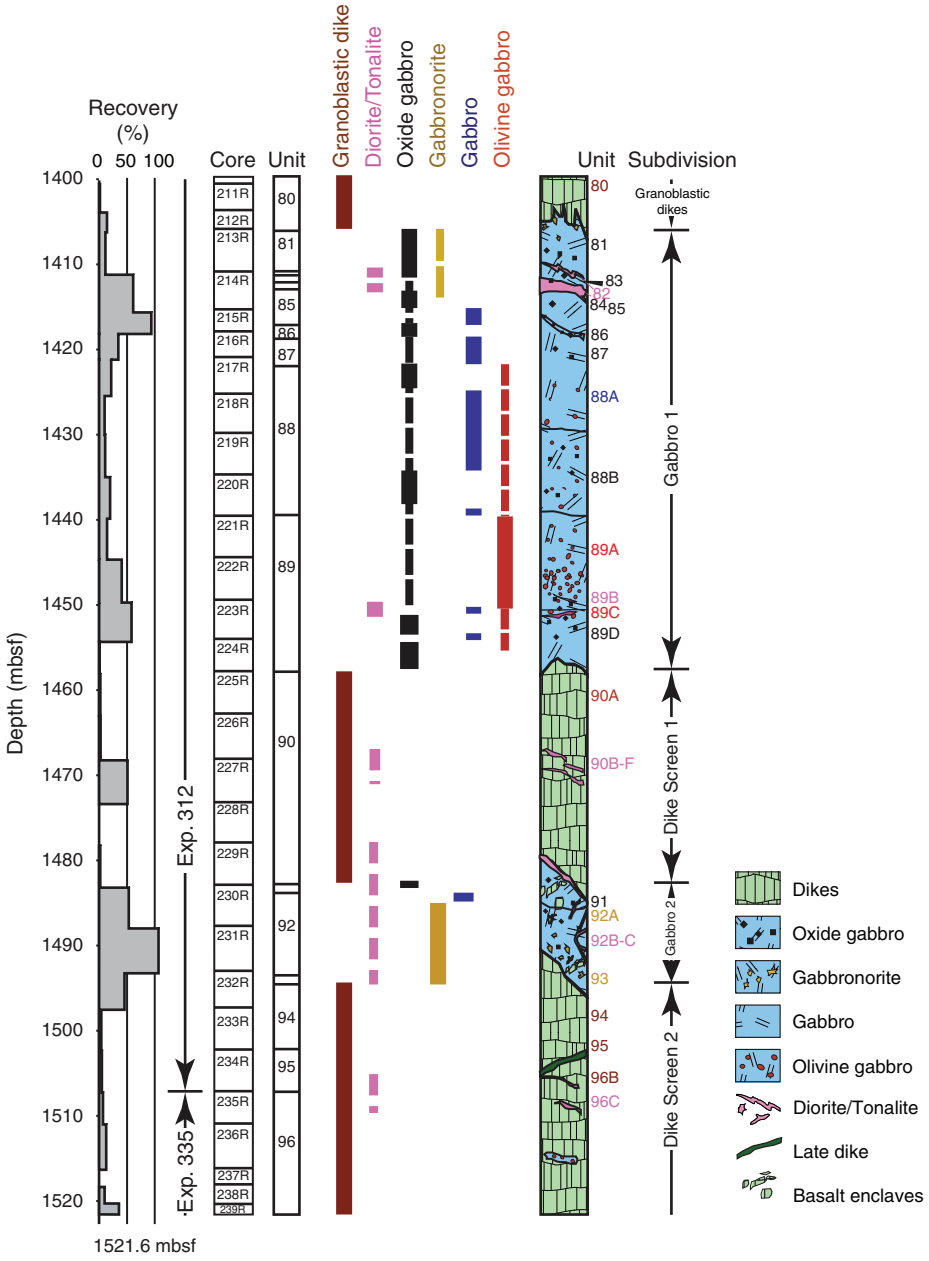

Figure F7. Downhole variation of olivine and orthopyroxene mode in the gabbroic section recovered during Expedition 312. Data include both macroscopic estimates by Expedition 335 igneous petrologists (solid symbols) and thin section estimates made during Expedition 312 (open symbols). The vertical dashed line on the orthopyroxene mode plot indicates 5% orthopyroxene, separating the (olivine) gabbro field from the (olivine) gabbronorite field.

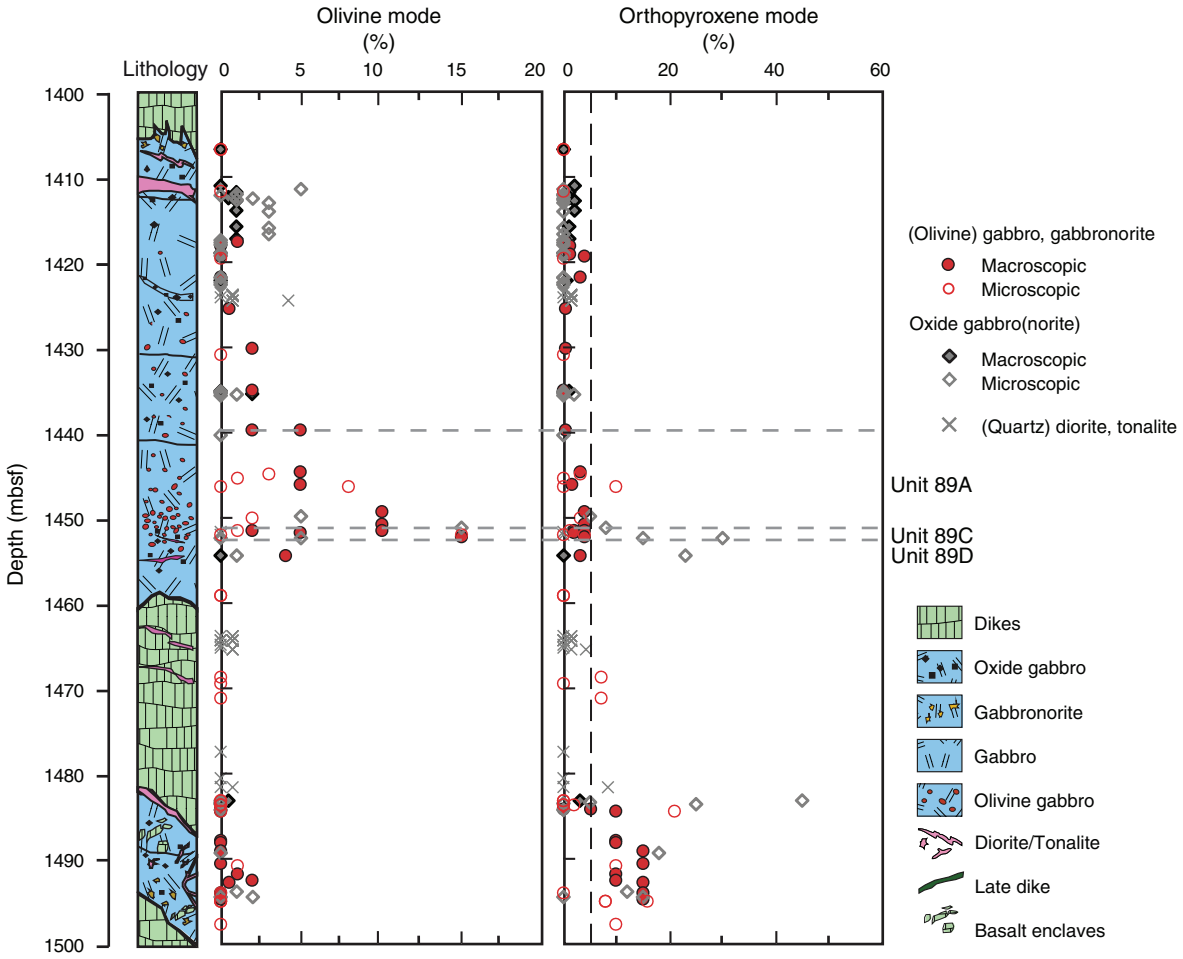

Figure F8. Olivine-rich and olivine-poor gabbro. **A.** Core photograph of sharp modal contact between upper olivine-rich (~20%) gabbro (Unit 1256D-89A) and lower olivine-poor (~2%) gabbro (Unit 1256D-89C) (interval 335(312)-1256D-223R-2, 64–75 cm [Piece 3]). **B.** Photomicrograph of the olivine-rich base of Unit 1256D-89A (Sample 335(312)-1256D-223R-2, 65–67 cm; Thin Section 1). Ol = olivine, Plag = plagioclase.

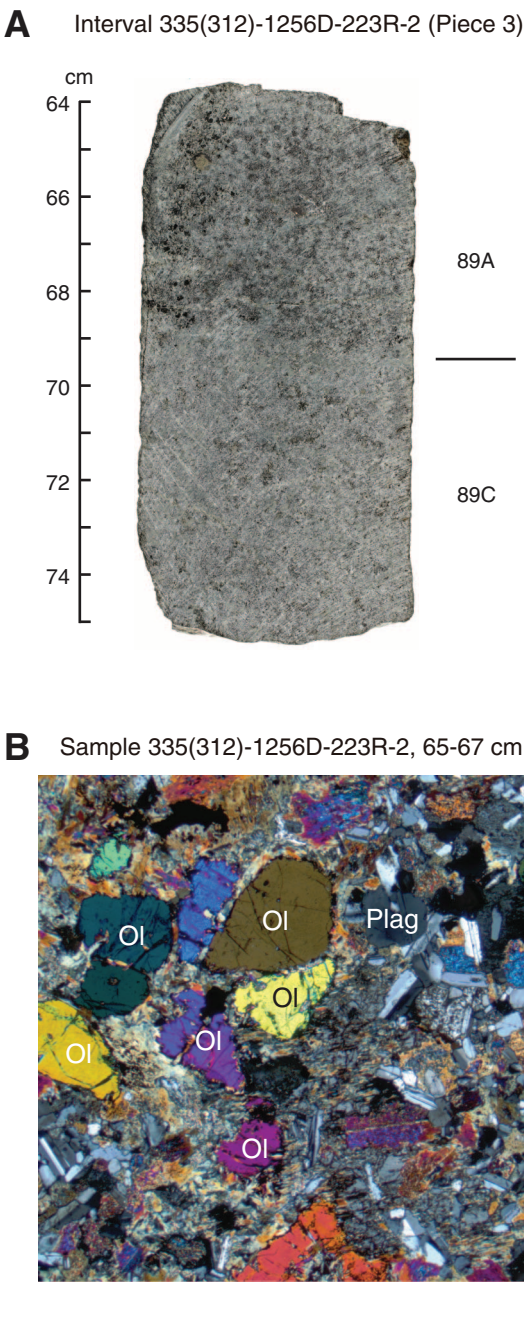

Figure F9. Photomicrographs of granoblastic basalt. **A.** Strongly granoblastic basalt of Unit 1256D-96A showing a relict intergranular texture (Sample 335-1256D-235R-1, 11–12 cm [Piece 1]; Thin Section 2) (cross-polarized light). **B.** Completely granoblastic basalt of Unit 1256D-96B showing a relict plagioclase microphenocryst with pyroxenes and oxide inclusions in its core (Sample 335-1256D-236R-1, 38–39 cm [Piece 7]; Thin Section 5) (plane-polarized light). Yellow-pink chain of orthopyroxene (Opx) crystals represents a metamorphic vein.

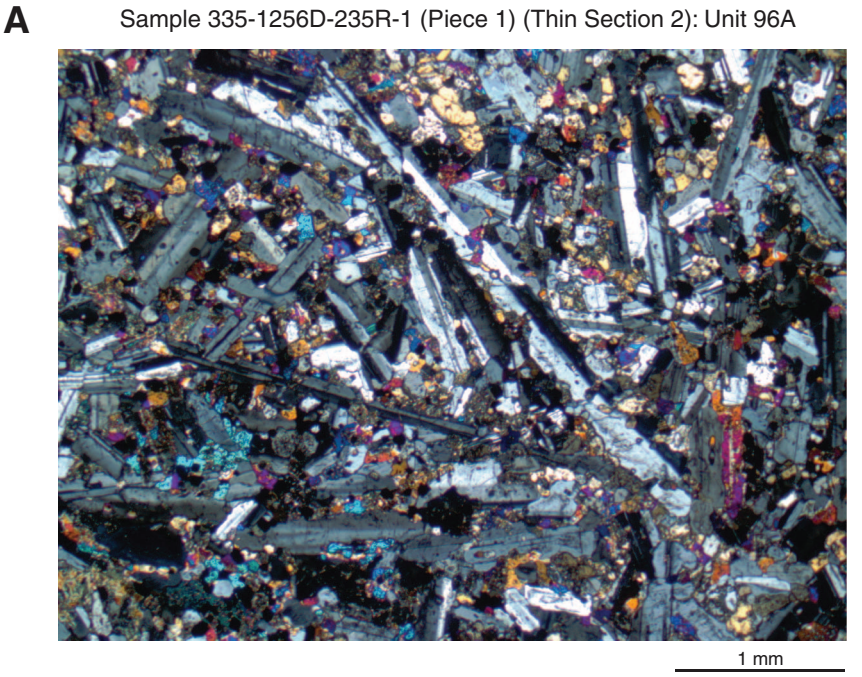

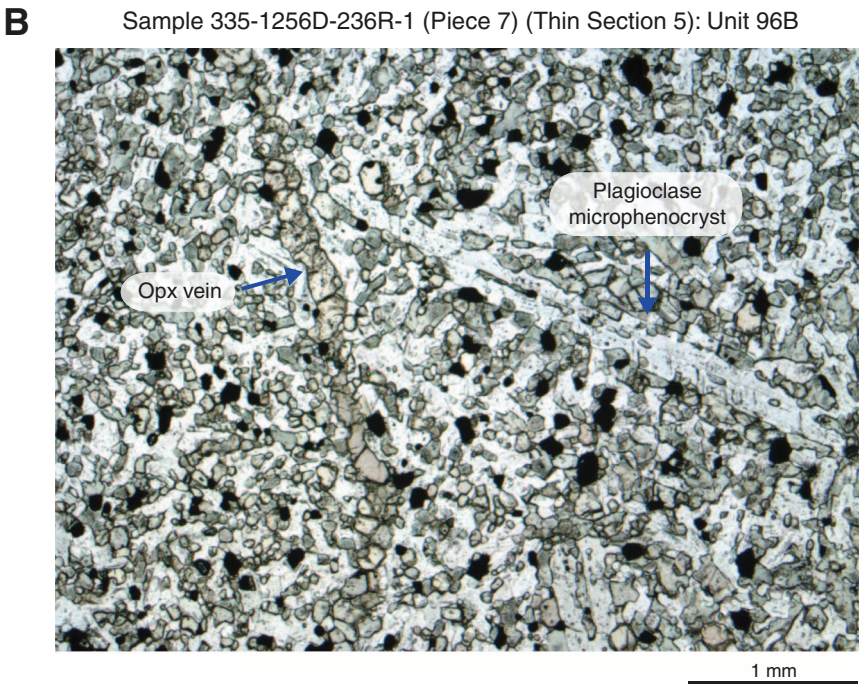

Figure F10. Close-up photograph of Section 335-1256D-235R-1 (Pieces 4–7), showing the occurrence of tonalite in oxide diorite (Piece 5) and quartz diorite (Piece 7) within the granoblastic basalt sequence (Pieces 4 and 6).

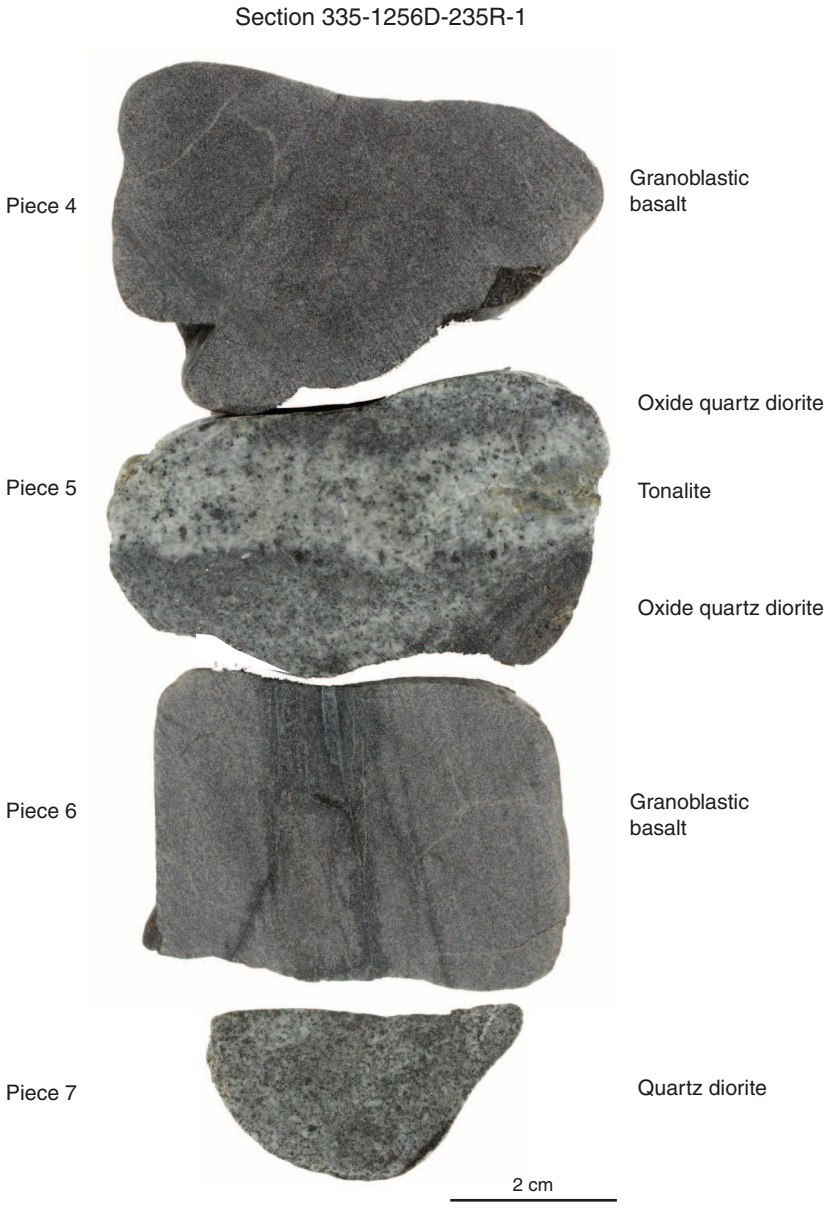

Figure F11. Photomicrographs (plane-polarized light) of tonalite (Sample 335-1256D-235R-1, 11–12 cm [Piece 5]; Thin Section 3), showing the presence of (**A**) euhedral, primary amphibole (Amph) and (**B**) zircon (Zrc). Qtz = quartz.

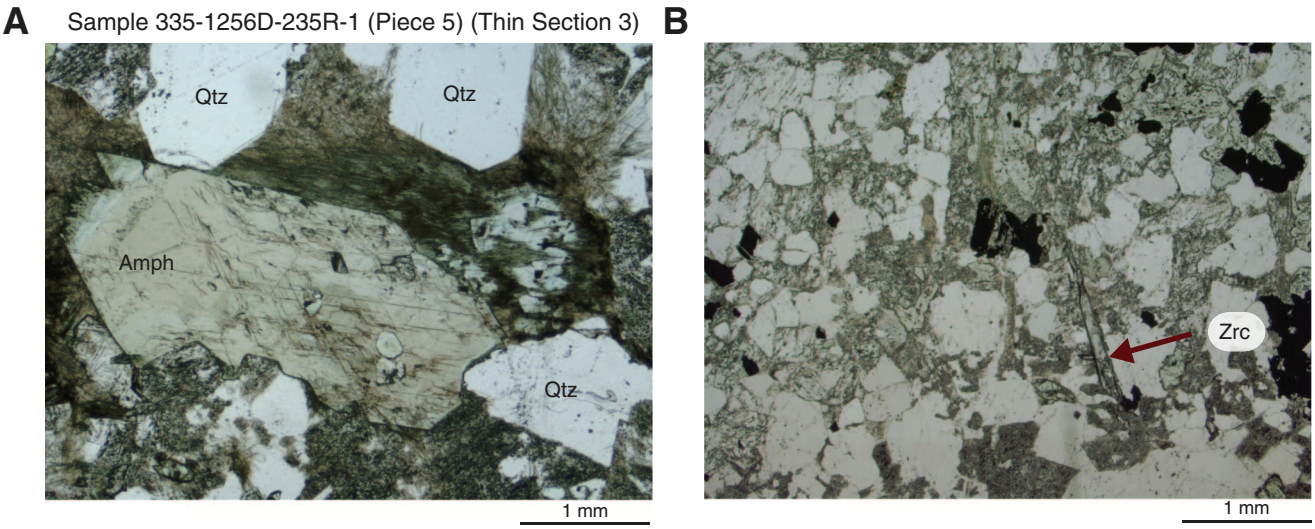

Figure F12. Photomicrograph (plane-polarized light) of oxide quartz diorite illustrating the association of subhedral, likely primary amphibole (Amph) with apatite (Ap), quartz (Qtz), and zircon (Zrc) (Sample 335-1256D-235R-1, 23–25 cm [Piece 5]; Thin Section 3). Plag = plagioclase.

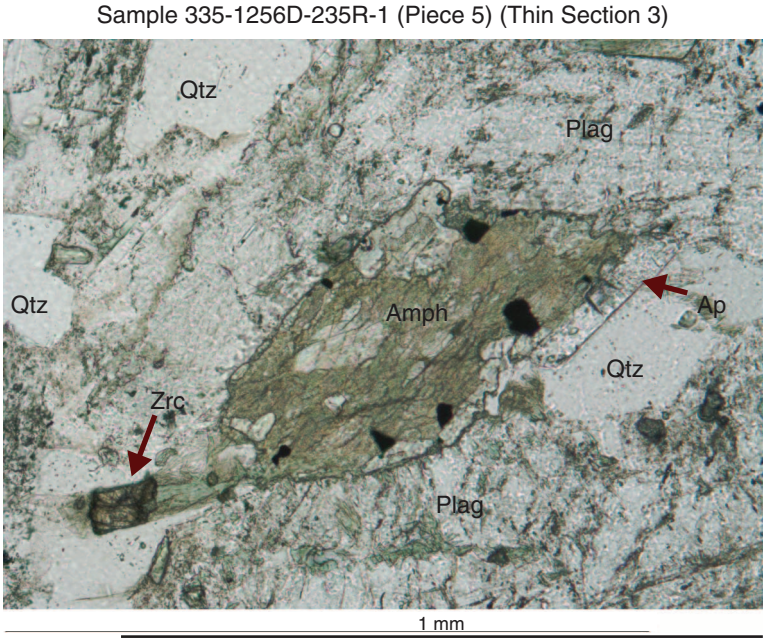

Figure F13. Photomicrographs of leucocratic Sample 335-1256D-236R-1, 0–4 cm (Thin Section 4), illustrating the occurrence of (**A, B**) epidote poikiloblasts and granular plagioclase and (**C, D**) a relict plagioclase microphenocryst. A and C are plane-polarized light; B and D are cross-polarized light.

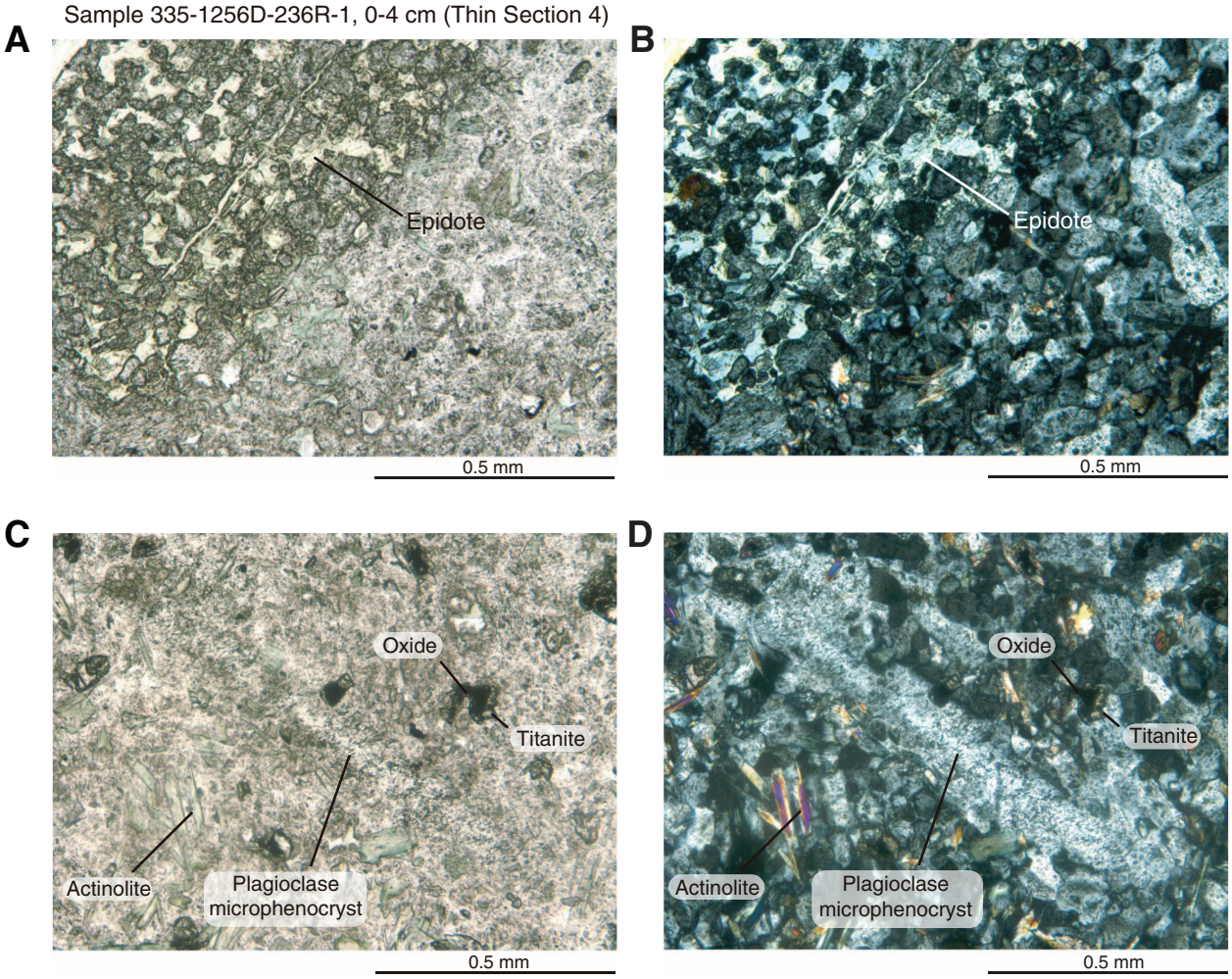

Figure F14. Close-up photograph of Sample 335-1256D-239R-1, 16–24 cm (Piece 5), illustrating the occurrence of oxide diorite patches within granoblastic basalt (Unit 1256D-96D).

Figure F15. Dike/dike contact (Sample 335-1256D-Run12-RCJB-Rock S). **A.** Close-up photograph showing a sharp, planar contact between a light-colored, fine-grained domain (right) and a darker, coarser grained domain (left), interpreted as a dike/dike contact. **B.** Photomicrograph of the contact in plane-polarized light (red dashed line; Thin Section 26). The coarse domain is crosscut by a metamorphic orthopyroxene (Opx) vein.

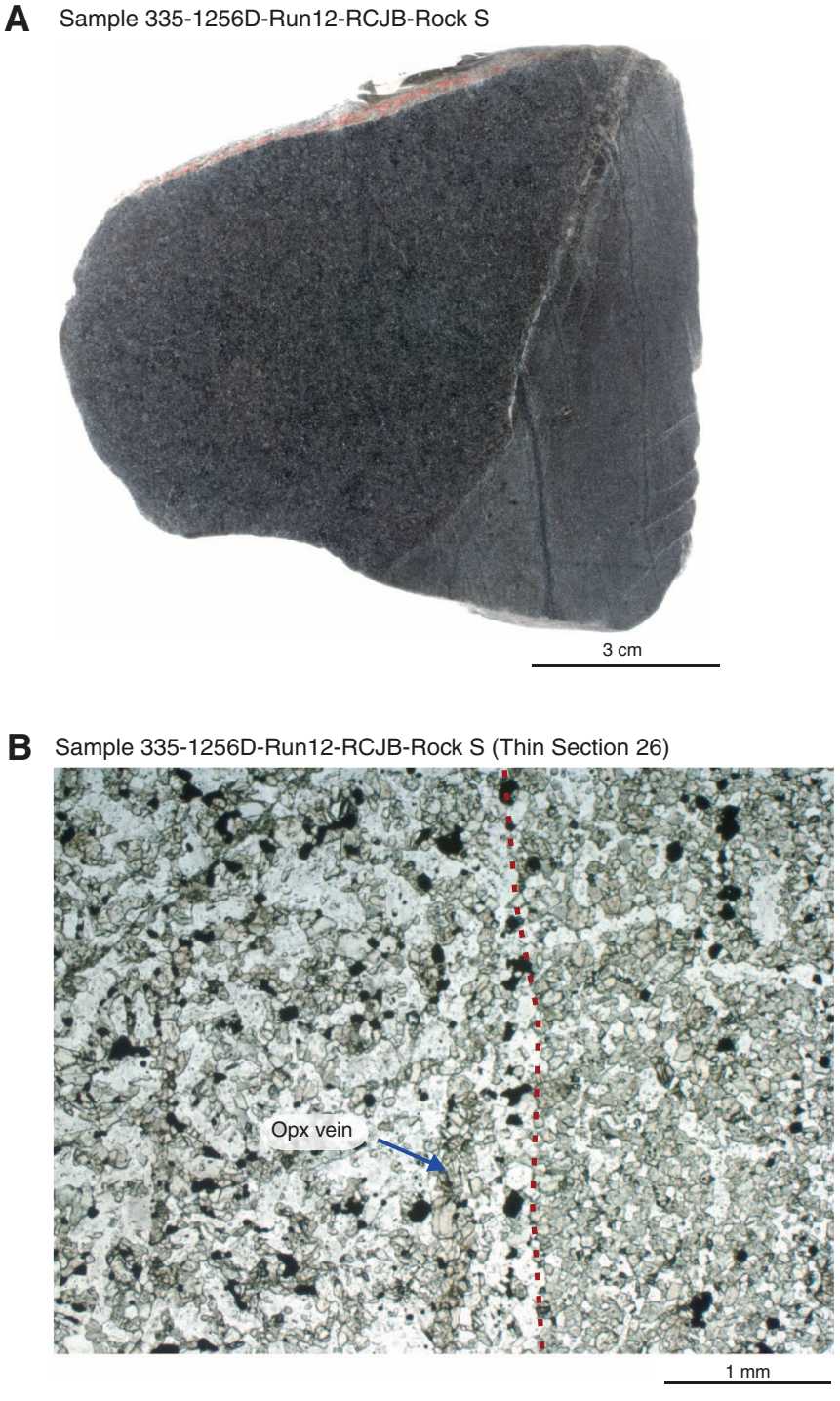

Figure F16. Photomicrographs of plagioclase. **A.** Relict plagioclase phenocryst within a granoblastic basalt showing relatively high anorthite (An) core surrounded by a lower An, reversely zoned rim (determined by Michel-Levy method) (Sample 335-1256D-Run15-EXJB; Thin Section 35) (cross-polarized light). The contact between the relict core and rim is marked by small granular pyroxene and Fe-Ti oxide crystals. **B.** Reverse zoning in plagioclase of the granoblastic matrix of the same thin section (cross-polarized light).

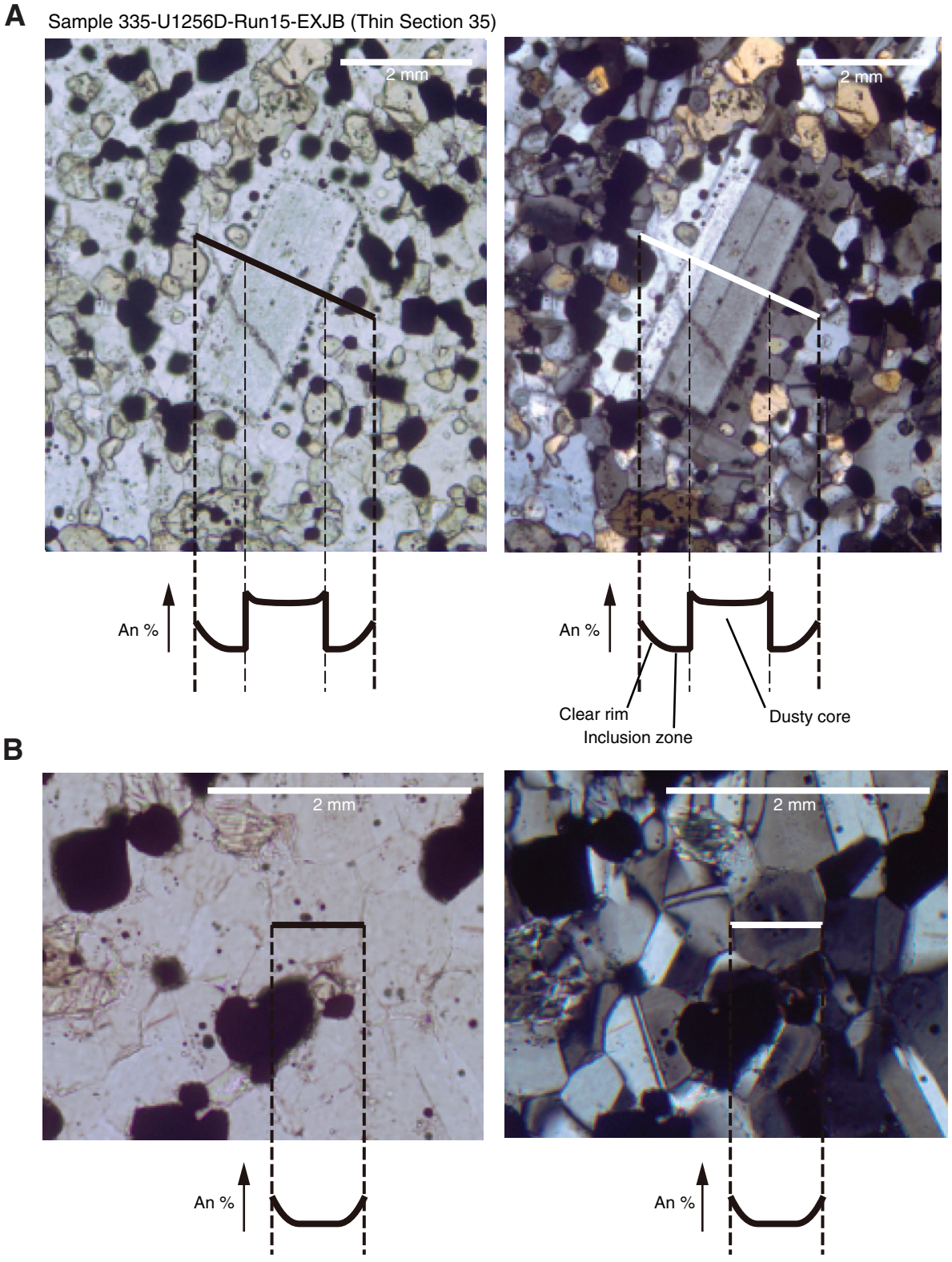

Figure F17. Close-up photographs illustrating the occurrence of dioritic to tonalitic patches within granoblastic basalt. Offshoots of the patches crosscut the granoblastic basalt, forming dioritic veins. **A.** Sample 335-1256D-Run12-RCJB-Rock B. **B.** Sample 335-1256D-Run13-RCJB-Rock A.

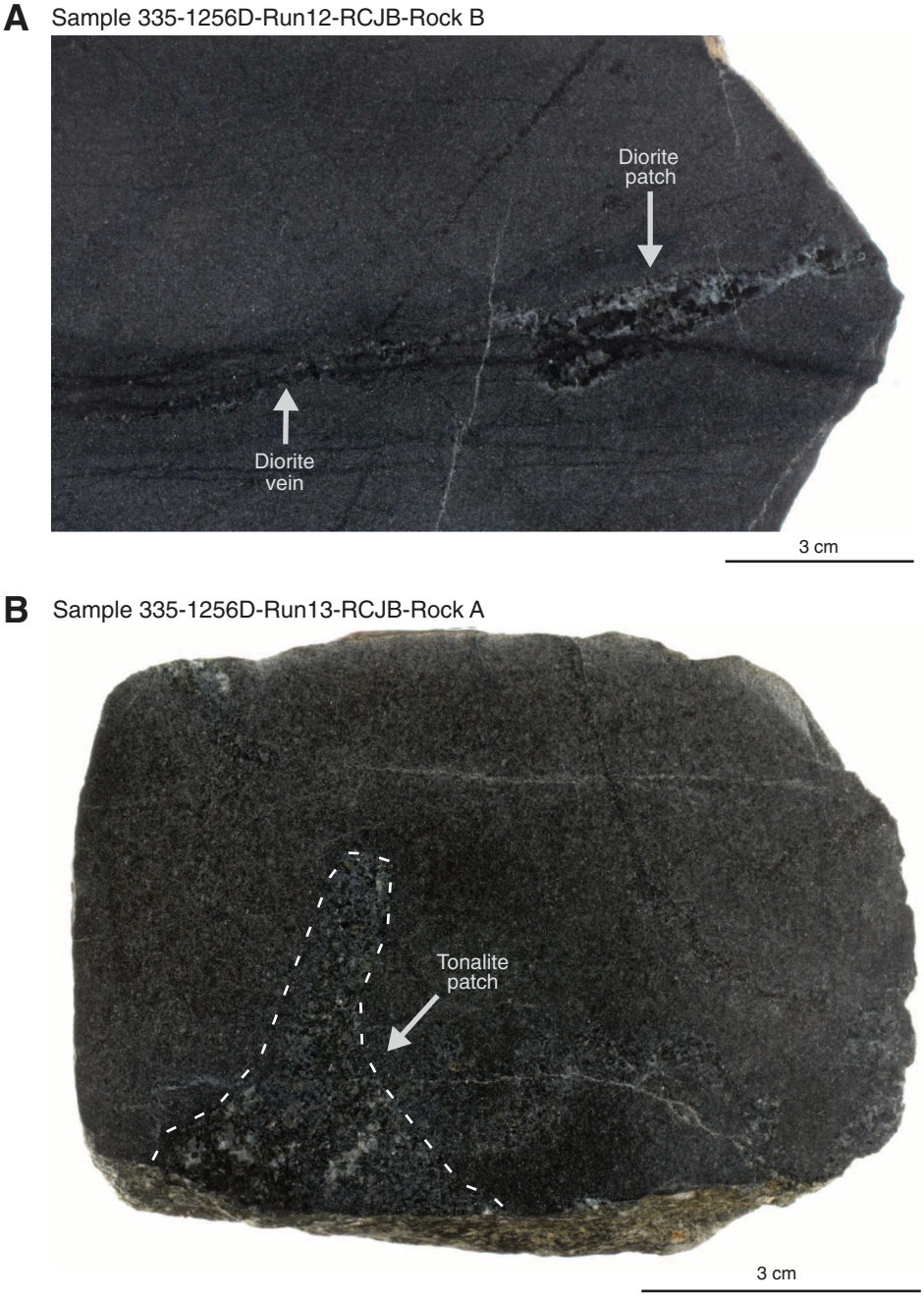

Figure F18. Photomicrographs of Sample 335-1256D-Run11-EXJB (Thin Section 13). Plag = plagioclase. **A.** Overview of a diorite patch in a fine-grained granoblastic aphyric basalt (cross-polarized light). An offshoot of the diorite crosscuts the granoblastic basalt, demonstrating that the diorite is intrusive. **B.** Subhedral amphibole (Amph) grows around clinopyroxene (Cpx). Clean, sharp grain boundaries between the amphibole and clinpyroxene indicate that the amphibole is of primary magmatic origin. **C.** Subhedral to euhedral zircon (Zrc).

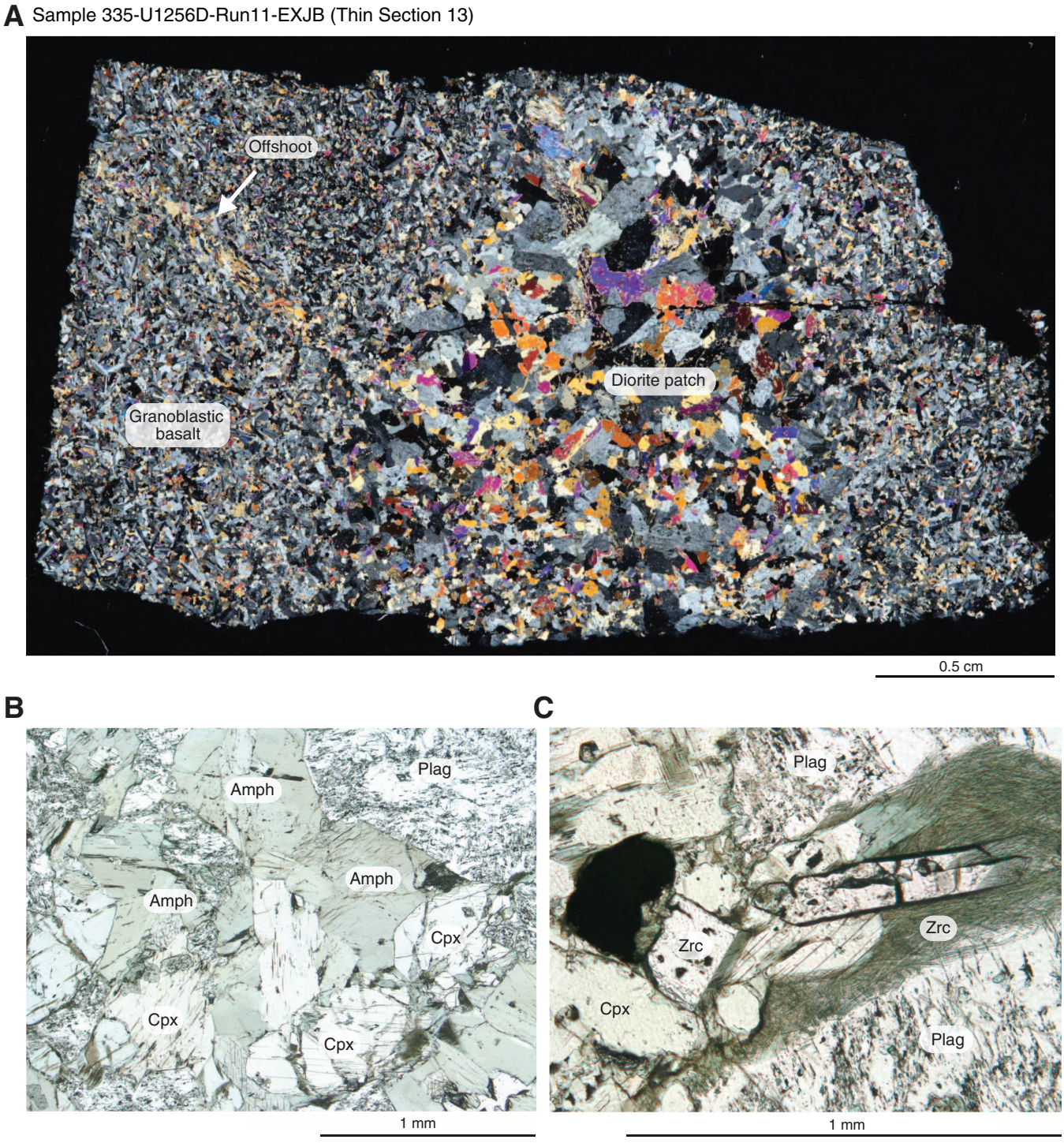

Figure F19. Photomicrograph showing diorite dikelet crosscutting granoblastic basalt (Sample 335-1256D-Run19-RCJB-Rock C; Thin Section 40). Note that the dikelet has a medium-grained center and a fine-grained marginal facies and that a diffuse vein issues from the dikelet.

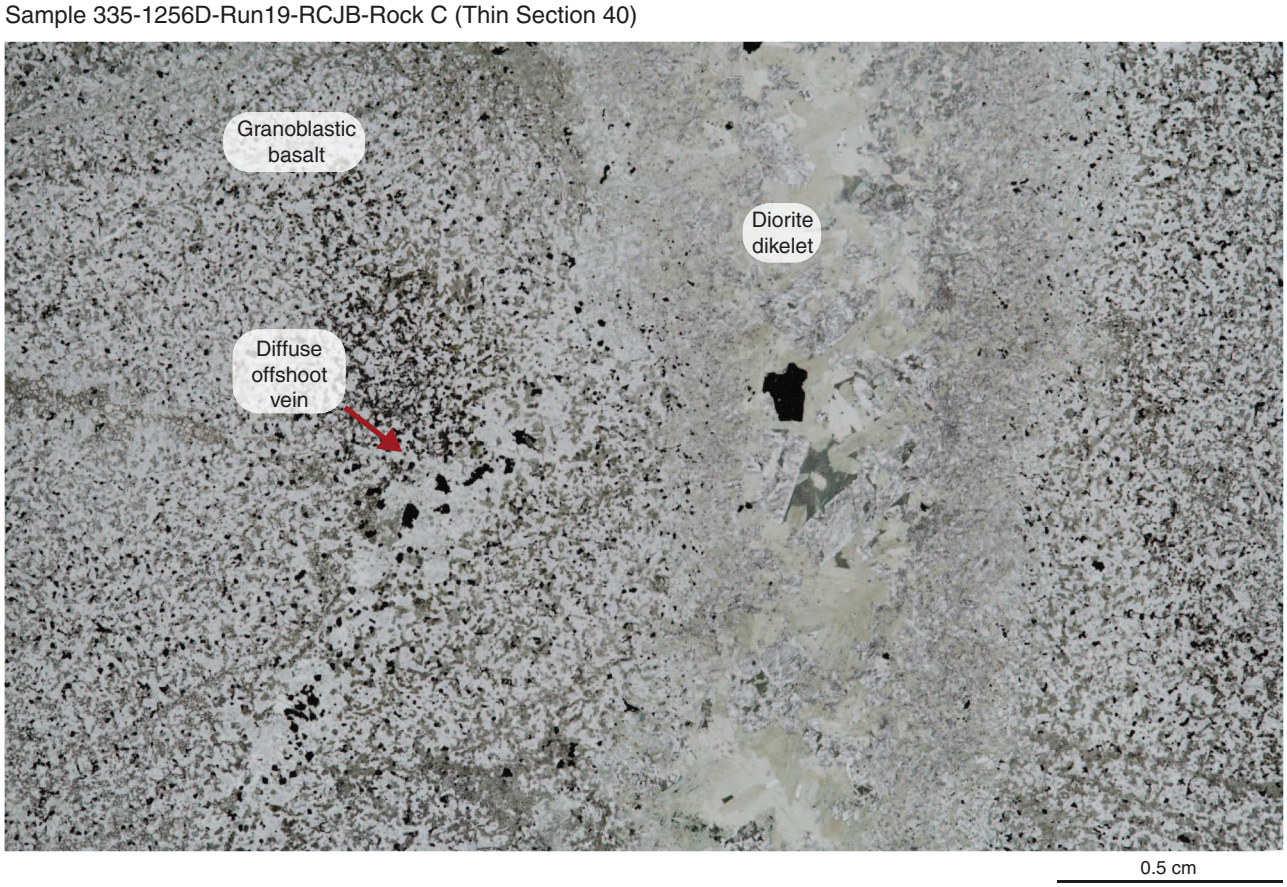

Figure F20. Photomicrographs of tonalite (Sample 335-1256D-Run13-RCJB-Rock A; Thin Section 31) patch in plane-polarized (left) and cross-polarized (right) light. Cpx = clinopyroxene, Amph = amphibole, Ox = Fe-Ti oxide, Plag = plagioclase, Qtz = quartz.

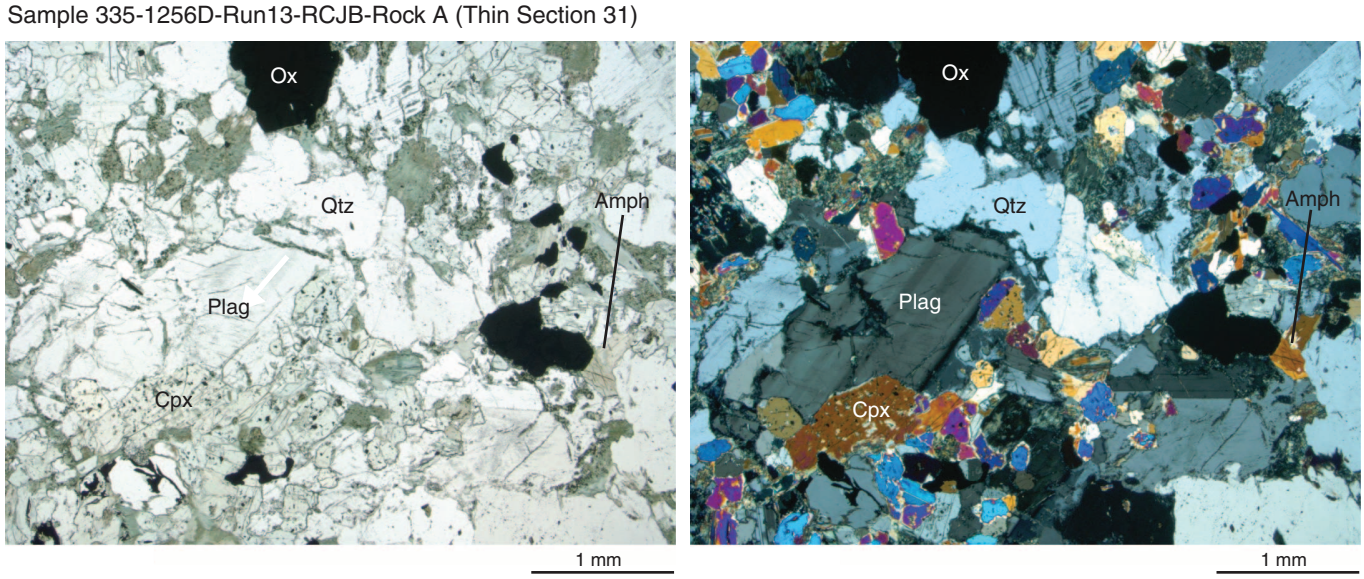

Figure F21. Photomicrographs of relationships within veins crosscutting granoblastic basalt. Cpx = clinopyroxene, Plag = plagioclase. **A, B, D.** Sample 335-1256D-Run12-RCJB-Rock D (Thin Section 23): (A) relics of granular orthopyroxene (Opx), (B) granular plagioclase chadacrysts enclosed in clinopyroxene oikocryst, (D) micrometer-sized pyroxene inclusions in plagioclase. **C.** Clinopyroxene chadacrysts enclosed in plagioclase oikocryst (Sample 335-1256D-Run12-RCJB-Rock J; Thin Section 24).

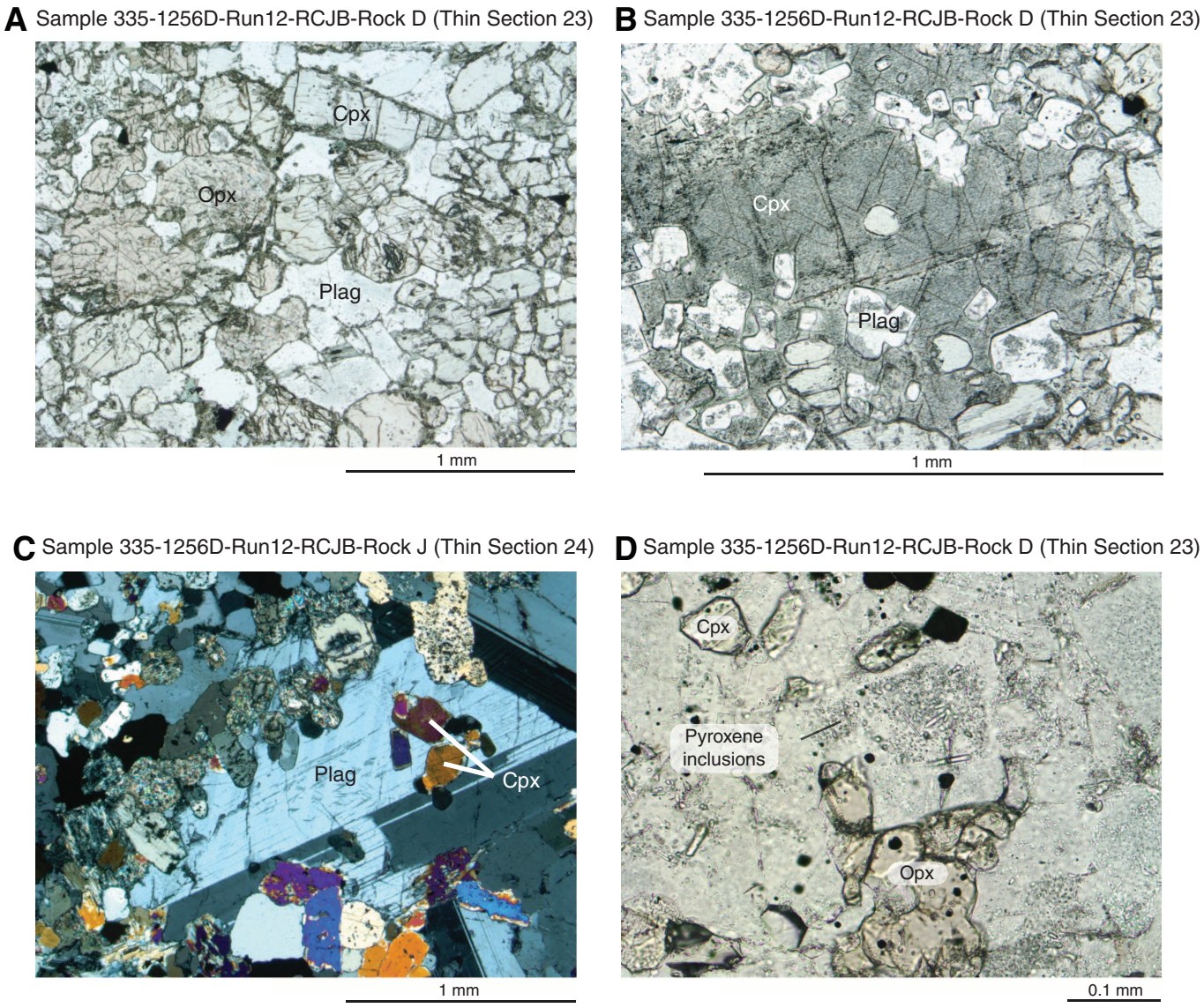

Figure F22. Diorite dikelet (Sample 335-1256D-Run19-RCJB-Rock C). **A.** Close-up photograph illustrating the occurrence of a diorite dikelet crosscutting granoblastic basalt. The diorite contains abundant black amphibole and has a fine-grained margin. Both the granoblastic basalt and the diorite dikelet are crosscut by a hydrothermal amphibole vein. **B.** Photomicrographs of amphiboles (Amph) intergrown with plagioclase (Plag) in the diorite dikelet in plane-polarized (left) and cross-polarized (right) light (Thin Section 40).

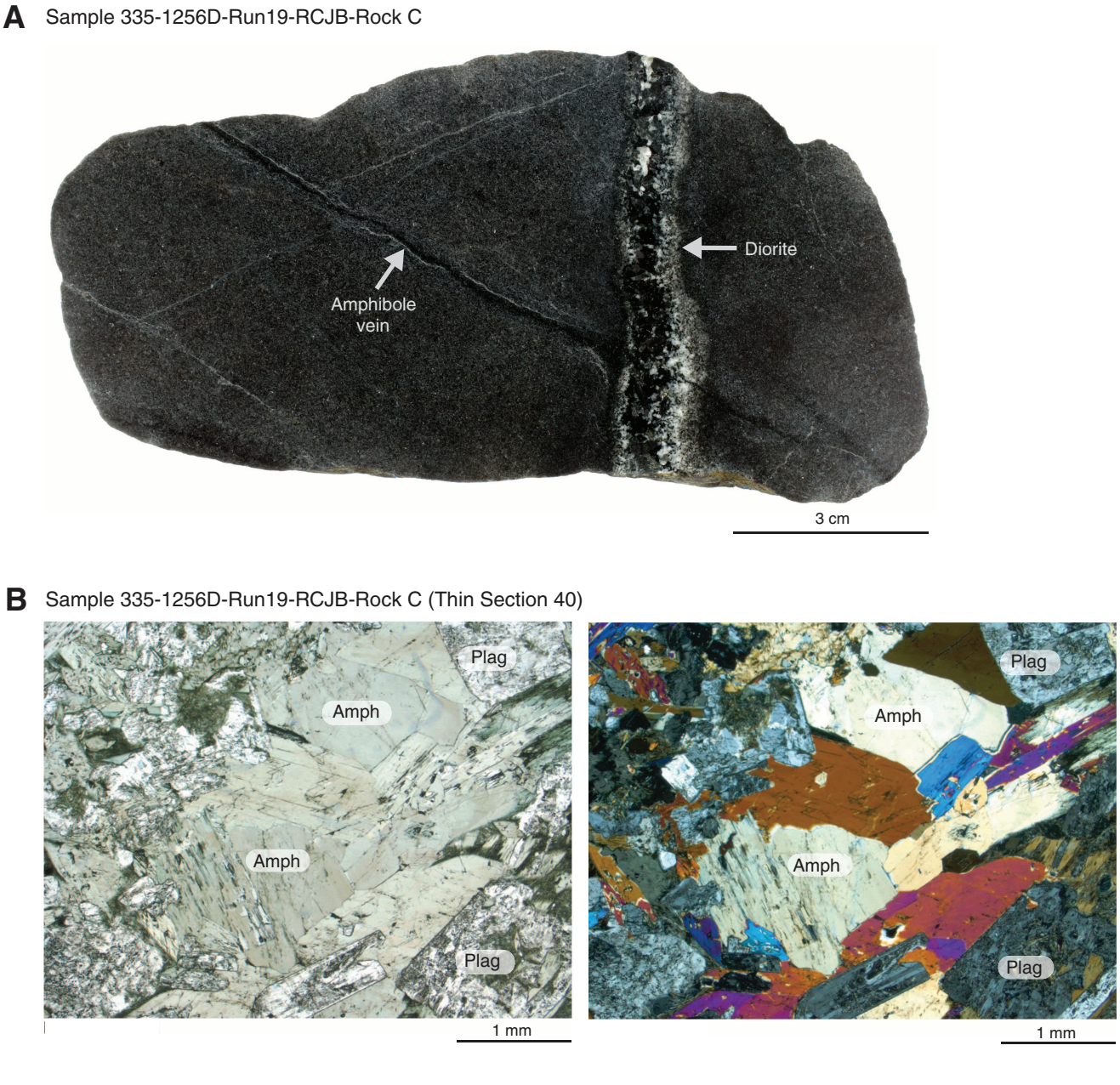

Figure F23. Photomicrographs (plane-polarized light) of gabbro (Sample 335-1256D-Run11-EXJB; Thin Section 12), illustrating its seriate nature. The texture ranges from (**A**) granular in the coarser grained part to (**B**) subophitic in the finer grained part.

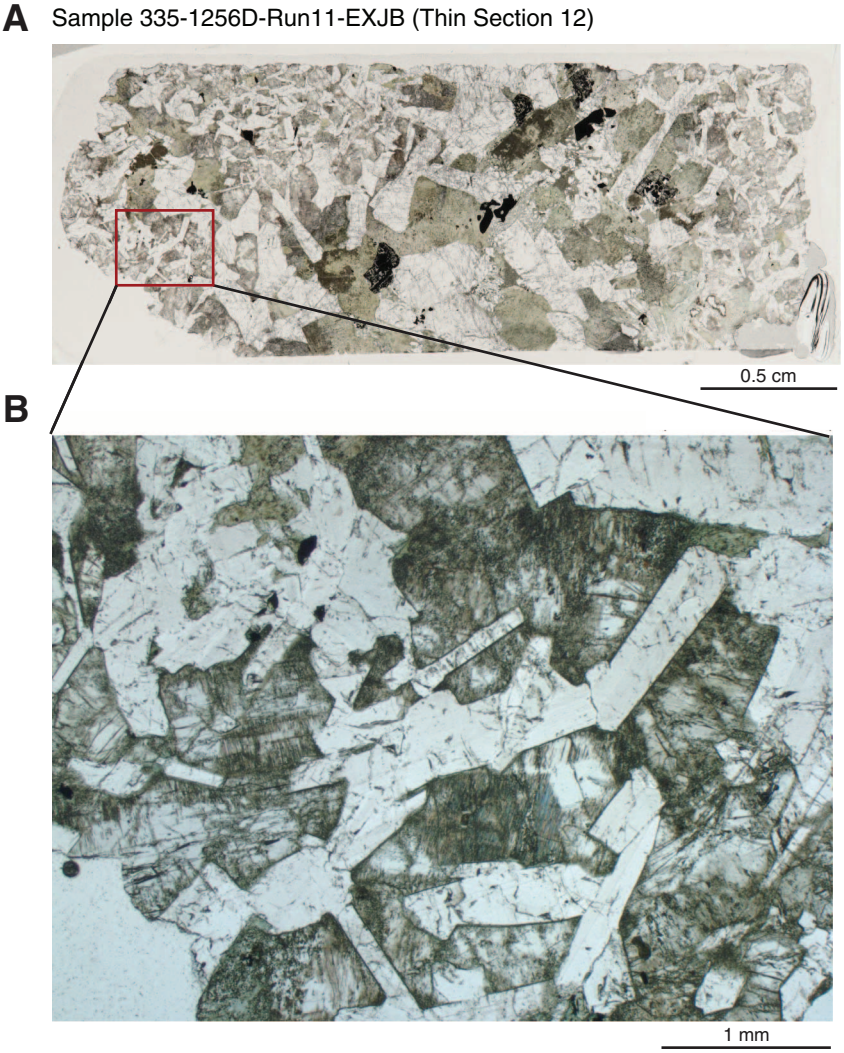

Figure F24. Photomicrographs of a symplectite-like intergrowth of two clinopyroxenes in gabbro (Sample 335-1256D-Run11-EXJB; Thin Section 12]). **A.** Plane-polarized light. **B.** Cross-polarized light.

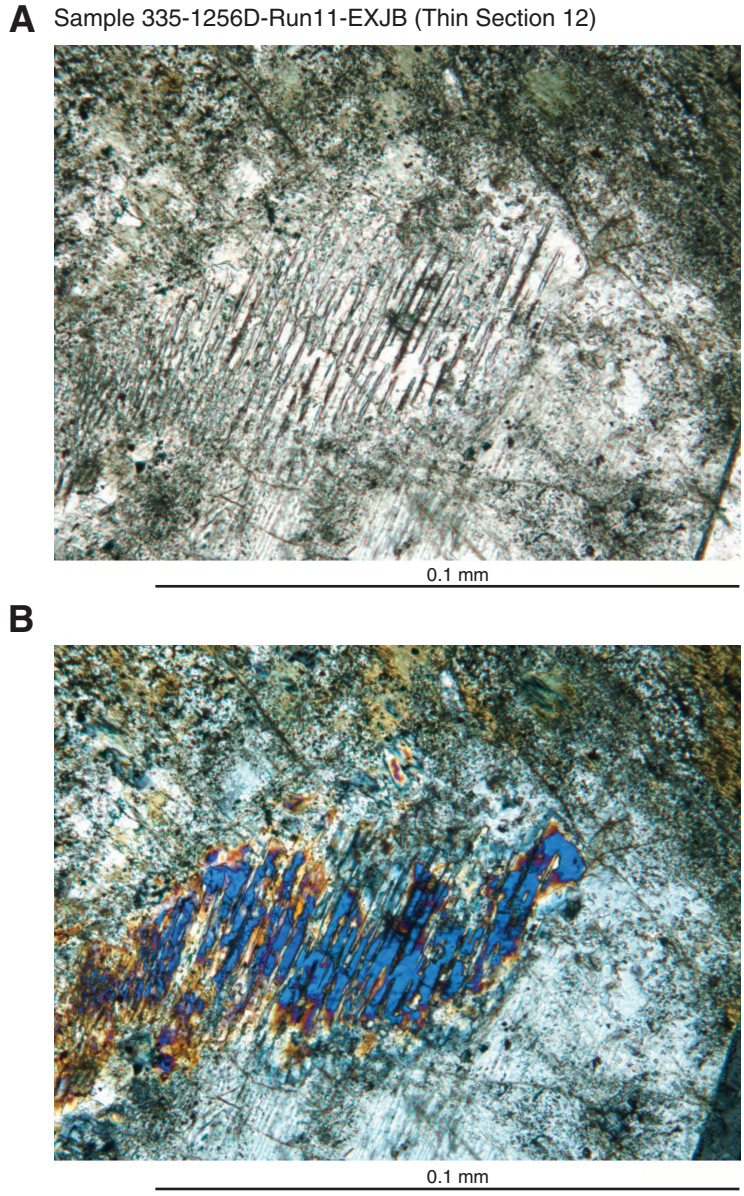

Figure F25. Photomicrograph of Fe-Ti oxide (?) exsolution in olivine from disseminated oxide olivine gabbronorite (Sample 335-1256D-Run11-EXJB; Thin Section 29) (plane-polarized light).

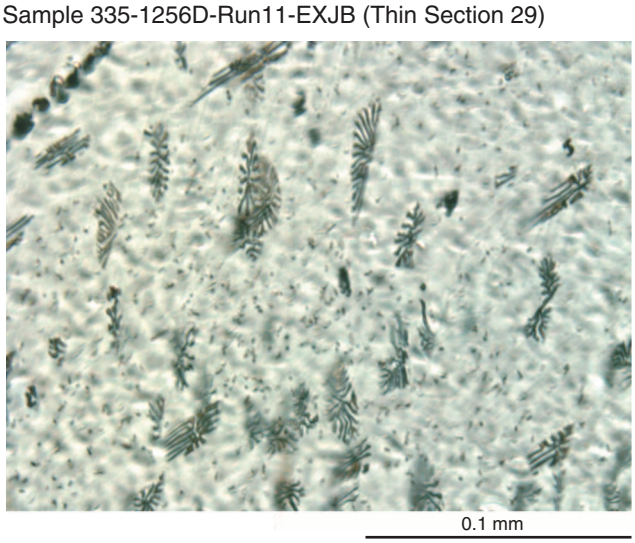

Figure F26. Orthopyroxene-bearing olivine gabbro (Sample 335-1256D-Run20-RCJB-Rock C; Thin Section 37). Cpx = clinopyroxene, Ol = olivine, Plag = plagioclase. **A.** Close-up photograph. **B.** Photomicrograph (cross-polarized light). **C.** Plagioclase commonly displays patchy zoning.

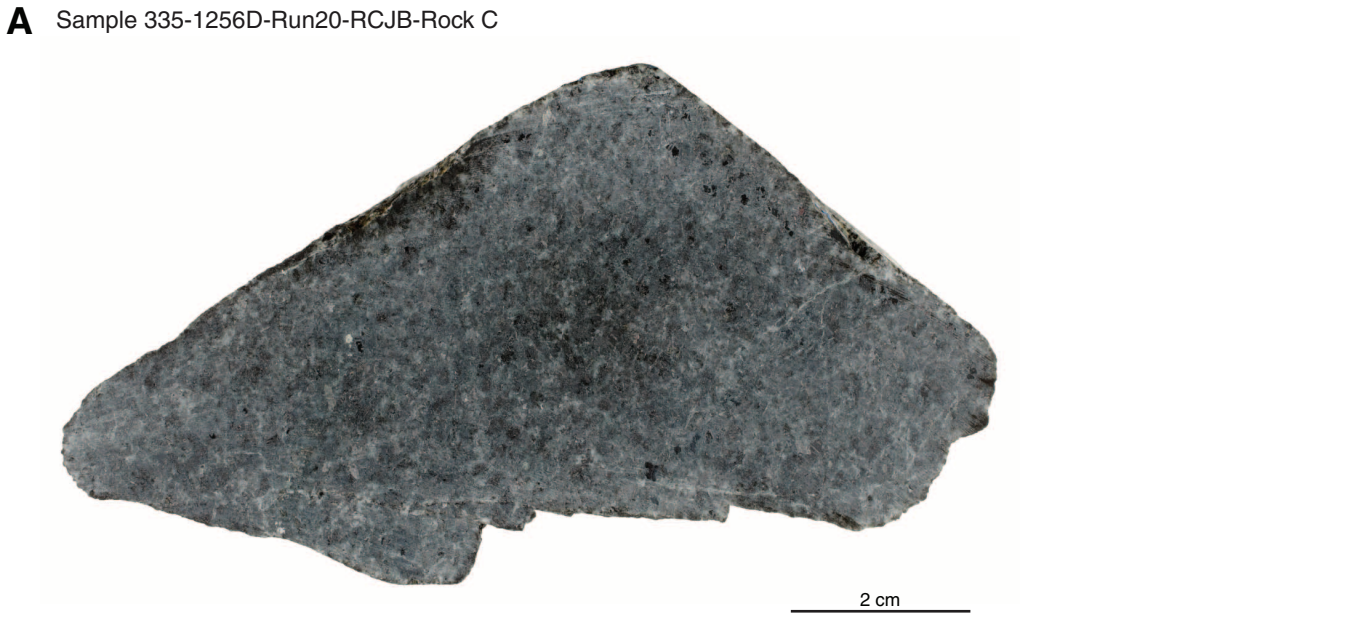

Figure F27. Photomicrograph (plane-polarized light) of a basalt (Sample 335-1256D-Run11-EXJB; Thin Section 10), showing intersertal texture defined by altered glass between a network of partially altered plagioclase with swallow-tail texture.

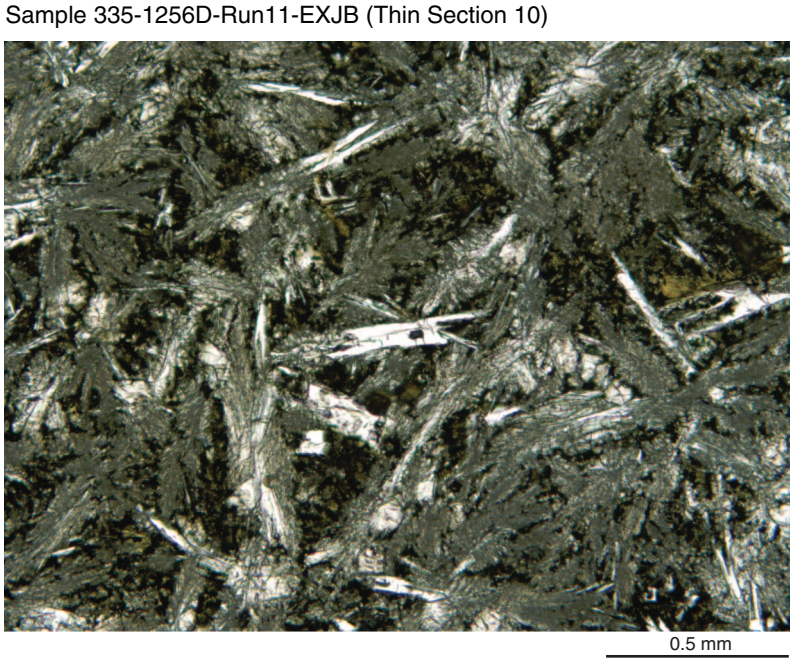

Figure F28. Photographs of albitite in junk basket material. **A.** Sample 335-1256D-Run17-BSJB. **B.** Sample 335-1256D-Run14-EXJB. **C.** Albitite in contact with a coarse-grained diorite (Sample 335-1256D-Run20-RCJB-Rock D).

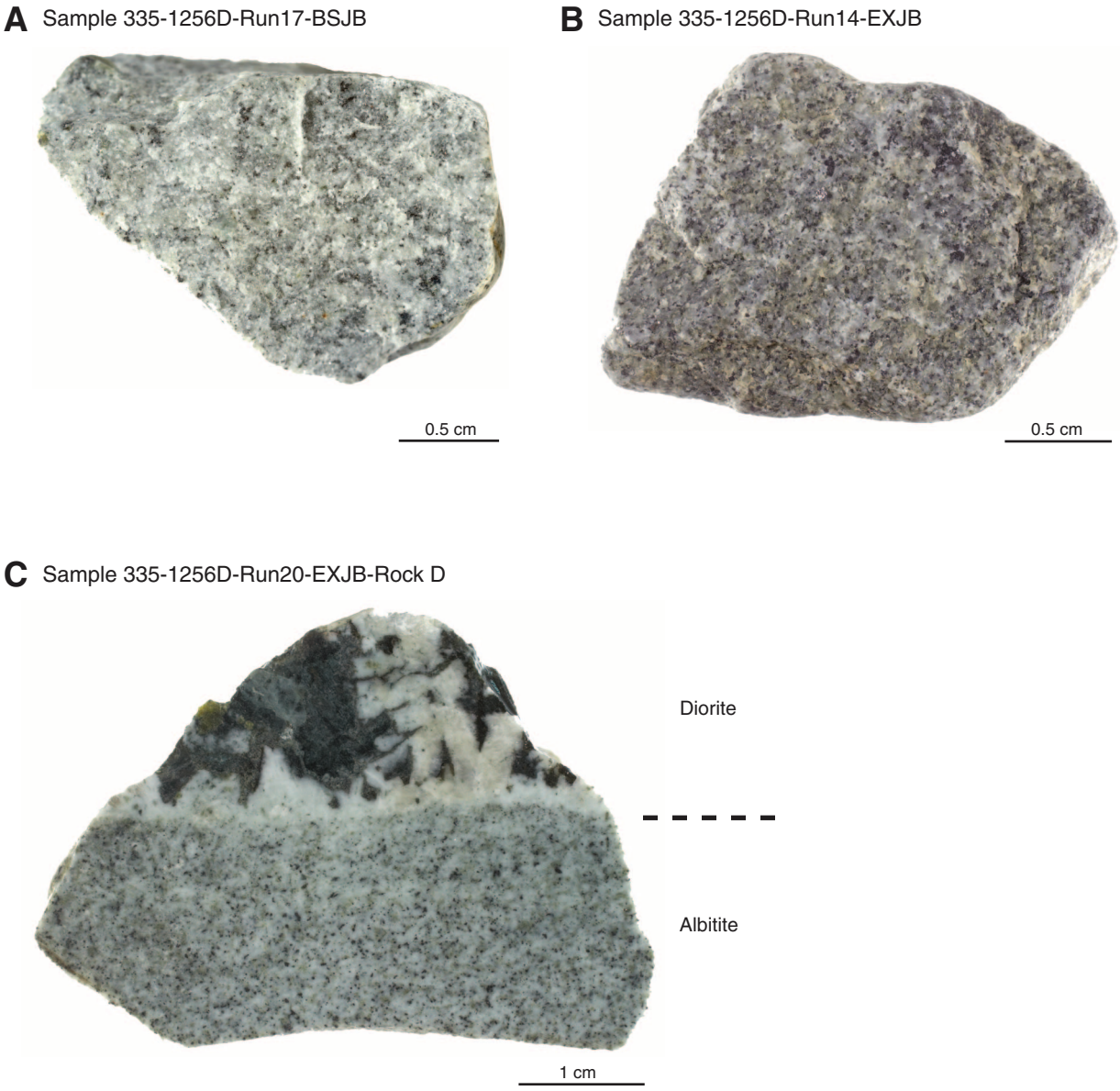

Figure F29. Photomicrographs of albitite. **A.** Relict plagioclase microphenocryst (Sample 335-1256D-Run13-RCJB; Thin Section 34]) (cross-polarized light). **B.** Distribution of roundish oxide grains in Sample 335-1256D-Run20-RCJB (Thin Section 39) (plane-polarized light).

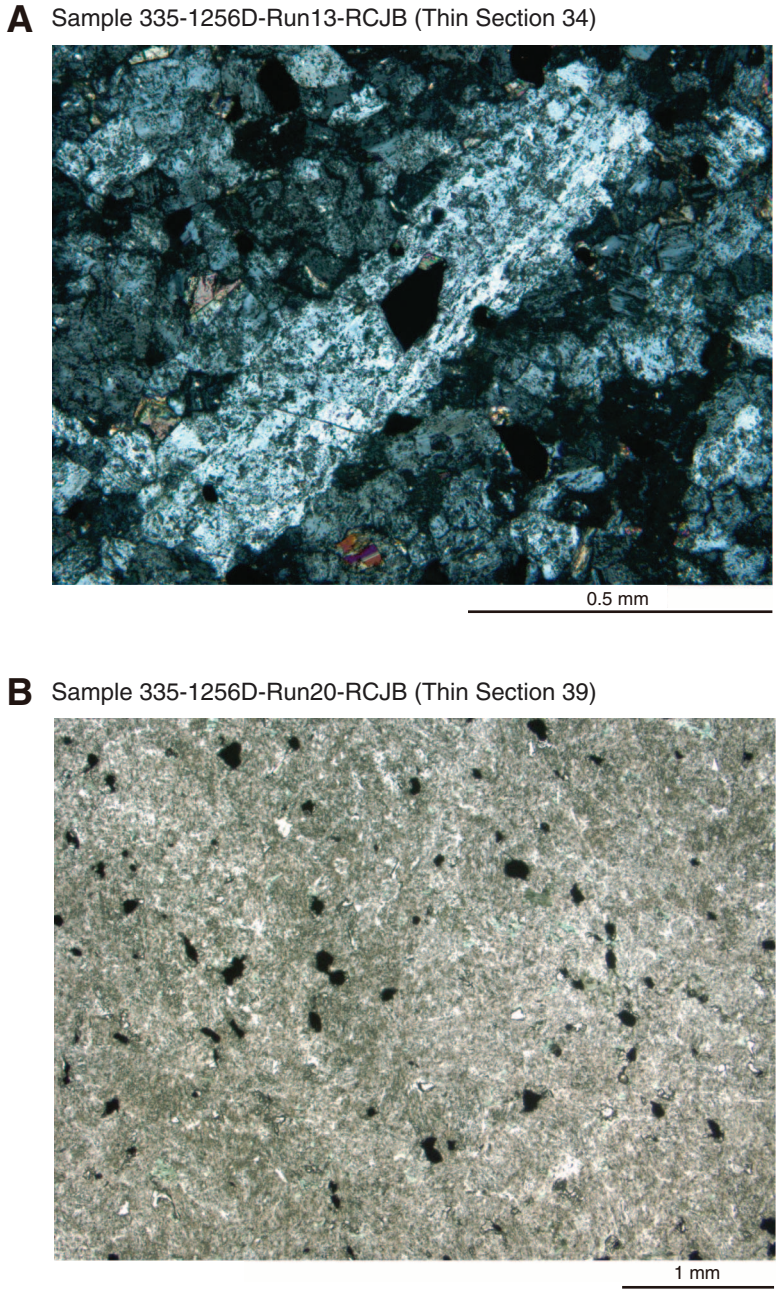

Figure F30. Plot of loss on ignition (LOI) compared with total H_2O and CO_2 for samples analyzed during Expedition 335. Values for LOI are most likely minimum values because of the effects of iron oxidation, whereas water values are most likely overestimates because of the overlap between water and S peaks (see the "Methods" chapter [Expedition 335 Scientists, 2012b]). C = cored samples, JB = samples retrieved during junk basket runs.

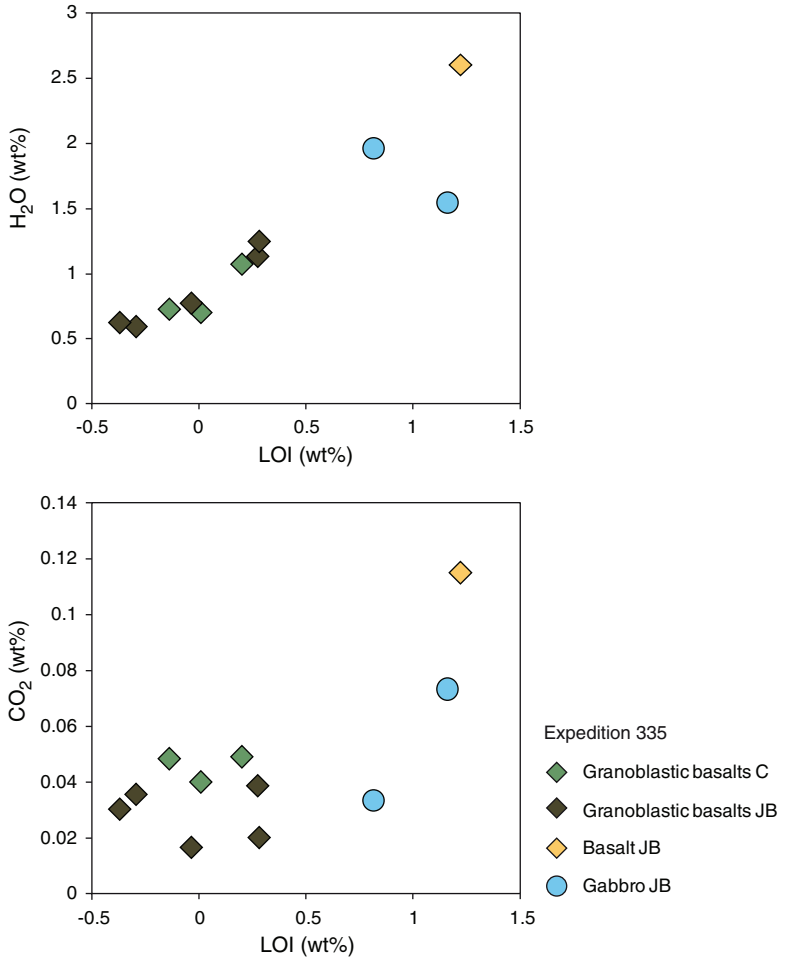

Figure F31. Summary plot of major element compositions of samples collected during Expedition 335 compared with existing previous data from Hole 1256D (Neo et al., 2009; Yamazaki et al., 2009; Teagle et al., unpubl. data). Granoblastic dikes = granoblastic dikes from above Gabbro 1 and granoblastic basalts from Dike Screens 1 and 2 sampled during previous expeditions. C = cored samples, JB = samples retrieved during junk basket runs.

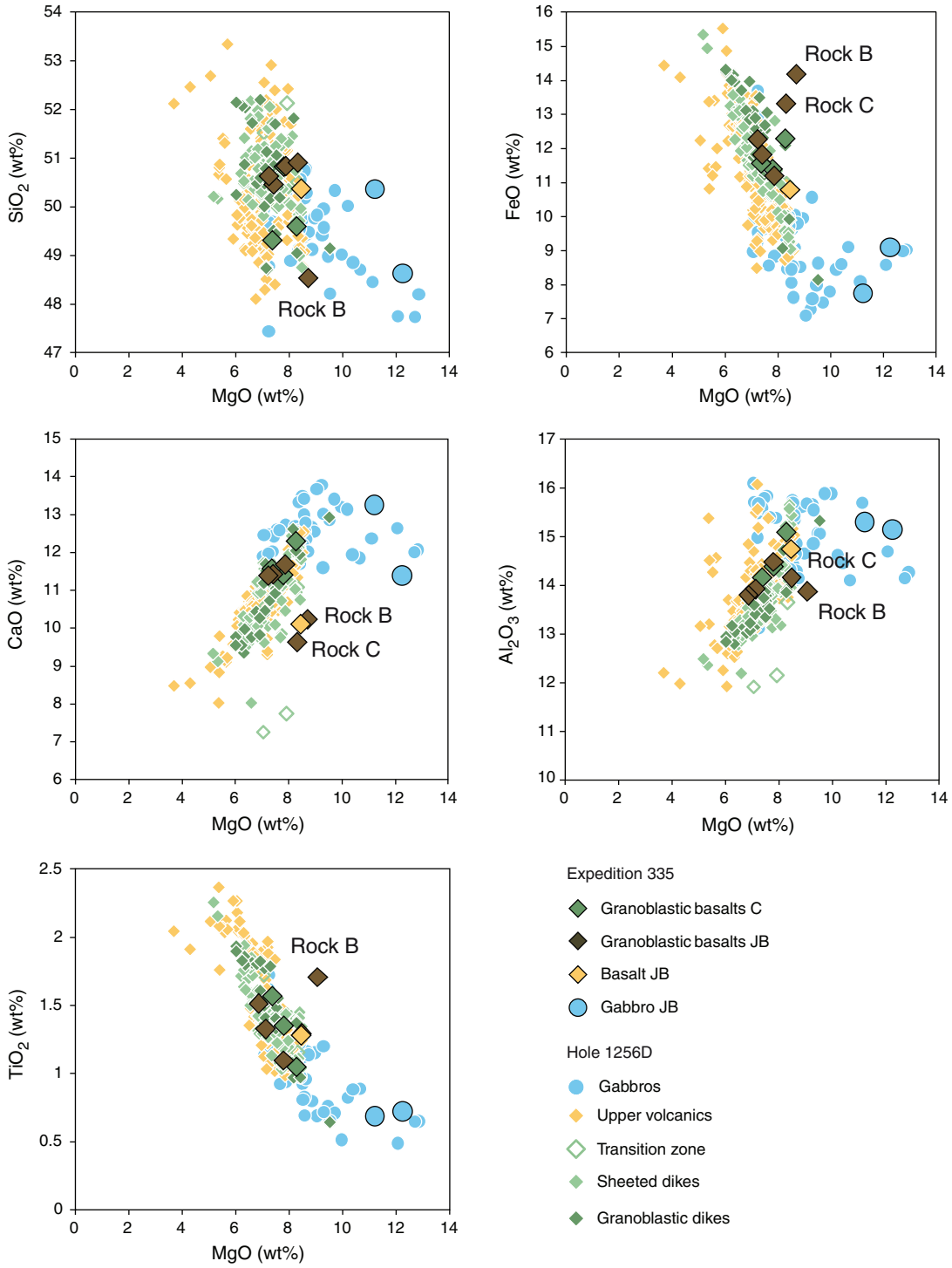

Figure F32. Plot of variability of Cr, Sc, Ni, V, Cu, and Zn contents as a function of MgO in samples collected during Expedition 335 compared with existing previous data from Hole 1256D (Neo et al., 2009; Yamazaki et al., 2009; Teagle et al., unpubl. data). Granoblastic dikes = granoblastic dikes from above Gabbro 1 and granoblastic basalts from Dike Screens 1 and 2 sampled during previous expeditions. C = cored samples, JB = samples retrieved during junk basket runs.

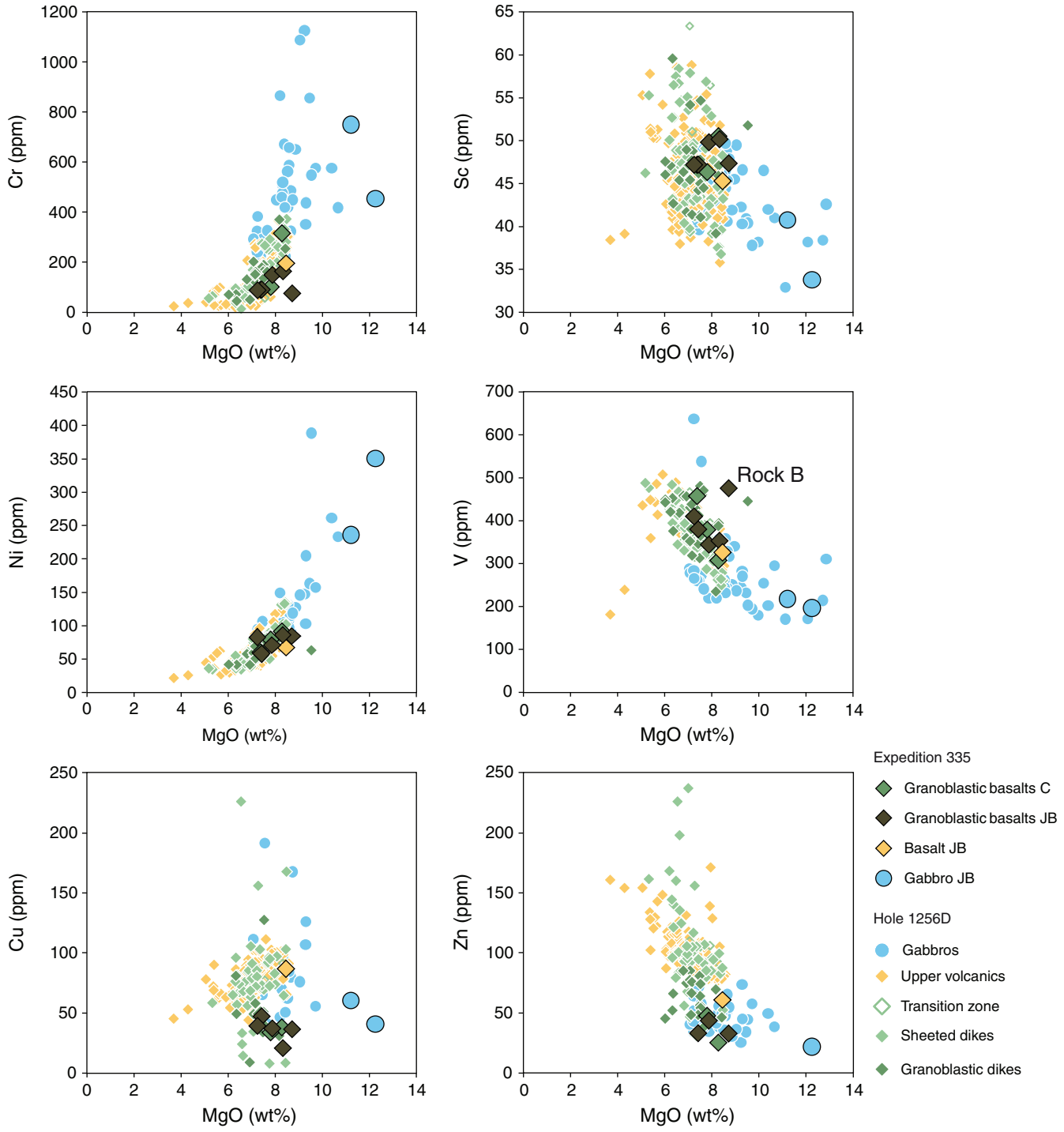

Figure F33. Plot of variability of Ba, Sr, Zr, and Y contents as a function of MgO in samples collected during Expedition 335 compared with existing previous data from Hole 1256D (Neo et al., 2009; Yamazaki et al., 2009; Teagle et al., unpubl. data). Granoblastic dikes = granoblastic dikes from above Gabbro 1 and granoblastic basalts from Dike Screens 1 and 2 sampled during previous expeditions. C = cored samples, JB = samples retrieved during junk basket runs.

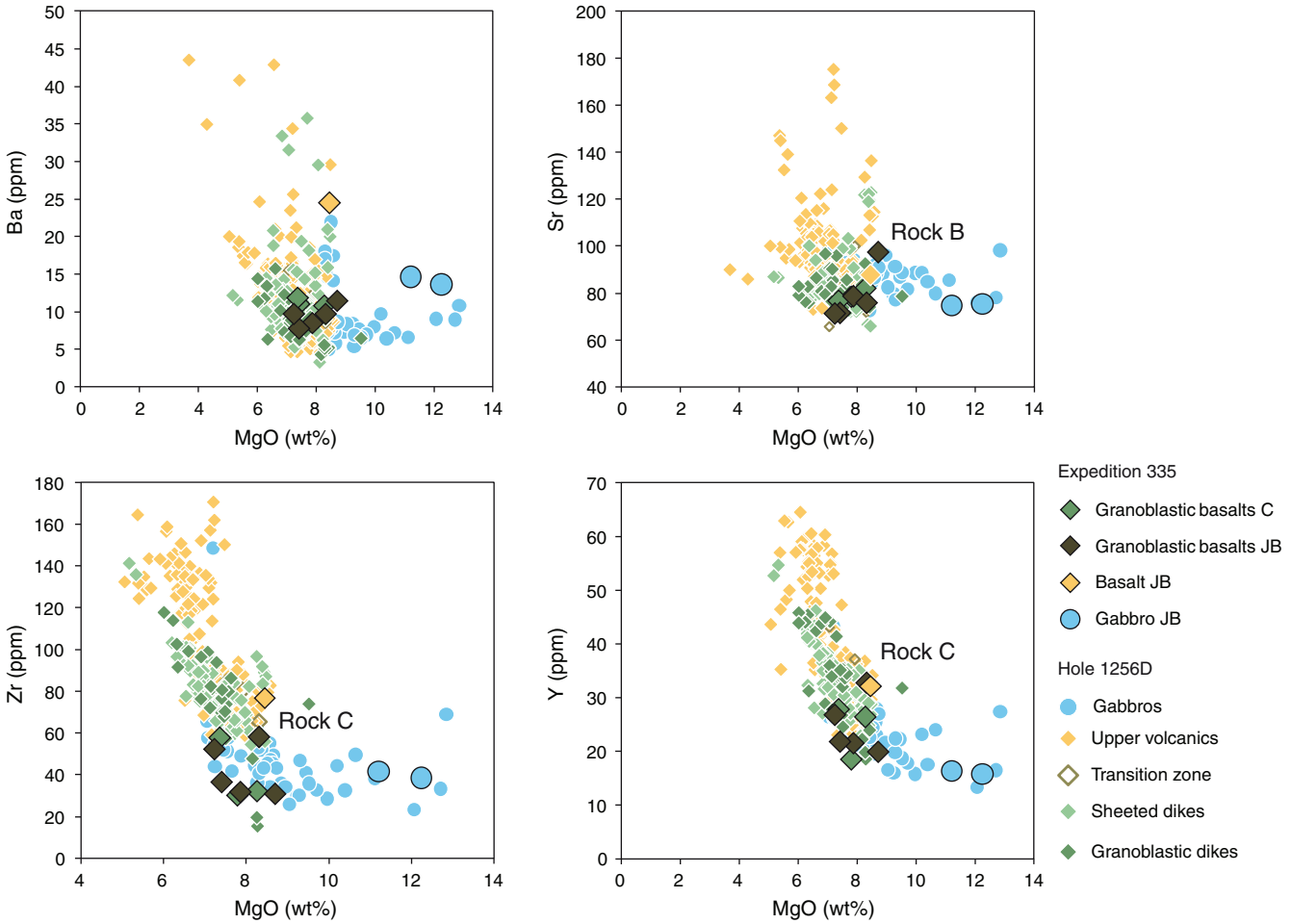

Figure F34. Plot of variability of Ca#, TiO_2, and Ni as a function of Mg# for gabbros analyzed during Expedition 335 (Gabbro 1 and Gabbro 2) compared with existing data from Hole 1256D (Gabbro JB) (Neo et al., 2009; Yamazaki et al., 2009; Teagle et al., unpubl. data). Also shown for comparison are published data for gabbros sampled on the Mid-Atlantic Ridge (MAR) during Leg 153 (Mid-Atlantic Ridge Kane Fracture Zone area; Agar et al., 1997), at Atlantis Massif (MAR 30°N; Godard et al., 2009), and on the Southwest Indian Ridge (SWIR) in Hole 735B (Dick, Natland, Miller, et al., 1999). JB = samples retrieved during junk basket runs.

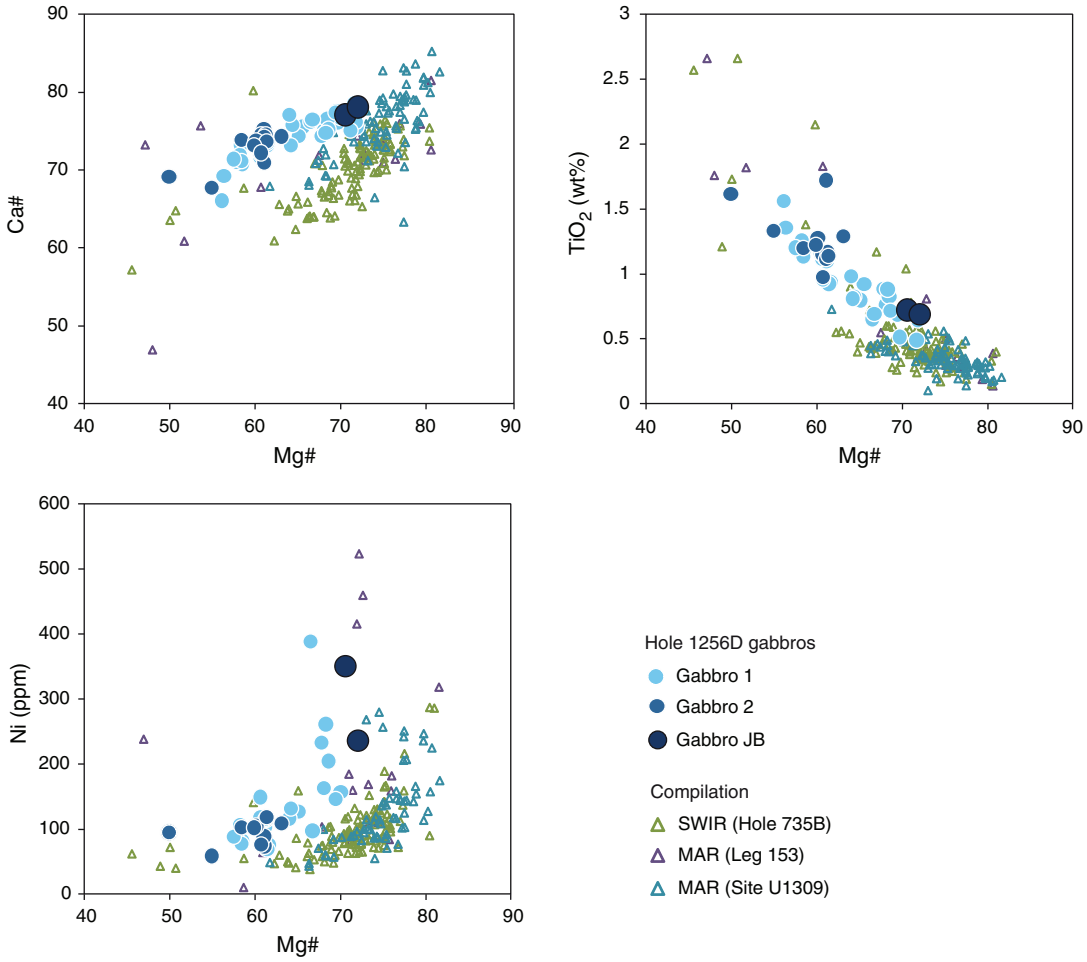

Figure F35. Depth profiles for the lower part of Hole 1256D for Mg#, Zr, Zr/Y (mass ratio), Zn, and Cu. Rock samples retrieved from junk basket (JB) runs to the bottom of the hole (BOH) are plotted in the bottom boxes. C = cored.

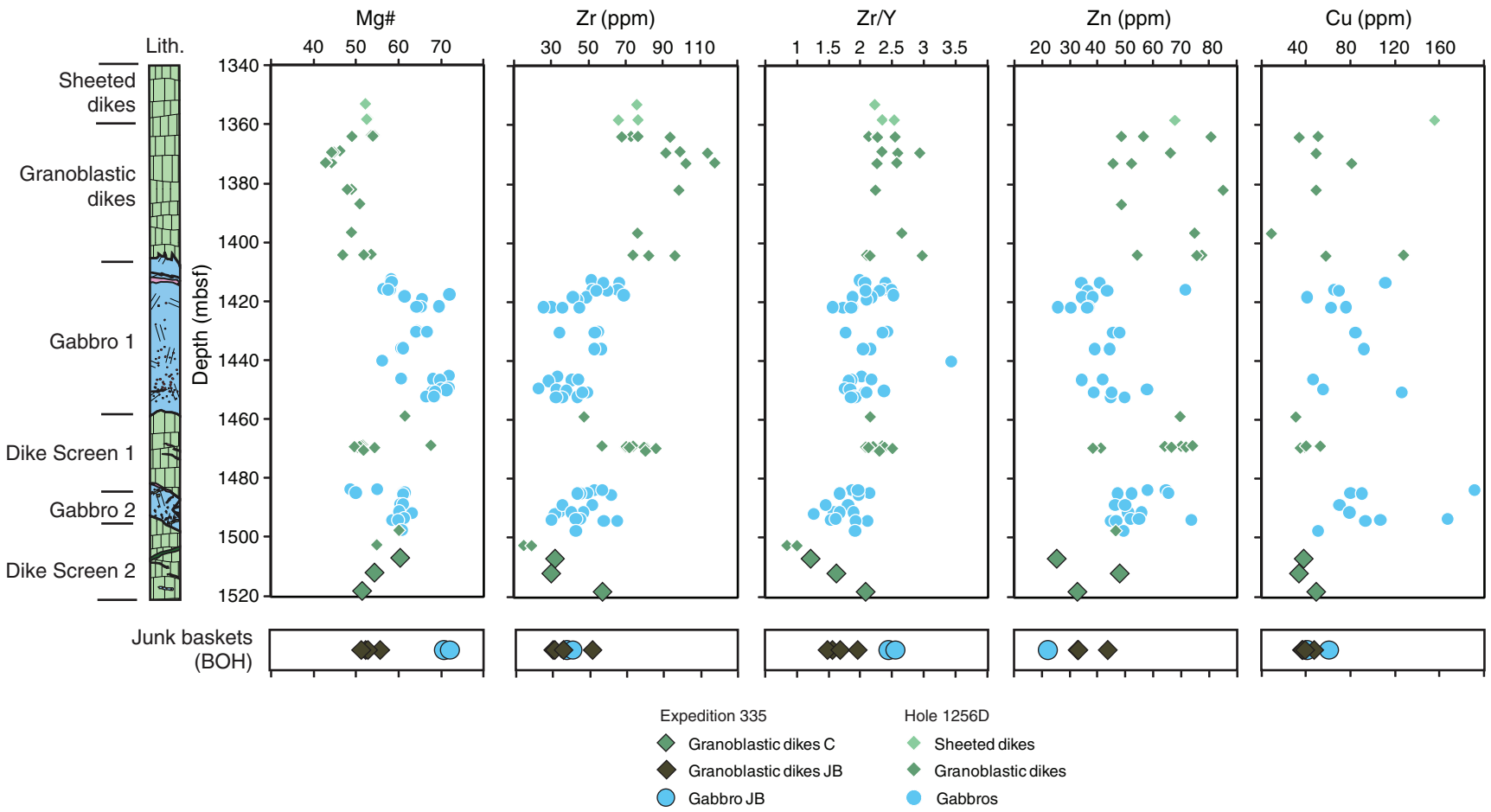

Figure F36. Plot of distributions of pervasive background alteration, patchy alteration, recrystallized granoblastic alteration, and volume percent recrystallized domains (xenoliths) in the plutonic section of Hole 1256D.

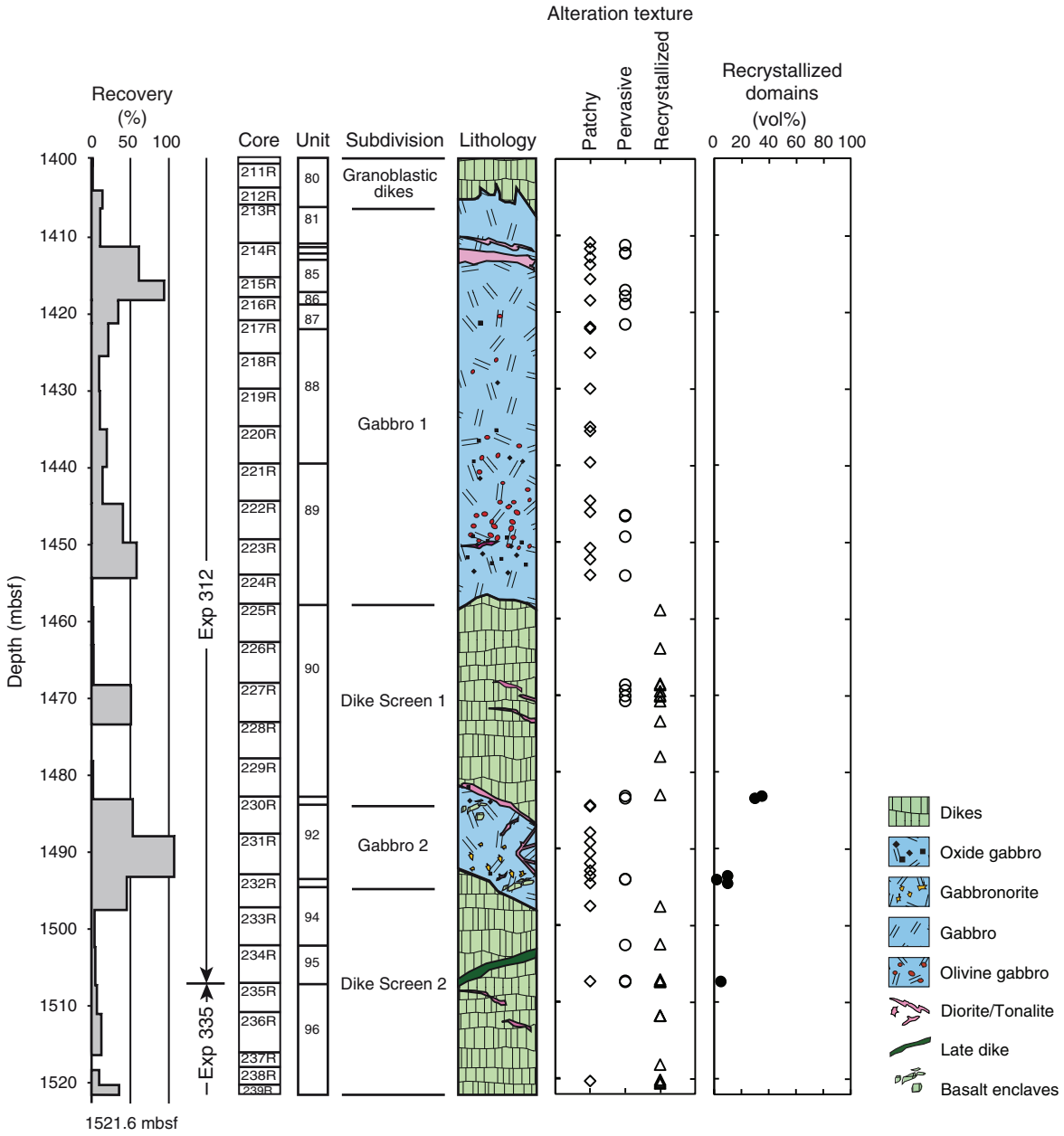

Figure F37. Plot of secondary minerals in the dike–gabbro transition zone in Hole 1256D. Mineral identifications based on hand specimen, thin section, and X-ray diffraction during Expeditions 335 and 312 (Teagle, Alt, Umino, Miyashita, Banerjee, Wilson, and the Expedition 309/312 Scientists, 2006).

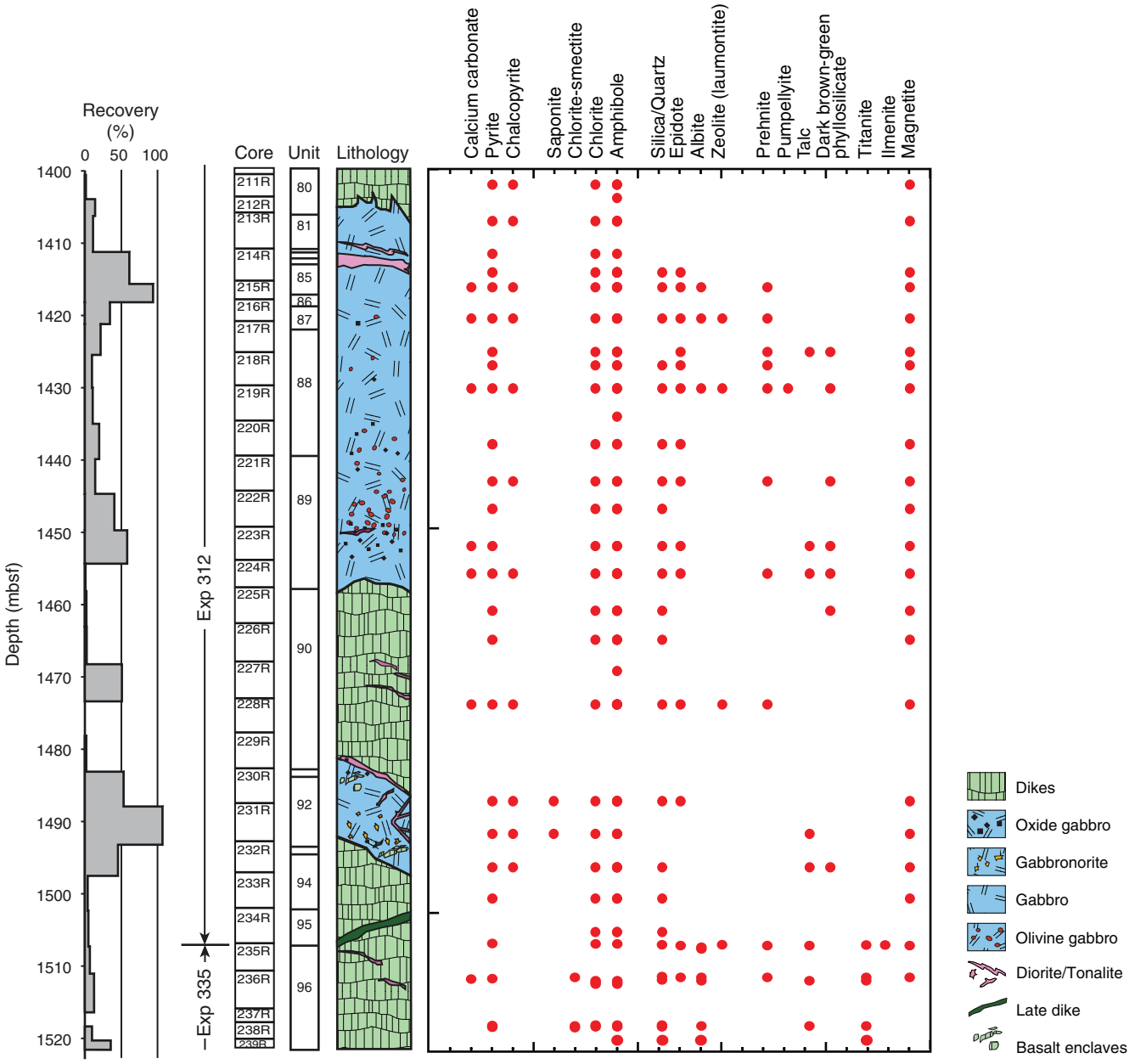

Figure F38. Plot of background alteration in the dike–gabbro transition zone in Hole 1256D.

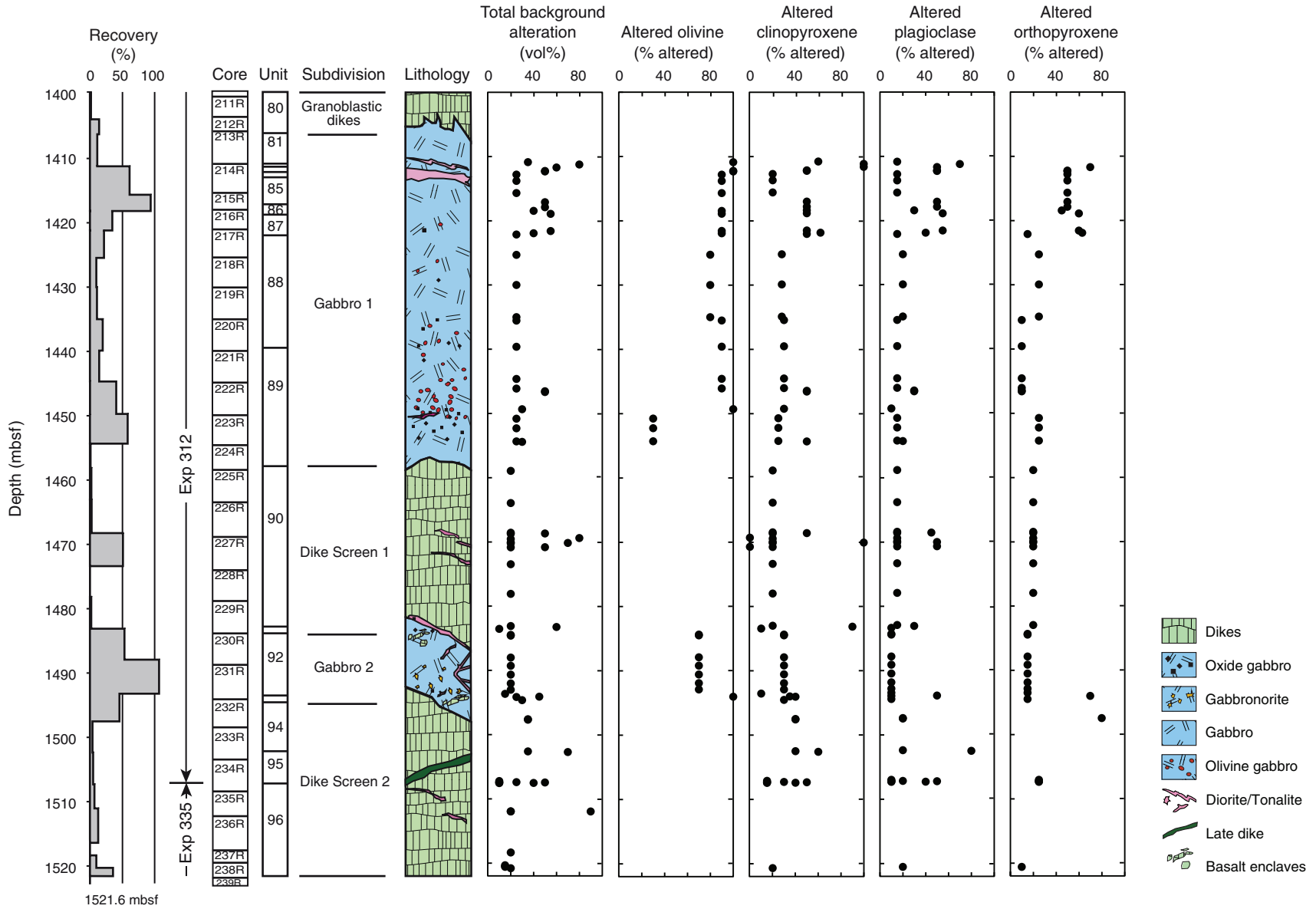

Figure F39. Plot of secondary mineralogy replacements of primary phases in background alteration in the dike–gabbro transition zone in Hole 1256D. Oxide refers to Fe-oxyhydroxide and magnetite.

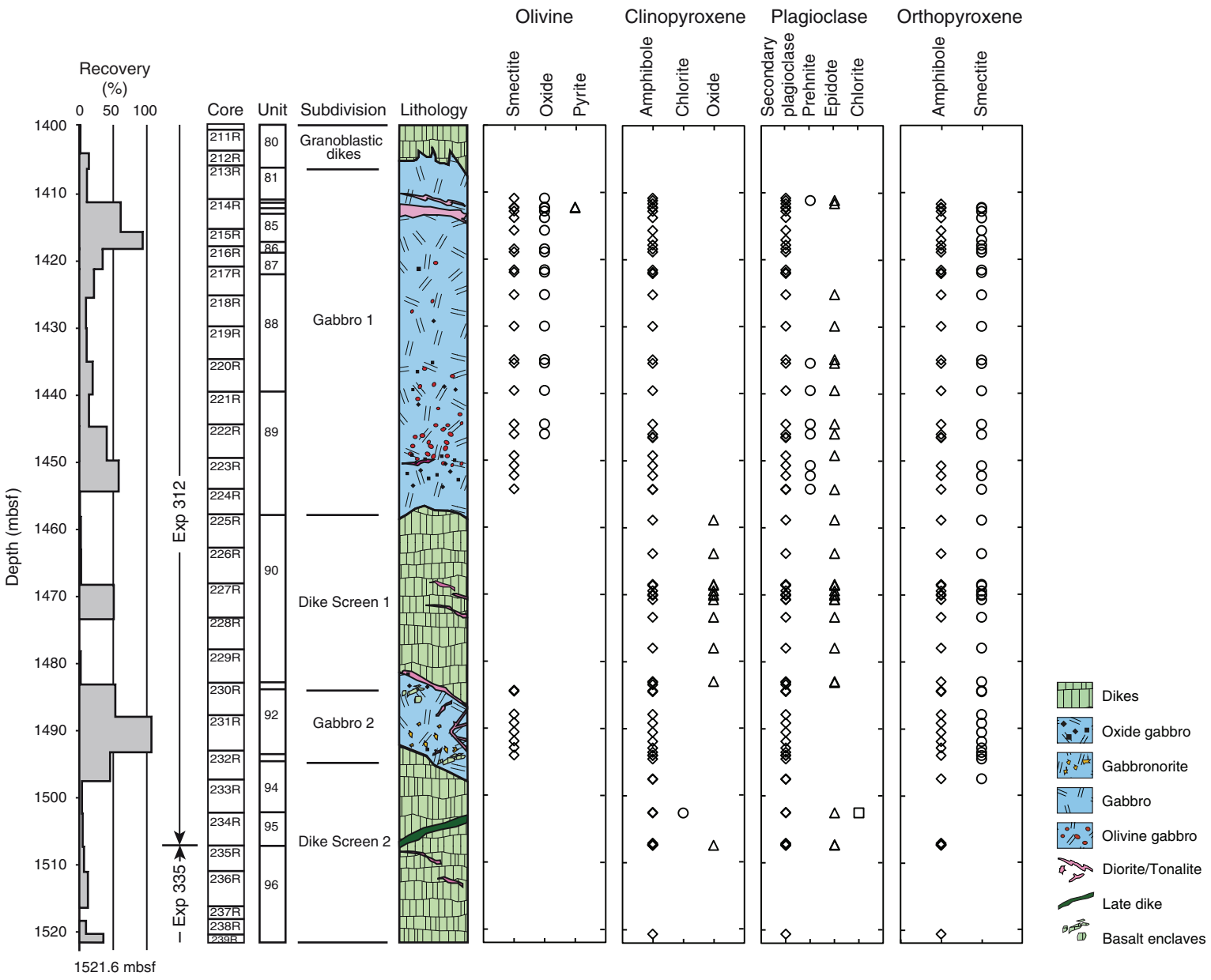

Figure F40. Plot of alteration patches and alteration within patches in the dike–gabbro transition zone in Hole 1256D.

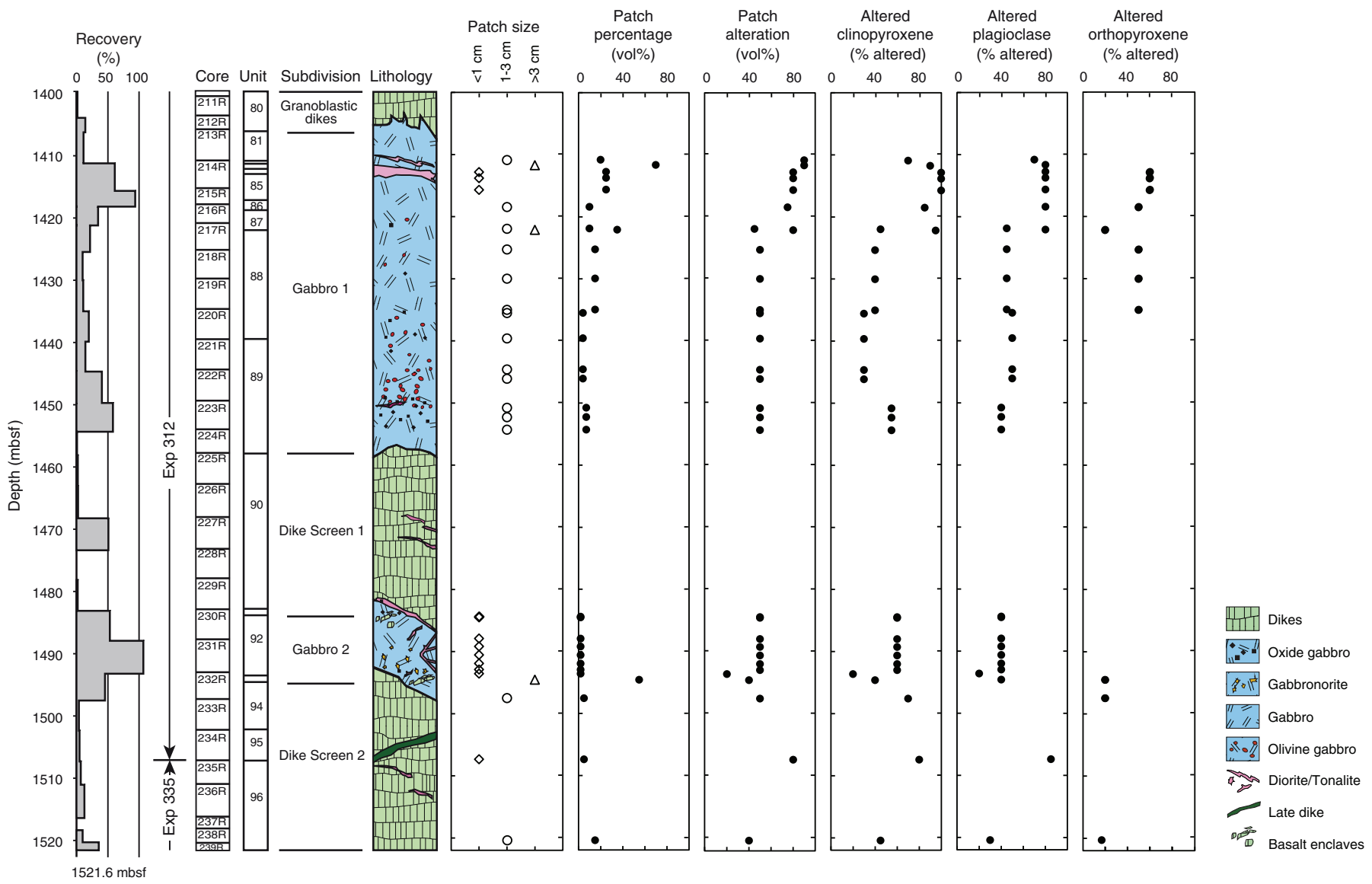

Figure F41. Photograph of alteration patch in gabbro (interval 312-1256D-214R-2, 60–68 cm) (from Teagle, Alt, Umino, Miyashita, Banerjee, Wilson, and the Expedition 309/312 Scientists, 2006).

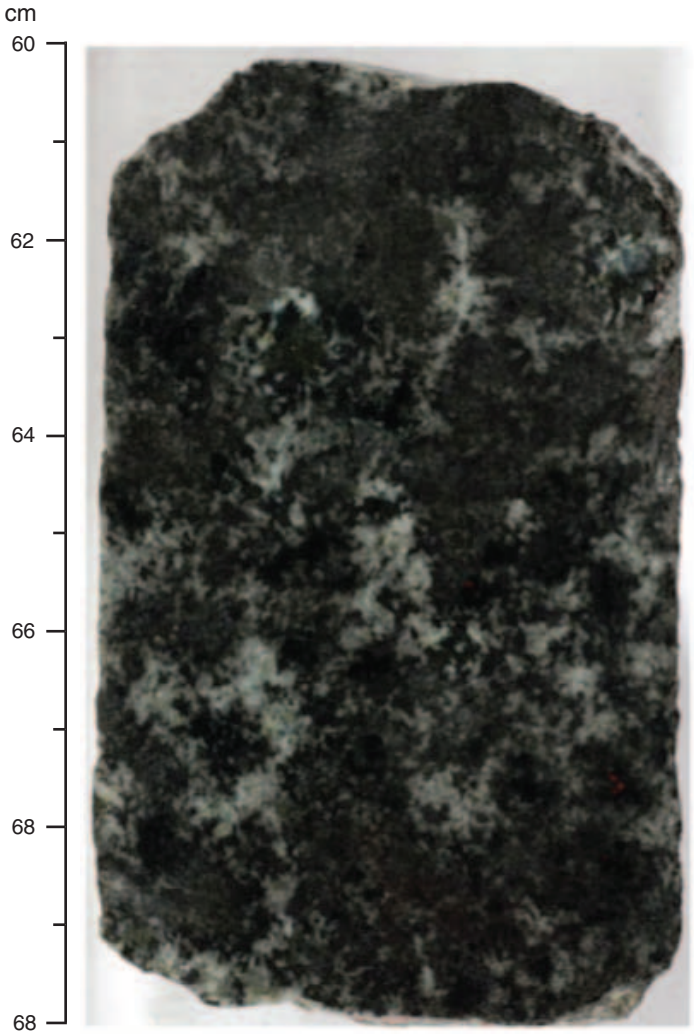

Figure F42. Plot of alteration mineralogy of alteration patches in the dike–gabbro transition zone in Hole 1256D.

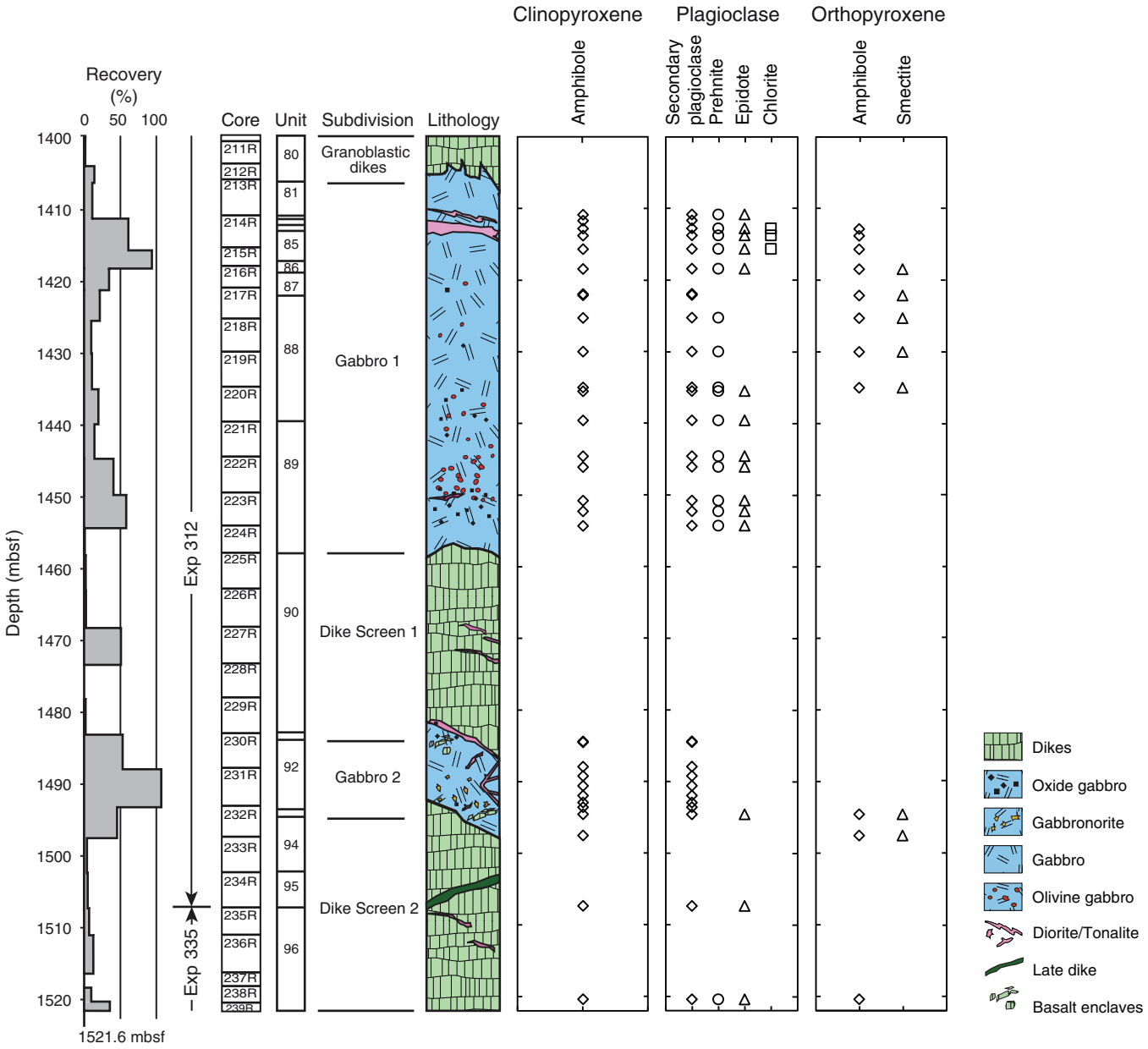

Figure F43. Plot of vein density in the dike–gabbro transition zone in Hole 1256D.

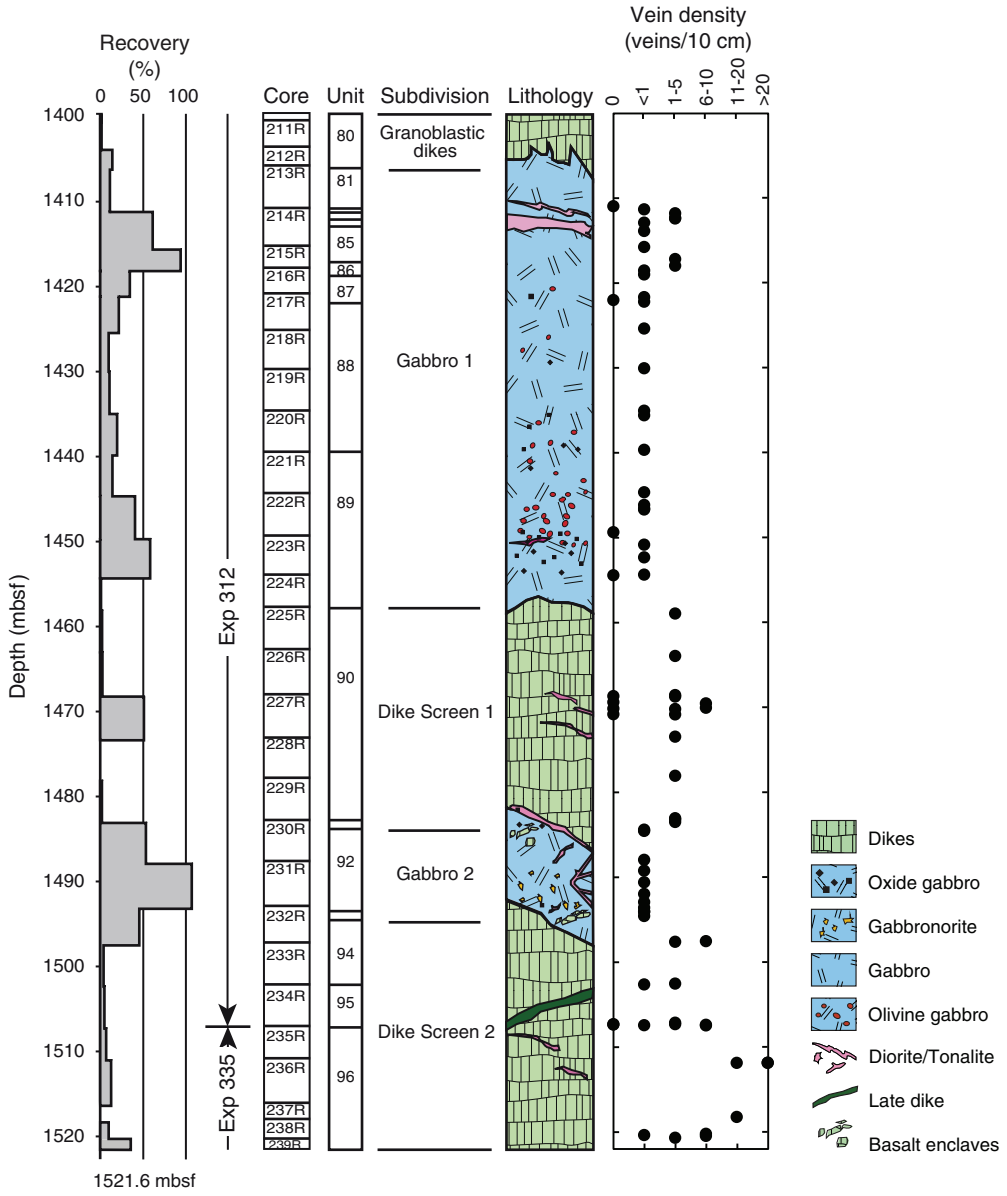

Figure F44. Plot of distribution of veins (veins per meter for each core) in the dike–gabbro transition zone in Hole 1256D.

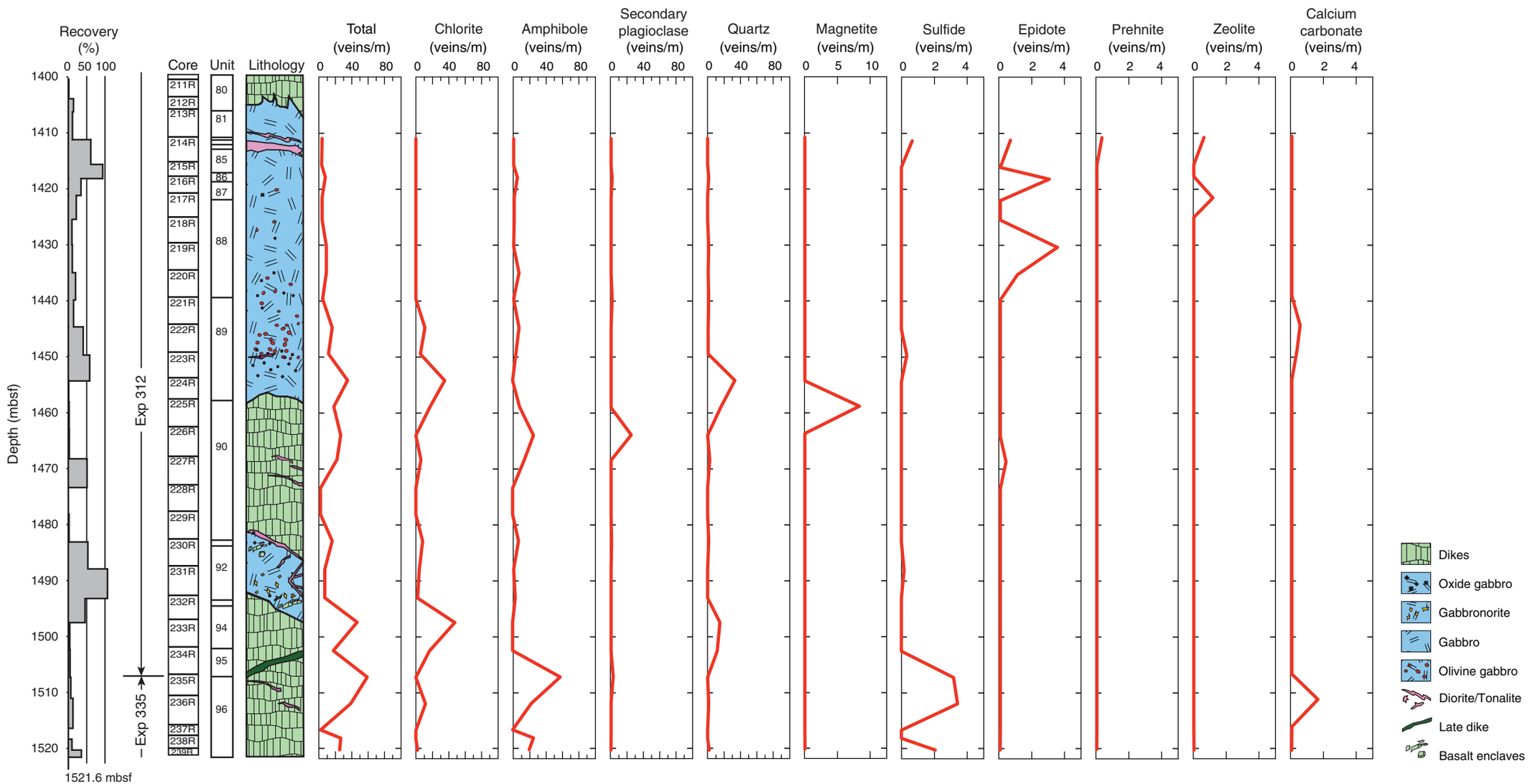

Figure F45. Plot of volume percent veins (per core) in the dike–gabbro transition zone in Hole 1256D.

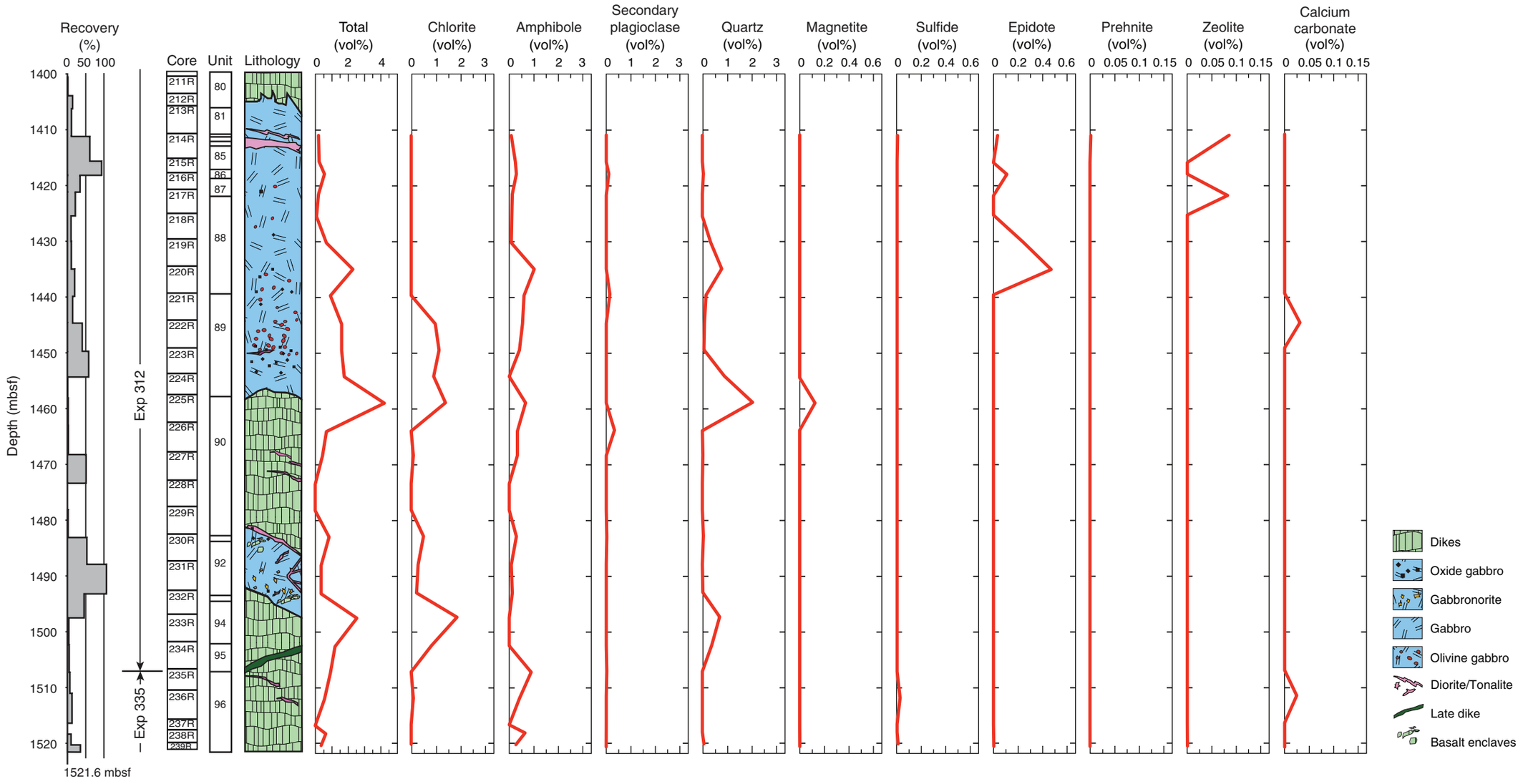

Figure F46. Plot of alteration (subsequent to contact metamorphism and development of granoblastic textures) vs. degree of contact metamorphic recrystallization for Hole 1256D dikes and gabbros. Dikes from below Gabbro 2 (Expedition 335 cores and junk basket rocks) are less altered by hydrous post-contact metamorphism than dikes from above Gabbro 1 (Expedition 312 dikes). Degrees of recrystallization are based on thin section observations, using the relative scale of Teagle, Alt, Umino, Miyashita, Banerjee, Wilson, and the Expedition 309/312 Scientists (2006) (see Fig. F12 in the "Methods" chapter [Expedition 335 Scientists, 2012b]).

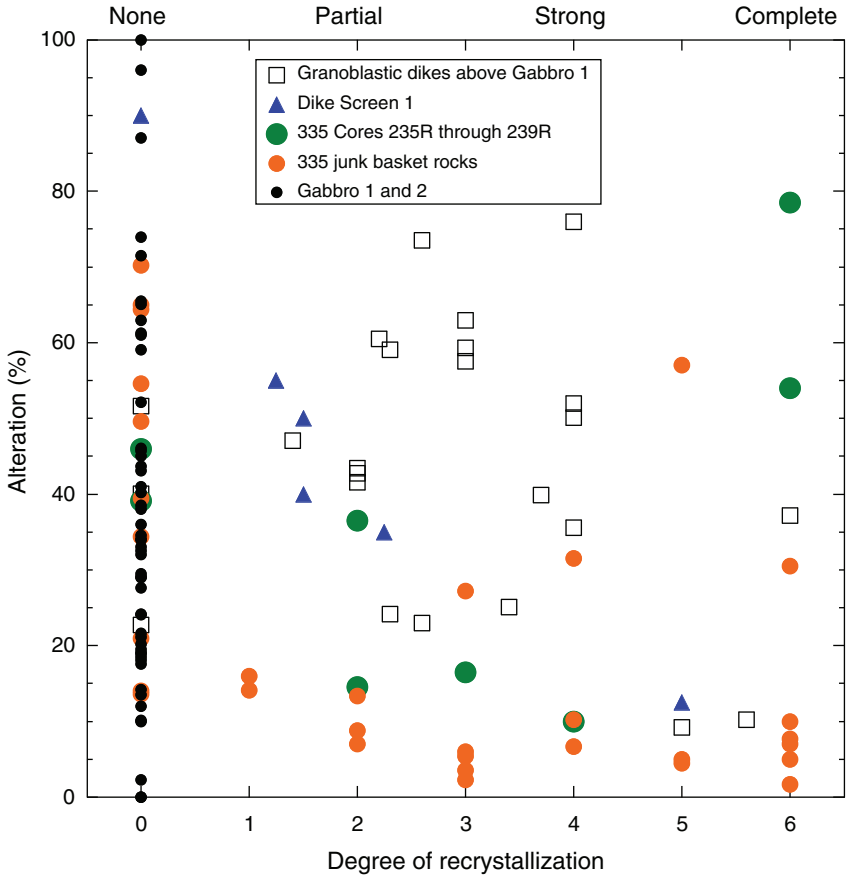

Figure F47. A. Plot of degree of granoblastic recrystallization in Hole 1256D. **B.** Histogram showing degree of recrystallization in rocks from junk baskets. Based on Expedition 335 observations and other sources for Expedition 312 section (L. France, unpubl. data; Teagle, Alt, Umino, Miyashita, Banerjee, Wilson, and the Expedition 309/312 Scientists, 2006).

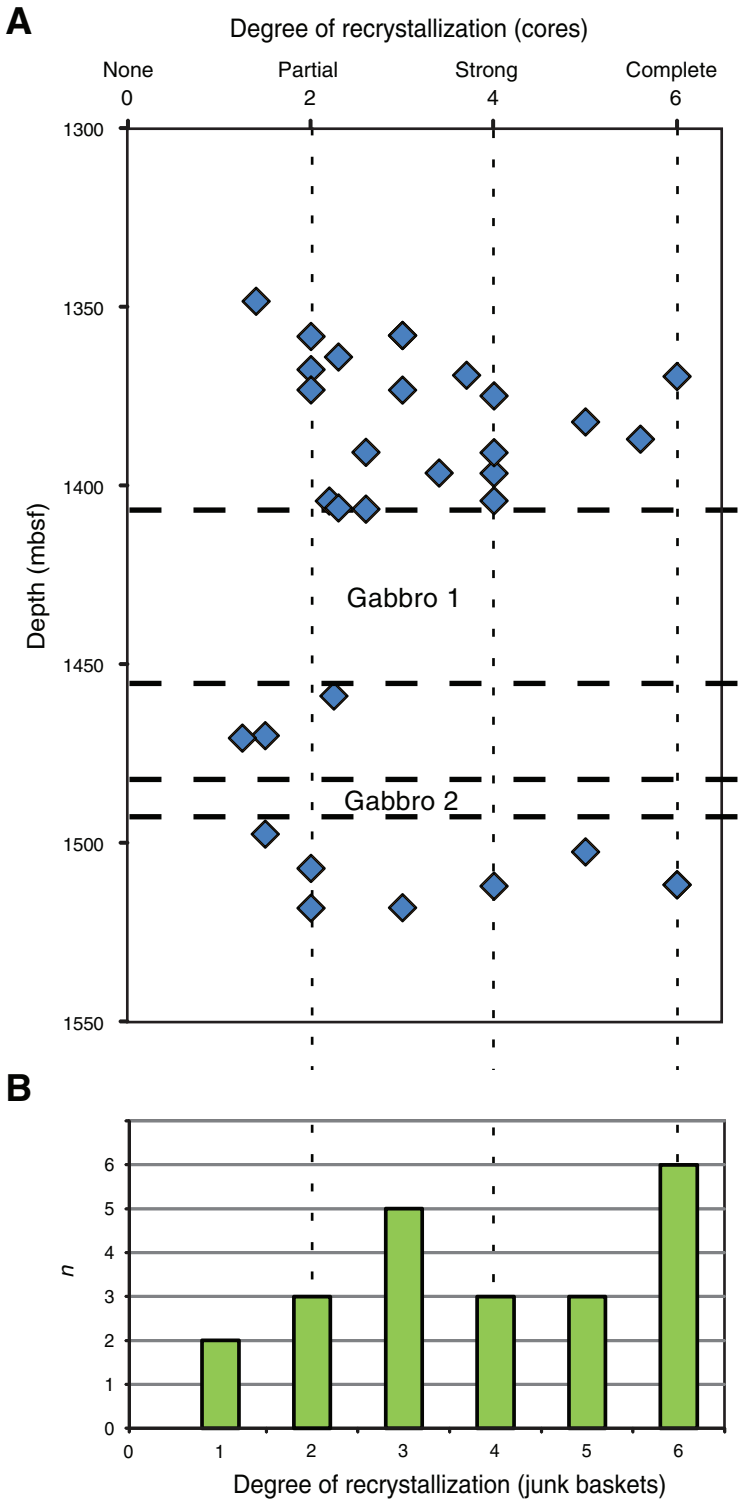

Figure F48. Photomicrographs of granoblastic recrystallization textures. **A.** Moderate recrystallization to granoblastic assemblage of clinopyroxene, orthopyroxene, plagioclase and Fe-Ti oxides (Sample 335-1256D-Run13-RCJB-Rock B; Thin Section 30) (plane-polarized light). Note relict lath shapes of plagioclase. **B.** Sample completely recrystallized to granoblastic texture (Sample 335-1256D-Run12-RCJB-Q; Thin Section 25) (cross-polarized light). **C.** Orthopyroxene-rich vein cutting recrystallized background (recrystallization degree = 4; see Fig. F44) (Sample 335-1256S-Run11-EXJB-J3; Thin Section 11) (plane-polarized light).

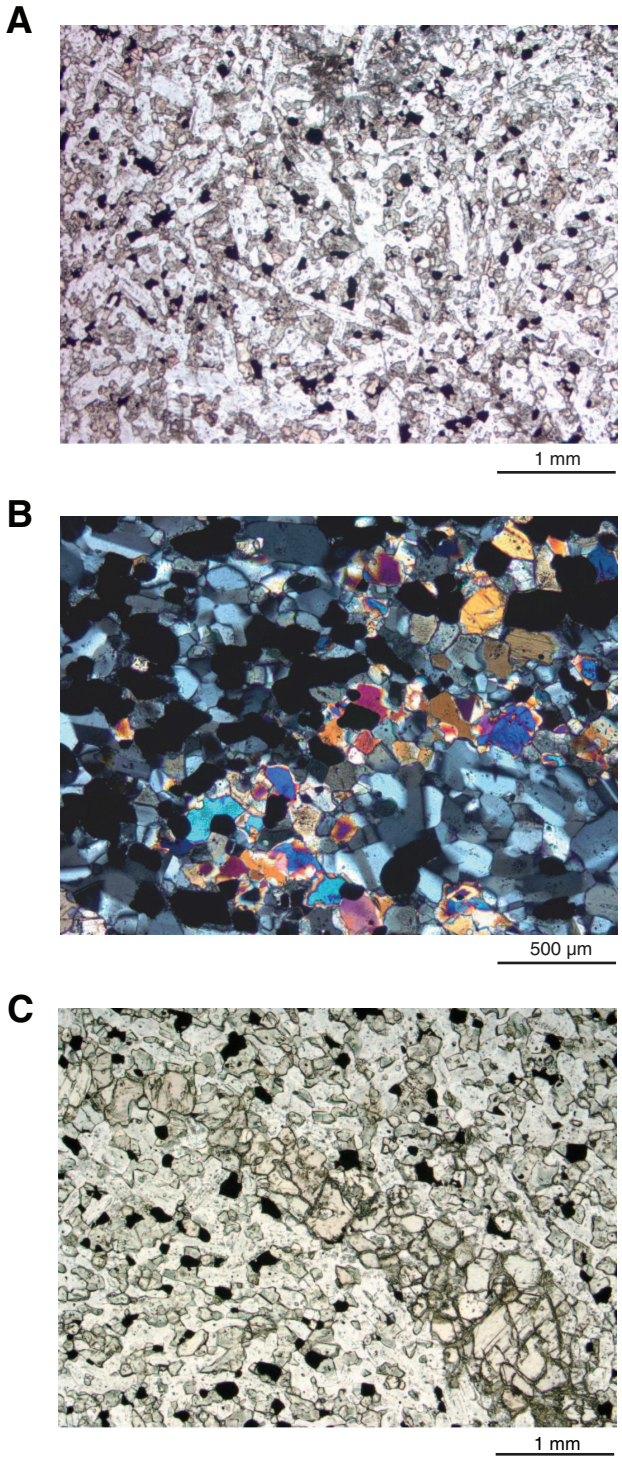

Figure F49. Photomicrographs of alteration of granoblastic material. **A.** Orthopyroxene replaced by amphibole and talc (Sample 335-1256D-238R-1, 2–4 cm; Thin Section 6) (plane-polarized light). **B.** Contact between granoblastic material (bottom) intruded and overgrown by coarser gabbroic material (top) (Sample 335-1256D-Run12-RCJB-Rock D; Thin Section 23) (plane-polarized light). Granoblastic material within 5–10 mm of the contact is more highly altered (pyroxenes replaced by amphibole) than the granoblastic host rock. **C.** Granoblastic "vein," 1 mm wide, consisting of plagioclase, clinopyroxene, and orthopyroxene, along with sparse Fe-Ti oxides, cut by discontinuous brown amphibole vein (Sample 335-1256D-238R-1, 13–15 cm; Thin Section 7) (plane-polarized light). Host rock contains 5 mm wide amphibole-rich alteration halo, where pyroxenes are replace by amphibole.

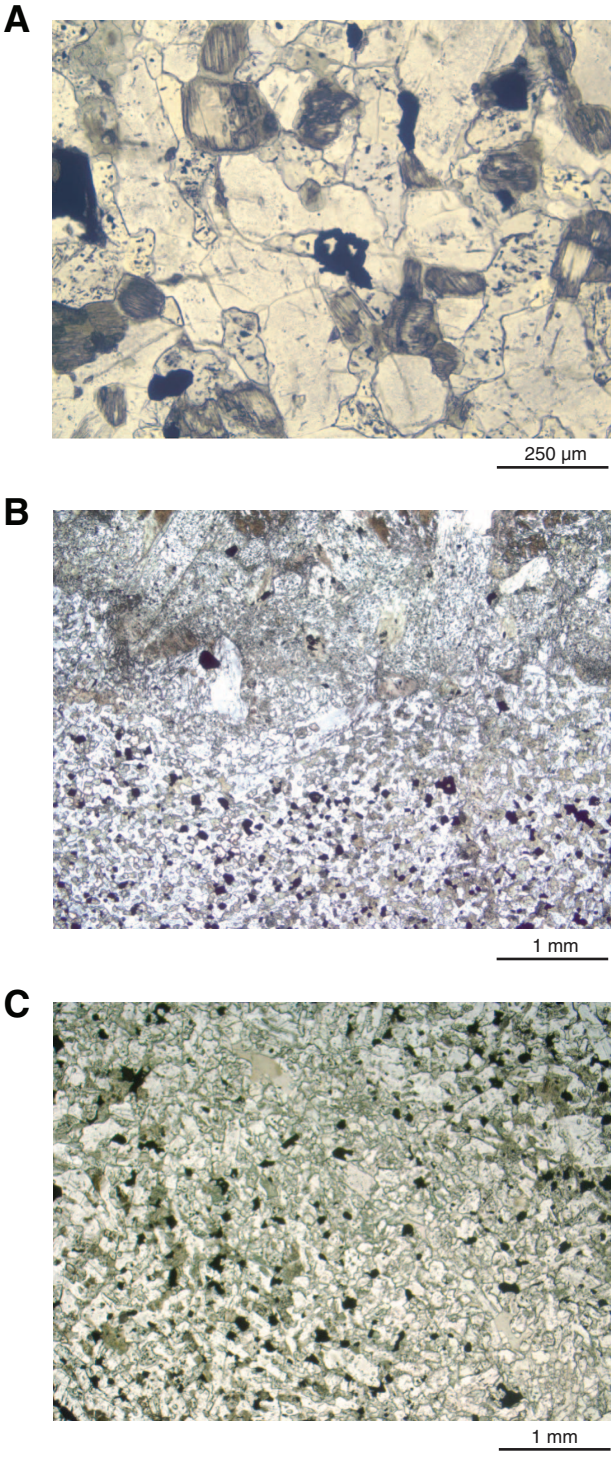

Figure F50. Veins (Sample 335-1256D-238R-1, 2–4 cm [Piece 1]; Thin Section 6). **A.** Photograph of granoblastic recrystallized vein (gray, left) and amphibole vein (dark, top middle to middle right) that are both cut by micrometer-sized amphibole veins. **B.** Photomicrograph of crosscutting relationship between a hornblende vein and a micrometer-sized branching actinolite vein (close-up of A; plane-polarized light).

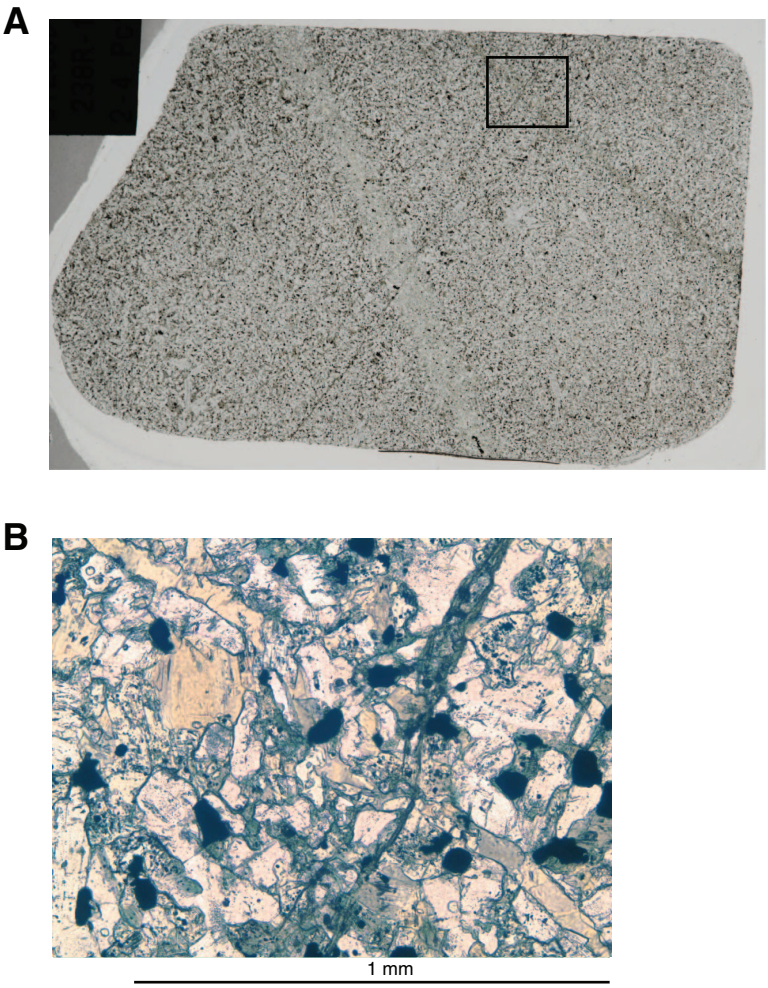

Figure F51. Photographs of amphibole veins (Sample 335-1256D-Run12-RCJB-Rock B; Thin Section 21). **A.** Amphibole vein with a layered alteration halo, adjacent to a felsic intrusion (bottom center) that tapers upward in photo to an amphibole vein. **B.** Amphibole vein lined with acicular magnetite crystals (close-up of A; plane-polarized light). In the alteration halo along the vein, pyroxenes are replaced by amphibole close to the vein, and farther from the vein clinopyroxenes are altered to dusty clinopyroxene.

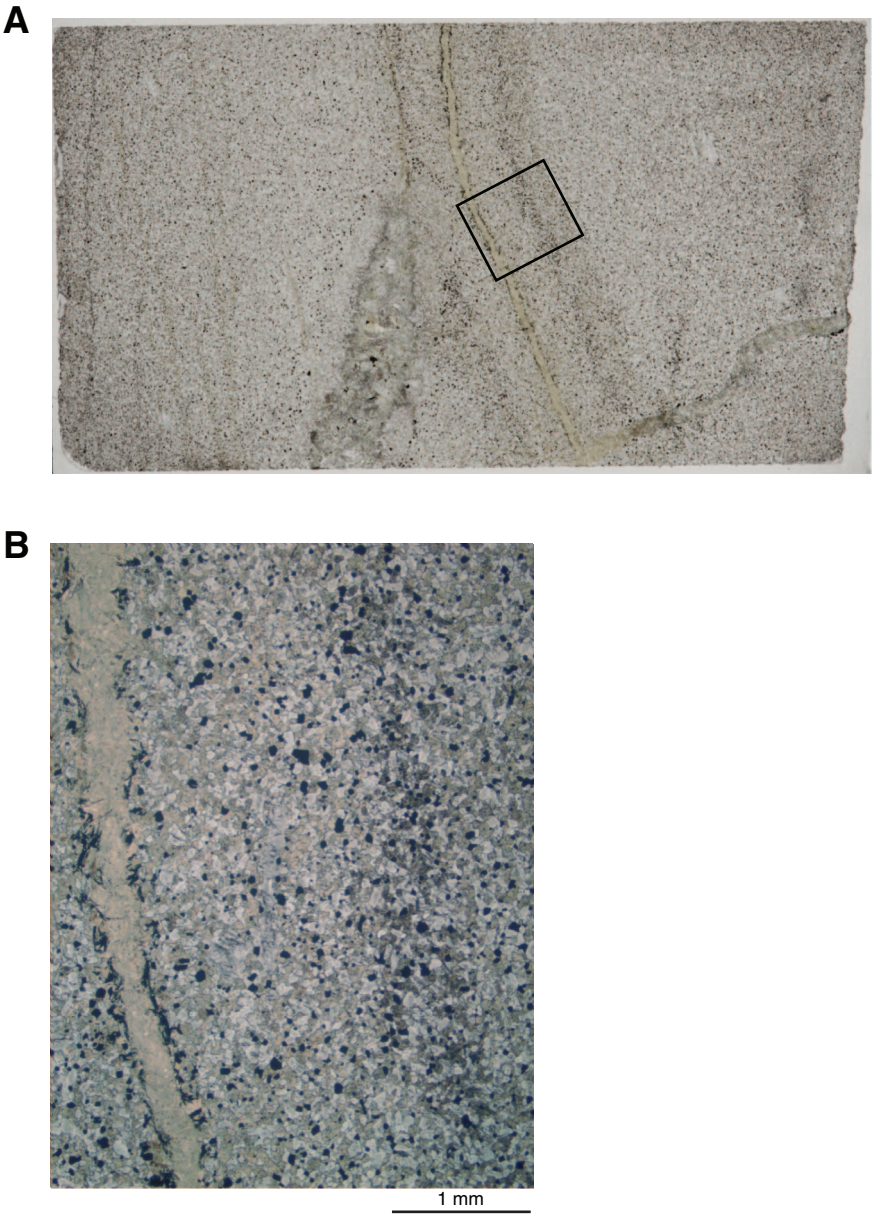

Figure F52. Photomicrographs of veins. **A.** Micrometer-sized amphibole vein (Sample 335-1256D-235R-1, 11–12 cm [Piece 1]; Thin Section 2) (plane-polarized light). The vein both cuts and follows grain boundaries. Where clinopyroxene crystals are bisected, most of the crystal is replaced by amphibole. **B, C.** Sample 335-1256D-236R-1, 0–4 cm (Thin Section 4): (B) prehnite vein with minor actinolite needles (cross-polarized light), (C) poikiloblastic epidote (1 mm) enclosing small pyroxene crystals (plane-polarized light).

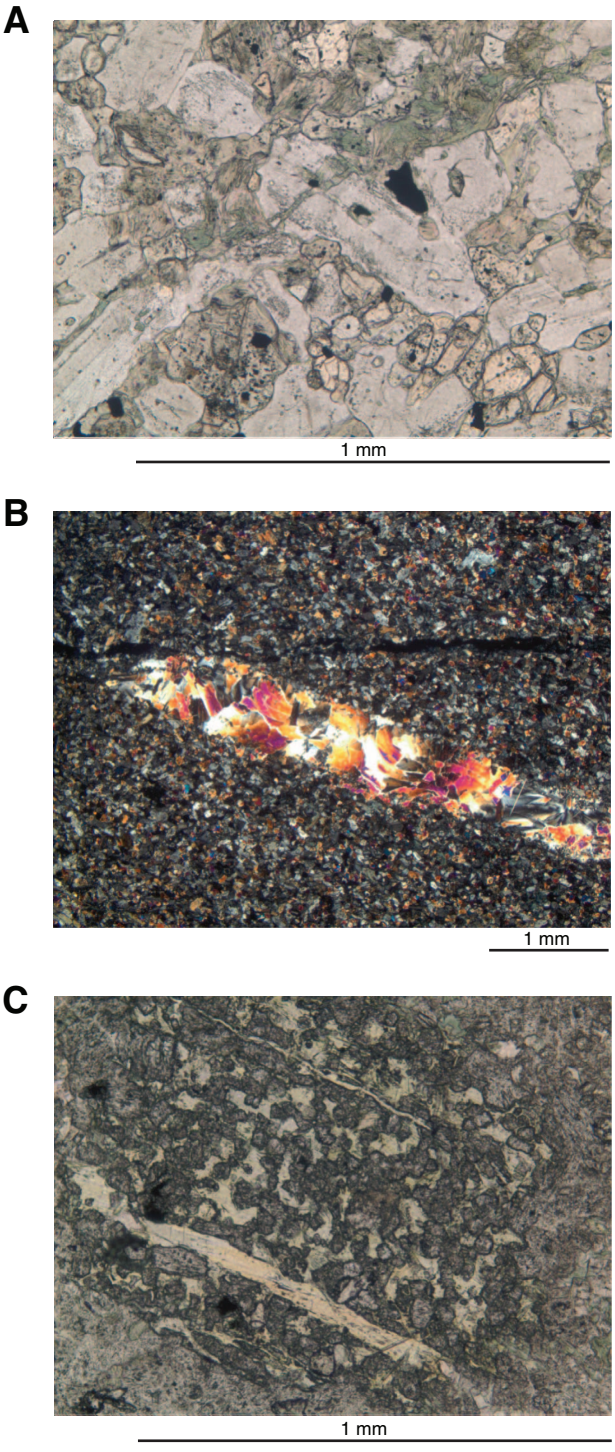

Figure F53. Alteration of felsic material (Sample 335-1256D-235R-1, 23–35 cm; Thin Section 3). **A.** Photograph of foliated diorite intruded by tonalitic vein and cut by later amphibole vein at center. **B.** Photomicrograph of plagioclase replaced by secondary plagioclase, epidote, and minor amphibole (cross-polarized light). Quartz containing needles of actinolite on right (white).

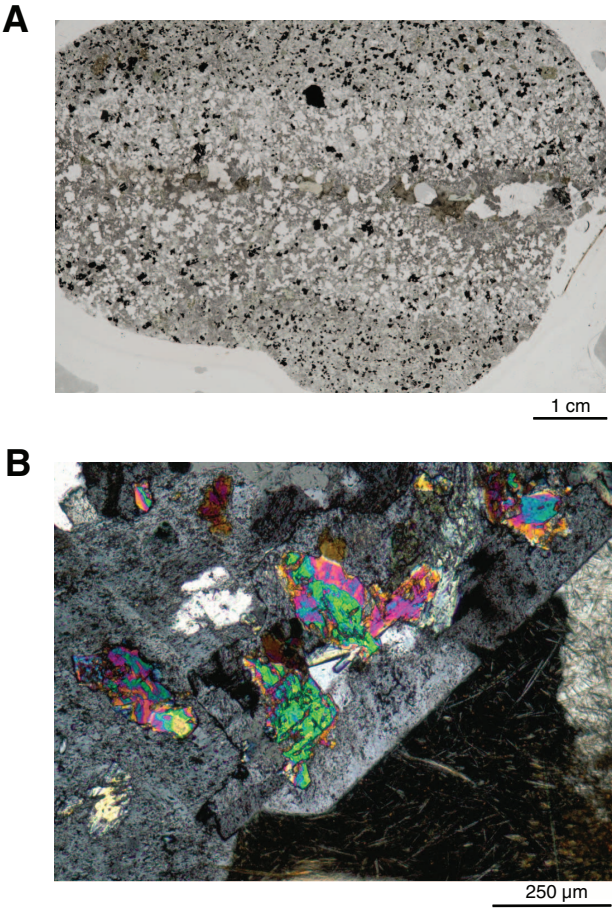

Figure F54. Photographs of recrystallized dike contact. **A.** Fine-grained darker gray dike at left was chilled against the coarser lighter gray dike at right. Rock is now recrystallized to granoblastic assemblages, which are cut by small amphibole veins (arrows), one of which cuts across the dike contact at center. **B.** Close-up of A showing dike contact and granoblastic textures throughout both dikes. Orthopyroxene veins at center and right are former hydrothermal veins that were recrystallized during contact metamorphism.

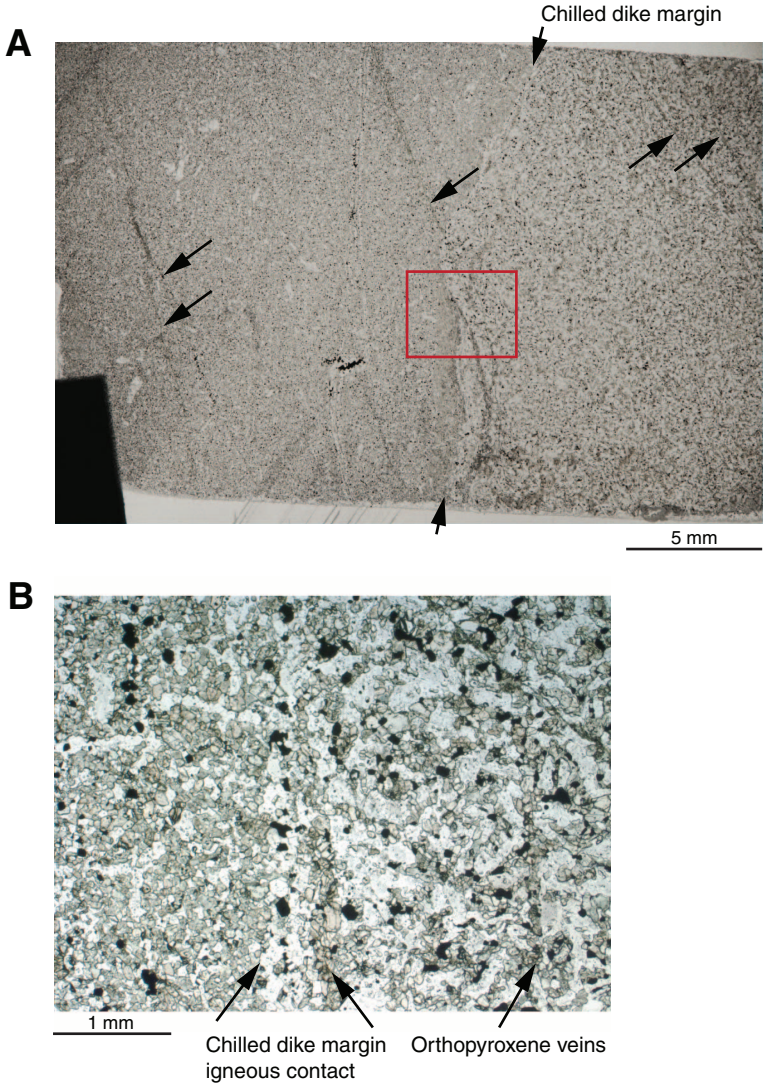

Figure F55. Chilled margin and brecciated clast texture (Sample 335-1256D-Run14-EXJB-Foliated). **A.** Thin section scan, showing angular clasts (gray), greenish interstitial material, and banded material at left center and right (see text for description). **B.** Detail of the plagioclase-rich clast (gray in left panel, cross-polarized light; white in right panel, plane-polarized light) and orthopyroxene-rich matrix (colors at top of left panel; grayish at top of right panel).

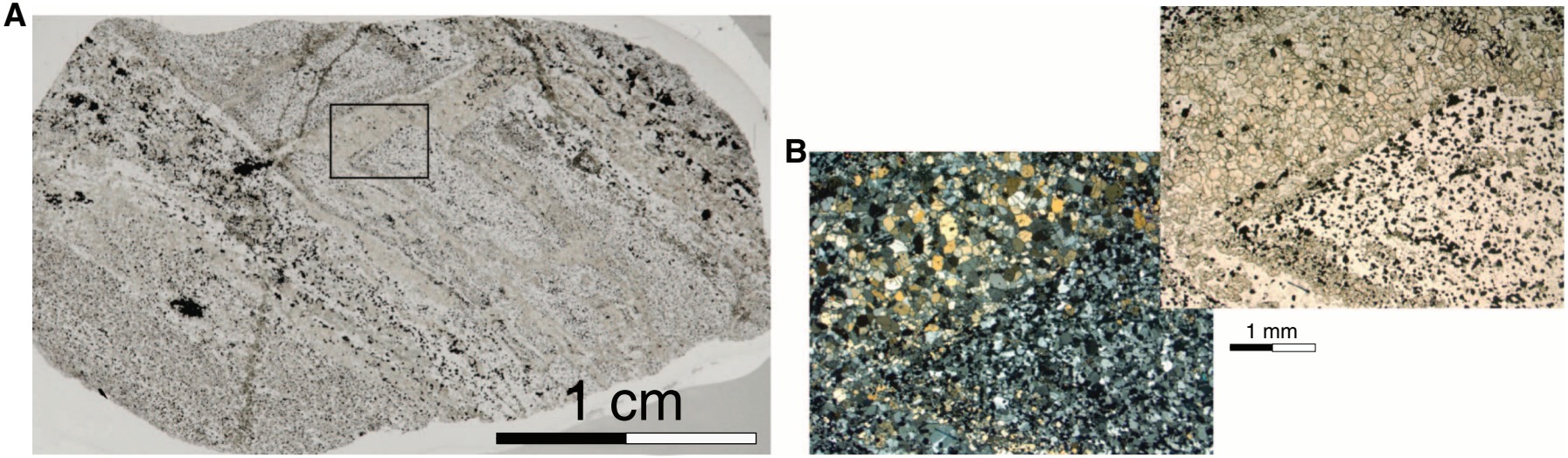

Figure F56. Photomicrographs of alteration of gabbroic rocks. **A, B.** Sample 335-1256D-Run11-EXJB-J4 (Thin Section 12): (A) Clinopyroxene replaced by amphibole + trace magnetite (plane-polarized light). Plagioclase is partly altered to secondary plagioclase along numerous fractures. Fe-Ti oxide (black) is highly altered to titanite at right. (B) Coronitic alteration of olivine (cross-polarized light). Olivine rim is altered to magnetite (black) and amphibole + talc. Veinlets of magnetite + talc cut the olivine. **C.** Plagioclase (gray) highly altered to secondary plagioclase + amphibole (Sample 335-1256D-Run12-RCJB-Rock B; Thin Section 21) (cross-polarized light). Clinopyroxene partly altered to amphibole + magnetite and interstitial areas altered and filled with amphibole.

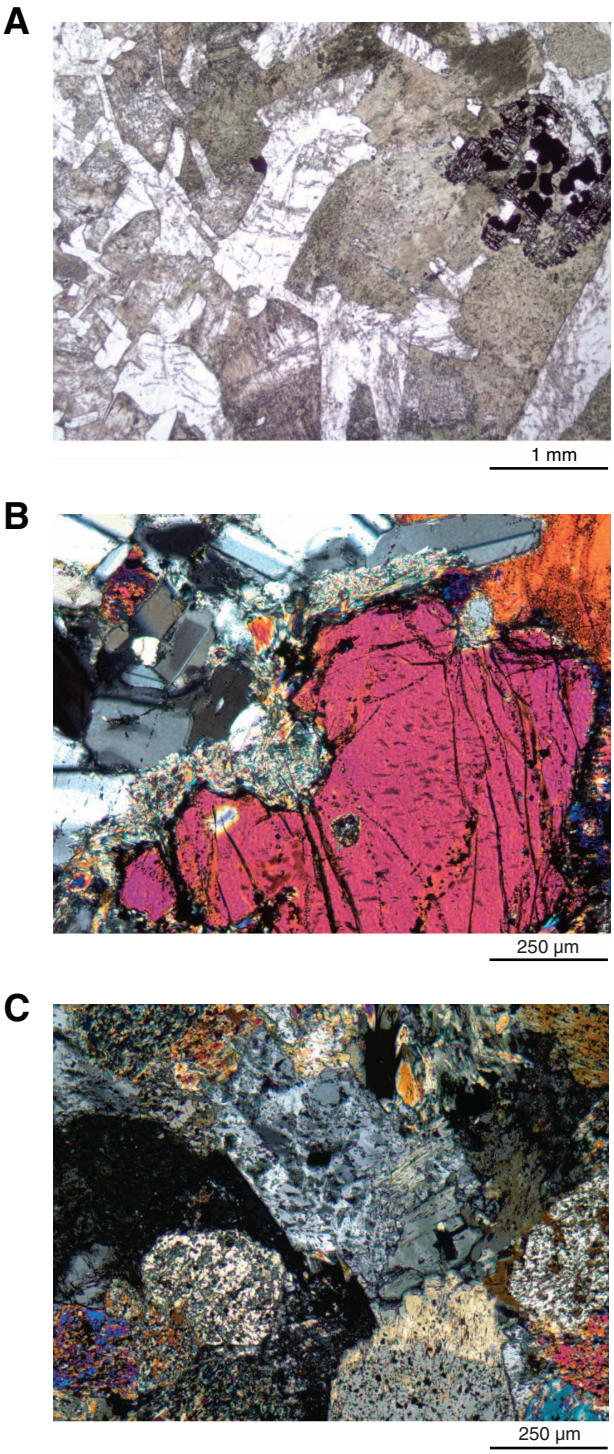

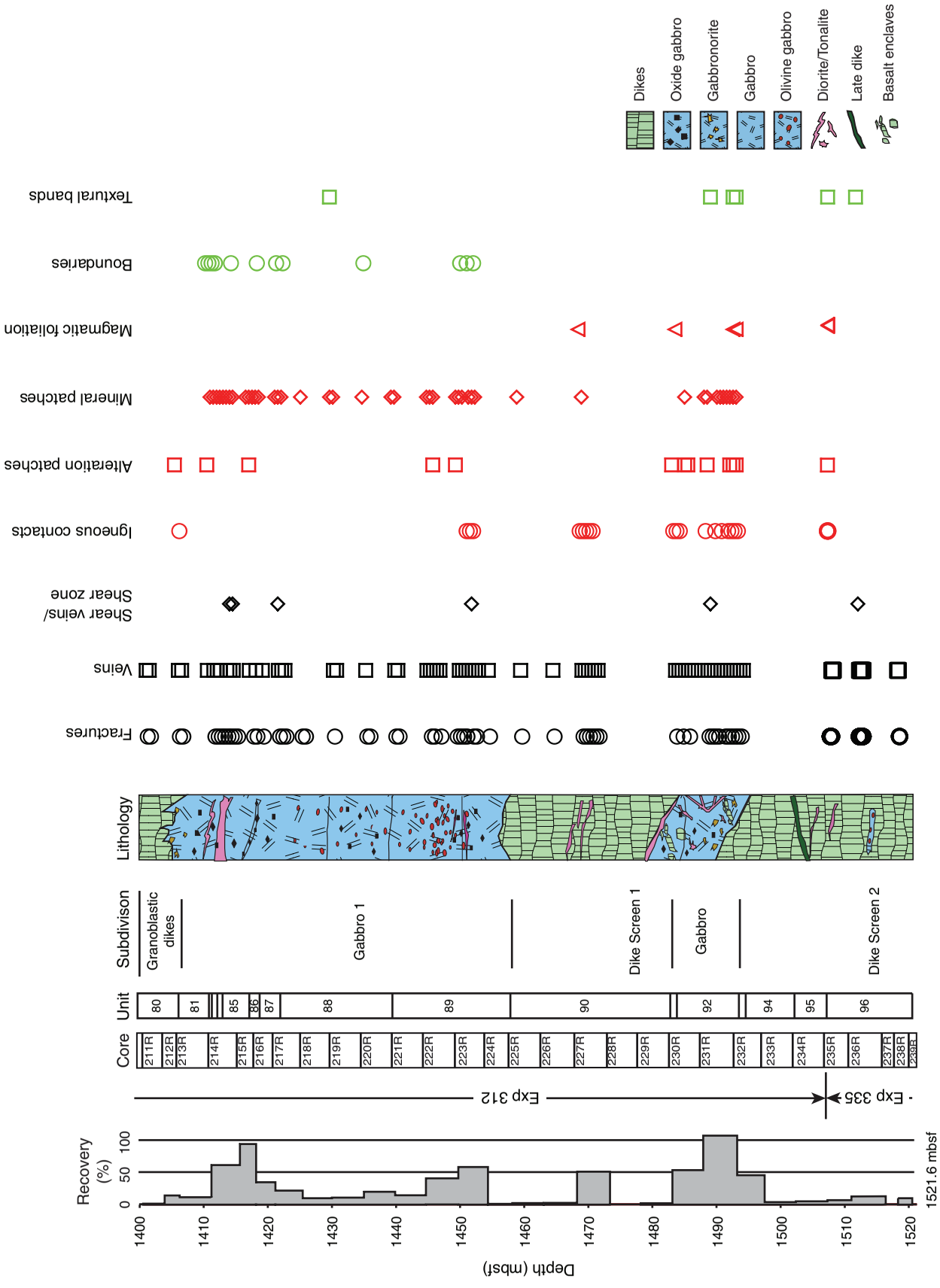

Figure F57. Observed and measured structures in the Hole 1256D plutonic section.

Figure F58. Structural synthesis of Hole 1256D plutonic section. Structures with an asterisk are tentatively reoriented into the geographic reference frame (see STRUCTURE_LOGS_312_335 in DESCRIPTIONS in **"Supplementary material"**). Igneous contacts between gabbros and aphyric basalt with granoblastic texture and between aphyric basalt with and without granoblastic textures are in red text. Boundaries in blue text are internal boundaries in Gabbro 1 that accompany changes in modal percent of leucocratic zones, SPO, and magnetic susceptibility (see Fig. **F64**). Boundaries in black text are internal unit/unit boundaries. High-T = high-temperature. Note that horizontal length is exaggerated, which artificially reduces the dip of structures. (Figure shown on next three pages.)

Figure F58 (continued). A. Cores 213R through 221R. (Continued on next page.)

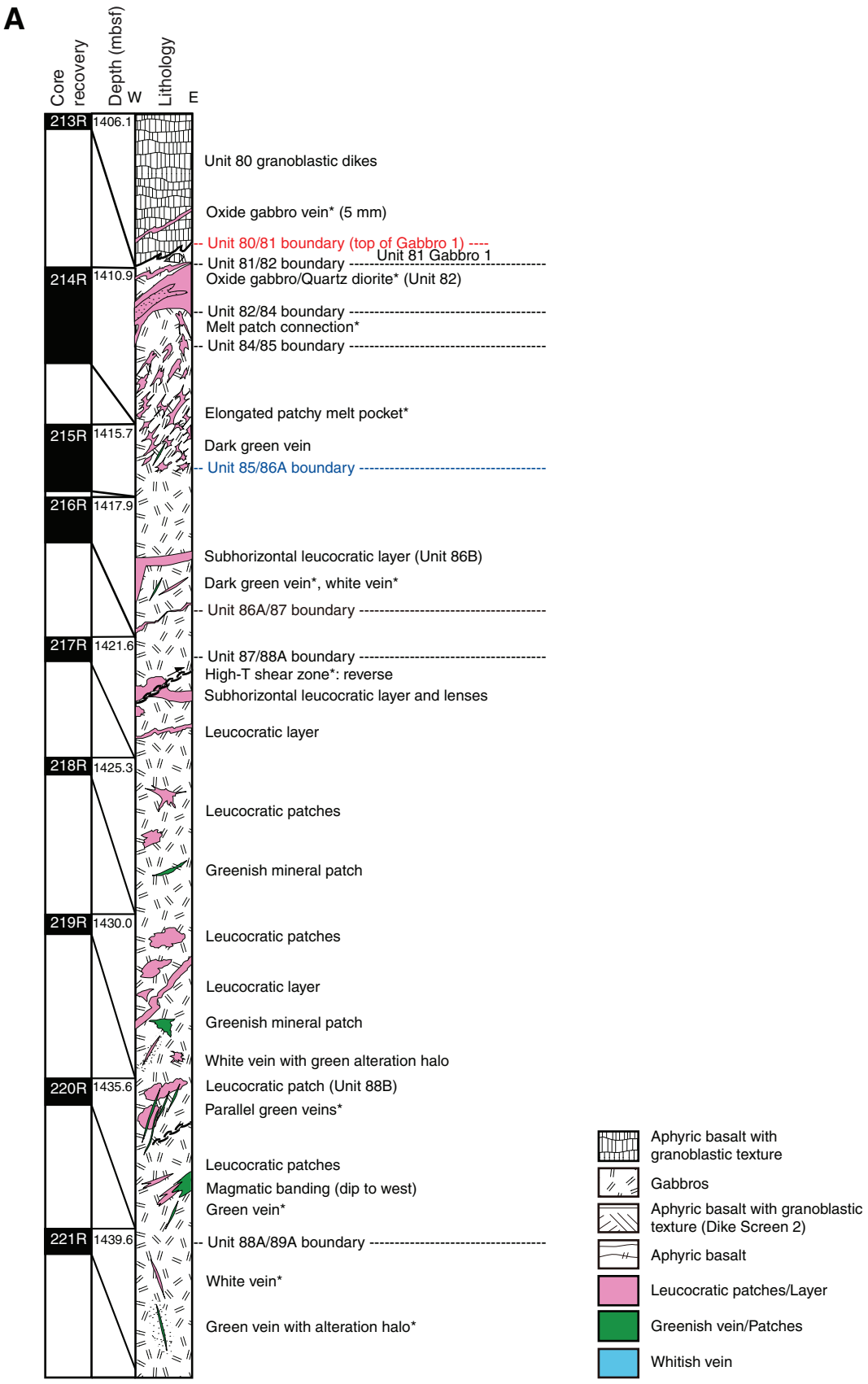

Figure F58 (continued). B. Cores 222R through 229R. (Continued on next page.)

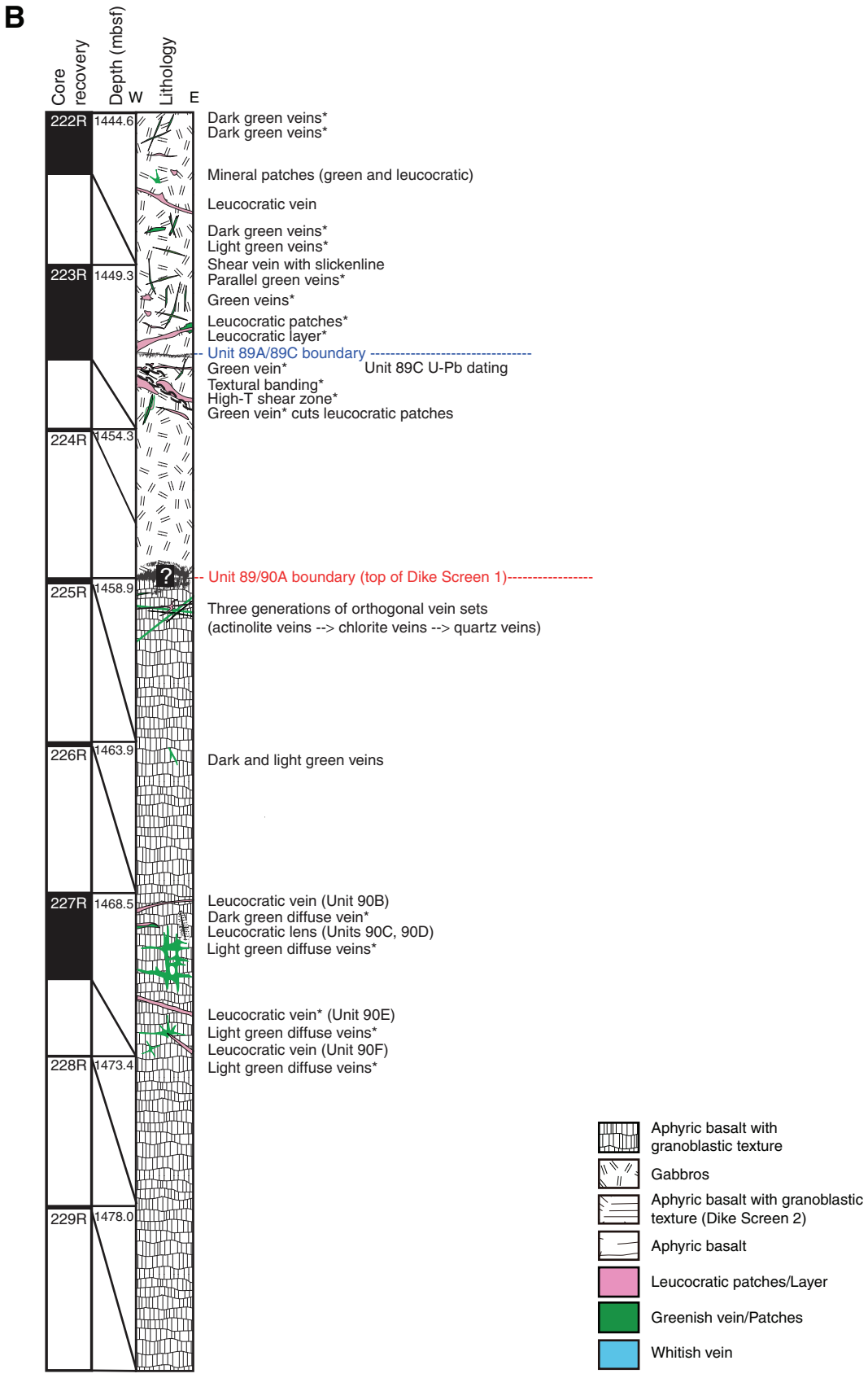

Figure F58 (continued). C. Cores 230R through 239R.

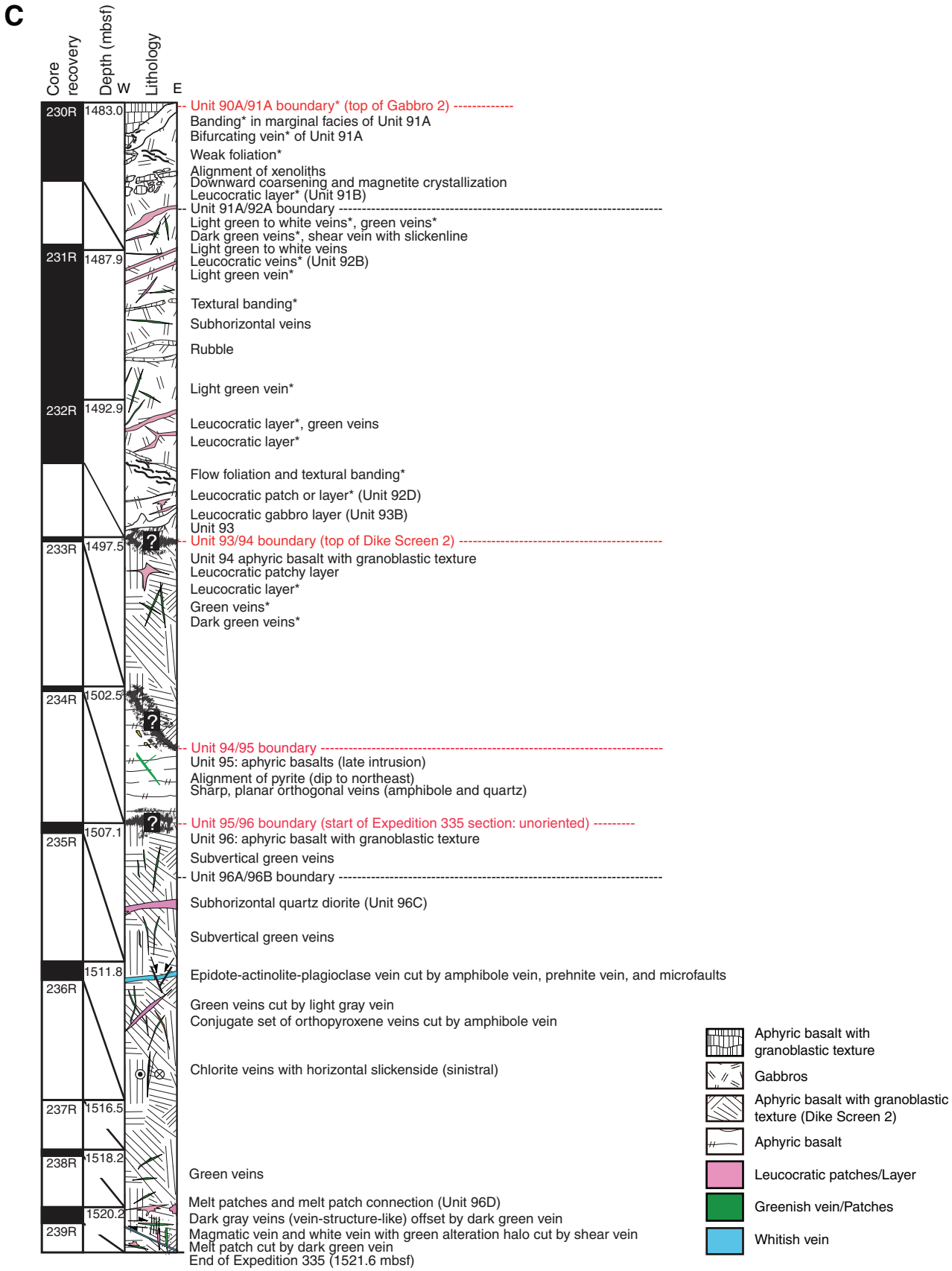

Figure F59. Distribution of igneous contact orientations, Expedition 335. **A.** Histogram of dip angles for all measured planar contacts and igneous patches. **B.** Equal-angle stereographic projection of contacts plotted as poles to planes for samples that have been tentatively azimuthally reoriented. Major igneous contacts are marked in black, and contacts of minor igneous veins are marked in red.

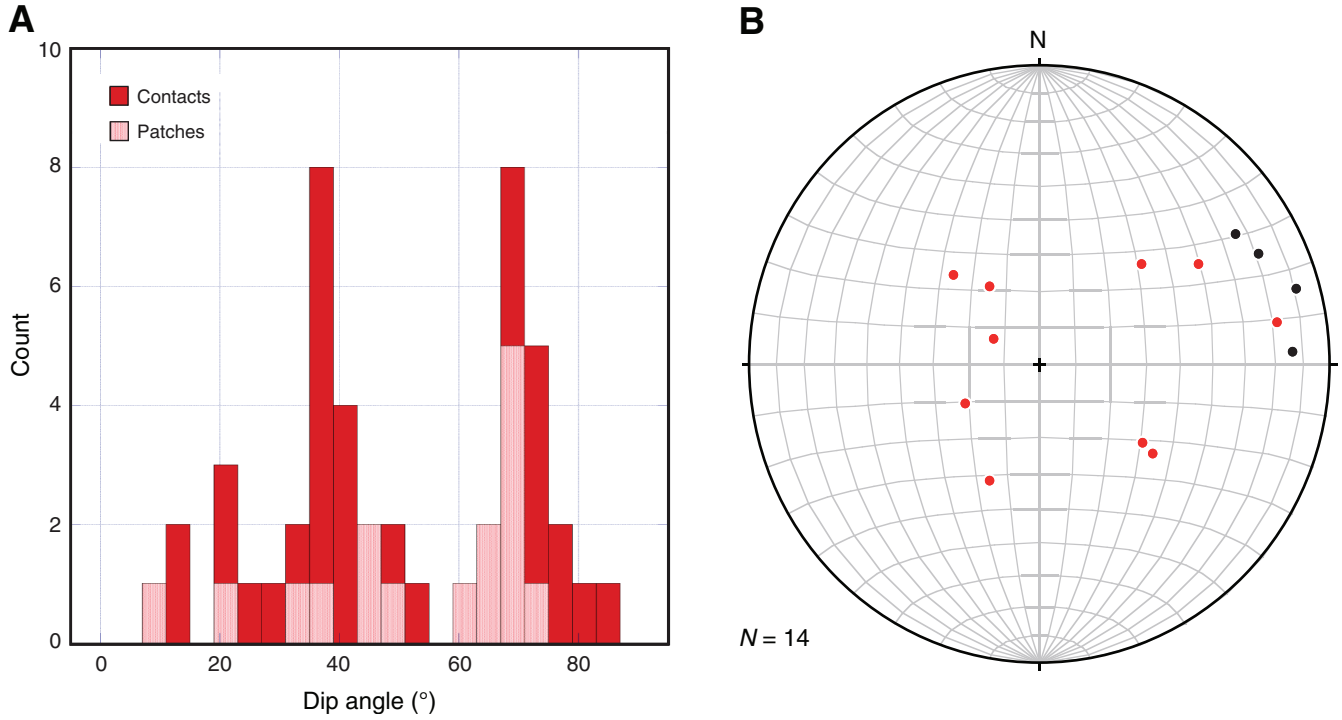

Figure F60. Distribution of vein orientations, Hole 1256D. **A.** Histogram of dip angles for all measured veins, divided by vein type. **B.** Equal-angle stereographic projection of veins plotted as poles to planes for samples that have been tentatively azimuthally reoriented.

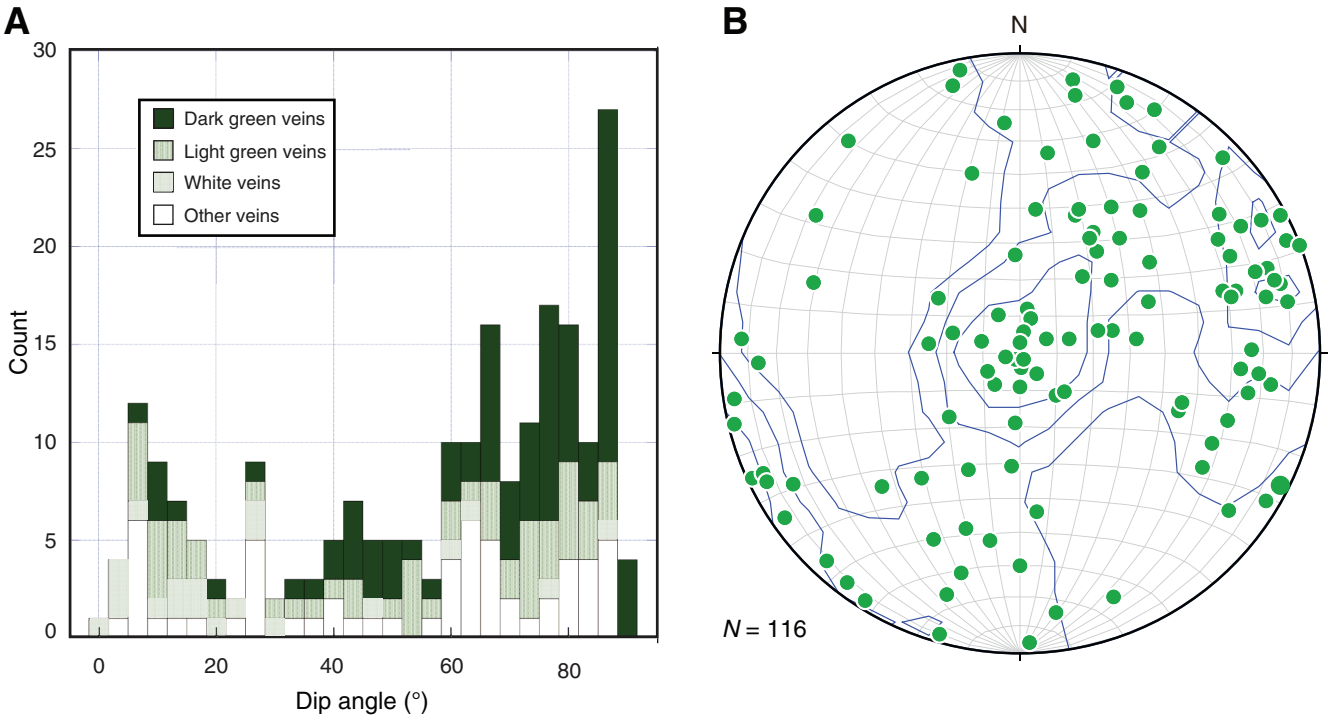

Figure F61. Rose diagrams of tentatively reoriented veins in Gabbro 1 (Sections 312-1256D-214R-1 through 224R-1), Dike Screen 1 (Sections 225R-1 through 230R-1) and Gabbro 2 (Sections 230R-1 through 232R-2). The vein azimuth is plotted as the right-hand rule convention, so dip direction is always to the right of the strike direction.

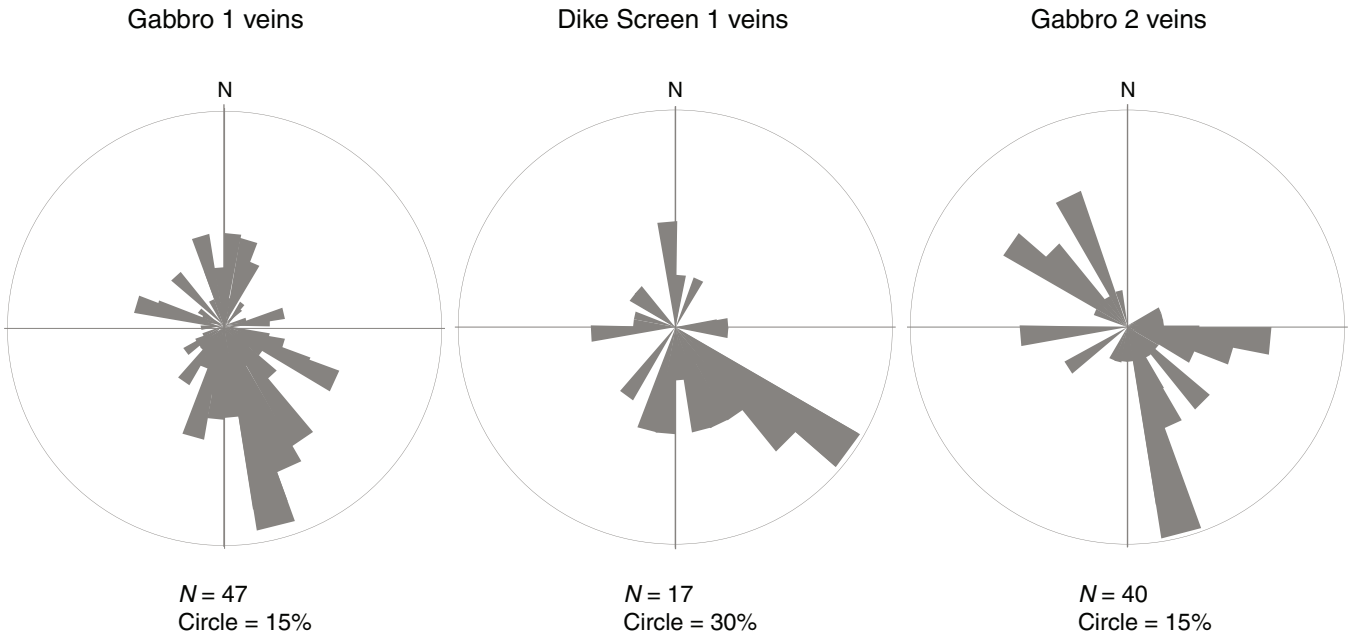

Figure F62. Downhole series of binary images from Gabbro 1 in Hole 1256D (pictures were taken on wet archive halves). Zone 1 is characterized by large and abundant leucocratic (plagioclase-rich) patches. Zone 2 is dominated by relatively small and few leucocratic patches, with the exception of Sample 335-1256D-217R-1A, 87–92 cm, which shows an anomalously high percentage of patches. Zone 3 is characterized by a higher abundance of patches than Zone 2 and an increasing abundance of patches toward the top of the zone.

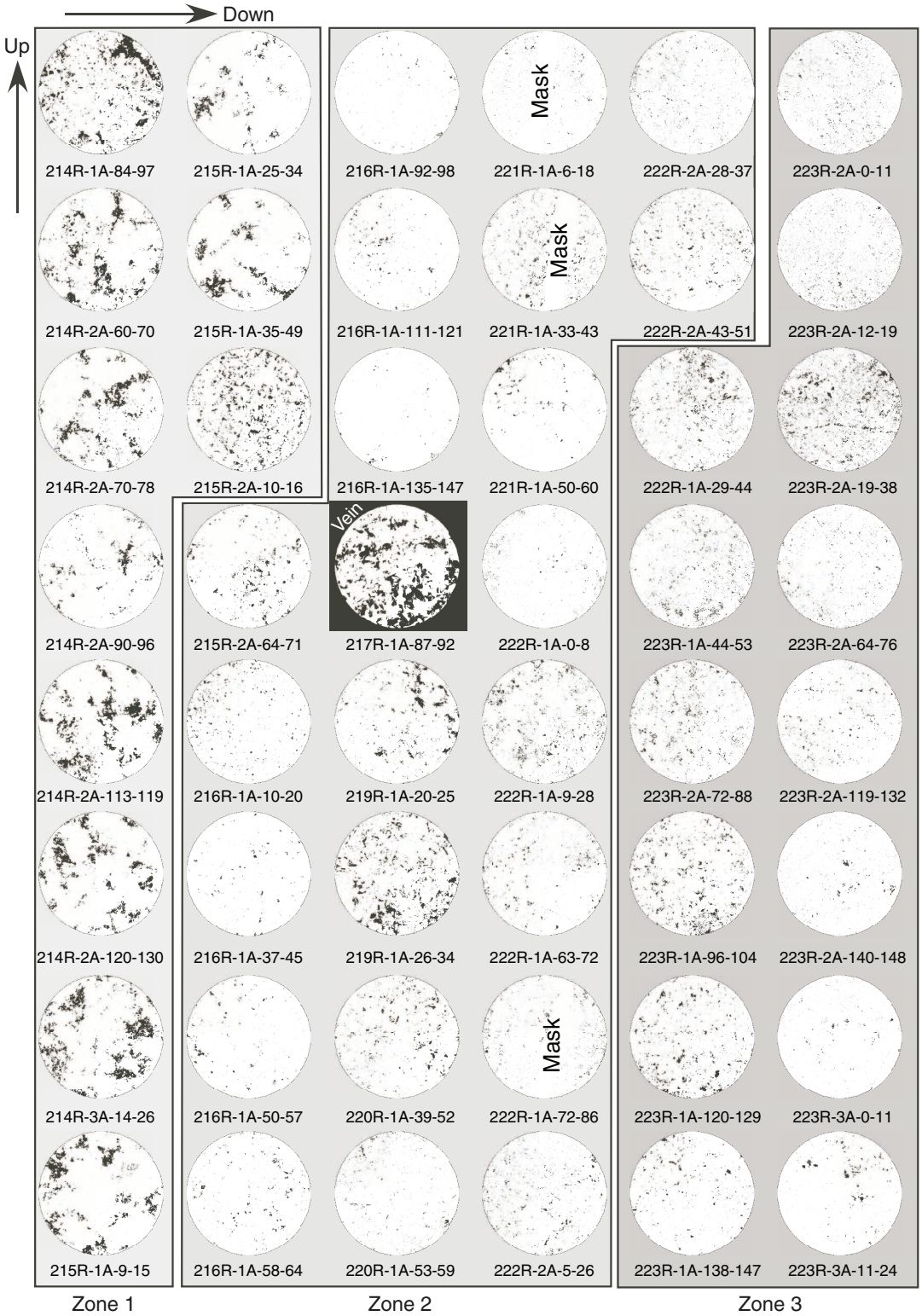

Figure F63. Shape-preferred orientation (SPO) of leucocratic patches in Gabbro 1, Hole 1256D. The binary image is upright in the vertical plane of the core cut face and shows objects of interest as black on a white background. SPO symmetry varies downhole. The red line represents the long axis of the elliptical best fit to the rose of directions. P = modal percentage of the analyzed phase, SR = shape ratio of the SPO ellipse, α = angle between the ellipse long axis and the core axis, recorded in a clockwise sense from up on the split core face.

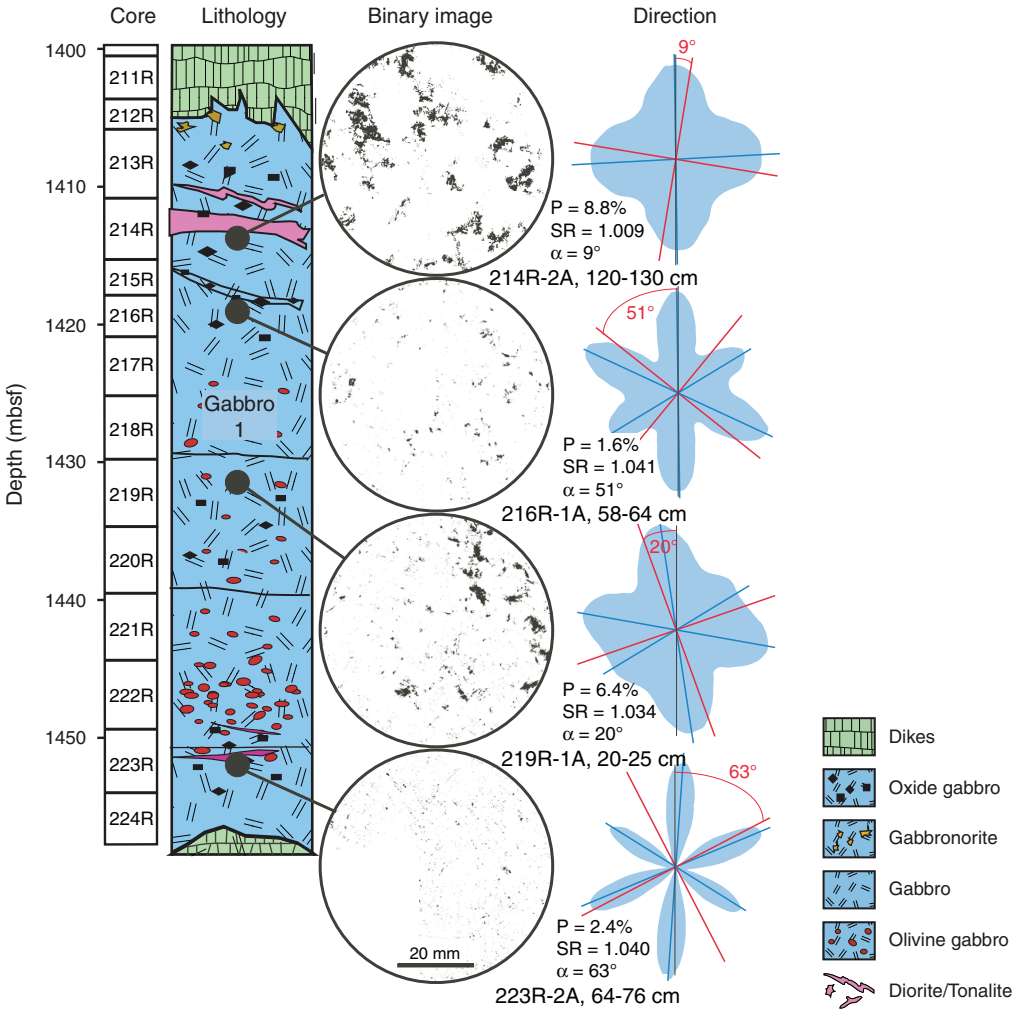

Figure F64. Downhole variation of shape-preferred orientation (SPO) parameters, Hole 1256D: percentage of leucocratic patches, shape ratio (SR), and orientation with respect to core axis. Magnetic susceptibility is plotted to support the delineation of magmatic fabric units within Gabbro 1. Major changes in contents of leucocratic patches and magnetic susceptibility decreasing generally downward coincide with Unit 85/86A and 89A/89C boundaries (see Fig. F58).

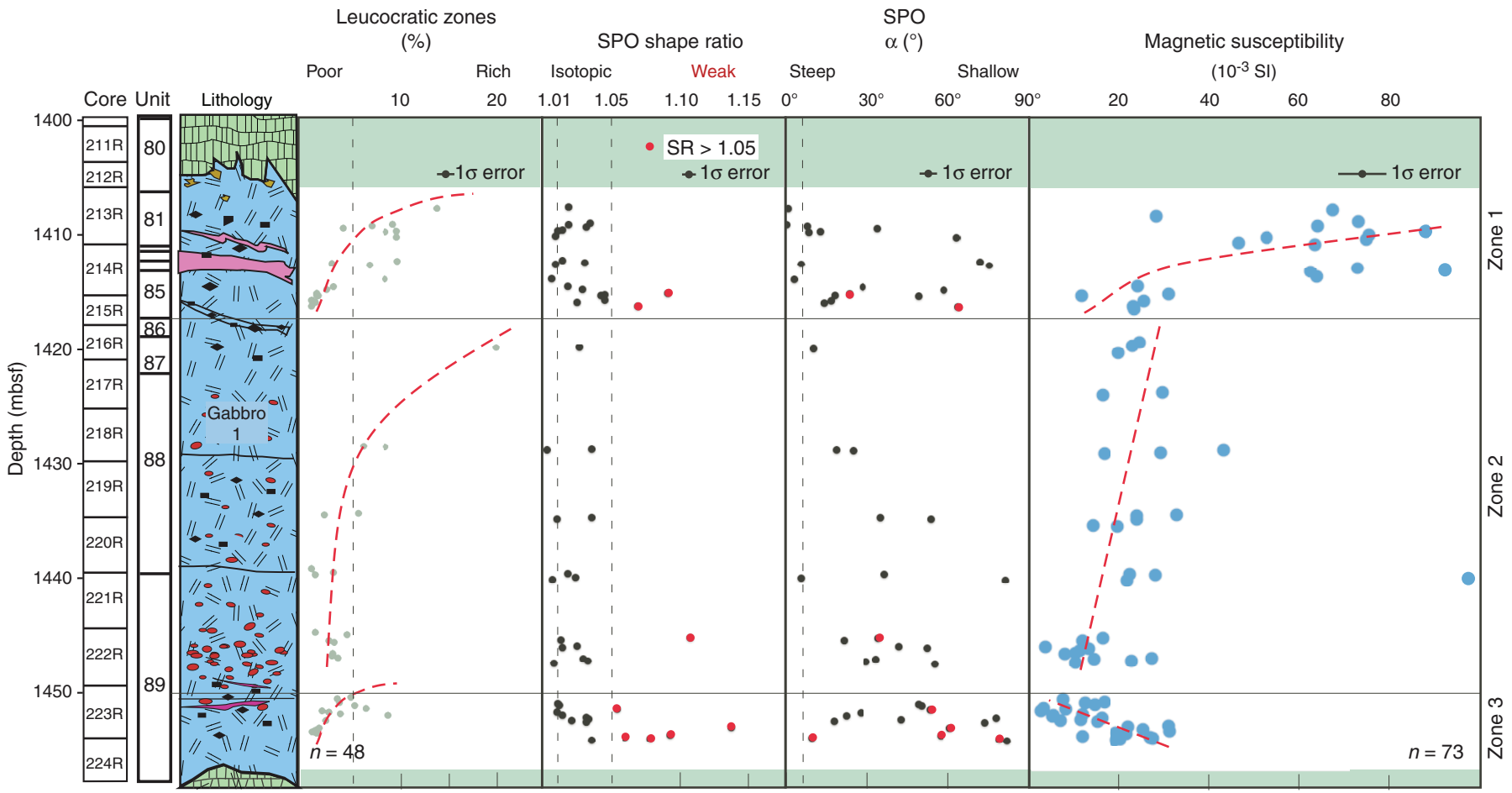

Figure F65. Variation of shape-preferred orientation (SPO) shape ratio with percentage of leucocratic zones in Gabbro 1, Hole 1256D. Anisotropic samples are characterized by a low percentage of leucocratic patches, whereas the most leucocratic patch–rich samples are either weakly anisotropic or isotropic.

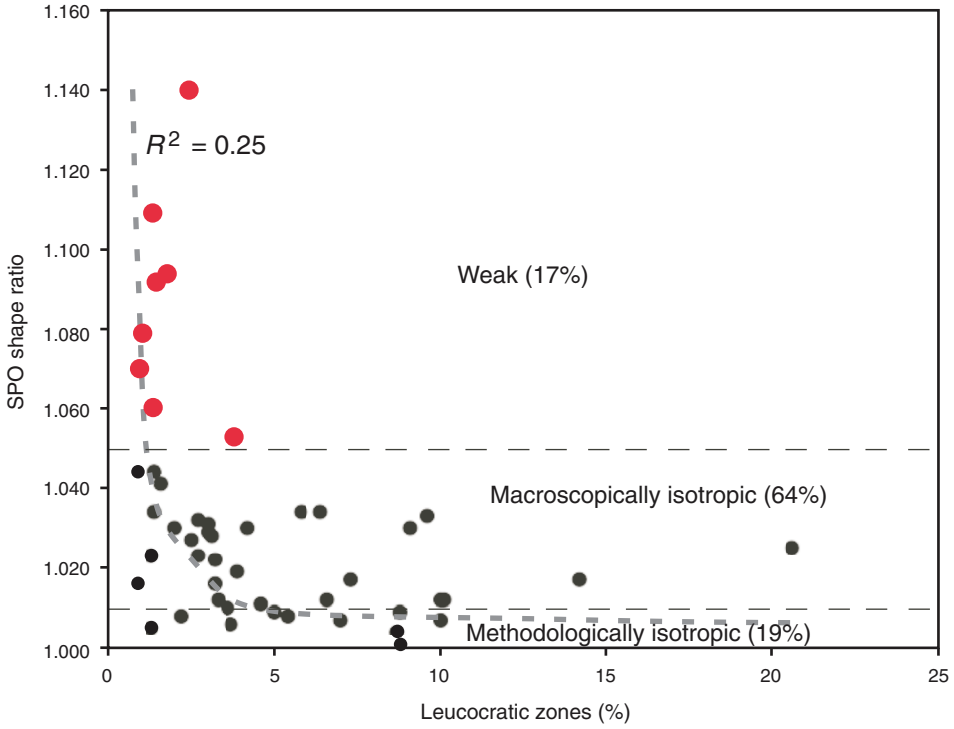

Figure F66. Downhole variation of shape-preferred orientation (SPO) attitude in Gabbro 1, Hole 1256D, showing that Zone 1 is characterized by a higher abundance of steep SPO fabrics. Zone 3 shows the largest proportion (35%) of gently dipping SPO. SR = shape ratio.

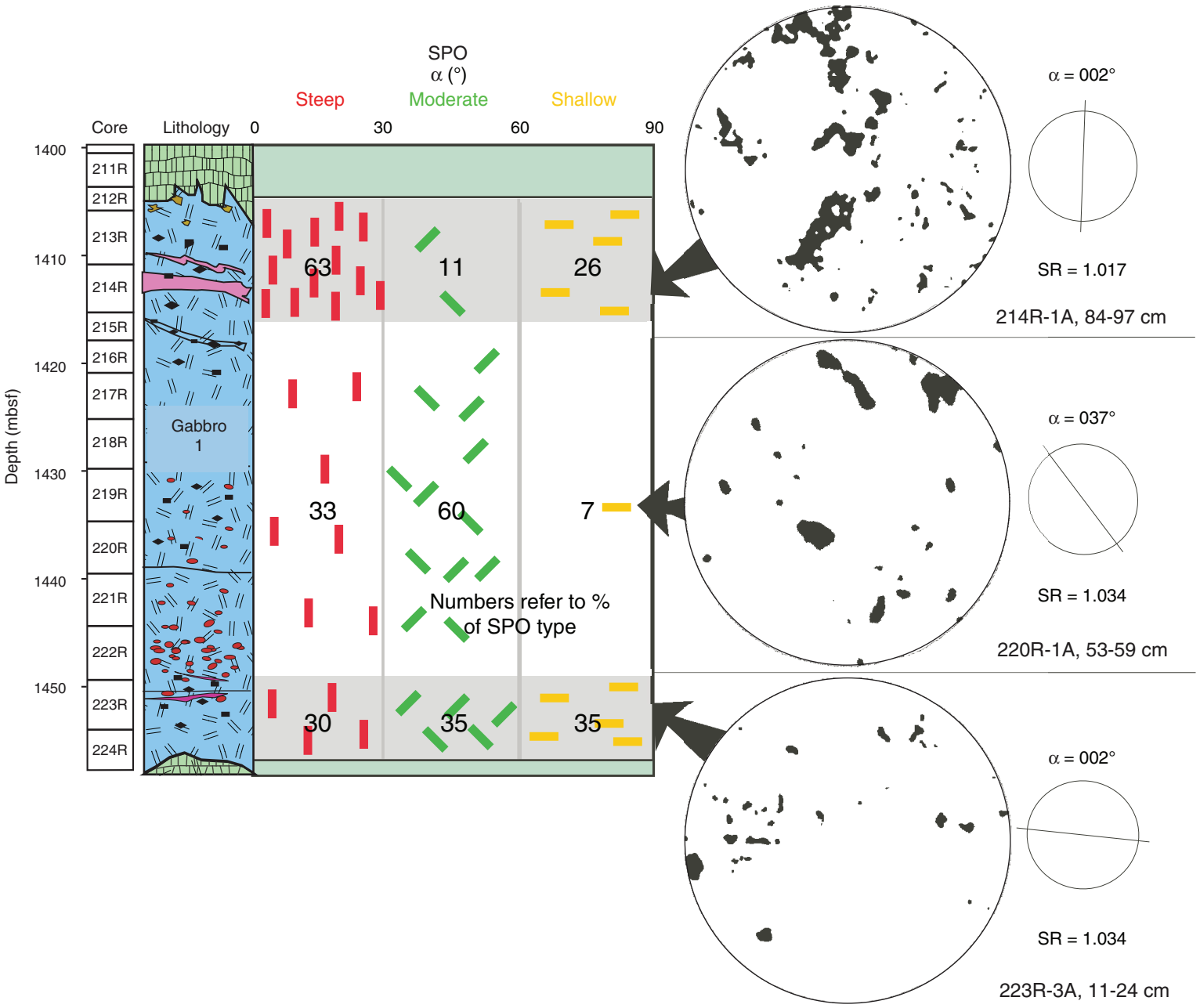

Figure F67. Distribution of fracture orientations, Hole 1256D. **A.** Histogram of dip angles for all measured fracture planes with SIFs plotting at dip angles <20°. **B.** Equal-angle stereographic projection of fractures plotted as poles to planes for samples that have been tentatively azimuthally reoriented.

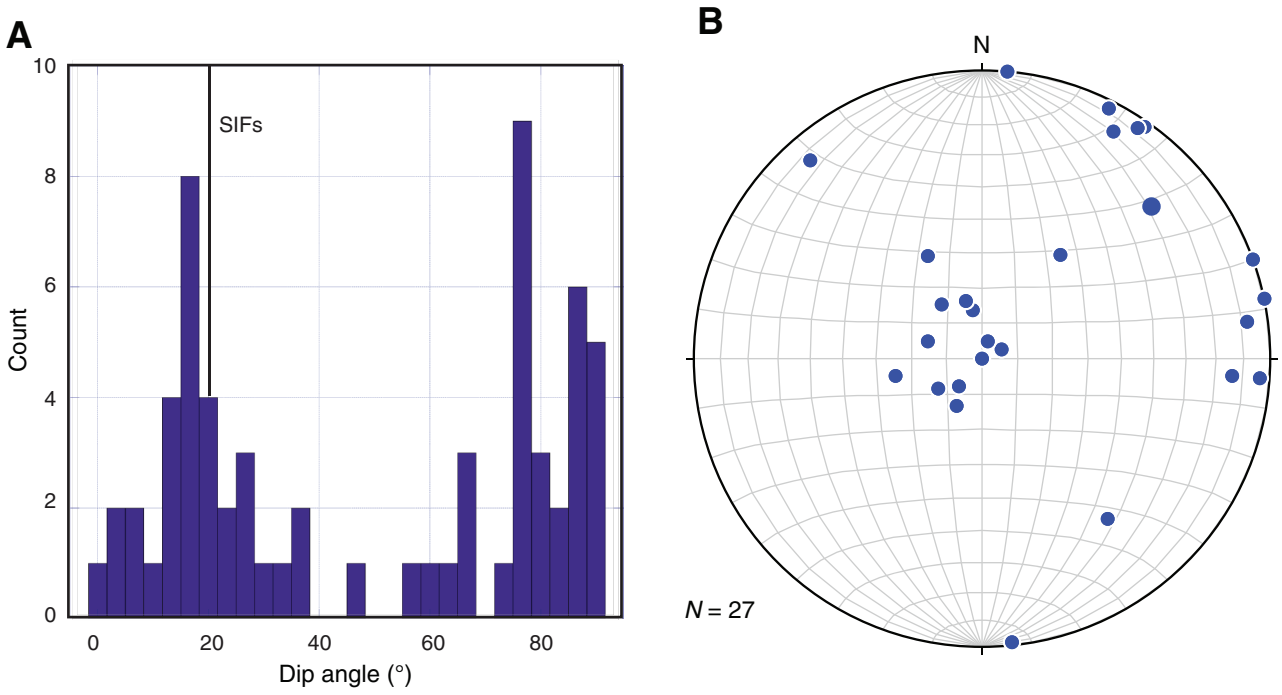

Figure F68. Downhole plot of density of subhorizontal irregular fractures (SIFs; red) and density of other, steeper fractures (blue), Hole 1256D. Zones with high SIF density coincide with the major igneous contacts.

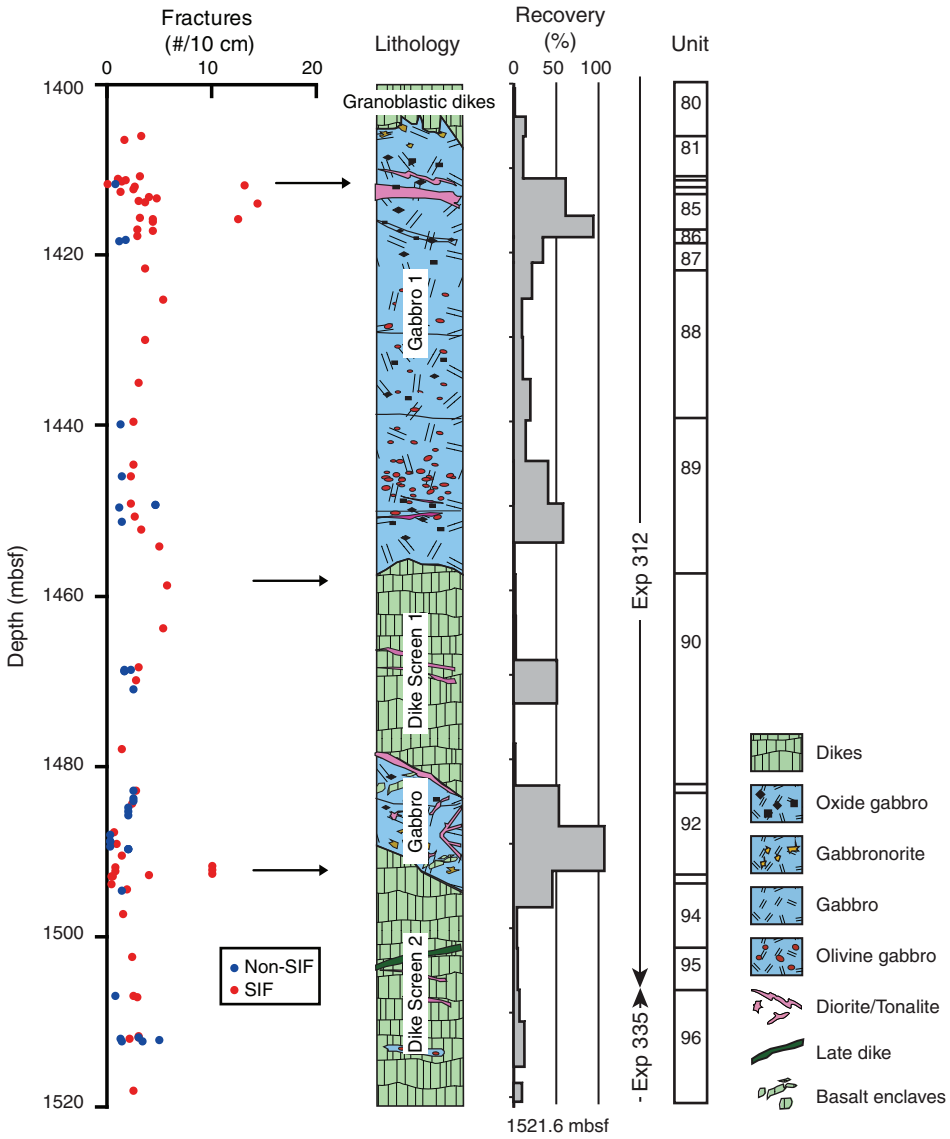

Figure F69. Photomicrographic atlas of gabbro microstructures (Sample 335(312)-U1256D-223R-2W; Thin Section 1) (cross-polarized light). **A.** Magmatic texture in an altered olivine (Ol) gabbro. **B.** Elongated plagioclase crystal in clinopyroxene (Cpx) grain. **C.** Complex plagioclase (Pl)-plagioclase boundaries with straight, embayed, and interfingered morphologies. **D, E.** Deformation twins in plagioclase grains. **F.** Radial cracks in olivine around altered inclusions.

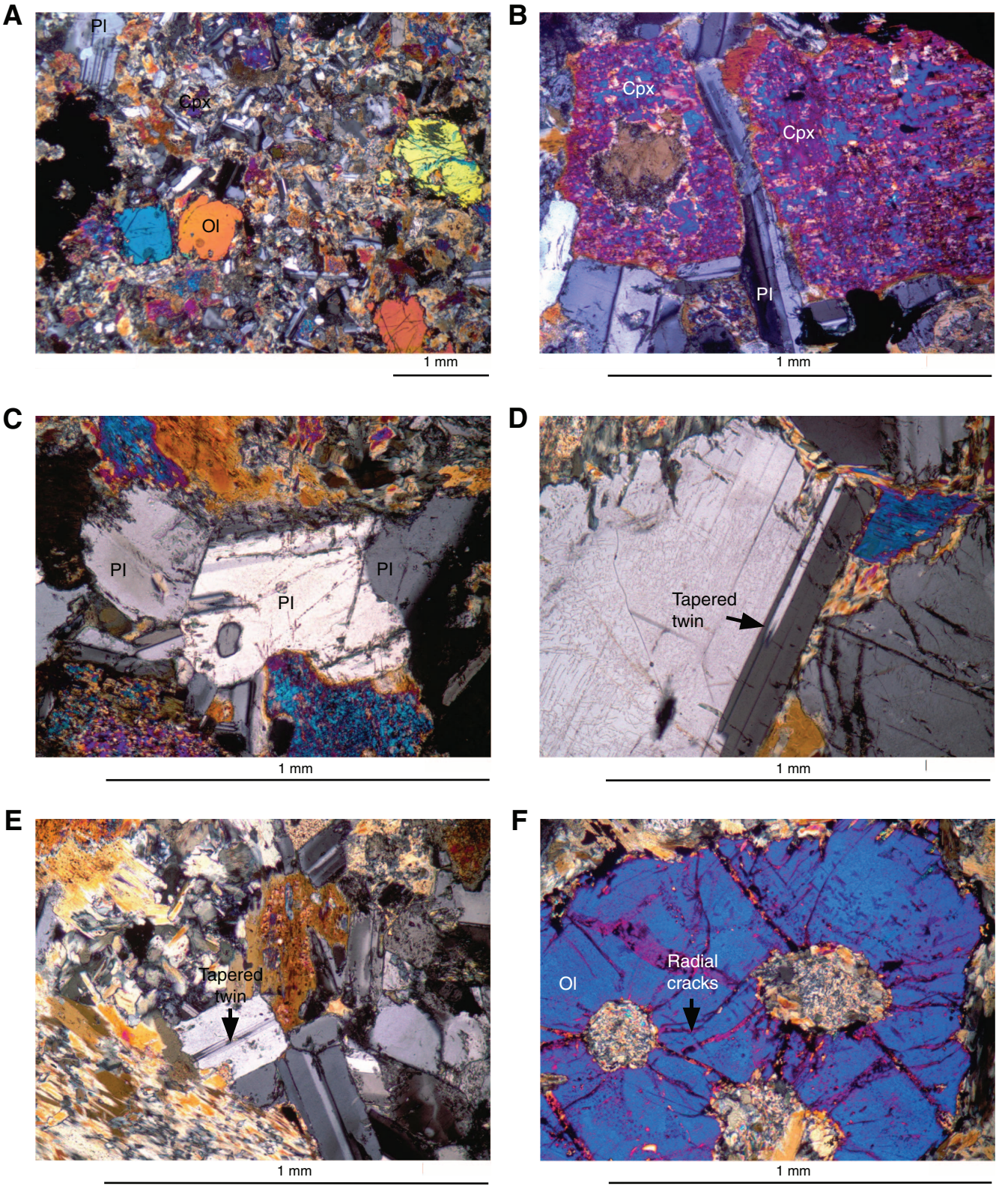

Figure F70. Photomicrographic atlas of granoblastic dike microstructures (Sample 335-U1256D-Run20-RCJB; Thin Section 37) (cross-polarized light). **A.** Equilibrated microstructure due to static recrystallization. **B, C.** Deformation twins in plagioclase grains. **D.** Deformation of elongated plagioclase grain. **E.** Banding and foliation defined by weakly aligned plagioclase laths. **F.** Submagmatic fracture and deformation twins in plagioclase grain.

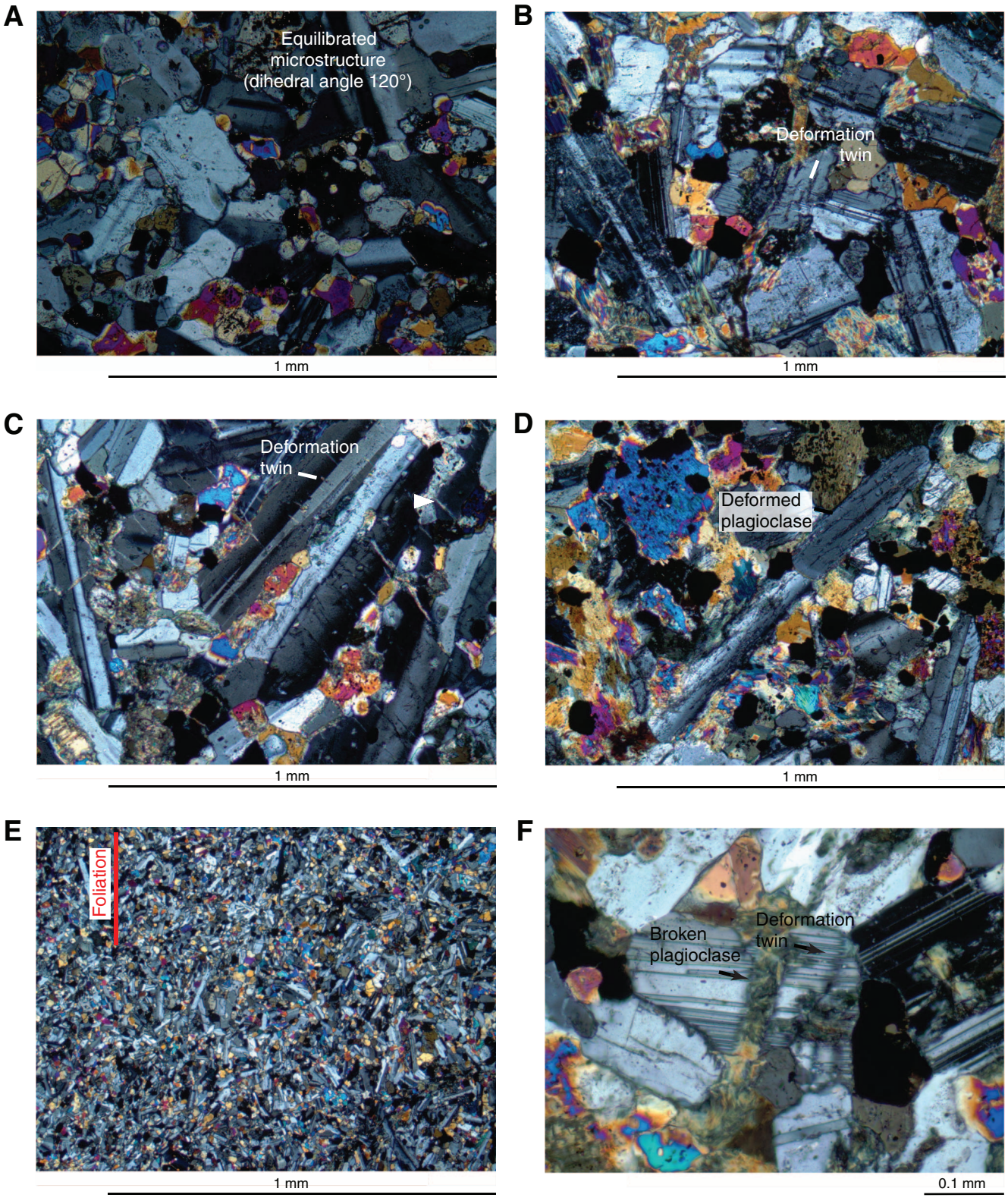

Figure F71. Foliated gabbro defined by aligned tabular plagioclase grains (Sample 335-1256D-Run12-RCJB-Rock Q; Thin Section 25). Larger plagioclase grains exhibit tapered twins, indicating crystal-plastic deformation. Finer grained plagioclase matrix has polygonal grain boundaries. **A.** Close-up image of gravel clast. **B.** Thin section image of orange box field in A exhibiting compositional banding. **C.** Photomicrograph of red box field in B.

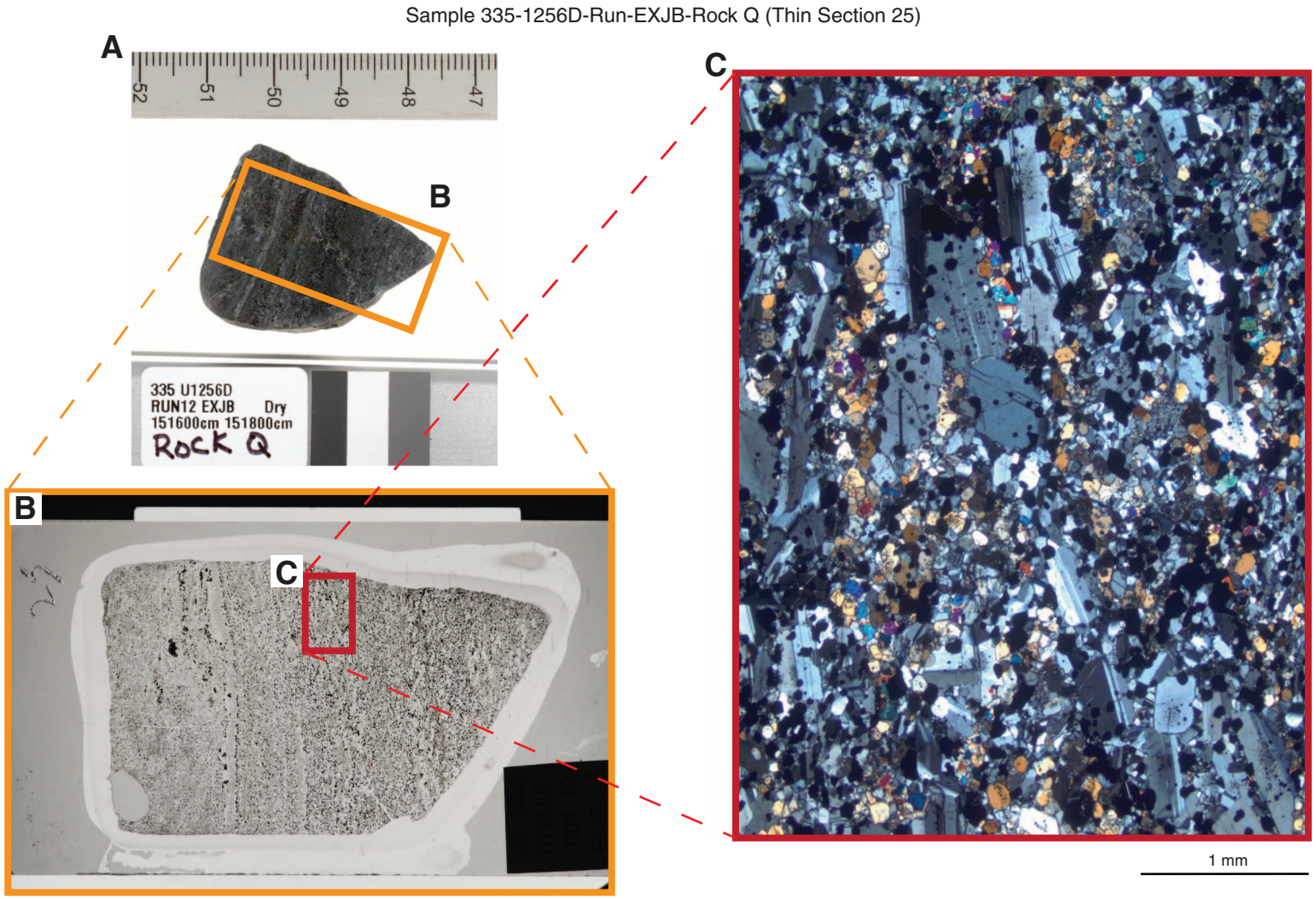

Figure F72. Complex vein network and crosscutting relationships (Sample 335-1256D-Run12-RCJB-Rock B; Thin Section 21). **A, B.** Thin section images in (A) plane-polarized and (B) cross-polarized light. **C.** Sketch of traced outline of veins. Pl = plagioclase, Cpx = Clinopyroxene, Opx = orthopyroxene. **D–F.** Photomicrographs of (D) orthopyroxene diffuse vein, (E) amphibole diffuse vein crosscutting the chilled margin of older magmatic vein, and (F, G) original magmatic (coarser grained) vein changed into amphibole vein because of hydrothermal alteration in (F) plane-polarized and (G) cross-polarized light.

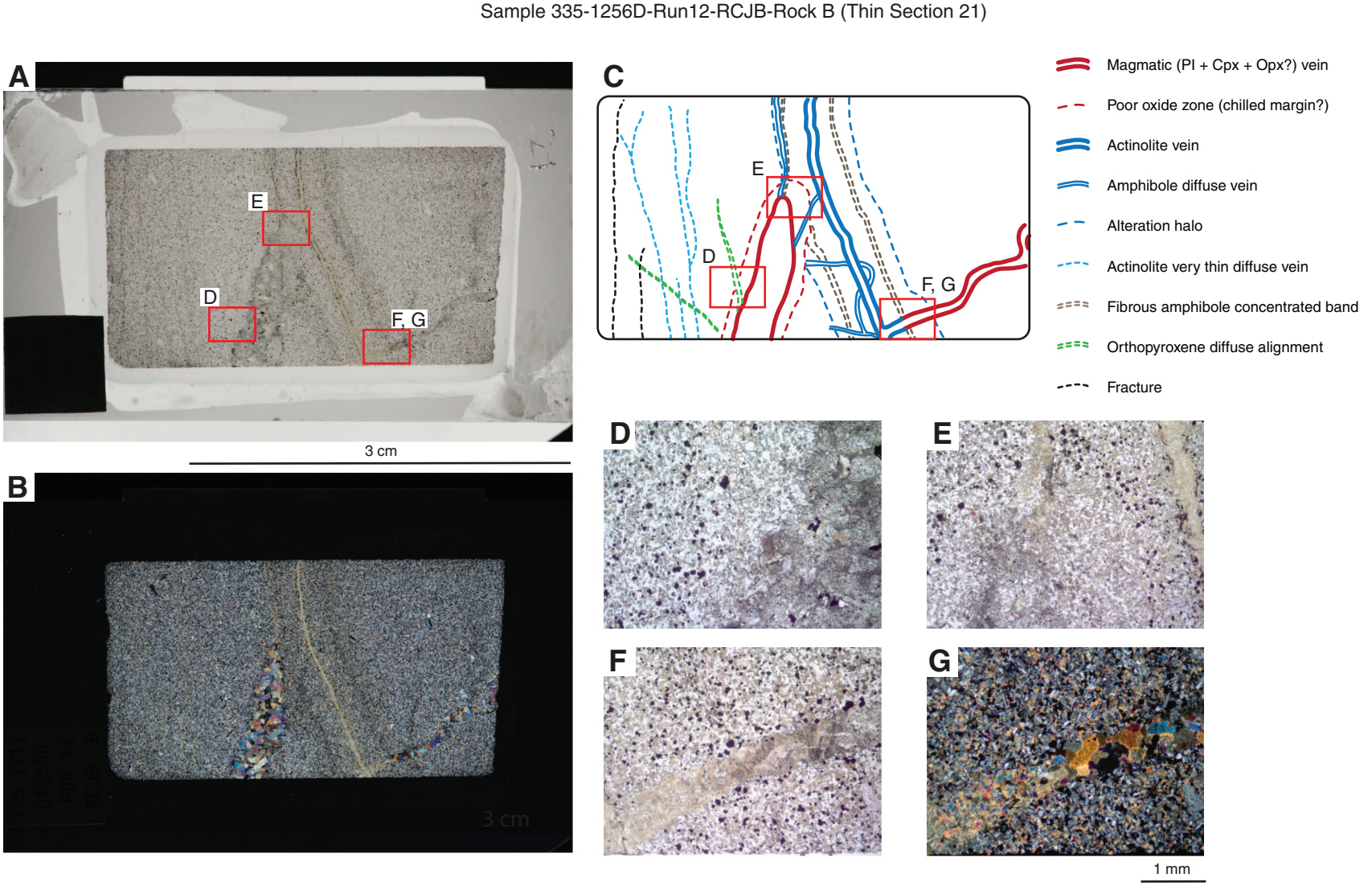

Figure F73. Photomicrographs of complex vein network and crosscutting relationships (Sample 335-1256D-Run12-RCJB-Rock C; Thin Section 22). **A, B.** Full thin section image in (A) plane-polarized and (B) cross-polarized light. **C, D.** Thick amphibole needle vein with alteration halo crosscuts the amphibole diffuse veins. **E, F.** Amphibole (Amp) vein derived from Orthopyroxene (Opx)-rich vein. Cpx = clinopyroxene, Pl = plagioclase. **G, H.** Example of a black vein crosscutting and being refracted in an amphibole vein. The crosscutting chlorite vein is represented in red for the main part of the sample and orange in the vein/alteration zone. The change in orientation is ~6° (C, D).

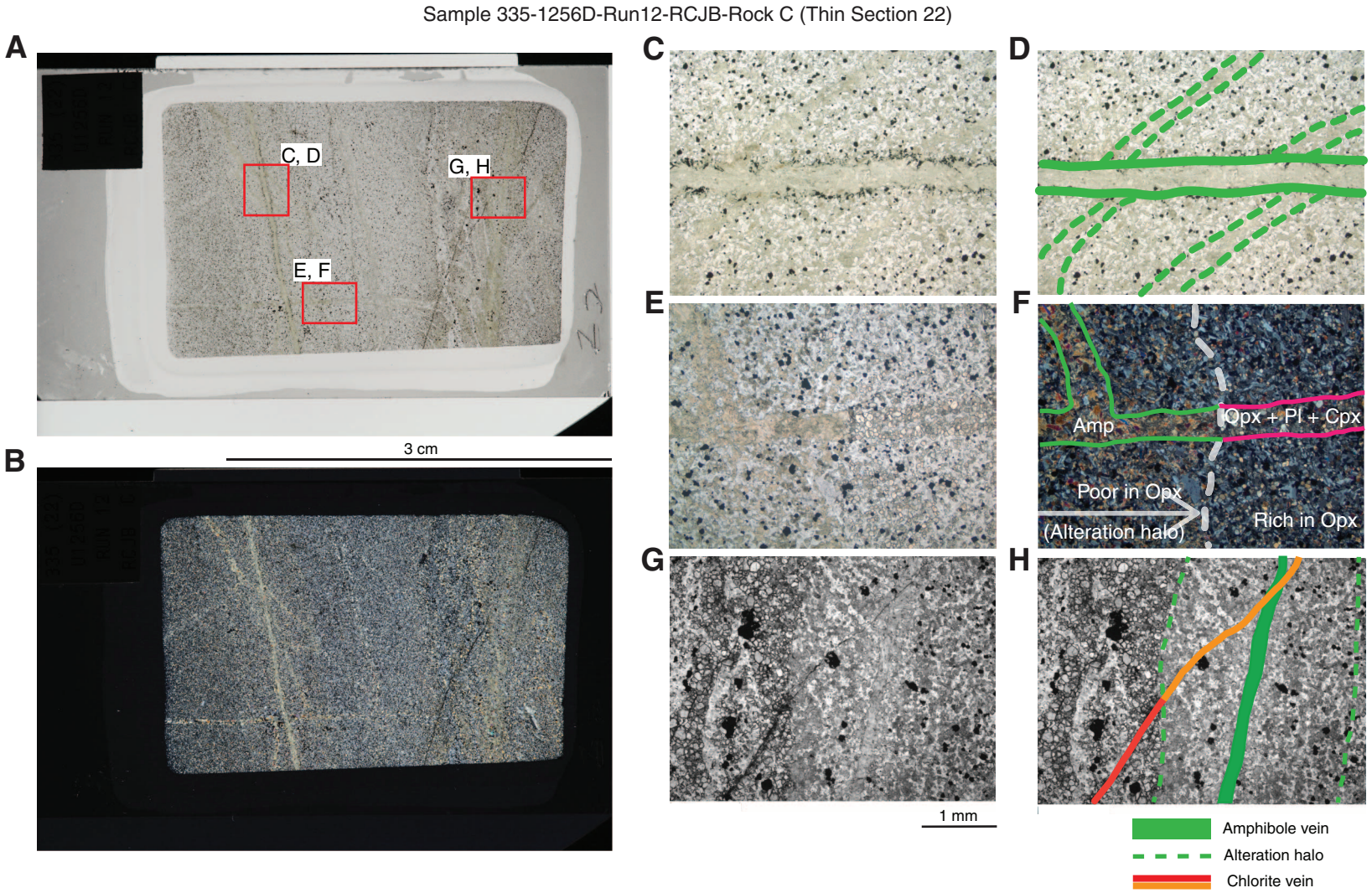

Figure F74. Photomicrographs of crosscutting relationships between green amphibole veins and actinolite-bearing thin black veins (Sample 335-1256D-238R-1, 2–4 cm; Thin Section 6). **A.** Plane-polarized light. **B.** Cross-polarized light. **C, D.** Black thin conjugate veins crosscut the amphibole vein and its alteration halos. **E, F.** Black thin veins crosscut the diffuse amphibole (partly including epidote) vein and its alteration halos.

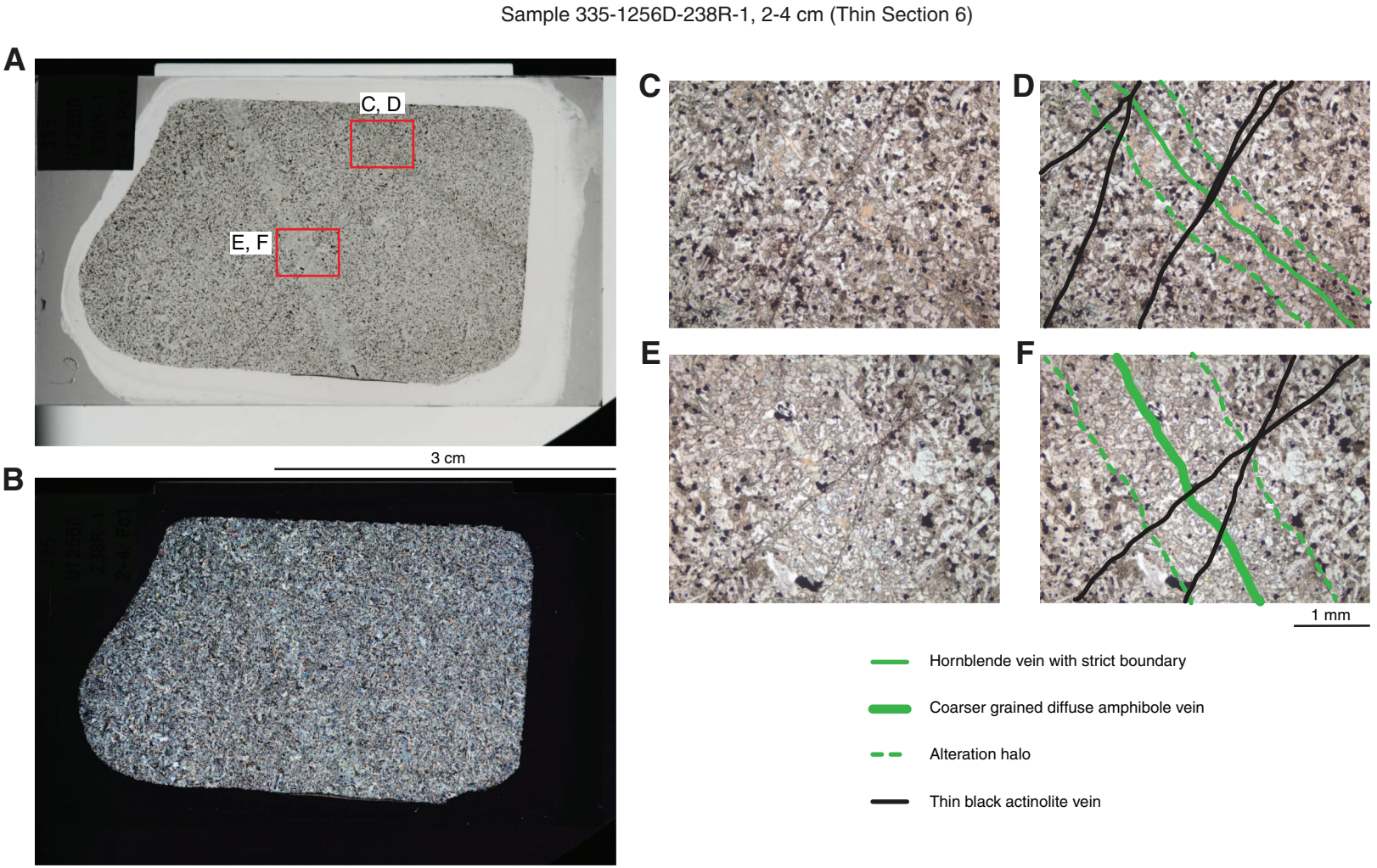

Figure F75. Several faults cut a contact between a leucrocratic material and granoblastic basaltic material but have been later mineralized with vein materials, indicating that the timing of faulting postdated the contact but was followed by a lower temperature stage of alteration (Sample 335-1256D-236R-1, 0–4 cm; Thin Section 4). The alteration halo around the contact contains evidence of semibrittle deformation. **A.** Close-up image. **B.** Hand-drawn sketch. **C, D.** Thin section images of orange box in B in (C) plane-polarized and (D) cross-polarized light. **E.** Brittle shear vein filling prehnite (V1). **F.** Prehnite diffuse vein crosscuts the amphibole vein. **G.** Amphibole vein crosscuts the prehnite vein.

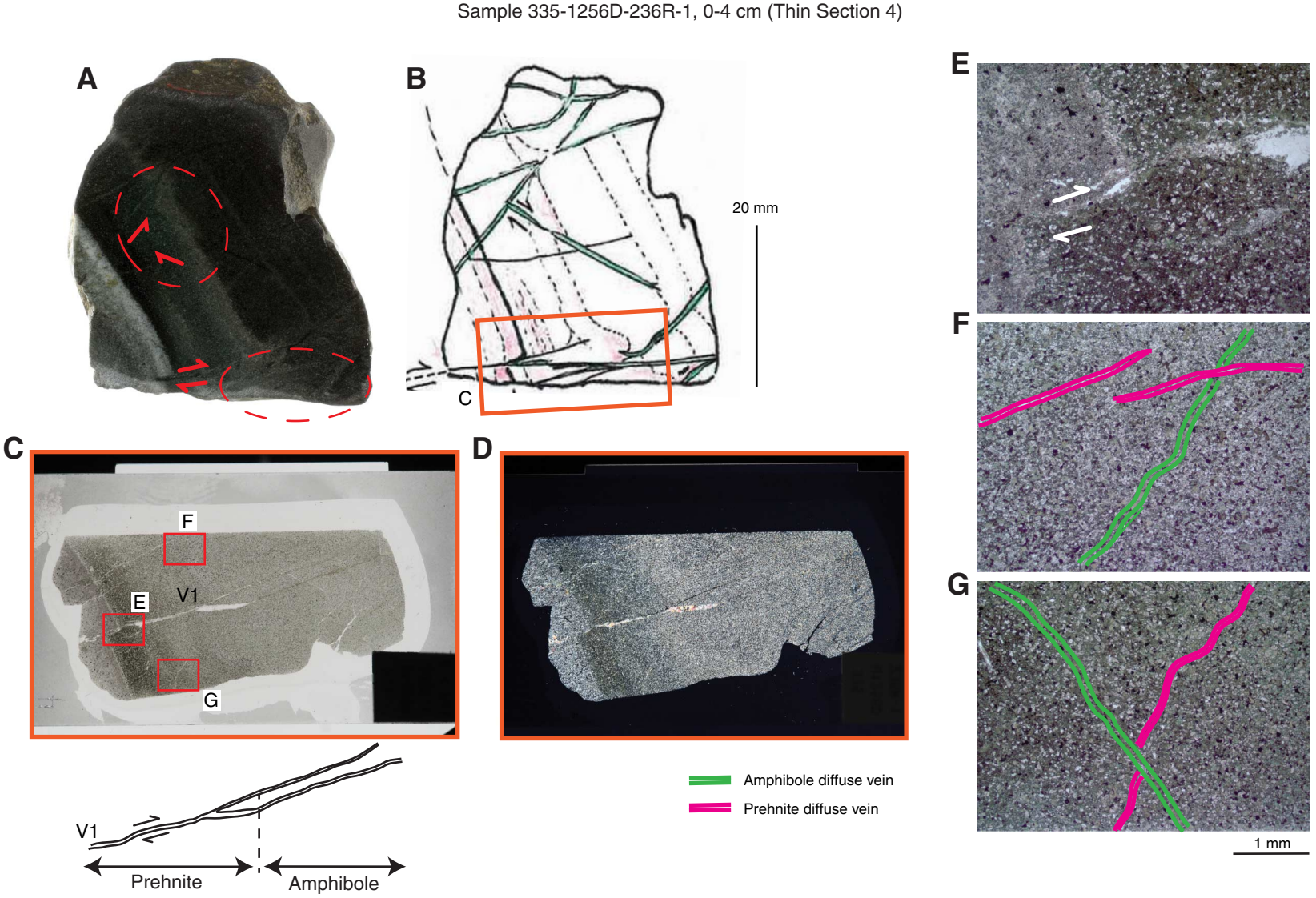

Figure F76. Shear veins with chlorite mineralization and slickenlines observed in interval 335-1256D-236R-1, 34–62 cm (Pieces 6–9). (**A**) Photographs and (**B**) sketches of adjacent pieces containing similar veins, illustrating the possible relationship of these features. Pieces 8 and 9 are unoriented, so the inferred vein relationship between pieces is tentative. **C.** Diagram of orientation of shear veins in Piece 8 in the core reference frame. **D.** Reflected light photomicrograph of chlorite slickenlines (arrow) along vein surface.

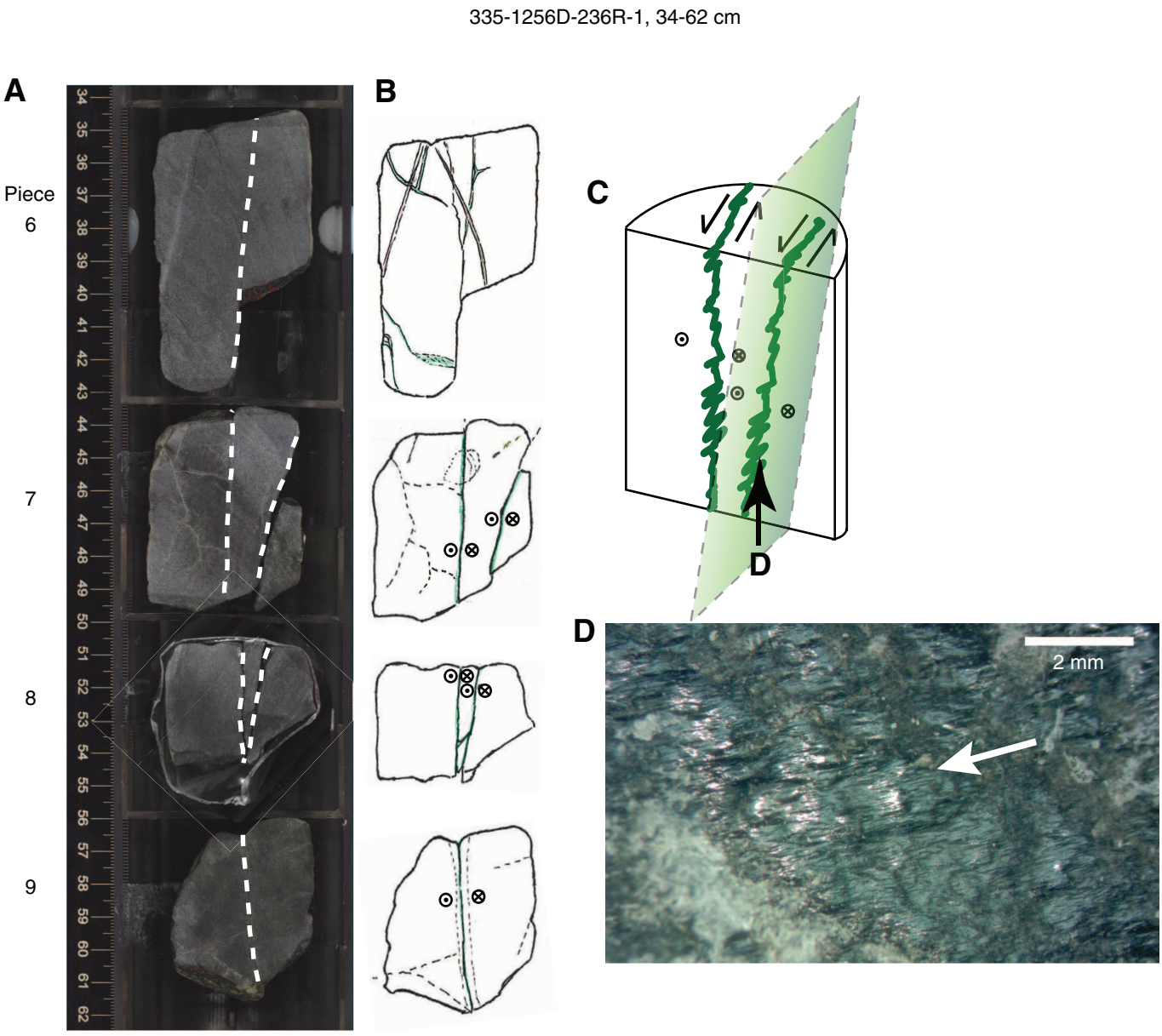

Figure F77. Results of alternating field (AF) demagnetization experiments. **A.** AF demagnetization of an archive half core piece using the in-line demagnetizing coils of the superconducting rock magnetometer (SRM) system (Sample 312-1256D-231R-3A, 54 cm). Natural remanent magnetization (NRM) to 40 mT data from shipboard measurements performed during Expedition 312; 40–80 mT data from measurements performed during Expedition 335. **B.** AF demagnetization of the equivalent working half piece (0–80 mT; Sample 335(312)-1256D-231R-3W, 54 cm) performed entirely during Expedition 335.

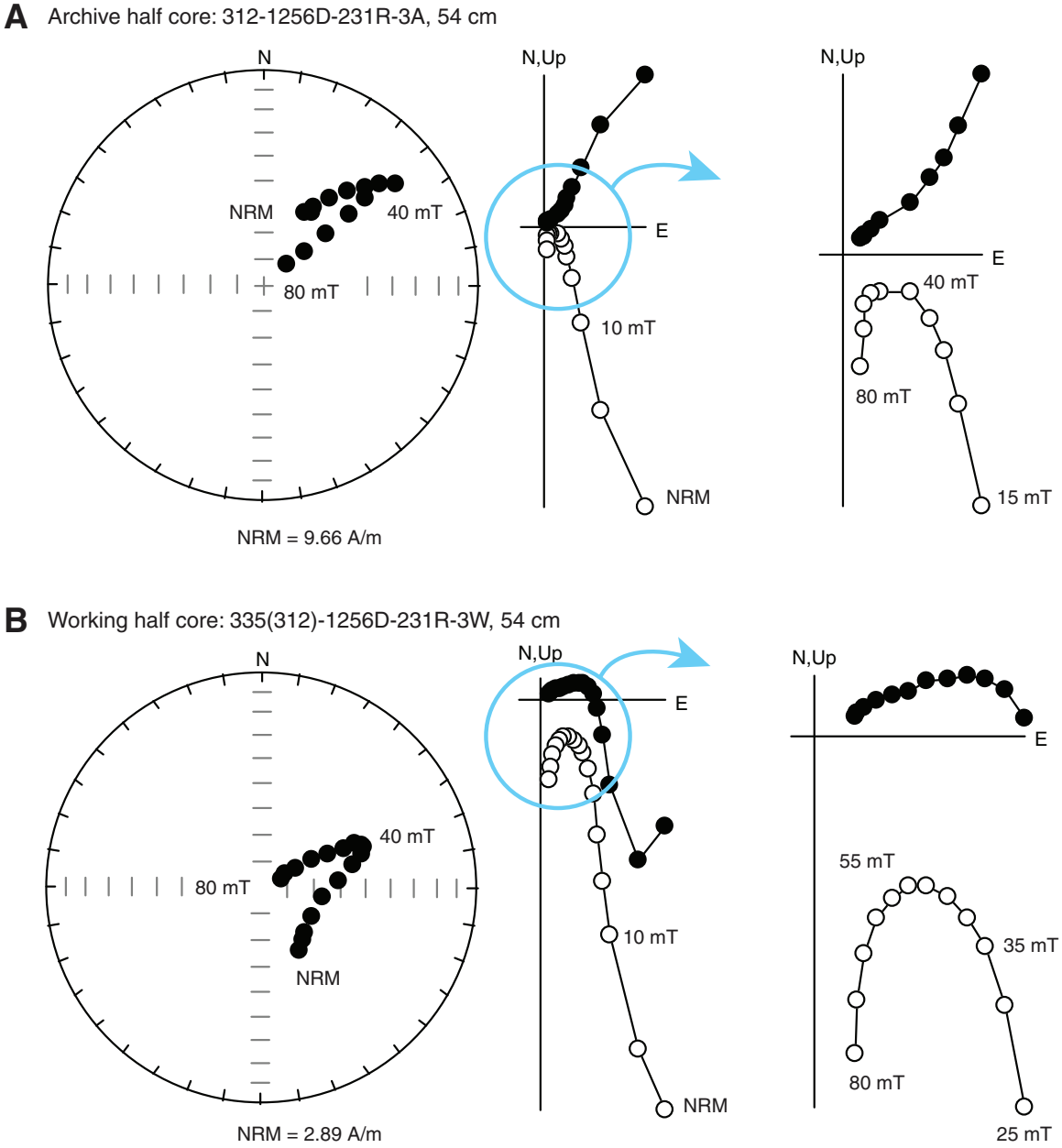

Figure F78. Results of alternating field demagnetization of the single archive half core piece recovered during Expedition 335 that exceeded the minimum acceptable length of 10 cm for analysis using the superconducting rock magnetometer (SRM) system. Note that data from demagnetization treatments above 60 mT are omitted for clarity and showed progressive steepening of inclination due to acquisition of spurious laboratory-induced remanence. NRM = natural remanent magnetization.

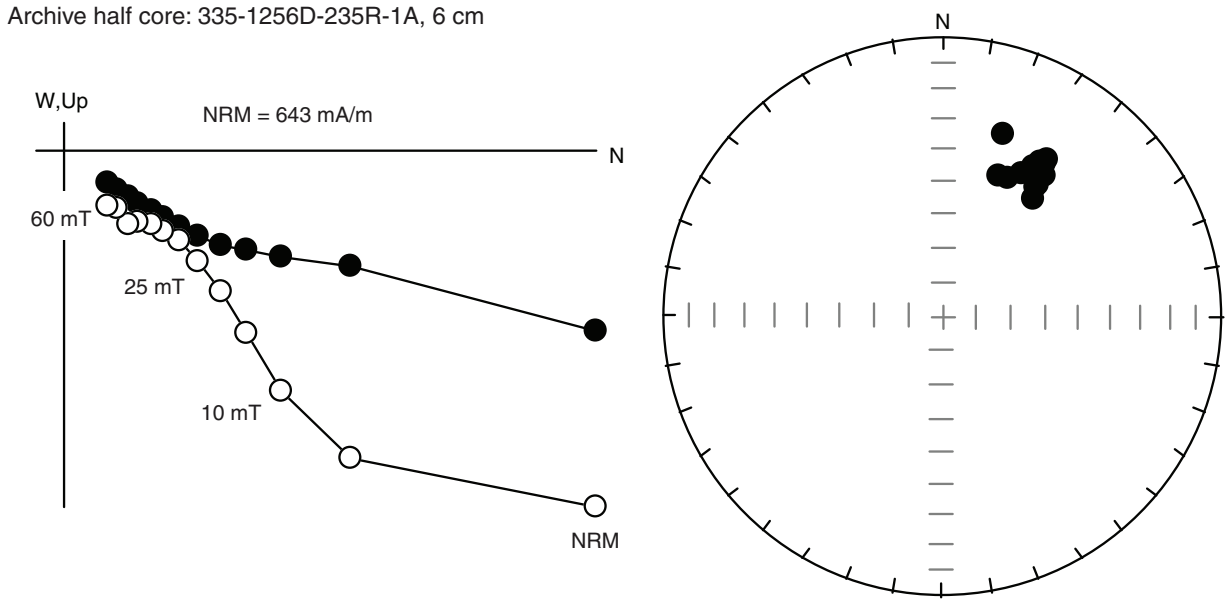

Figure F79. Orthogonal vector plots of alternating field (AF) demagnetization data from discrete samples prepared during Expedition 335 from working half core sections recovered during Expedition 312. Data were measured using the AGICO JR-6A spinner magnetometer and demagnetized using the DTech D-2000 system. Expanded views of Samples 335(312)-1256D-222R-1W, 13 cm, and 223R-2W, 6 cm (blue arrows), show details of characteristic remanence components isolated after removal of drilling-induced components by low AF treatments. Note removal of significant vertical drilling-induced remanence by low-temperature demagnetization (77 K step) in Sample 231R-3W, 53 cm. Solid circles = projection onto the horizontal plane, open circles = projection onto either the vertical north–south or east–west planes. NRM = natural remanent magnetization.

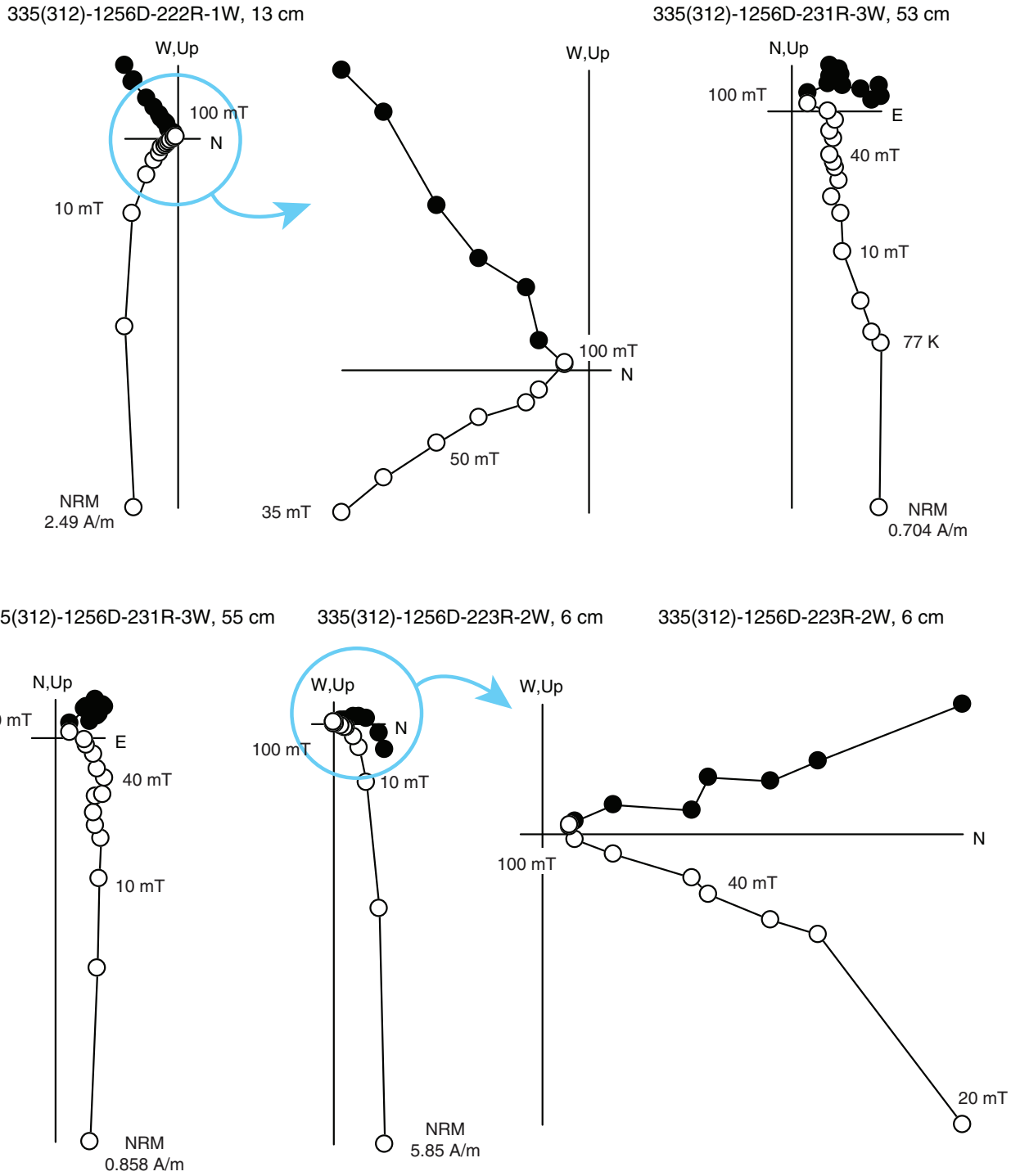

Figure F80. Orthogonal vector plots of thermal demagnetization data from discrete samples prepared during Expedition 335 from working half core sections recovered during Expedition 312. Data were measured using the AGICO JR-6A spinner magnetometer and demagnetized using the Schonstedt TSD-1 system. Expanded views (blue arrows) show details of characteristic remanence components isolated after removal of drilling-induced components. Solid circles = projection onto the horizontal plane, open circles = projection onto either the vertical north–south or east–west planes. NRM = natural remanent magnetization. **A.** Samples from Gabbro 1. Note removal of significant vertical drilling-induced remanence by low-temperature demagnetization (77 K step) in Sample 335(312)-1256D-222R-2W, 47 cm. (Continued on next page.)

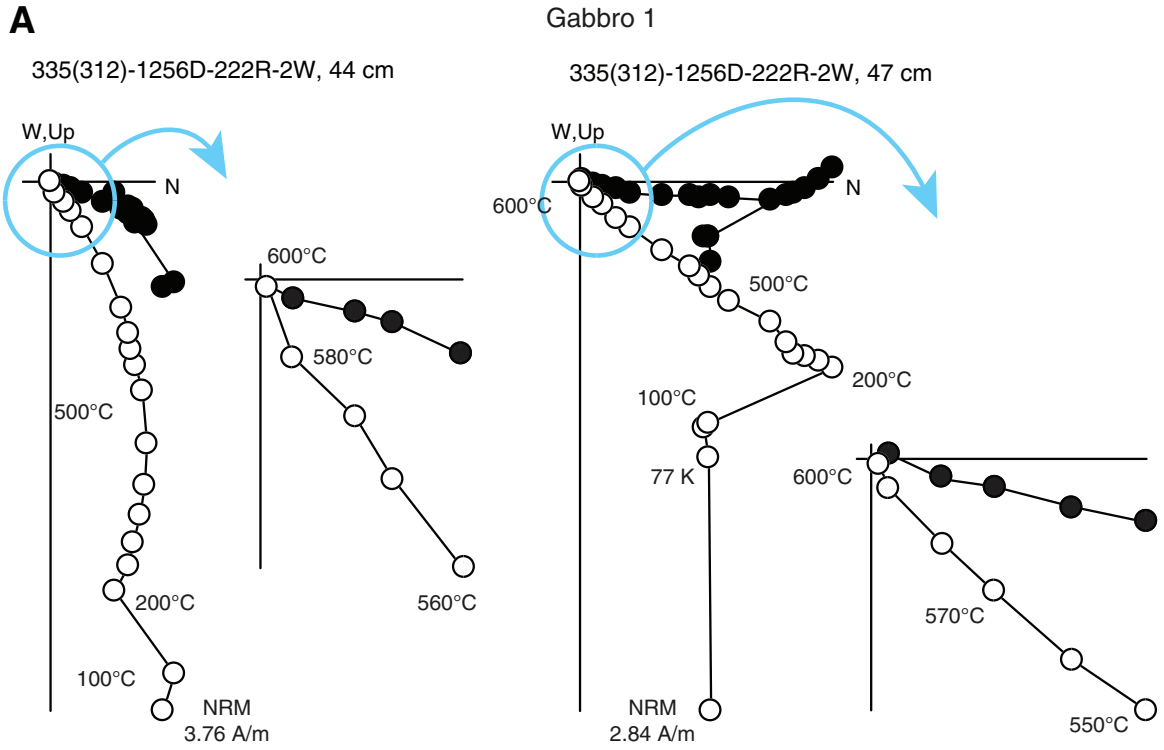

Figure F80 (continued). B. Samples from Gabbro 2. Note the presence of a clear multicomponent remanence structure in Sample 335(312)-1256D-231R-1W, 115 cm, with a negative inclination component that unblocks between 200° and 500°C and a positive inclination component that unblocks between 500° and 580°C.

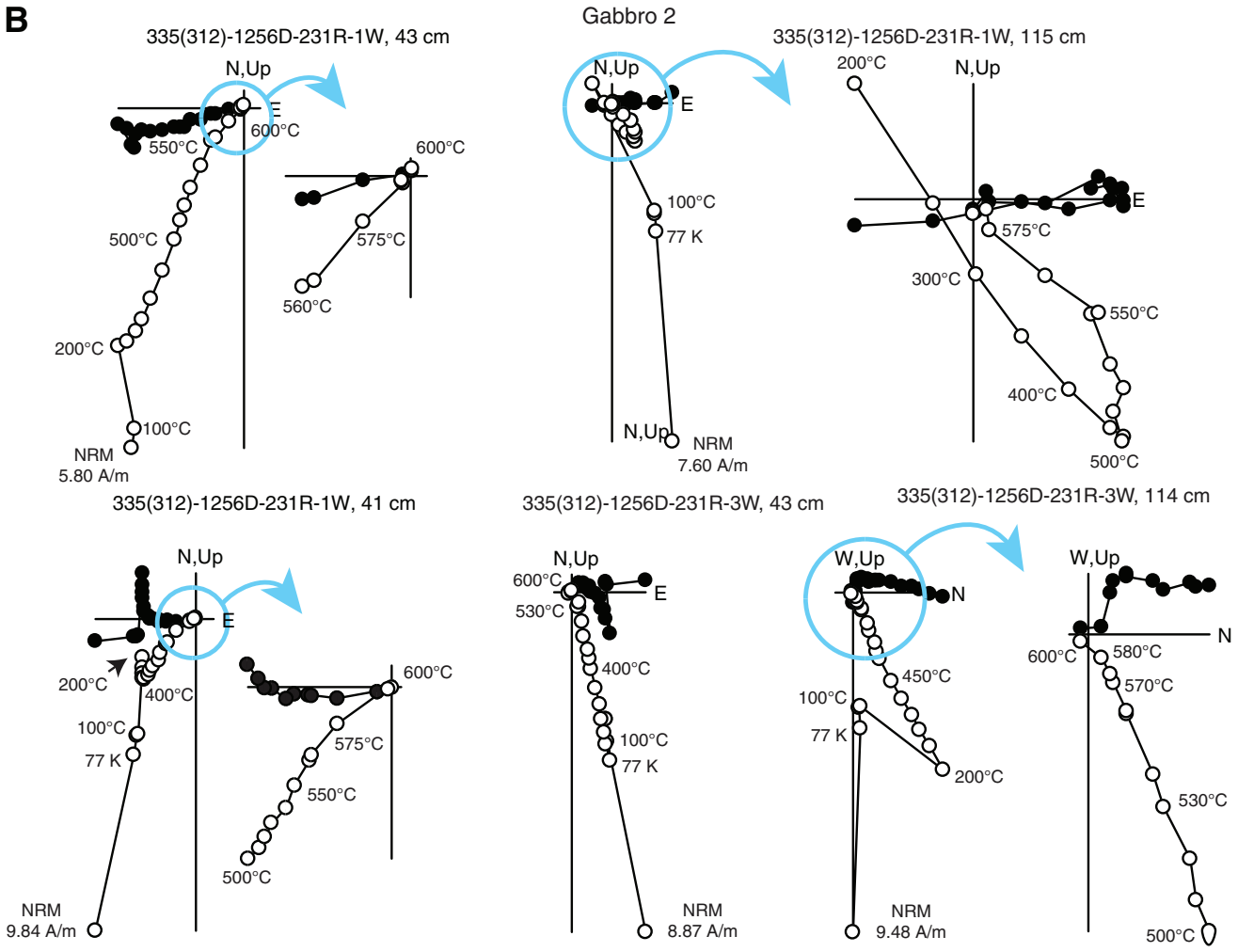

Figure F81. Equal-area stereographic projections showing remanence components in discrete samples distributed downhole from the top of Gabbro 1 (IODP core reference frame). **A.** Natural remanent magnetization (NRM) directions. **B.** Steep, low-coercivity/low-unblocking temperature components inferred to represent drilling-induced remanent magnetizations. **C.** High-coercivity/high-unblocking temperature characteristic remanence (ChRM) directions calculated from principal component analysis of alternating field and thermal demagnetization data. Note the spread of ChRM directions resulting from the lack of azimuthal control on the orientation of core pieces. Data represent a compilation of measurements on discrete samples taken from Expedition 312 core sections, from shipboard analyses conducted during Expedition 335 by Y.-M. Kim and A. Morris, and from shore-based analyses conducted by D. Wilson and R. Anma.

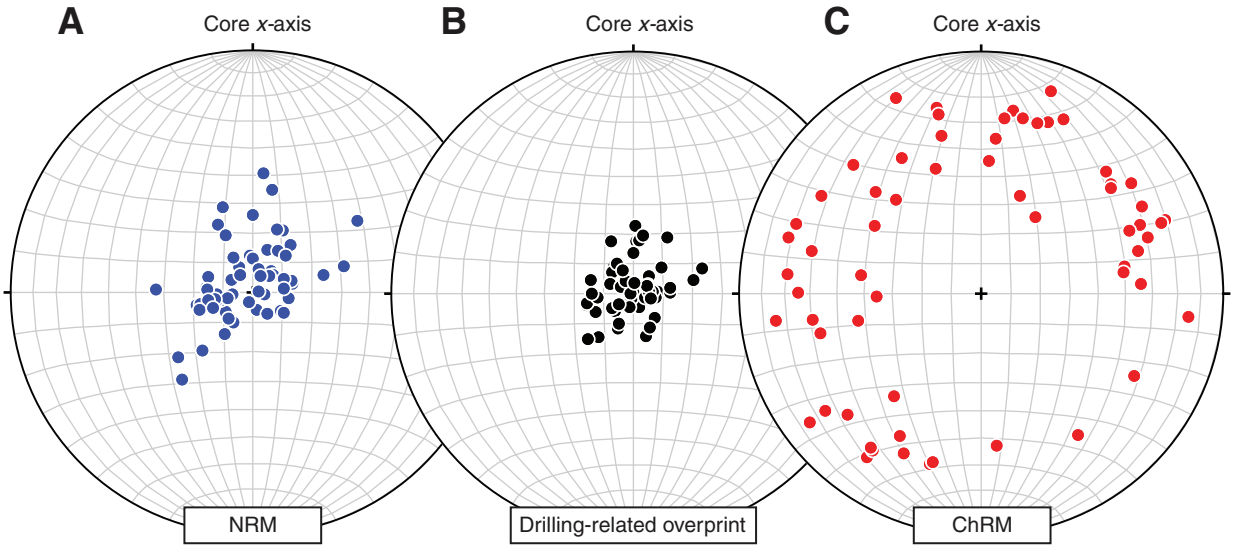

Figure F82. Plot of downhole variations in magnetic properties in Hole 1256D from the top of Gabbro 1. **A.** Summary of core recovery and lithostratigraphic units. **B.** Low-field magnetic susceptibility. Purple symbols = Section Half Multisensor Logger point susceptibility data, green symbols = Whole-Round Multisensor Logger loop susceptibility data. **C.** Natural remanent magnetization (NRM; blue symbols) and characteristic remanent magnetization (ChRM; red symbols) intensities from discrete samples. **D.** NRM (blue symbols) and ChRM (red symbols) inclinations from discrete samples. Green symbols = average ChRM inclinations for core pieces where multiple discrete samples are available. Pink vertical bar = mean ChRM inclination calculated using the maximum likelihood method of Arason and Levi (2010).

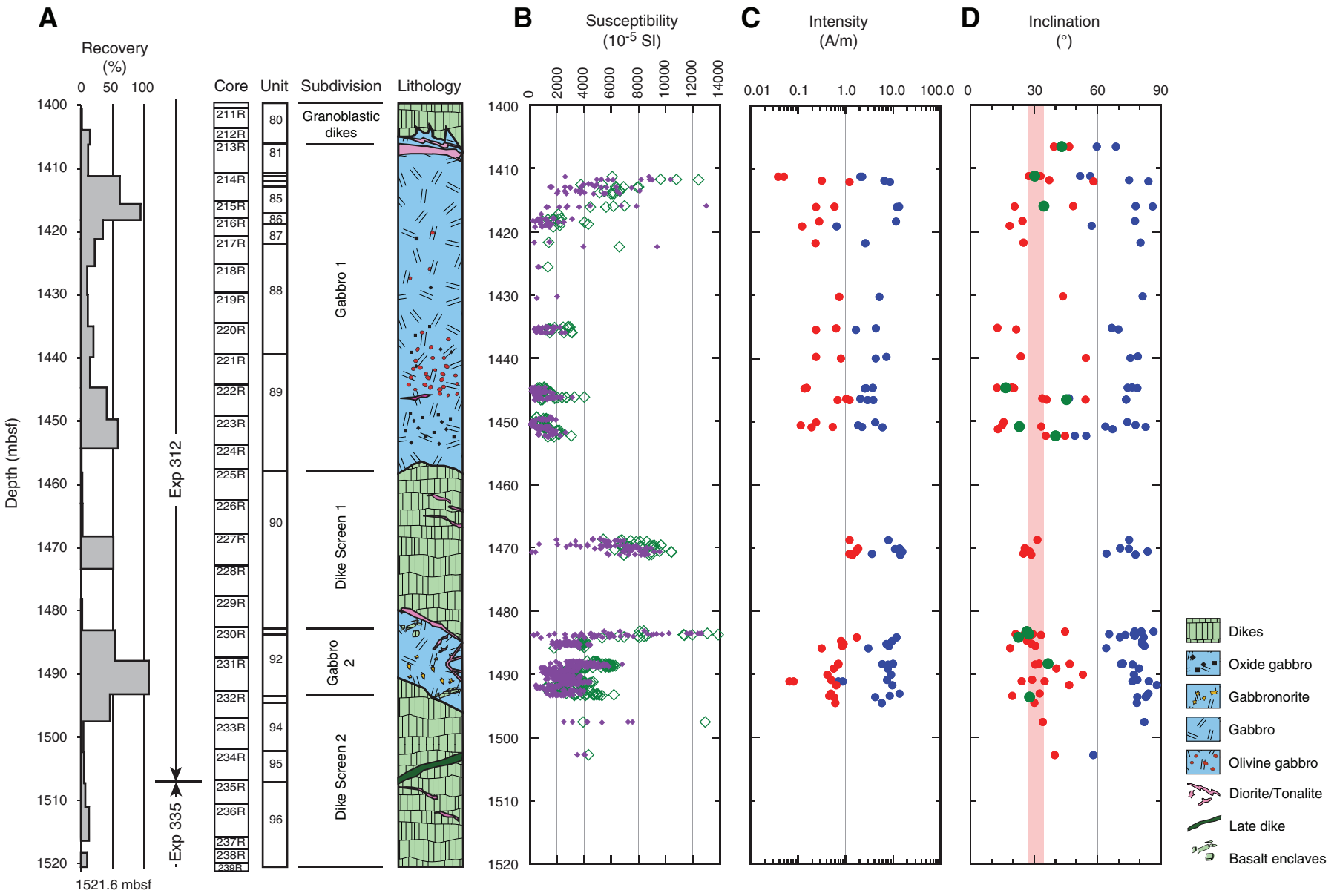

Figure F83. Plot of the ratio of the intensity of the drilling-induced remanent magnetization (DIRM) and the vector difference sum of the demagnetization path (VDS) against the inclination of the characteristic remanent magnetization (ChRM) for discrete samples from core sections from the top of Gabbro 1 downhole to the bottom of Hole 1256D. High values of DIRM/VDS indicate a remanence dominated by the drilling-induced component. Note the lack of systematic relationship between this parameter and ChRM inclination.

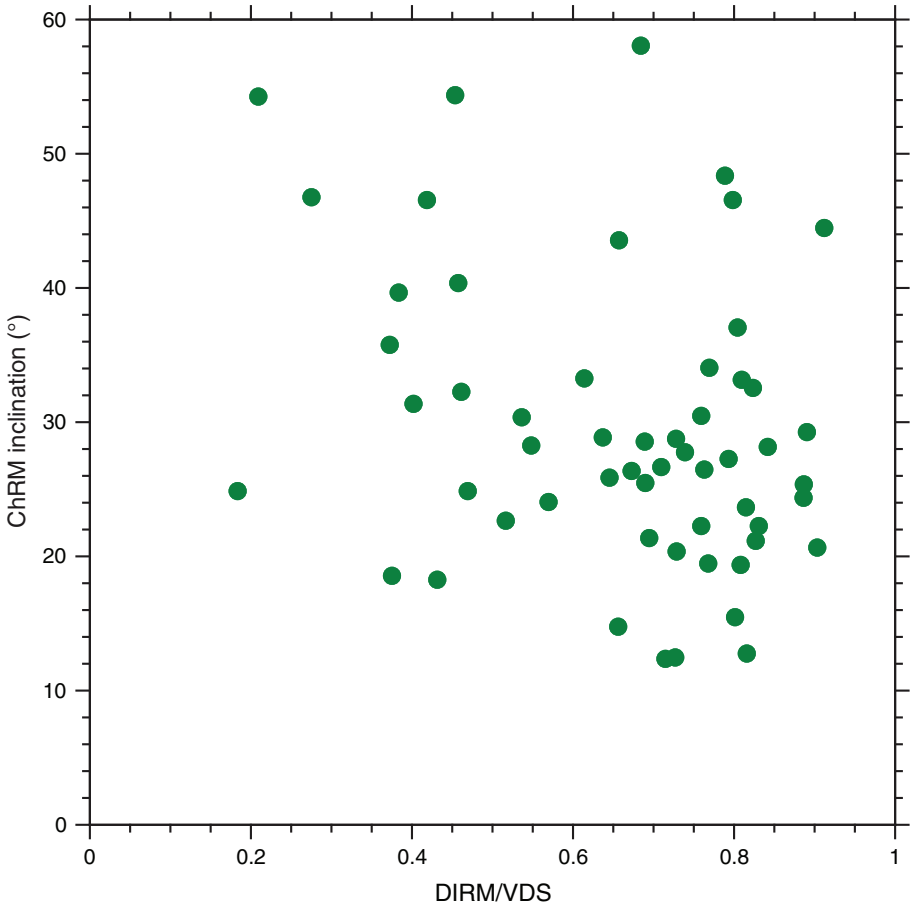

Figure F84. Equal-area stereographic projections showing instantaneous geomagnetic field directions calculated from 1000 realizations of the statistical field model TK03.GAD of Tauxe and Kent (2004) for the location of Hole 1256D. The distribution of these vectors predicts the variability of geomagnetic field directions at the site due to paleosecular variation. **A.** Data in the geographic reference frame. **B.** Data after rotation of the geocentric axial dipole direction to the vertical, demonstrating the north–south elongation in the distribution of predicted geomagnetic field directions. Data calculated for a normal polarity field only for clarity. Closed/open symbols indicate points on the lower/upper hemispheres, respectively.

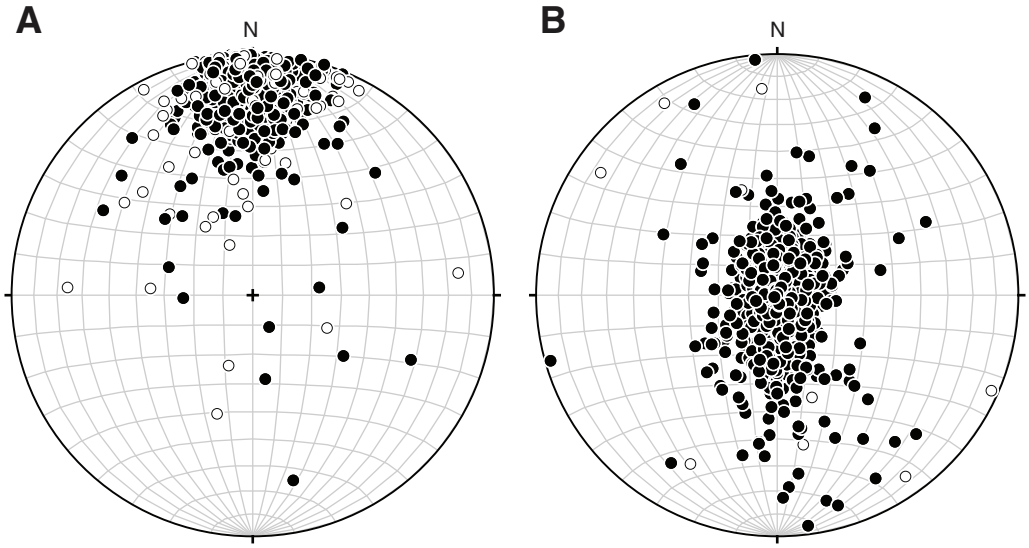

Figure F85. Equal-area stereographic projection demonstrating the potential effect of tectonic tilting on originally horizontal, normal, and reversed remanence directions, Hole 1256D. Purple line = locus of remanence directions resulting from tilting around a horizontal rotation axis trending 340° (parallel to the reconstructed trend of the East Pacific Rise at 14 Ma; Wilson, Teagle, Acton, et al., 2003), with numbers indicating the amount of tilting in degrees. Dashed lines = lines of equal inclination. Note that steepening of the remanence by 10° requires tectonic rotation >20°.

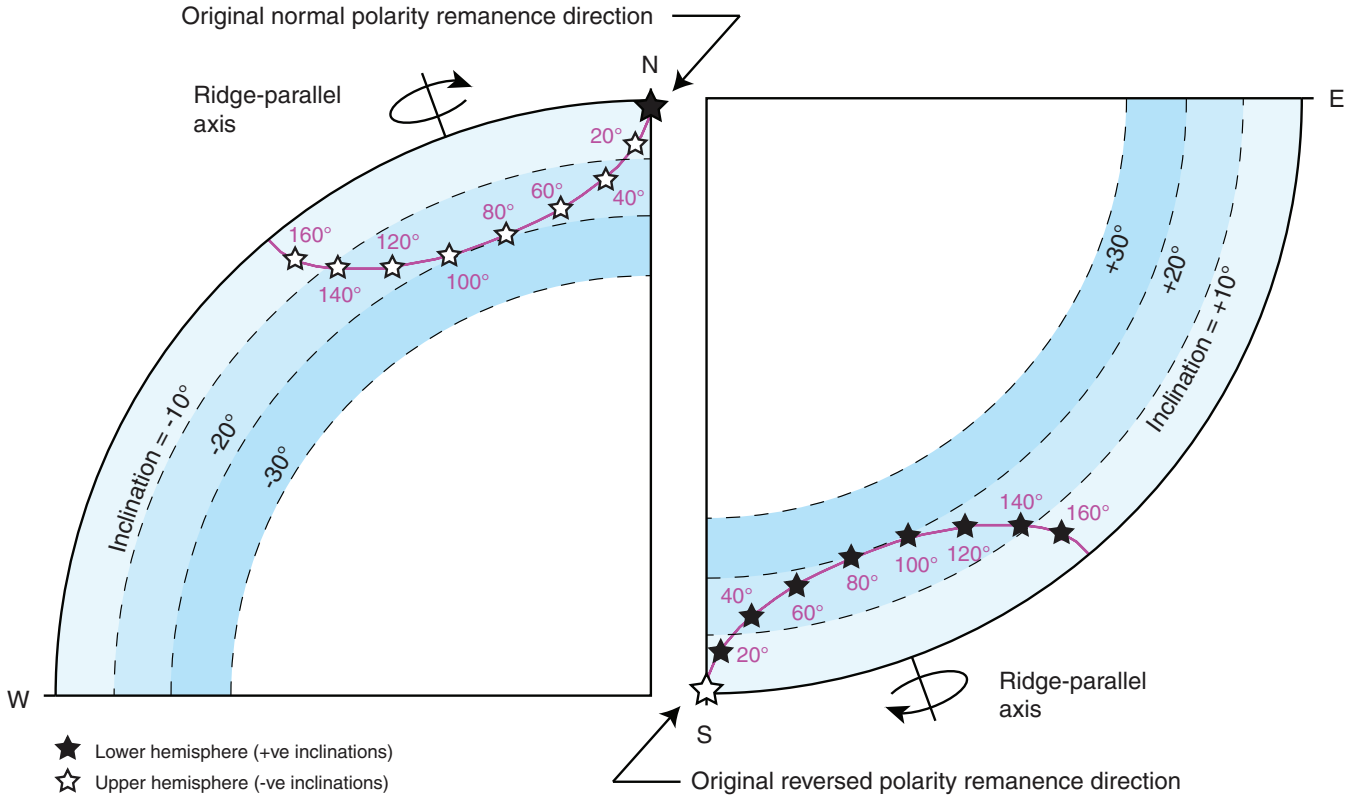

Figure F86. Log-log plot of natural remanent magnetization (NRM) and susceptibility of discrete samples from Hole 1256D (top of Gabbro 1 downward). Distribution of values compared to lines of constant *Q* (Königsberger ratio of remanent to induced magnetization; calculated for field of 27 A/m) shows that remanence is substantially greater than induced magnetization in most samples.

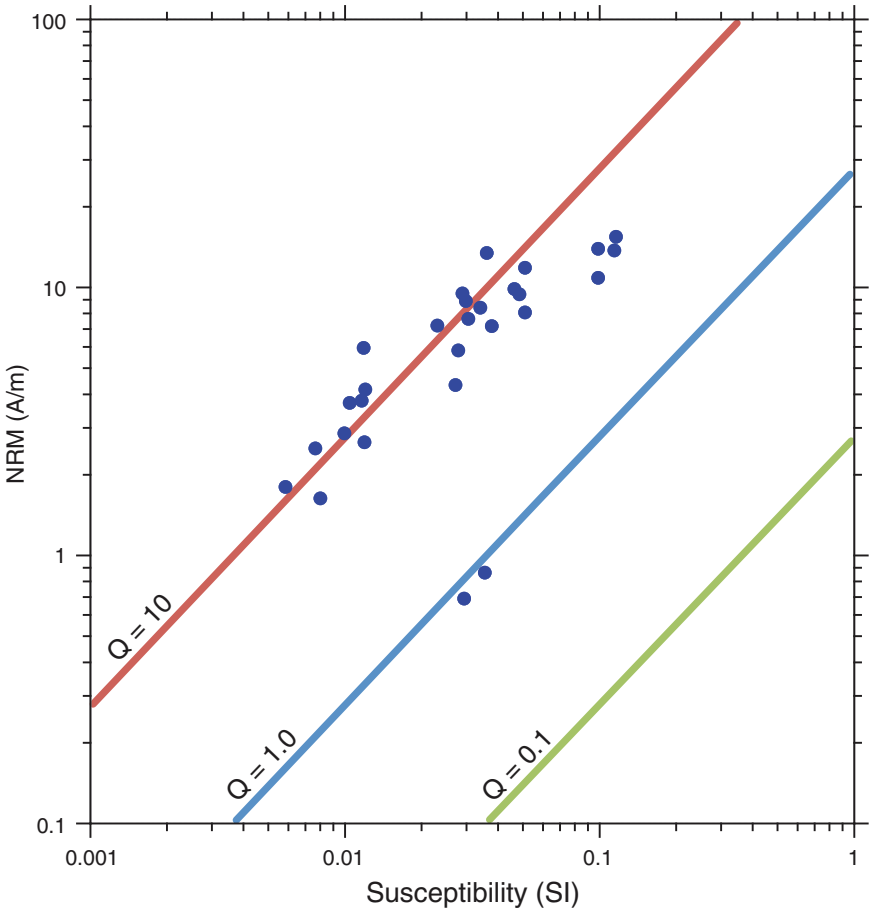

Figure F87. Summary plots of anisotropy of low-field magnetic susceptibility (AMS) data from discrete samples from Hole 1256D (top of Gabbro 1 downward). **A.** Data in the azimuthally unoriented IODP core reference frame. **B.** Data after restoration of characteristic remanent magnetization (ChRM) declinations to a common north (i.e., ignoring potential effects of paleosecular variation on the distribution of ChRMs). **C.** Samples with prolate AMS fabrics. **D.** Samples with oblate AMS fabrics. **E.** Jelinek plot of corrected anisotropy degree against shape parameter for all samples.

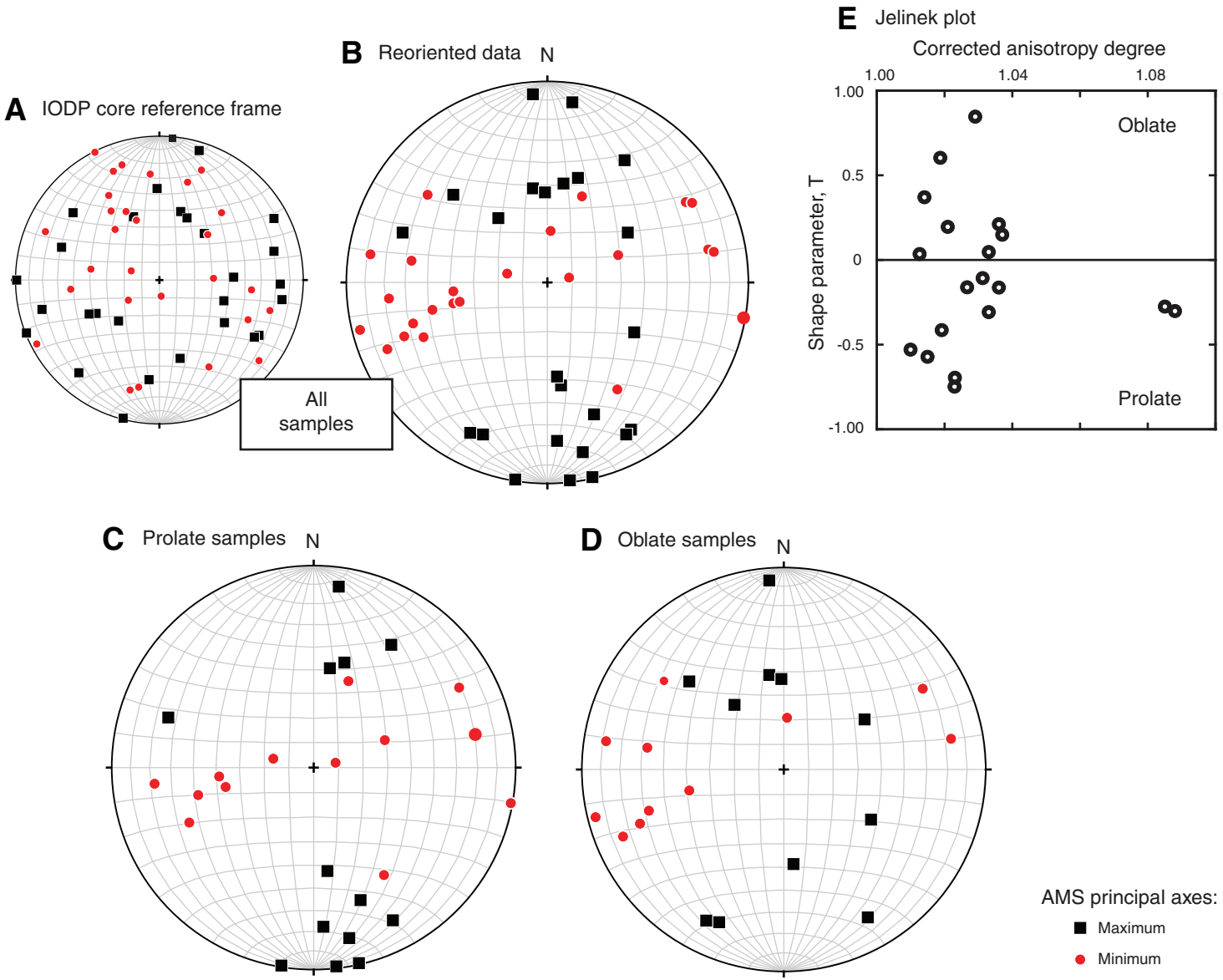

Figure F88. Downhole summary of Expedition 335(312) archive section half and Expedition 335 whole-round sections measured by Whole-Round Multisensor Logger (WRMSL), Section Half Multisensor Logger (SHMSL), and Natural Gamma Radiation Logger (NGRL). Pale symbols show the raw data; points with strong colors are the results after data culling for gaps between pieces. NGR = natural gamma radiation, GRA = gamma ray attenuation.

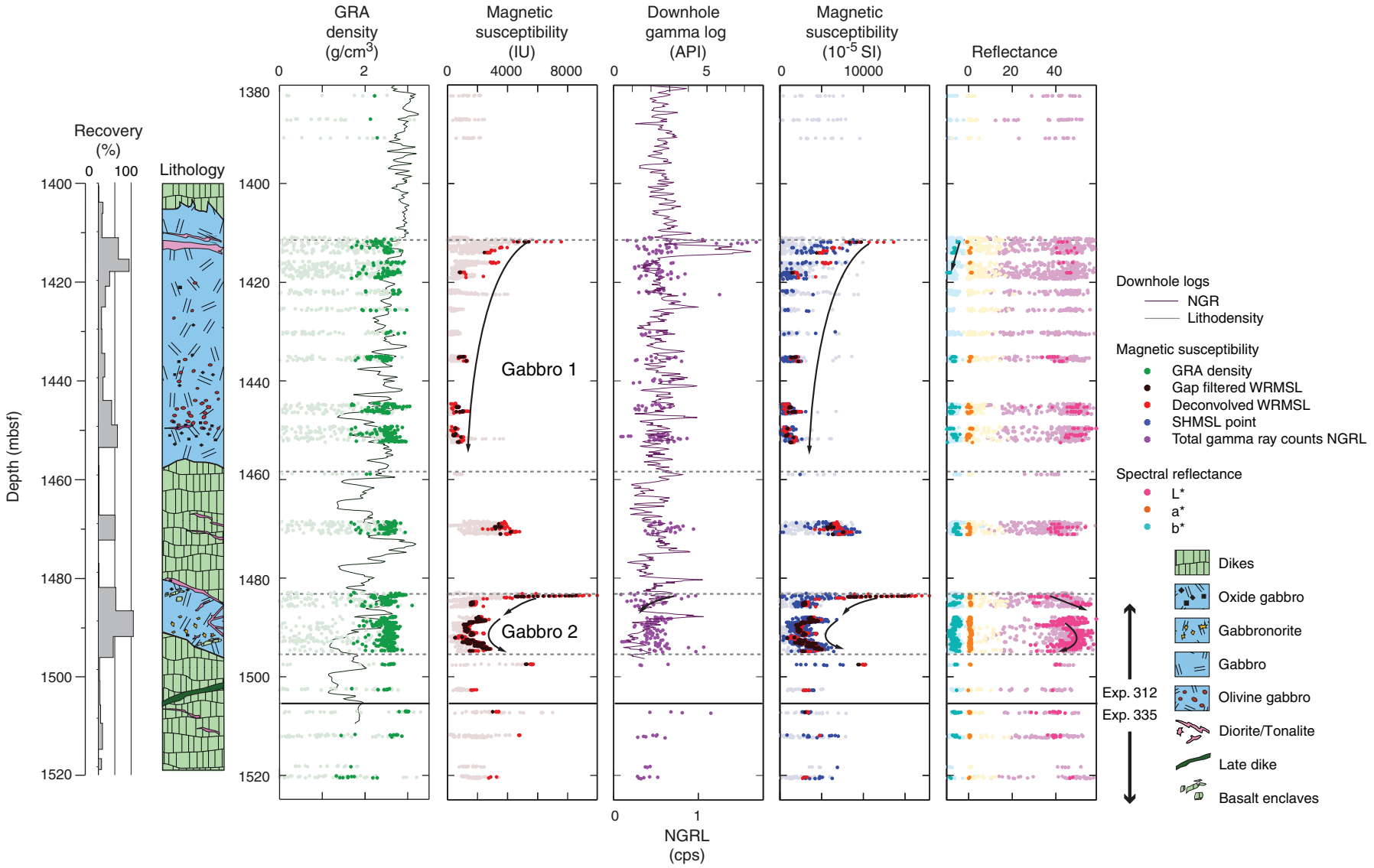

Figure F89. Results from the Natural Gamma Radiation Logger (NGRL) and observed concentrations of K, Th, and U measured after Expedition 312 (Gao et al., 2009; Neo et al., 2009; Yamazaki et al., 2009). **A.** Total counts from the NGRL. **B.** Counts in the K window and measured K_2O (wt%). **C.** Counts in the U window (cps) and U concentrations (ppm). **D.** Counts in the Th window and Th concentrations (ppm). Note the scales are different.

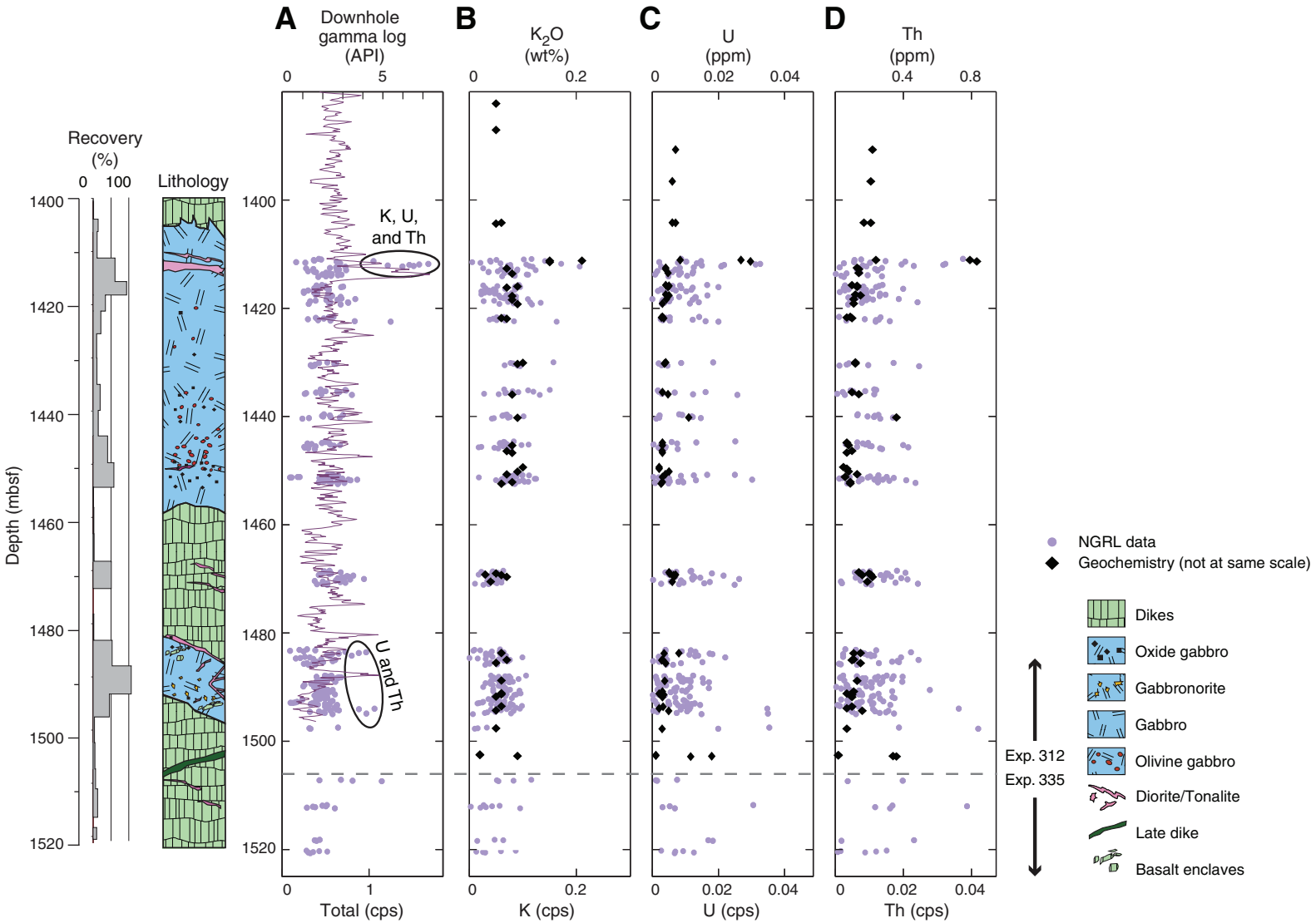

Figure F90. Magnified version of the color reflectance data from Figure F88 to emphasize subtle trends in Gabbros 1 and 2, Expedition 335.

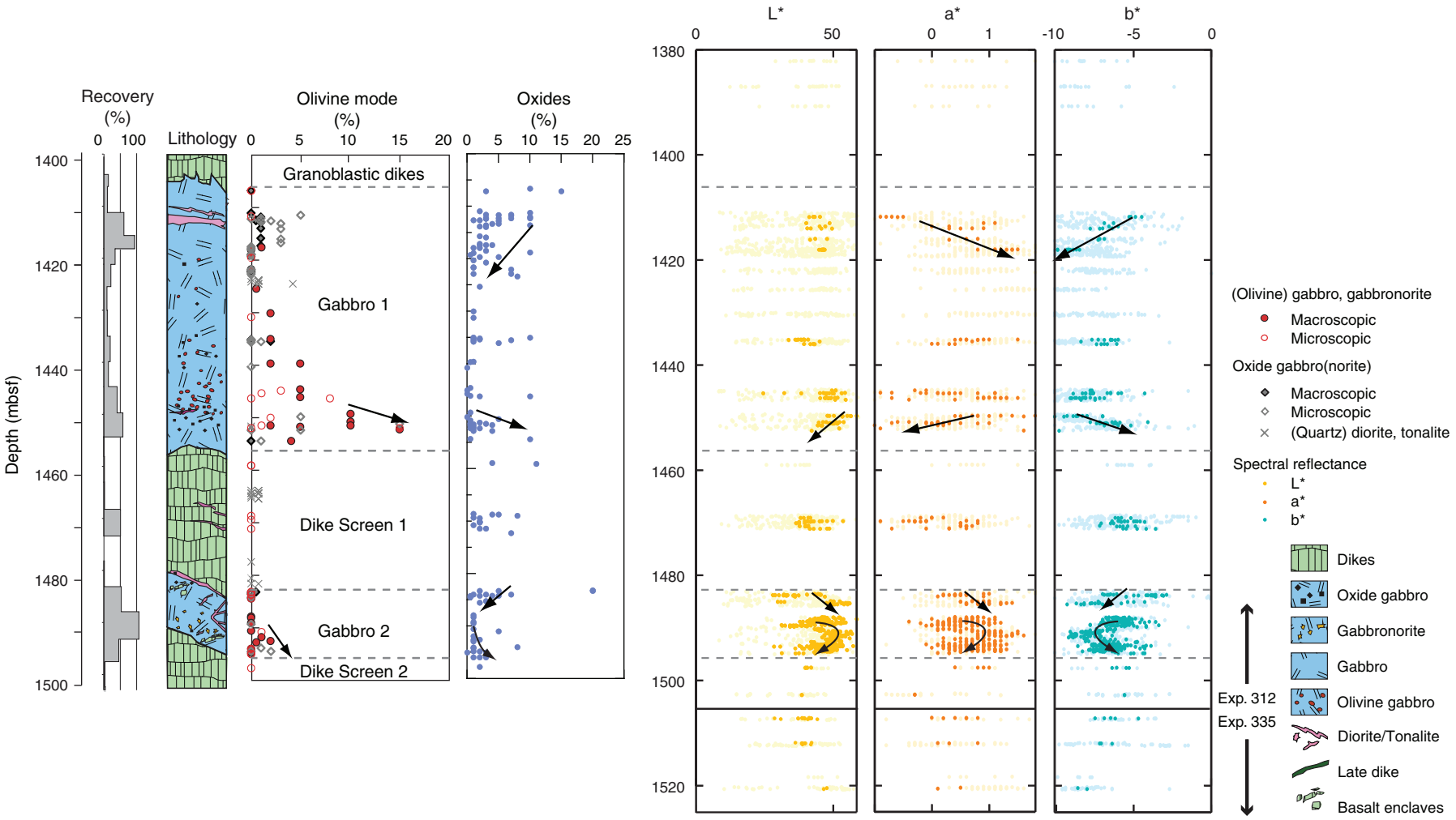

Figure F91. Expedition 335 thermal conductivity measurements and data collected during Expedition 312, compared to the observed lithology and olivine mode (%) as observed during Expedition 335.

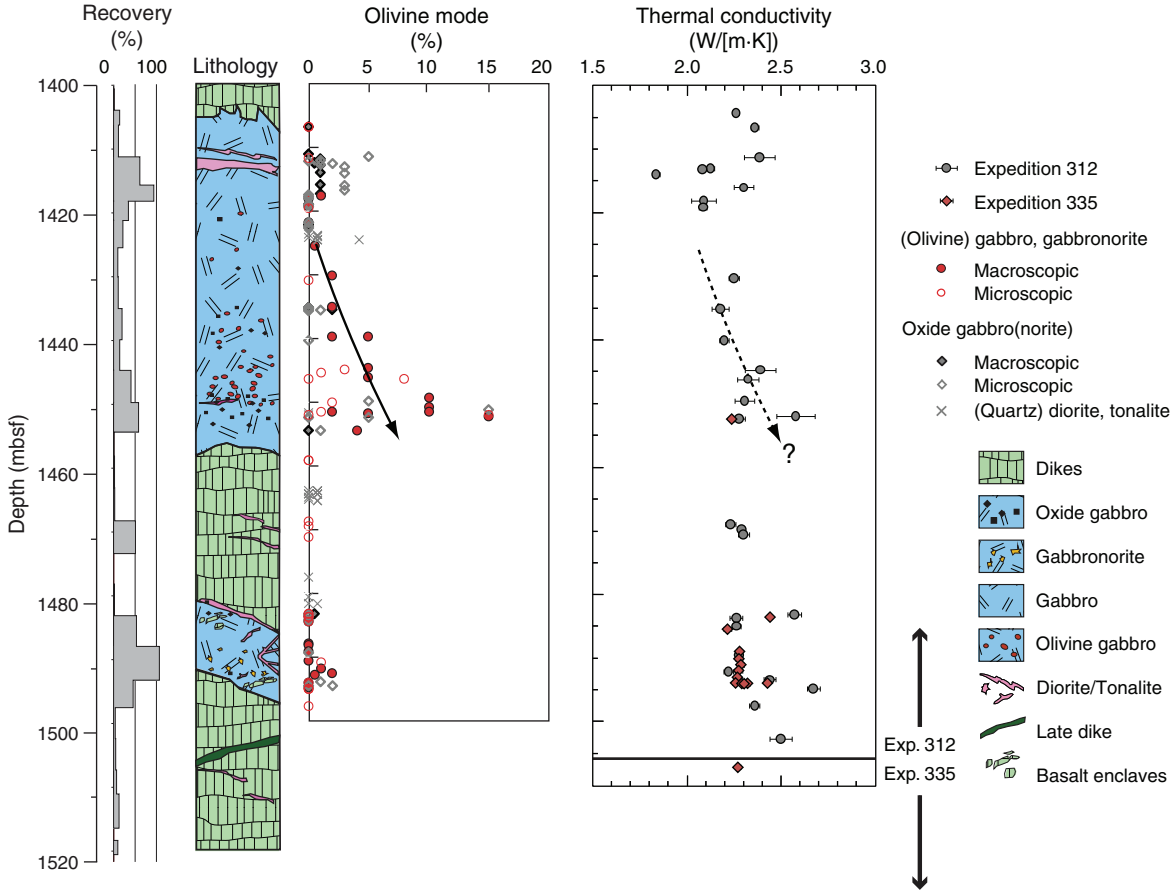

Figure F92. Sensitivity of thermal conductivity probe to distance from the edge of samples, measured on Sample 335-1256D-235R-1 (Piece 1).

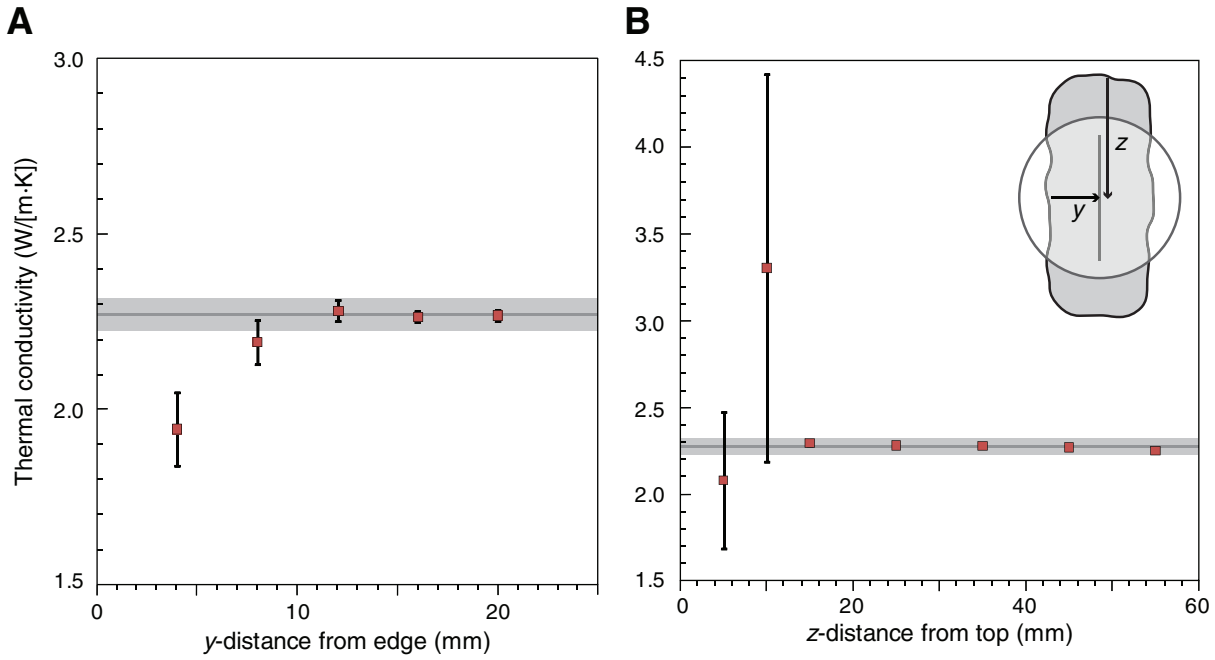

Figure F93. Thermal conductivity versus angle of half-space needle probe with respect to veins in Sample 335-1256D-RCJB-Run12-Rock C. As the probe becomes orthogonal to the veins, thermal conductivity measured perpendicular to the linear probe increases. Dashed line shows the fit to an ellipse with major and minor axes of 2.244 and 2.211 W/(m·K), respectively.

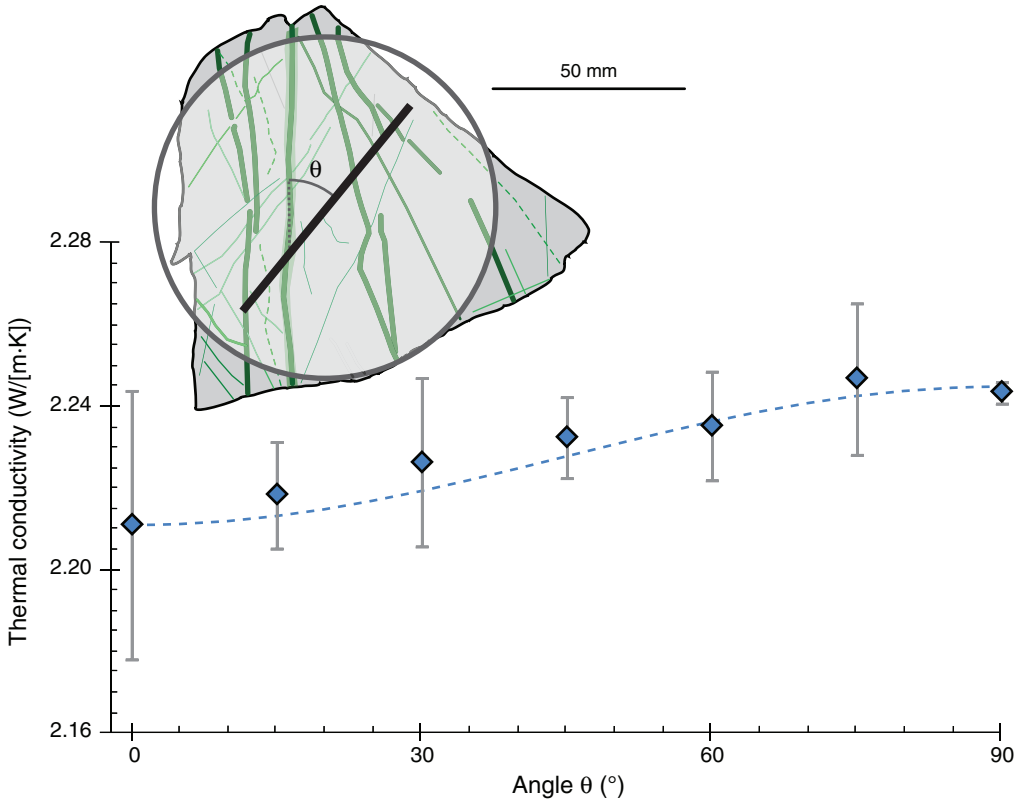

Figure F94. *P*-wave velocity for discrete samples from Expeditions 312 and 335. Solid diamonds represent revised velocities for gabbro samples obtained onboard Expedition 335. They were measured on samples submerged in seawater and deemed to be more representative of the in situ conditions. Open diamonds represent velocities measured during Expedition 335 following Expedition 312 protocol for comparison. Dashed lines tentatively correspond to potential depth intervals for the Expedition 335 samples recovered with the junk baskets.

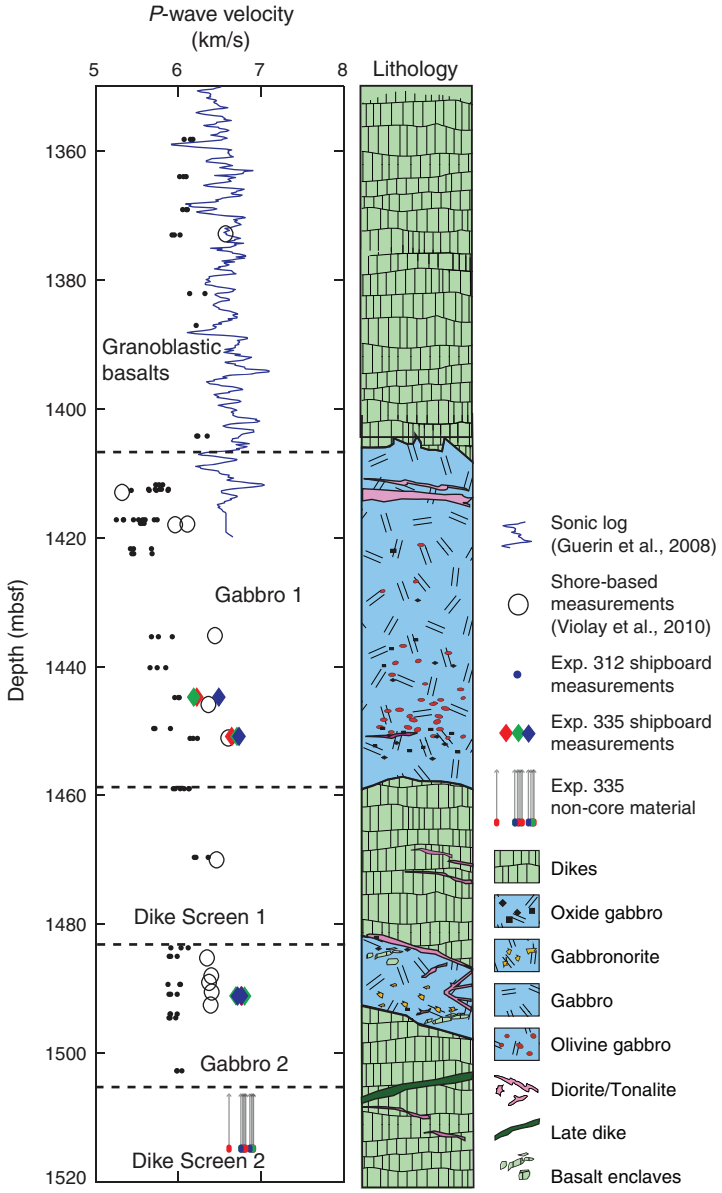

Figure F95. Bulk density, porosity, and average *P*-wave velocity for discrete samples measured below 1400 mbsf in Hole 1256D, shown together with lithology and recovery within the hole. Error bars on the average *P*-wave data are 1σ.

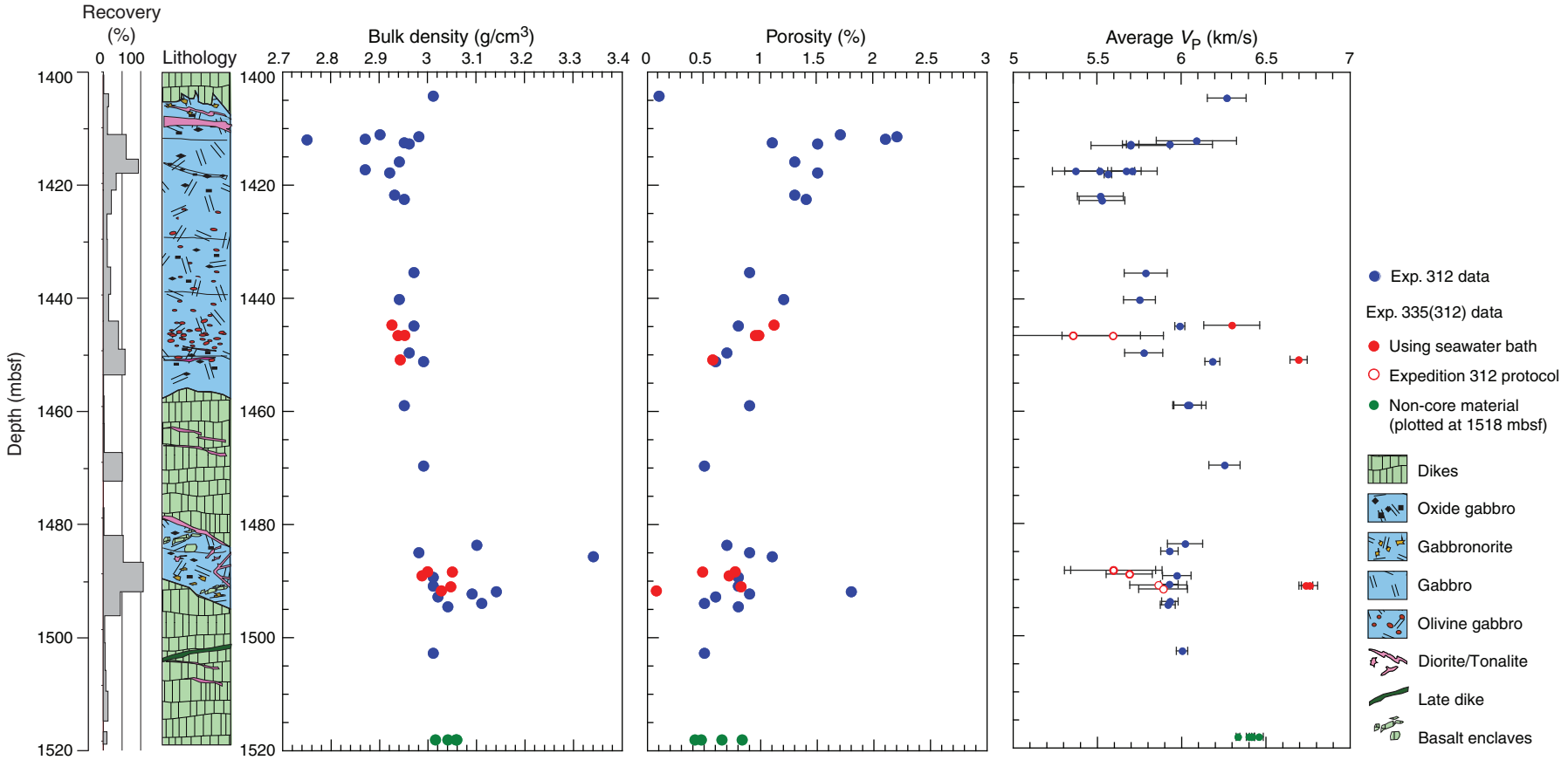

Figure F96. Results of magnetic susceptibility measurements on nonoriented material, all lithologies, with Bartington MS2F portable system. **A.** All measurements. **B.** Measurements of granoblastic basalts. **C.** Measurements of gabbro.

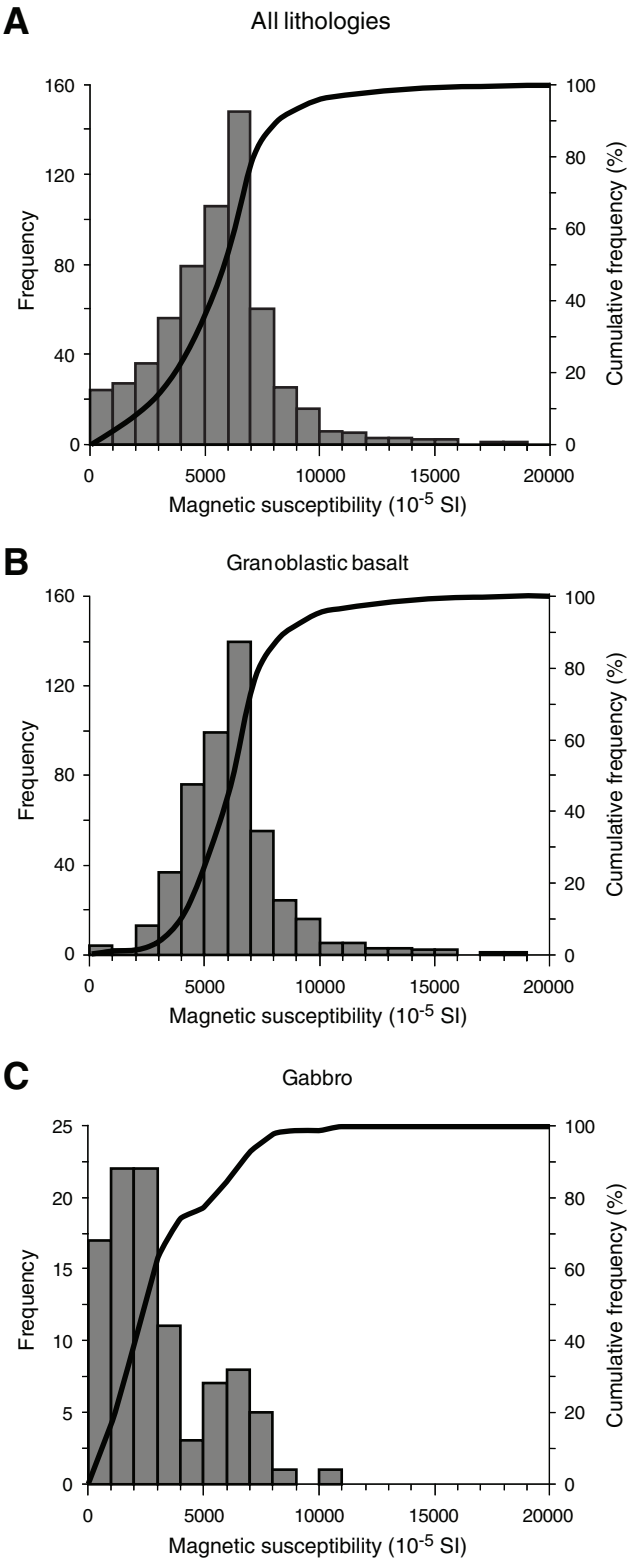

Figure F97. Summary of the logs recorded during Expedition 335 in Hole 1256D. Hole size was measured by the caliper of the Hostile Environment Litho-Density Sonde. Lithostratigraphy is based on observations made during Leg 206 and Expeditions 309/312 and 335. MAD = moisture and density measurements on core samples, EDTC = Enhanced Digital Telemetry Cartridge, MTT = Modular Temperature Tool.

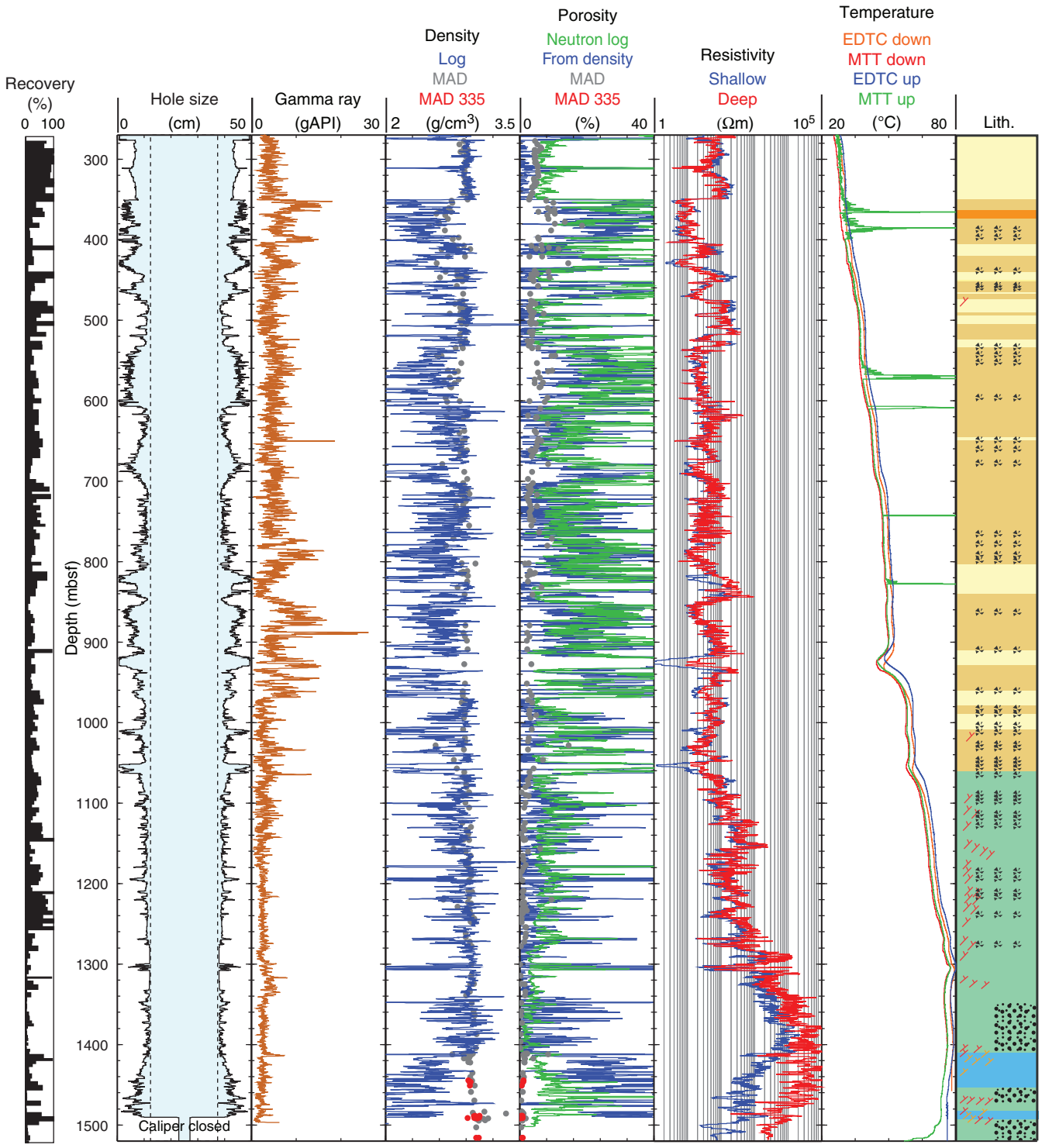

Figure F98. Comparison of the main logs recorded by the triple combo tool strings between Expedition 312 (black lines) and Expedition 335 (red lines). Density and porosity logs can be compared with the discrete measurements made on core samples (gray dots). Lithostratigraphy is based on observations made during Leg 206 and Expedition 309/312.

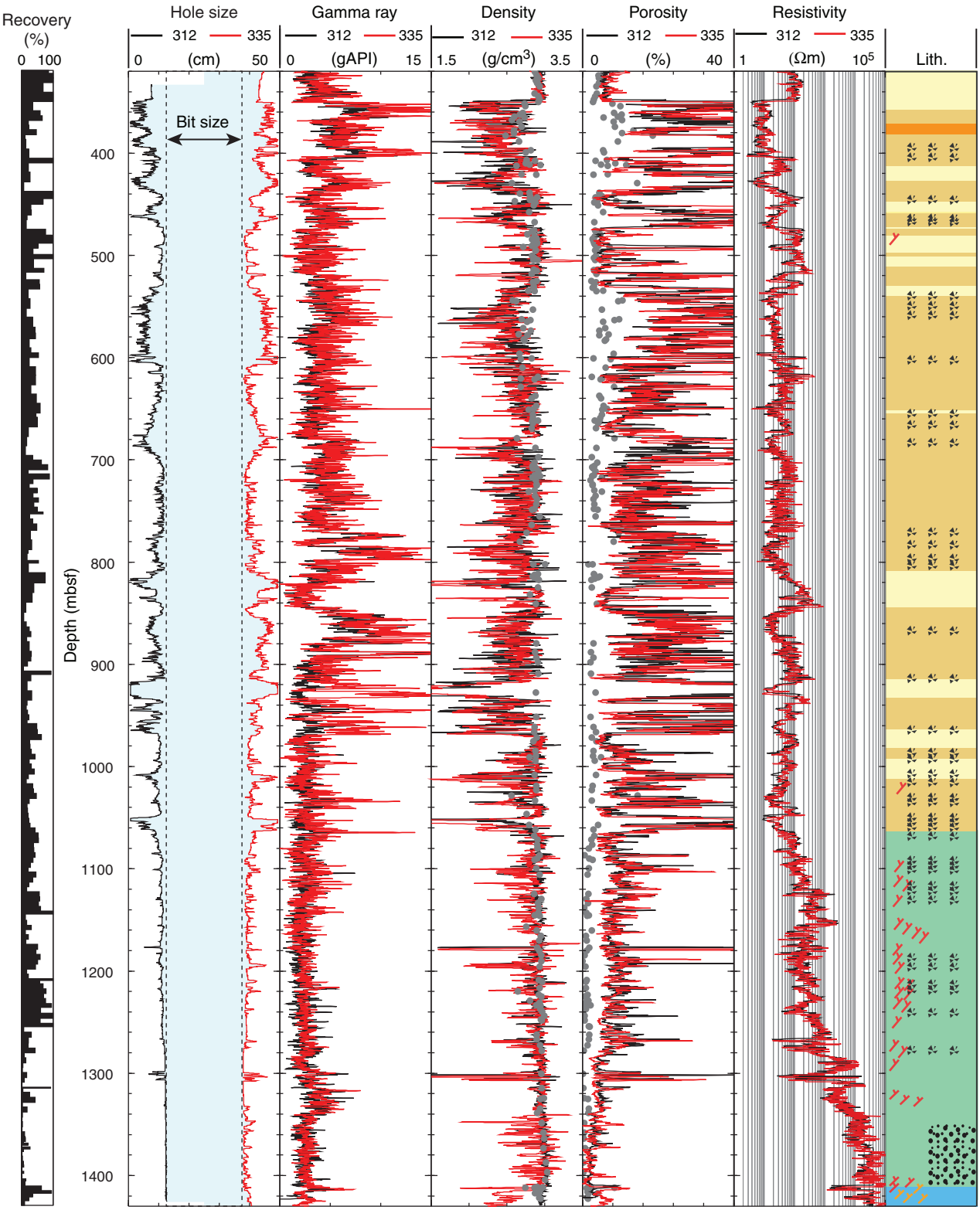

Figure F99. Comparison between hole size during Expedition 312 and Expedition 335. In both expeditions, hole size was measured by the caliper of the Hostile Environment Litho-Density Sonde. Differences observed in the gamma ray log between the two expeditions could indicate some of the intervals where cement accumulated.

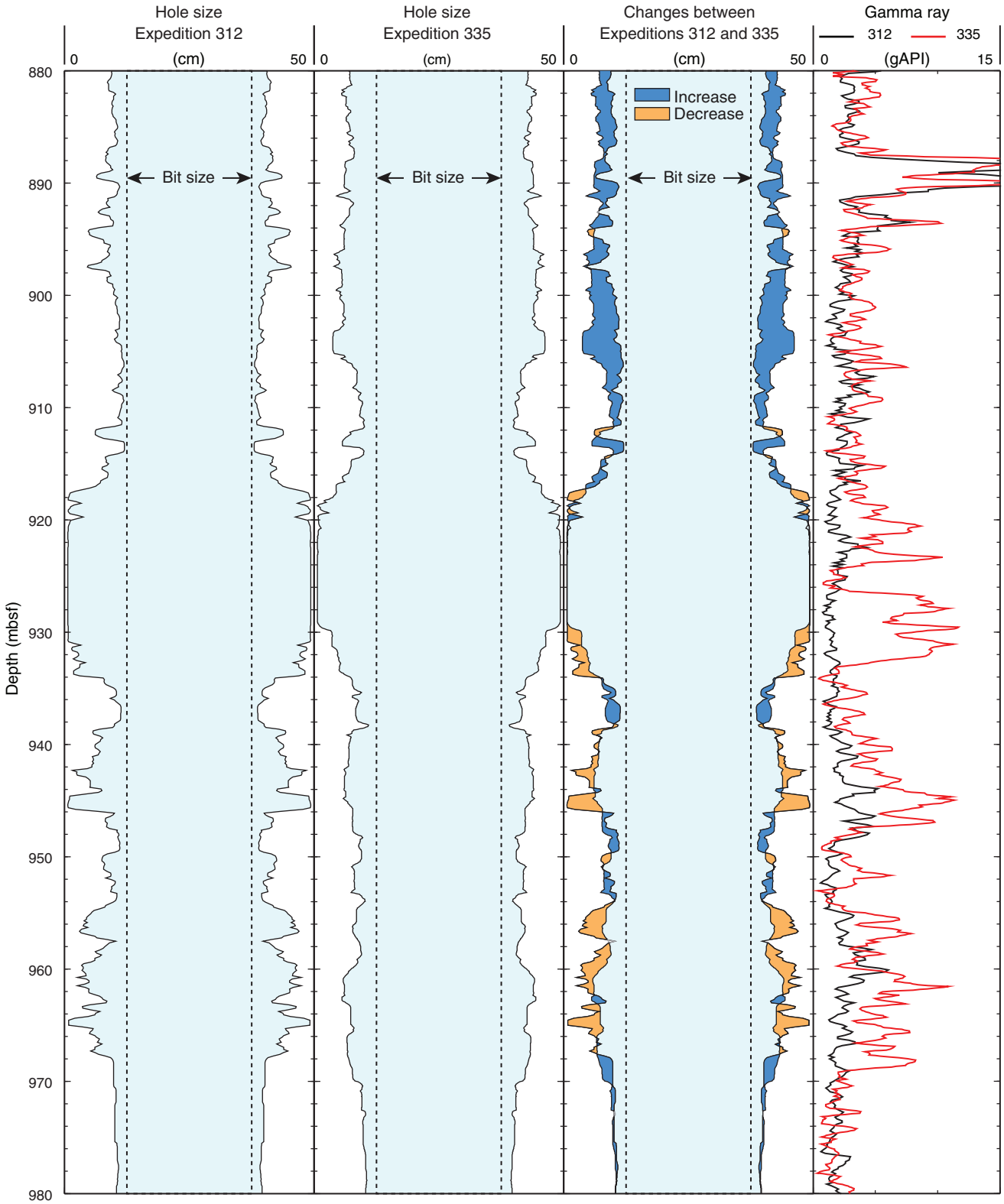

Figure F100. Summary of logs recorded during Expedition 335 in the deeper section of Hole 1256D. Hole size was measured by the caliper of the Hostile Environment Litho-Density Sonde. Lithostratigraphy is based on observations made during Expedition 309/312 and extended during Expedition 335 (see **"Igneous petrology"**). Archie = derived from the resistivity log using the relationship defined by Archie (1942). MAD = moisture and density measurements on core samples, EDTC = Enhanced Digital Telemetry Cartridge, MTT = Modular Temperature Tool.

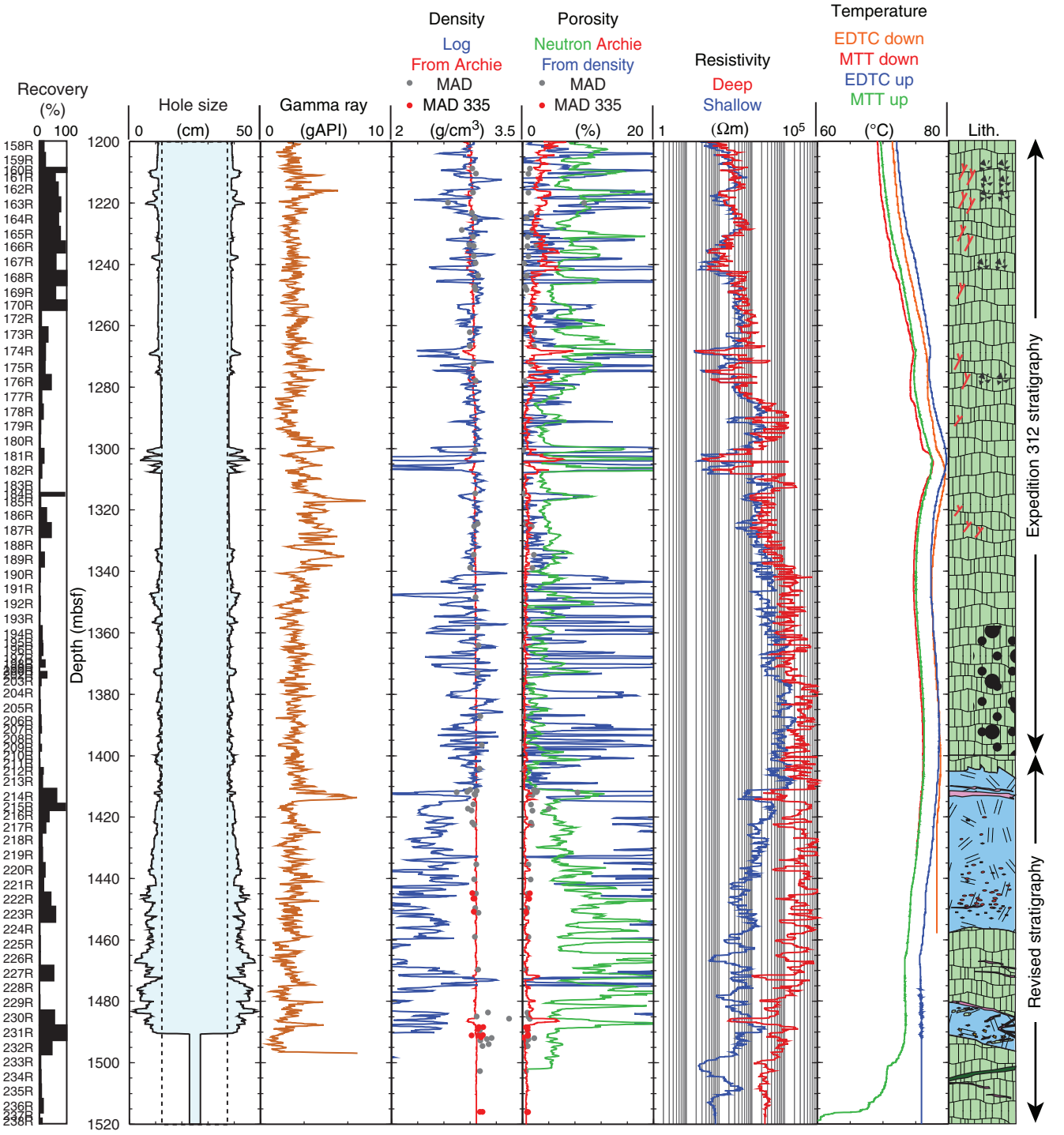

Figure F101. Temperature log recorded during Expedition 335 and comparison with previous temperature logs in Hole 1256D. The spikes observed in Fig. F97 and due to sensor malfunction have been removed. Lithostratigraphy is based on observations made during Expeditions 309/312 and 335. EDTC = Enhanced Digital Telemetry Cartridge, MTT = Modular Temperature tool, TAP = Temperature, Acceleration and Pressure tool.

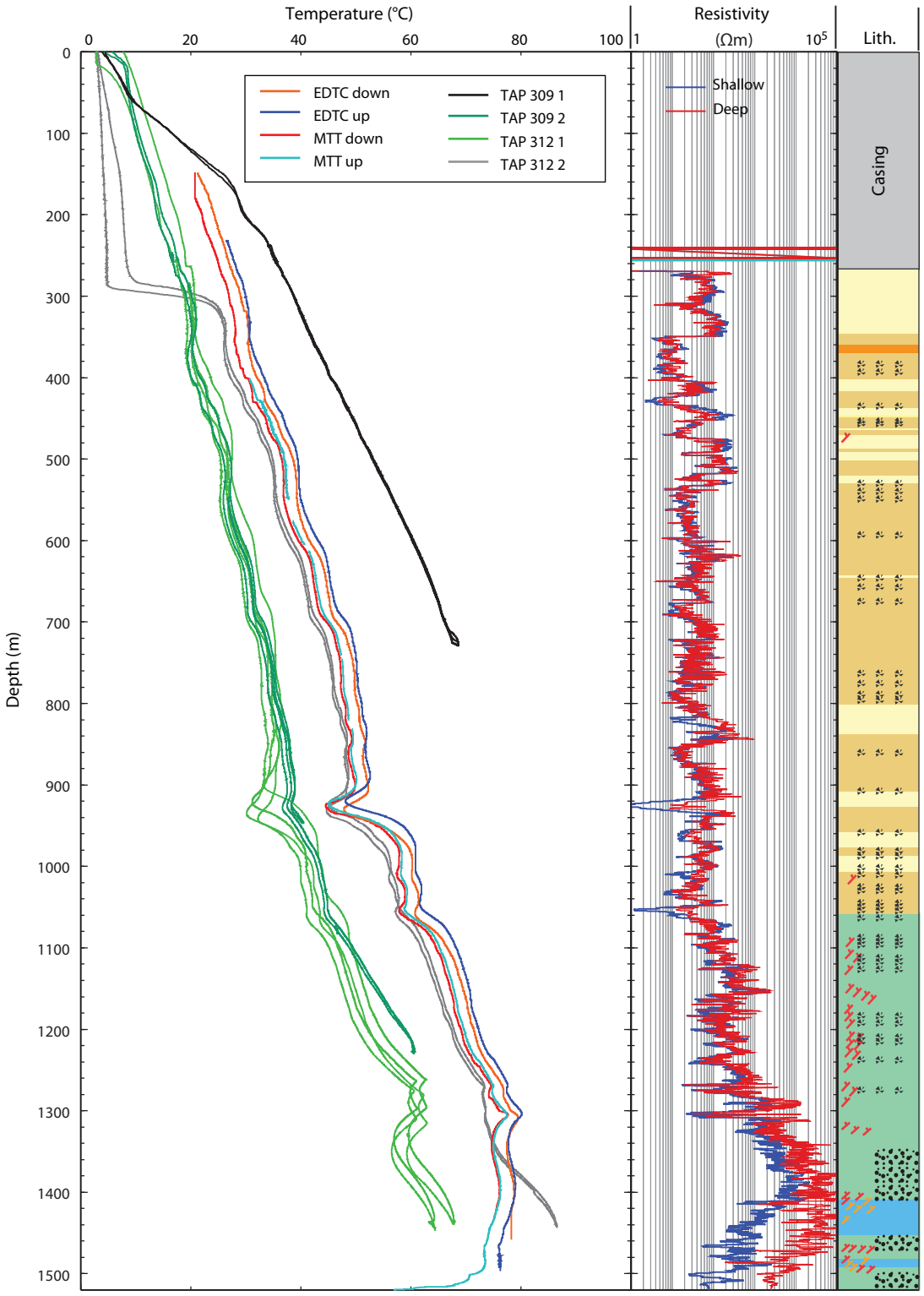

Figure F102. Photographs of Section 335-1256D-235R-1.

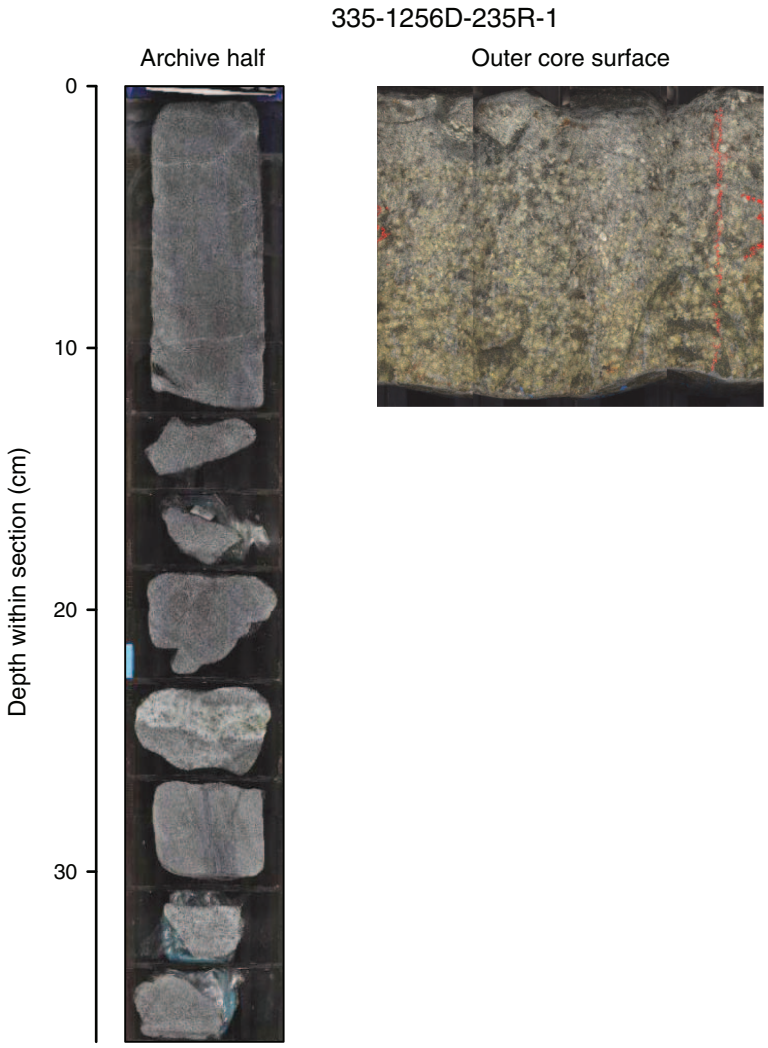

Figure F103. Photographs of Section 335-1256D-236R-1.

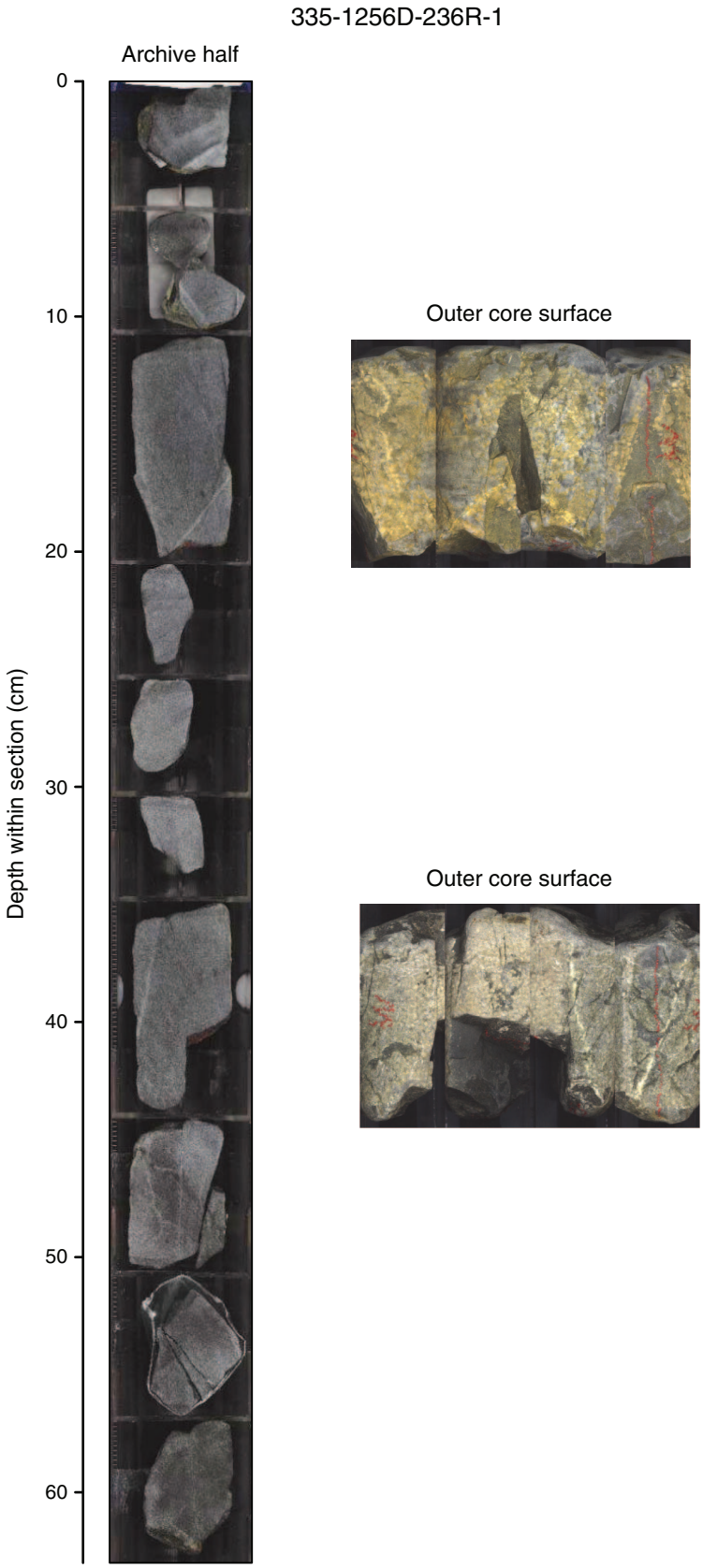

Table T1. Operation and sampling summary, Expedition 335.

Run	Maximum depth (mbsf)	Cumulative pipe trip (km)	Date (2011)	Local start time (h)	Duration (days)	Tools	Samples	Comments
1	925	9.1	19 Apr	0115	2.60	Tricone bit Smith 9-7/8 inch F9		Work obstruction at ~922 mbsf
2	923	18.3	21 Apr	1545	1.64	Tricone bit Reed 9-7/8 inch, IADC Type 517; external junk baskets	Run02-EXJB	Work obstruction at ~922 mbsf
3	922	27.4	23 Apr	0700	0.93	Used Reed tricone bit without jets		Cementing (5 bbl)
4	922	36.5	24 Apr	0515	1.04	Tricone bit 9-7/8 inch Atlas HP61		Work obstruction at ~922 mbsf
5	922	45.7	25 Apr	0615	0.90	Used Reed tricone bit without jets		Cementing (50 bbl)
6	923	54.8	26 Apr	0345	2.47	Tricone bit 9-7/8 inch Atlas HP61; external junk baskets	Run06-EXJB	Work obstruction at ~922 mbsf
7	1507.1	65.1	28 Apr	1500	3.49	Tricone bit Smith 9-7/8 inch		Work obstruction at ~922 mbsf; cleared on 29 April; hole open to bottom on 1 May, 0900 h
8	960.5	74.3	2 May	0245	1.02	Used Reed tricone bit without jets		Cementing the 920–940 mbsf trouble zone (60 bbl)
9	1507.1	84.7	3 May	0315	1.94	RCB assembly with RBI/9-7/8 inch RCB C-9	Ghost Cores 1G–6G; wash Core 7W	Work obstruction at ~922 mbsf; cleared on 29 April; hole open to bottom on 1 May, 0900 h
9	1516.5		5 May	0145	0.48	No liner, nonmagnetic core barrel	235R; 236R	0.33 m recovered, 7%; 0.61 m recovered, 13%
9	1520.2		5 May	1320	1.68	No liner, nonmagnetic core barrel	237R; 238R	0 m recovered; 0.20 m recovered, 10%; core catcher damaged, bit destroyed
10	1434	94.8	7 May	0545	1.43	9 inch Bowen fishing magnet; external junk baskets	Run10-DC, EXJB, and FM	Lost circulation; 4 m of fine cuttings plugging inside bit sub and two junk baskets
11	1520	105.1	8 May	1600	1.84	Tricone bit (Atlas 9-7/8 inch HP61); external junk baskets	Run11-DC and EXJB	Large cuttings in junk basket
12	1518	115.5	10 May	1215	1.74	Bowen 9.75 inch reverse circulation junk basket	Run12-DC, EXJB, and RCJB	~2.5 m of fill; BHA filled with ~50 m of fine cuttings, large rock samples (total = ~20 kg) in RCJB
13	1518	125.8	12 May	0600	1.28	Bowen 9.75 inch reverse circulation junk basket	Run13-DC, EXJB, and RCJB	~2 m of fill, approximately entire BHA filled with sand, large rock samples (largest = ~3.4 kg) in RCJB
14	1520.2	136.1	13 May	1245	1.34	Homco 9.75 inch flow-through junk basket; bit sub junk basket and float	Run14-FTJB, EXJB, and BSJB	2 cobbles (total = ~3.2 kg) in FTJB
15	1520.2	146.5	14 May	2100	1.80	Smith hard formation 9-7/8 inch 7JS tricone bit; single junk basket	Run15-EXJB	Rock fragments and fine cuttings
16	1520.2	156.8	16 May	1615	1.76	9-7/8 inch Smith FH3VPS tricone		
17	1520.2	167.1	18 May	1030	1.70	9-5/8 inch flat-bottomed mill; bit sub junk basket	Run17-BSJB	Rock fragments and fine cuttings
18	1520.2	177.5	20 May	3015	1.40	9 inch flat mill; bit sub junk basket	Run18-BSJB	Rock fragments and fine cuttings
19	1520.2	187.8	21 May	1245	1.22	Reverse circulating junk basket; three external junk baskets (BSJB + 2 EXJB)	Run19-RCJB, BSJB, and EXJB	4 large rocks in RCJB (total = ~8.9 kg; largest = ~3.9 kg); gravel-sized cuttings to small pebbles in EXJB and BSJB
20	1520.2	198.1	22 May	1800	1.46	Reverse circulating junk basket; three external junk baskets (BSJB + 2 EXJB)	Run20-RCJB, BSJB, and EXJB	3 rocks in RCJB (total = ~5.0 kg), 1 is gabbro (1.4 kg); gravel-sized cuttings to small pebbles in EXJB and BSJB
21	1520.2	208.5	24 May	0500	1.14	Reverse circulating junk basket; three external junk baskets (BSJB + 2 EXJB)	Run21-RCJB, BSJB, and EXJB	4 small cobbles in RCJB; gravel-sized cuttings to small pebbles in EXJB and BSJB
22	1520.2	218.8	25 May	0815	1.03	9 inch Bowen fishing magnet; three external junk baskets (BSJB + 2 EXJB)	Run22-BSJB and EXJB	Fishing magnet clear, very little metal debris; rock fragments and fine cuttings in EXJB and BSJB
23	218	226.5	26 May	0900	2.13	Logging (triple combo, FMS, and UBI)		FMS-sonic stuck in logging bit; only triple combo run
24	1521.6	236.83	28 May	1200	1.83	Ulterra RCB-9 coring bit	239R	0.5 m recovered, 35.7%; Cementing bottom (15 bbl) and 910–940 mbsf zone (50 bbl)

IADC = International Association of Drilling Contractors, EXJB = external junk basket, RCB = rotary core barrel, RBI = Rock Bit International, DC = drill collar, FM = fishing magnet, RCJB = reverse circulation junk basket, BHA = bottom-hole assembly, FTJB = flow-through junk basket, BSJB = bit sub junk basket, FMS = Formation MicroScanner, UBI = Ultrasonic Borehole Imager. This table is available in **ASCII** and in Microsoft Excel format (see 103_T01.XLS in CHAPTER_103 in TABLES in **"Supplementary material"**).

Table T2. Grain counting and identification of six subsamples of fine-grained cuttings from fishing Runs 11 and 12, Expedition 335.

Sample	Granoblastic basalt		Basalt		Gabbro		Metal		Unidentified		Total grains
	Number of grains	%	Number of grains	%	Number of grains	%	Number of grains	%	Number of grains	%	
335-1256D-Run11-EXJB-Grains-TS15	339	52.07	265	40.71	27	4.15	4	0.61	16	2.46	651
335-1256D-Run12-EXJB-TS16 (fine)	541	44.13	427	34.83	205	16.72	38	3.10	15	1.22	1226
335-1256D-Run12-EXJB-TS17 (coarse)	122	57.82	76	36.02	10	4.74	0	0.00	3	1.42	211
335-1256D-Run12-DC-TS18 (coarse)	71	47.97	49	33.11	15	10.14	1	0.68	12	8.11	148
335-1256D-Run12-DC-TS19 (fine)	539	42.78	495	39.29	195	15.48	6	0.48	25	1.98	1260
335-1256D-Run12-EXJB-TS20	248	75.38	61	18.54	20	6.08	0	0.00	0	0.00	329
Totals:	1860	48.63	1373	35.90	472	12.34	49	1.28	71	1.86	3825

See Figure F4. This table is available in ASCII and in Microsoft Excel format (see 103_T02.XLS in CHAPTER_103 in TABLES in "Supplementary material").

Table T3. Junk basket sample summary, Hole 1256D, Expedition 335. (Continued on next page.)

Date (2011)	Local time (h)	Depth (mbsf) Top	Depth (mbsf) Bottom	Volume (cm^3)	Sample	Comments
23 Apr	0600	0	923	3000	Run02-EXJB	Basaltic cuttings (2 bags; fine gravel to rounded pebbles)
28 Apr	0715	0	923	700	Run06-EXJB	Cuttings and rock pieces (1 bag + series of pebbles)
8 May	0715	0	1434	1500	Run10-DC	Fine cuttings from bit sub in BHA
8 May	0715	0	1434	2000	Run10-EXJB	Fine cuttings
8 May	0715	0	1434	100	Run10-EXJB	Rock pieces
8 May	0715	0	1434	1500	Run10-FM	Fine metal + rock cuttings from fishing magnet
8 May	0715	0	1434	100	Run10-FM	Mud from fishing magnet
10 May	1130	1353	1520	5000	Run11-EXJB	Fine cuttings to large pieces of rock, mostly granoblastic basalt (multiple bags; various grain size), some gabbro (1 bag of rock chips)
11 May	2130	1328	1518	5000	Run12-DC	Rock material (fine cuttings) from BHA
11 May	2130	1328	1518		Run12-EXJB	Fine cuttings and pebbles (2 bags granoblastic; 1 small bag gabbro)
11 May	2130	1516	1518	5000	Run12-RCJB	Fine cuttings and pebbles (multiple bags) and large cobbles (see list below)
11 May	2130	1516	1518	1512	Run12-RCJB-Rock A	Cobble (granoblastic)
11 May	2130	1516	1518	1058	Run12-RCJB-Rock B	Cobble (granoblastic)
11 May	2130	1516	1518	454	Run12-RCJB-Rock C	Cobble (granoblastic)
11 May	2130	1516	1518	302	Run12-RCJB-Rock D	Cobble (granoblastic)
11 May	2130	1516	1518	151	Run12-RCJB-Rock E	Cobble (granoblastic)
11 May	2130	1516	1518		Run12-RCJB-Rock F	Cobble (granoblastic)
11 May	2130	1516	1518	302	Run12-RCJB-Rock G	Cobble (granoblastic)
11 May	2130	1516	1518		Run12-RCJB-Rock H through Rock Y	Cobble (granoblastic)
13 May	1100	270	1518	5000	Run13-DC	Large amount of fine-grained cuttings from BHA
13 May	1100	270	1518	5000	Run13-EXJB	Fine-grained cuttings
13 May	1100	270	1518	2000	Run13-RCJB	Multiple bags of fine cuttings to pebbles (mostly granoblastic rocks)
13 May	1100	270	1518		Run13-RCJB-Rock A	Cobble (granoblastic)
13 May	1100	270	1518		Run13-RCJB-Rock B	Cobble (granoblastic)
14 May	2010	1518	1520	2000	Run14-BSJB	3 bags of cuttings (various grain size, fine to gravel)
14 May	2010	1518	1520	2000	Run14-EXJB	Multiple bags of cuttings (various grain size, fine to pebbles; some gabbro chips)
14 May	2010	1518	1520		Run14-FTJB-Rock A	Cobble (granoblastic)
14 May	2010	1518	1520		Run14-FTJB-Rock B	Cobble (granoblastic)
16 May	1545	1518	1520	5000	Run15-EXJB	Multiple bags of cuttings (various grain size, fine to pebbles; granoblastic)

Table T3 (continued).

Date (2011)	Local time (h)	Depth (mbsf) Top	Depth (mbsf) Bottom	Volume (cm^3)	Sample	Comments
19 May	0315	1520	1521	2000	Run17-BSJB	7 bags of cuttings (various grain size, gravel to pebbles; granoblastic)
21 May	1230	1518	1521	5000	Run18-BSJB	4 bags of cuttings (various grain size, fine to pebbles; granoblastic); 2 small bags of leucocratic gravel
22 May	1645	1510	1520	5000	Run19-BSJB	2 bags of fine-grained cuttings
22 May	1645	1510	1520	300	Run19-EXJB1	Pebbles of basalt and granoblastic rocks, gravel
22 May	1645	1510	1520	100	Run19-EXJB2	Pebbles of basalt and granoblastic rocks, gravel
22 May	1645	1518	1521	50	Run19-RCJB	Pebbles (granoblastic + 1 gabbro)
22 May	1645	1518	1521		Run19-RCJB-Rock A	Cobble (granoblastic with diorite vein)
22 May	1645	1518	1521		Run19-RCJB-Rock B	Cobble (granoblastic)
22 May	1645	1518	1521		Run19-RCJB-Rock C	Cobble (granoblastic)
22 May	1645	1518	1521		Run19-RCJB-Rock D	Cobble (granoblastic)
24 May	0215	1510	1520	5000	Run20-BSJB	2 bags (fine to gravel-sized cuttings); 1 small bag of pebbles
24 May	0215	1510	1520	5000	Run20-EXJB1	4 bags of cuttings (various grain size, fine to pebbles; granoblastic)
24 May	0215	1510	1520	3000	Run20-EXJB2	1 bag of granoblastic pebbles; 1 bag of leucocratic pebbles
24 May	0215	1518	1521	500	Run20-RCJB	Large cobbles (see list below)
24 May	0215	1519	1519.5		Run20-RCJB-Rock A	Cobble (granoblastic)
24 May	0215	1519	1519.5		Run20-RCJB-Rock B	Cobble (granoblastic)
24 May	0215	1519	1519.5		Run20-RCJB-Rock C	Cobble (gabbro)
24 May	0215	1519	1519.5		Run20-RCJB-Rock D	Pebble (leucocratic material)
24 May	0215	1519	1519.5		Run20-RCJB-Rock E	Pebble (leucocratic material)
25 May	0700	1510	1520	2000	Run21-BSJB	3 bags of cuttings (various grain size, fine to gravel)
25 May	0700	1510	1520	200	Run21-EXJB1	2 small bags of pebbles (granoblastic)
25 May	0700	1510	1520	200	Run21-EXJB2	3 small bags of pebbles (granoblastic)
25 May	0700	1518	1520	200	Run21-RCJB	3 small bags of pebbles (granoblastic)
26 May	0800	1519	1520		Run22-BSJB	2 bags (fine and gravel-sized cuttings)
26 May	0800	1519	1520		Run22-EXJB	1 bag of cuttings (pebbles and chips)
26 May	0800	1519	1520		Run22-FM	Small bag of metal + fine-grained cuttings

EXJB = external junk basket, DC = drill collar, BHA = bottom-hole assembly, FM = fishing magnet, RCJB = reverse circulation junk basket, BSJB = bit sub junk basket, FTJB = flow-through junk basket. This table is available in **ASCII** and in Microsoft Excel format (see 103_T03.XLS in CHAPTER_103 in TABLES in **"Supplementary material"**).

Table T4. Igneous unit description for rocks cored in Hole 1256D during Expeditions 335 and 312. (Continued on next page.)

Igneous unit	Upper contact: Depth (mbsf)	Upper contact: Core, section, interval (cm)	Thickness (m)	Lithology	Upper unit boundary	Lower unit boundary	Description
Rocks drilled during Expedition 312—relogged during Expedition 335:							
81	1406.62	213R-1, 52	4.60	Medium-grained orthopyroxene-bearing oxide gabbro	Intrusive margins in Section 213R-1 (Piece 13)	Intrusive margin in Section 214R-1 (Piece 9)	Mixed gabbro and altered dike material. The gabbro occurs in two dikes, 5 and 40 mm thick. This gabbro has an intrusive contact with the altered basalt host. There is a 0.5 mm wide band of oxides on the margin of the intrusion but little change in grain size in the gabbro toward the margin. The gabbro appears to have a broadly equigranular grain size distribution and granular texture.
82	1411.22	214R-1, 32	0.66	Medium-grained oxide quartz-diorite	Intrusive margins in Section 213R-1 (Piece 9)	Intrusive margin with Unit 84 in Section 214R-1 (Piece 26)	Narrow (<1 m) intrusion into Units 81 and 83. Primary minerals include abundant quartz (20%–25%), abundant interstitial Fe-Ti oxides (>20%), and a primary mafic phase that was probably hornblende. It has a seriate grain size distribution and granular texture.
83	1411.66	214R-1, 76	0.36	Medium-grained orthopyroxene-bearing oxide gabbro	Intrusive margin with Unit 82 in Section 214R-1 (Piece 15)	Not recovered	This oxide gabbro is characterized by a patchy texture, with dark patches diffusely invaded by subordinate leucocratic patches. It has a seriate grain size distribution and subophitic texture.
84	1412.24	214R-1, 134	0.43	Medium-grained orthopyroxene-bearing oxide gabbro	Intruded by Unit 82 in Piece 26 of Section 214R-1	Not recovered	Unit 84 is very similar to Unit 83 and may indeed be part of the same magmatic body. Both are intruded by Unit 82; because they are not contiguous in the core they are defined as separate units. Locally, a poikilitic texture is developed.
85	1412.67	214R-2, 32	4.81	Medium-grained orthopyroxene- and olivine-bearing oxide gabbro	Not recovered	Not recovered	Similar to Unit 83, Unit 85 is characterized by the development of a distinct patchy texture, where 1 cm diameter roughly spherical dark patches are separated by 1–5 mm wide zones of leucocratic material. The dark domains include clinopyroxene oikocrysts 1 cm or more in diameter, and strands of the leucocratic network domains are 1–5 mm wide. It has an inequigranular seriate grain size distribution and subophitic to poikilitic texture.
86	1417.48	215R-2, 35	1.77	Medium-grained disseminated oxide gabbro	Gradational upper boundary based on textural change	Lower boundary based on further textural change	This unit is part of the same intrusion as Unit 85 and is defined on the basis of a gradual textural change from patchy in Unit 85 to more equigranular with subophitic to ophitic pyroxenes in Unit 86. Toward the base of the section, a number of large, elongate clinpyroxene crystals are present, with long axes as long as 25 mm. The unit contains a patch of amphibole-bearing oxide gabbro with a diffuse margin.
87	1419.25	216R-1, 135	2.79	Medium-grained orthopyroxene-bearing gabbro	Based on textural change between Pieces 25 and 26	Appearance of coarse-grained and pale plagioclase patches from Section 217R-1 (Piece 11) downward	Unit 87 may be part of the same igneous body as Unit 86, but there is a marked change in texture, becoming poikilitic, containing oikocrysts as large as 30 mm.
88	1422.04	217R-1, 43.5	17.63	Medium-grained olivine-bearing disseminated oxide gabbro to olivine-bearing oxide gabbro	Appearance of coarse-grained and pale plagioclase patches from Section 217R-1 (Piece 11) downward	First appearance of olivine gabbro, Section 221R-1	Unit 88 is varitextured, being characterized by diffuse centimeter-scale coarse-grained patches that are highlighted by higher oxide mineral contents and by the absence of poikilitic clinopyroxene. Boundaries between the coarser and finer regions appear to be igneous but vary in nature, some being very diffuse and, in other cases, fairly sharp, occurring over a couple of millimeters or less. Unit 88 is also distinguished by the appearance of scattered olivine as small, highly altered interstitial grains with dark, oxide-rich alteration halos. It is crosscut by a coarse-grained oxide gabbro in Section 220R-1 (Unit 88B).
89	1439.66	221R-1, 6	19.24	Medium-grained orthopyroxene-bearing olivine gabbro	First appearance of olivine gabbro, Section 221R-1	Not recovered	Equigranular, subophitic olivine gabbro, occurring in three sequences (Units 89A, 89C, and 89D). Olivine mode is variable, ranging from <5% to 20%, with the highest concentrations at the base of Units 89A and 89C. Some coarser grained, locally poikilitic patches occur throughout. The unit is cut by a pair of narrow, coarse-grained, seriate oxide gabbro and oxide quartz diorite dikes and patches (Unit 89B), mineralogically similar to the diffuse network domains of Units 83–87.

Table T4 (continued).

Igneous unit	Upper contact: Depth (mbsf)	Upper contact: Core, section, interval (cm)	Thickness (m)	Lithology	Upper unit boundary	Lower unit boundary	Description
90	1458.90	225R-1, 0	24.28	Microcrystalline–fine aphyric basalt	Not recovered	Not recovered	Unit 90 consists of fine-grained (meta)basalts very similar to those at the base of the sheeted dike interval. The igneous texture appears to have been overprinted by a granular metamorphic texture cut by several thin gabbroic and leucocratic dikes. At its lower boundary, Unit 90 is intruded by gabbronorite from Gabbro 2. Approaching the contact, secondary granular orthopyroxene appears to progressively replace clinopyroxene, suggesting that orthopyroxene formed by prograde reactions that were more intense in the boundary zone. Units 90B–90F are small narrow dikes of medium-grained quartz diorite (Units 90B, 90D, and 90E) and fine-grained tonalite (Units 90C and 90F).
91	1483.18	230R-1, 18	1.06	Medium-grained oxide gabbro	Significant increase in grain size in Section 230R-1 (Piece 5)	Disappearance of basaltic xenoliths in gabbro from Section 230R-1 (Piece 12)	This complex marginal unit contains medium-grained oxide gabbro, fine-grained basaltic fragments, and a coarser oxide gabbro (commonly altered) in Pieces 5, 6, and 8, adjacent to the margin. In Piece 5, this coarse gabbro cuts a large basaltic fragment, which is likely part of Unit 90A. The intrusion of gabbro into the finer grained dike material is confirmed by the crosscutting relationships. Fine-grained basaltic fragments of varying size and shape are found within this unit, and the end of the unit is defined by their disappearance. In Pieces 7 and 8, a zone of dark, fine-grained material is present. Basaltic fragments are slightly pink, implying the presence of orthopyroxene in the groundmass (cf. dike rocks in Unit 90A). The interval 49–69 cm contains abundant 1–2 mm magnetite grains and has extremely high magnetic susceptibility. Unit 91B is a 10 mm wide disseminated oxide gabbro vein that cuts Unit 91A at a high angle.
92	1484.24	230R-1, 131	9.94	Fine–medium gabbronorite	Disappearance of basaltic xenoliths in gabbro from Section 230R-1 (Piece 12)	Not recovered	Unit 92 is an equigranular to seriate, dominantly subophitic disseminated oxide gabbronorite. It is characterized by the presence of centimeter-sized, diffuse, equidimensional patches of coarser grain size and higher oxide content. Olivine occurs in small abundance. It is intruded by veins of diorite (Unit 92B), disseminated oxide quartz diorite (Unit 92C), and oxide diorite (Unit 92D).
93	1494.18	232R-2, 20	0.77	Fine–medium disseminated oxide gabbronorite	Appearance of basaltic enclaves in disseminated oxide gabbronorite of Unit 92A	Sharp contact with basalt in Piece 9	This marginal unit is very similar to Unit 91, described at the upper contact of this Gabbro 2, containing disseminated oxide gabbronorite with fine-grained basaltic fragments (Unit 93A) and a coarser disseminated oxide gabbronorite adjacent to the lower margin (Unit 93B). The lower contact in Piece 9A is fairly sharp and sutured and shows no decrease in the gabbro grain size toward the contact.
94	1494.95	232R-2, 97	7.64	Microcrystalline–fine aphyric basalt	Intrusive contact with gabbronorite in Piece 9	Not recovered	Unit 94 is orthopyroxene-rich, cryptocrystalline to fine-grained rock of basaltic composition. It is extensively recrystallized with well-developed granoblastic textures, but in some areas, especially away from its contact with Unit 93, it retains an igneous intergranular texture. It is cut by a medium-grained oxide-rich diffuse vein.
95	1502.59	234R-1, 9	4.51	Aphyric basalt	Not recovered	Not recovered	Cryptocrystalline aphyric basalt, which is distinguished from Unit 94 by its lighter gray color and finer grain size. It is also distinct from the other units of dike screens in its relatively low metamorphic grade and degree of alteration.
Rocks drilled during Expedition 335:							
96	1507.10	235R-1, 0	13.10	Aphyric basalt	Not recovered	Not recovered	This unit is predominantly composed of fine-grained granoblastic basalt. The first 12.5 cm (Section 235R-1, Piece 1) is strongly recrystallized (Unit 96A), whereas the granoblastic rocks in the rest of the unit are completely recrystallized (Unit 96B). The unit contains small amounts of leucocratic rocks (tonalite, quartz diorite, and albitite; Unit 96C). Some of the granoblastic rocks contain centimeter-sized patches of oxide diorite (Unit 96D).

This table is available in **ASCII** and in Microsoft Excel format (see 103_T04.XLS in CHAPTER_103 in TABLES in **"Supplementary material"**).

Table T5. Weight and relative abundance of material >1 cm in size recovered during cleaning operations in Hole 1256D during Expedition 335.

	Weight (g)											
	Strongly granoblastic basalt			Completely granoblastic basalt								
Sample	Coarse*	Medium*	Fine*	Coarse*	Medium*	Fine*	Granoblastic basalt total	Basalt	Gabbro	Diorite	Leucocratic rocks	Overall total
335-U1256D-												
Run 11 EXJB	494	1,548	257	266	433	206	3,204	152	416	0	0	3,772
Run 12 EXJB and RCJB	863	1,769	13,339	0	0	1,465	17,436		0	0	0	17,436
Run 13 RCJB	54	8,465	131	0	0	0	8,650	31	0	10	5	8,696
Run 14 FTJB	0	1,366	337	0	278	27	2,008	166	52	4	98	2,328
Run 15 EXJB	319	705	161	7	197	56	1,445		0	0	0	1,445
Run 17 EXJB	387	392	149	0	87	118	1,133	31	5	0	31	1,200
Run 18 BSBJ	4	76	7	0	0	0	87	0	0	0	0.5	87
Run 19 EXJB	2	74	31	0	0	0	107	84	0	0	0	191
Run 19 RCJB	22	9,090	24	0	0	0	9,136	0	4.5	0	19	9,159
Run 20 RCJB	2,220	170	0	0	0	0	2,390	0	969	0	0	3,359
Run 20 BSJB	0	56	119	0	16.5	0	192	64	2.5	25	0	283
Run 20 EXJB1	0	416	93	0	0	0	509	34.5	0	0	0	544
Run 21 RCJB	0	170	131	0	155	0	456	81.5	0	6	0	544
Run 22 EXJB	0	97	107	0	0	0	204	15	0	0	0	219
Totals:	4,364.77	24,394	14,885	273	1,167	1,872	46,954	659	1,449	45	154	49,261

* = These terms refer to relative grain size within the recovered rocks and do not imply absolute grain size. EXJB = external junk basket, RCJB = reverse circulation junk basket, FTJB = flow-through junk basket, BSBJ = bit sub junk basket. This table is available in ASCII and in Microsoft Excel format (see 103_T05.XLS in CHAPTER_103 in TABLES in "Supplementary material").

Table T5 (continued).

	Weight (%)											
	Strongly granoblastic basalt			Completely granoblastic basalt								
Sample	Coarse*	Medium*	Fine*	Coarse*	Medium*	Fine*	Granoblastic basalt total	Basalt	Gabbro	Diorite	Leucocratic rocks	Overall total
335-U1256D-												
Run 11 EXJB	13.1	41.0	6.8	7.1	11.5	5.5	84.9	4.0	11.0	0	0	
Run 12 EXJB and RCJB	4.9	10.1	76.5	0	0	8.4	100.0	0	0	0	0	
Run 13 RCJB	0.6	97.3	1.5	0	0	0	99.5	0.4	0	0.1	0	
Run 14 FTJB	0	58.7	14.5	0	11.9	1.2	86.3	7.1	2.2	0.2	4	
Run 15 EXJB	22.1	48.8	11.1	0.5	13.6	3.9	100.0	0	0	0	0	
Run 17 EXJB	32.3	32.7	12.4	0	7.3	9.8	94.4	2.6	0.4	0	2.6	
Run 18 BSBJ	4.6	86.8	8.0	0	0	0	99.4	0	0	0	1	
Run 19 EXJB	1.0	38.8	16.0	0	0	0	55.9	44.1	0	0	0	
Run 19 RCJB	0.2	99.2	0.3	0	0	0	99.7	0	0	0	0	
Run 20 RCJB	66.1	5.1	0	0	0	0	71.2	0	28.8	0	0	
Run 20 BSJB	0	19.8	42.0	0	5.8	0	67.7	22.6	0.9	8.8	0	
Run 20 EXJB1	0	76.5	17.1	0	0	0	93.7	6.3	0	0	0	
Run 21 RCJB	0	31.3	24.1	0	28.5	0	83.9	15.0	0	1.1	0	
Run 22 EXJB	0	44.3	48.9	0	0	0	93.2	6.8	0	0.0	0	
Totals:	8.9	49.5	30.2	0.6	2.4	3.8	95.3	1.3	2.9	0.09	0.3	

Table T6. Size and weight of cobbles recovered during cleaning and fishing operations in Hole 1256D during Expedition 335.

Sample	Length (cm)	Width (cm)	Height (cm)	Weight (g)
335-U1256D-				
Run 12 RCJB Rock A	20.0	10.0	11.0	4535.9
Run 12 RCJB Rock B	15.5Å	11.0	8.5	3175.1
Run 12 RCJB Rock C	12.0	12.0	9.0	1360.8
Run 12 RCJB Rock D	15.0	6.5	8.5	907.2
Run 12 RCJB Rock E	9.0	8.0	7.5	453.6
Run 12 RCJB Rock F	7.7	6.5	6.0	226.8
Run 12 RCJB Rock G	9.0	8.0	7.0	907.2
Run 12 RCJB Rock H	5.5	5.5	5.0	244.0
Run 12 RCJB Rock I	8.5	4.0	3.5	219.5
Run 12 RCJB Rock J	5.0	5.5	3.0	172.0
Run 12 RCJB Rock K	5.5	6.5	5.0	297.0
Run 12 RCJB Rock L	5.5	5.8	3.0	218.0
Run 12 RCJB Rock M	7.0	4.5	2.0	135.5
Run 12 RCJB Rock N	7.5	4.5	3.0	219.0
Run 12 RCJB Rock O	6.5	7.0	4.5	452.0
Run 12 RCJB Rock P	8.7	5.5	2.0	165.0
Run 12 RCJB Rock Q	6.5	3.5	2.5	98.5
Run 12 RCJB Rock R	4.5	4.0	2.1	99.7
Run 12 RCJB Rock S	7.0	6.5	4.5	401.4
Run 12 RCJB Rock T	6.0	4.5	3.0	214.3
Run 13 RCJB Rock A	21.0	13.5	6.5	3628.7
Run 13 RCJB Rock B	12.8	12.0	4.0	907.2
Run 14 FTJB Rock A	15.0	12.0	6.0	1814.4
Run 14 FTJB Rock B	15.0	9.5	5.0	1360.8
Run 19 RCJB Rock A	23.0	14.5	14.0	3855.5
Run 19 RCJB Rock B	18.0	14.0	8.5	2721.5
Run 19 RCJB Rock C	14.5	12.0	7.5	1360.8
Run 19 RCJB Rock D	13.5	10.5	6.0	1134.0
Run 20 RCJB Rock A	18.5	15.0	6.5	1360.8
Run 20 RCJB Rock B	11.0	9.5	5.0	859.0
Run 20 RCJB Rock C	12.0	12.0	125.0	969.0
Run 20 RCJB Rock D	5.0	4.0	2.0	60.0
Run 20 RCJB Rock E	5.5	3.0	1.8	50.0

This table is available in **ASCII** and in Microsoft Excel format (see 103_T06.XLS in CHAPTER_103 in TABLES in **"Supplementary material"**).

Table T7. Whole-rock major and trace element compositions of basalt, granoblastic dikes, and gabbros sampled during Expedition 335.

Core, section, interval (cm)	Depth (mbsf)	Igneous unit	Rock name	Thin section	*N* (ICP analyses)	Major element oxide (wt%)										
						SiO_2	TiO_2	Al_2O_3	$Fe_2O_3^T$	MgO	MnO	CaO	Na_2O	K_2O	P_2O_5	Total
335-1256D-																
235R-1W, 7–9	1507.2	96A	Granoblastic dike	TS_02	2	49.61	1.05	15.10	10.77	8.27	0.16	12.30	2.24	0.03	0.08	99.59
236R-1W, 34.5–38	1512.2	96B	Granoblastic dike	TS_05	2	50.83	1.35	14.39	12.97	7.79	0.25	11.41	2.45	0.01	0.00	101.47
238R-1W, 15–17	1518.4	96B	Granoblastic dike	TS_07	3	49.32	1.57	14.17	13.77	7.36	0.22	11.58	2.54	0.03	0.11	100.67
Run02-EXJB	923		Basalt	None	3	50.38	1.28	14.75	11.99	8.45	0.18	10.10	2.74	0.18	0.12	100.18
Run11-EXJB	1520		Olivine gabbronorite	TS29	3	48.64	0.72	15.15	10.12	12.24	0.14	11.39	1.87	0.09	0.09	100.45
Run12-RCJB-RockB	1518		Granoblastic dike	TS21	2	48.54	1.61	13.97	15.76	8.70	0.22	10.24	2.56	0.02	0.00	101.61
Run12-RCJB-RockG	1518		Granoblastic dike	TS24	2	50.84	1.20	14.37	12.45	7.86	0.21	11.68	2.53	0.02	0.07	101.24
Run13-RCJB-RockB	1518		Granoblastic dike	TS30	1	50.46	1.35	14.00	13.14	7.41	0.18	11.42	2.38	0.02	0.10	100.47
RUN19-RCJB-Rock C	1521		Granoblastic dike	TSB40	1	50.91	1.33	14.15	14.80	8.31	0.18	9.64	2.74	0.01	ND	102.08
RUN20-RCJB-Rock A	1519.5		Granoblastic dike	TSB41	1	50.63	1.48	13.92	13.64	7.23	0.20	11.39	2.42	0.02	ND	100.93
RUN20-RCJB-Rock C	1519.5		Olivine gabbro	TSB37	1	50.37	0.69	15.30	8.61	11.21	0.14	13.25	2.05	0.07	ND	101.70

ICP = inductively coupled plasma–atomic emission spectroscopy. $Fe_2O_3^T$ = all Fe as Fe_2O_3. Mg# = cationic Mg/(Mg + Fe) ratio with all Fe as Fe^{2+}, Ca# = cationic Ca/(Ca + Na). LOI = loss on ignition. ND = not determined. This table is available in **ASCII** and in Microsoft Excel format (see 103_T07.XLS in CHAPTER_103 in TABLES in **"Supplementary material"**).

Table T7 (continued).

Core, section, interval (cm)	Depth (mbsf)	Mg#	Ca#	LOI (wt%)	H_2O (wt%)	CO_2 (wt%)	Trace element (ppm)										Sample ID
							Sc	V	Cr	Ni	Cu	Zn	Sr	Y	Zr	Ba	
335-1256D-																	
235R-1W, 7–9	1507.2	60.3	75.2	0.008	0.703	0.040	51	307	316	92	38	25	82	26	32	11	QRND3224091
236R-1W, 34.5–38	1512.2	54.3	72.0	-0.139	0.728	0.048	46	379	102	79	34	48	78	19	30	9	QRND3224131
238R-1W, 15–17	1518.4	51.4	71.6	0.199	1.076	0.049	47	457	91	60	49	33	77	28	58	12	QRND3224201
Run02-EXJB	923	58.3	67.1	1.220	2.603	0.115	45	326	196	67	87	61	88	32	77	25	CUTS3215501
Run11-EXJB	1520	70.6	77.1	0.815	1.964	0.034	34	196	454	351	41	22	75	16	38	14	CUTS3225281
Run12-RCJB-RockB	1518	52.2	68.9	0.273	1.134	0.039	47	476	76	84	37	33	97	20	31	11	CUTS3225261
Run12-RCJB-RockG	1518	55.6	71.8	-0.293	0.597	0.036	50	344	150	71	37	44	79	21	32	8	CUTS3225271
Run13-RCJB-RockB	1518	52.8	72.6	-0.369	0.628	0.030	47	380	91	58	47	33	72	22	37	8	CUTS3225371
RUN19-RCJB-Rock C	1521	52.7	66.0	0.280	1.247	0.020	50	353	165	86	21	ND	76	33	58	10	CUTS3226431
RUN20-RCJB-Rock A	1519.5	51.2	72.2	-0.036	0.775	0.017	47	410	88	83	39	ND	71	27	52	10	CUTS3226451
RUN20-RCJB-Rock C	1519.5	72.1	78.1	1.161	1.546	0.073	41	217	750	236	60	ND	75	16	42	15	CUTS3226421

Table T8. Paleomagnetic summary of samples measured during Expedition 335.

Core, section, interval (cm)	Lithologic unit	Measured using	NRM declination (°)	NRM inclination (°)	NRM (A/m)	Demagnetization type	Drilling-induced remanent magnetization							
							N	PCA type	MAD (°)	Declination (°)	Inclination (°)	Low (mT, °C)	High (mT, °C)	Magnitude (A/m)
335(312)-1256D-														
222R-1W, 13	Gabbro 1	JR6A	235.0	78.8	2.52E+00	AF	3	F	3.6	24.2	89.7	0	10	1.94E+00
222R-2W, 44	Gabbro 1	JR6A	42.4	73.4	3.80E+00	Th	5	F	6.1	225.0	68.3	200	400	7.79E–01
222R-2W, 47	Gabbro 1	JR6A	30.4	73.6	2.87E+00	LTD/Th	4	F	1	83.2	84.8	0	100	1.48E+00
223R-2W, 6	Gabbro 1	JR6A	25.6	82.7	5.98E+00	AF	3	F	1.4	59.9	84.4	0	10	5.01E+00
231R-1W, 41	Gabbro 2	JR6A	257.2	71.9	9.91E+00	LTD/Th	4	F	0.5	264.0	77.8	0	100	6.00E+00
231R-1W, 43	Gabbro 2	JR6A	251.9	71.1	5.85E+00	Th	4	F	5.8	153.7	77.3	0	250	1.73E+00
231R-1W, 115	Gabbro 2	JR6A	82.2	79.5	7.68E+00	LTD/Th	4	F	0.4	60.7	84.8	0	100	5.10E+00
231R-3W, 43	Gabbro 2	JR6A	80.7	77.2	8.95E+00	LTD/Th	4	F	0.9	87.2	78.9	0	100	5.52E+00
231R-3W, 53	Gabbro 2	JR6A	74.0	76.4	6.94E–01	LTD/AF	5	F	7.2	83.0	83.4	0	10	4.47E–01
231R-3W, 55	Gabbro 2	JR6A	60.8	84.2	8.67E–01	AF	5	F	1.5	209.8	87.0	0	20	6.69E–01
231R-3W, 114	Gabbro 2	JR6A	80.8	88.1	9.55E+00	LTD/Th	4	F	0.5	104.6	83.9	0	100	6.30E+00
335-1256D-														
235R-1, 6	Dike Screen 2	SRM	18.9	32.3	6.43E–01	AF								
Run12-RCJB-RockA-1	Granoblastic dikes (unspecified)	JR6A	341.4	17.5	2.89E+00	AF								

NRM = natural remanent magnetization, *N* = number of points used in PCA, PCA = principal component analysis, MAD = maximum angular deviation. AF = alternating field, Th = thermal demagnetization, LTD = low-temperature demagnetization. F = free, A = anchored to origin. ChRM = characteristic remanent magnetization. This table is available in **ASCII** and in Microsoft Excel format (see 103_T08.XLS in CHAPTER_103 in TABLES in **"Supplementary material"**).

Table T8 (continued).

Core, section, interval (cm)	Lithologic unit	Non-drilling-induced remanent magnetization principal components								
		Component	*N*	PCA type	MAD (°)	Declination (°)	Inclination (°)	Low (mT, °C)	High (mT, °C)	Magnitude (A/m)
335(312)-1256D-										
222R-1W, 13	Gabbro 1	ChRM	7	F	3.7	233.1	20.4	35	100	1.36E–01
222R-2W, 44	Gabbro 1	ChRM	6	F	2.5	21.5	54.3	550	600	6.77E–01
222R-2W, 47	Gabbro 1	ChRM	11	F	2.6	5.5	35.8	450	580	1.198
223R-2W, 6	Gabbro 1	ChRM	7	F	5.3	346.6	22.3	30	100	1.92E–01
231R-1W, 41	Gabbro 2	ChRM	3	F	4.2	256.2	32.3	570	580	7.04E–01
231R-1W, 43	Gabbro 2	ChRM	5	F	3.4	257.4	46.8	550	580	6.88E–01
231R-1W, 115	Gabbro 2	Comp A	6	F	3.1	264.3	–53.8	200	450	1.53E+00
		ChRM	6	F	7.8	81.3	40.4	550	600	5.60E–01
231R-3W, 43	Gabbro 2	ChRM	4	F	12.6	45.5	53.0	560	580	4.11E–01
231R-3W, 53	Gabbro 2	ChRM	3	F	8.8	53.8	24.1	70	100	6.50E–02
231R-3W, 55	Gabbro 2	ChRM	4	F	10.1	48.9	34.9	60	100	8.00E–02
231R-3W, 114	Gabbro 2	ChRM	6	A	6.3	302.6	46.6	550	600	6.33E–01
335-1256D-										
235R-1, 6	Dike Screen 2	ChRM	8	F	6.0	30.1	25.3	25	60	1.15E–01
Run12-RCJB-RockA-1	Granoblastic dikes (unspecified)	ChRM	5	F	2.4	7.7	17.4	30	100	5.76E–01

Table T9. Anisotropy of magnetic susceptibility (AMS) of samples measured during Expedition 335.

		AMS data in IODP core reference frame												AMS data reoriented by rotating ChRM declination to 000°					
Core, section, interval (cm)	Lithologic unit	K_{max} azimuth (°)	K_{max} plunge (°)	K_{int} azimuth (°)	K_{int} plunge (°)	K_{min} azimuth (°)	K_{min} plunge (°)	Susceptibility (SI)	Maximum eigenvalue	Intermediate eigenvalue	Minimum eigenvalue	Corrected anisotropy degree	Shape parameter	K_{max} azimuth (°)	K_{max} plunge (°)	K_{int} azimuth (°)	K_{int} plunge (°)	K_{min} azimuth (°)	K_{min} plunge (°)
335(312)-1256D-																			
222R-1W, 13	Gabbro 1	242.3	48.8	63.8	41.2	333.2	0.8	7.63E–03	0.3386	0.3329	0.3284	1.0312	–0.1062	9.2	48.8	190.7	41.2	100.1	0.8
222R-2W, 44	Gabbro 1	17	6.7	112.4	38.9	278.9	50.3	1.16E–02	0.3364	0.3357	0.3279	1.0290	0.8473	355.5	6.7	90.9	38.9	257.4	50.3
222R-2W, 47	Gabbro 1	194.7	1	104.4	16.8	287.9	73.2	9.91E–03	0.3379	0.3329	0.3292	1.0266	–0.1597	189.2	1.0	98.9	16.8	282.4	73.2
223R-2W, 6	Gabbro 1	337.8	50.7	148.8	39.0	242.4	4.4	1.18E–02	0.3365	0.3338	0.3297	1.0209	0.1967	351.2	50.7	162.2	39.0	255.8	4.4
231R-1W, 41	Gabbro 2	288.6	28.9	171.2	39.9	42.8	36.6	4.61E–02	0.3352	0.3328	0.3320	1.0099	–0.5285	32.4	28.9	275.0	39.9	146.6	36.6
231R-1W, 43	Gabbro 2	17.3	48.8	256.0	24.4	150.3	30.9	2.78E–02	0.3357	0.3345	0.3298	1.0187	0.6042	119.9	48.8	358.6	24.4	252.9	30.9
231R-1W, 115	Gabbro 2	248.3	0.6	157.9	36.7	339.0	53.3	3.04E–02	0.3368	0.3325	0.3307	1.0191	–0.4131	167.0	0.6	76.6	36.7	257.7	53.3
231R-3W, 43	Gabbro 2	358.4	36.4	219.1	45.8	105.3	21.4	2.97E–02	0.3353	0.3339	0.3308	1.0140	0.3716	312.9	36.4	173.6	45.8	59.8	21.4
231R-3W, 53	Gabbro 2	61.7	10.3	159.5	36.8	318.6	51.3	2.93E–02	0.3361	0.3324	0.3314	1.0149	–0.5703	7.9	10.3	105.7	36.8	264.8	51.3
231R-3W, 55	Gabbro 2	256	16.9	138.0	57.2	355.0	27.2	3.53E–02	0.3354	0.3334	0.3312	1.0126	0.0366	207.1	16.9	89.1	57.2	306.1	27.2
231R-3W, 114	Gabbro 2	119.1	22	253.6	60.1	21.0	19.3	2.88E–02	0.3377	0.3316	0.3307	1.0229	–0.7470	176.5	22.0	311.0	60.1	78.4	19.3

ChRM = characteristic remanent magnetization. This table is available in **ASCII** and in Microsoft Excel format (see 103_T09.XLS in CHAPTER_103 in TABLES in **"Supplementary material"**).

Table T10. Thermal conductivity measurements on Expedition 312 cores and Expedition 335 non-core material.

Core, section, interval (cm)	Top depth (mbsf)	Thermal conductivity (W/[m·K]) Mean	±1σ	*N*	Probe rotation (°)	Comments/Lithology
335(312)-1256D-						
223R-3A, 12–24	1452.40	2.238	0.059	63		Olivine gabbro
230R-1A, 49–61	1483.49	2.440	0.013	6		Gabbronorite
230R-2A, 90–103	1485.40	2.215	0.019	4		Gabbronorite
231R-1A, 105–121	1488.95	2.279	0.004	5		Gabbronorite
231R-2A, 92–105	1490.11	2.276	0.020	6		Gabbronorite
231R-3A, 48–63	1491.04	2.286	0.015	5		Gabbronorite
231R-4A, 0–15	1491.93	2.274	0.034	10		Gabbronorite
231R-4A, 109–126	1493.02	2.268	0.010	5		Gabbronorite
232R-1A, 50–62	1493.90	2.258	0.020	5		Gabbro country rock
232R-1A, 50–62	1493.93	2.427	0.009	5		Over a thin vein/fracture
232R-1A, 50–62	1493.96	2.321	0.017	5		Across a felsic vein that runs perpendicular to the core
232R-1A, 50–62	1493.99	2.291	0.008	5		Across an oblique vein
232R-1A, 50–62	1494.02	2.303	0.005	5		Across an oblique vein at the bottom of the piece
335-1256D-						
RCJB12-C	1516.00	2.226	0.007		0	Granoblastic dike
RCJB12-C	1516.00	2.218	0.013		15	Granoblastic dike
RCJB12-C	1516.00	2.226	0.021		30	Granoblastic dike
RCJB12-C	1516.00	2.232	0.010		45	Granoblastic dike
RCJB12-C	1516.00	2.235	0.013		60	Granoblastic dike
RCJB12-C	1516.00	2.303	0.092		75	Granoblastic dike
RCJB12-C	1516.00	2.244	0.007		90	Granoblastic dike
RCJB13-B	1516.00	2.333	0.028		NA	Granoblastic dike

N = number of observations. RCJB = reverse circulation junk basket. Probe rotation is clockwise with respect to veins. NA = not applicable. This table is available in **ASCII** and in Microsoft Excel format (see 103_T10.XLS in CHAPTER_103 in TABLES in **"Supplementary material"**).

Table T11. Thermal conductivity measurements on Section 335-1256D-235R-1 (Piece 1).

Test	Value (° or mm)	*N*	*k* (W/[m·K])	1σ (W/[m·K])	1σ (%)	95% confidence
Rotation	–30	4	2.255	0.004	0.2	0.004
Rotation	–20	5	2.246	0.019	0.8	0.016
Rotation	–10	10	2.287	0.015	0.6	0.009
Rotation	0	5	2.253	0.010	0.4	0.009
Rotation	10	5	2.292	0.020	0.9	0.018
Rotation	20	5	2.282	0.011	0.5	0.009
Rotation	30	5	2.263	0.029	1.3	0.026
Across core	4	5	1.944	0.105	5.4	0.092
Across core	8	5	2.192	0.063	2.9	0.056
Across core	12	5	2.281	0.030	1.3	0.027
Across core	16	5	2.264	0.016	0.7	0.014
Across core	20	5	2.267	0.015	0.7	0.013
Down core	5	5	2.079	0.393	18.9	0.345
Down core	10	5	3.306	1.118	33.8	0.980
Down core	15	5	2.295	0.016	0.7	0.014
Down core	25	5	2.281	0.012	0.5	0.011
Down core	35	5	2.280	0.006	0.3	0.006
Down core	45	5	2.270	0.014	0.6	0.013
Down core	55	5	2.251	0.016	0.7	0.014

N = number of measurements. Rotation = rotating angle of measurement, Across core = moving probe across the core from the edge to the center, Down core = moving probe vertically down the core. This table is available in **ASCII** and in Microsoft Excel format (see 103_T11.XLS in CHAPTER_103 in TABLES in **"Supplementary material"**).

Table T12. Density, porosity, and compressional velocity measurements, Expedition 335.

Core, section, interval (cm)/ Sample label ID	Depth (mbsf)		Rock type	Density (g/cm^3)		Porosity (vol%)	V_P x (m/s)	
	Top	Bottom		Bulk	Grain		Value	±1σ
335(312)-1256D-								
222R-1W, 12–15	1444.72	1444.75	Olivine gabbro	2.925	2.946	1.117	6222	30
223R-2W, 5–7	1450.83	1450.85	Olivine gabbro	2.942	2.953	0.574	6643	24
231R-3W, 52–54	1491.08	1491.10	Gabbronorite	2.919	2.934	0.789	6755	37
231R-3W, 54–56	1491.10	1491.12	Gabbronorite	2.991	3.007	0.789	6766	56
222R-2W, 43–45	1446.53	1446.56	Olivine gabbro	2.951	2.970	0.981	4922	154
222R-2W, 46–48	1446.56	1446.58	Olivine gabbro	2.937	2.956	0.951	5258	172
231R-1W, 40–42	1488.30	1488.32	Diorite	2.998	3.014	0.772	5666	189
231R-1W, 42–44	1488.32	1488.34	Gabbronorite	3.049	3.059	0.485	5866	117
231R-1W, 114–116	1489.04	1489.06	Gabbronorite	2.987	3.001	0.718	5744	213
231R-3W, 42–44	1490.98	1491.00	Gabbronorite	3.046	3.063	0.825	5869	114
231R-3W, 113–115	1491.69	1491.71	Gabbronorite	3.026	3.028	0.075	5904	259
335-1256D-Run12-RCJB-Rock C	1516.00		Granoblastic dike					
335-1256D-Run12-RCJB-RockC-MADC_01	1516.00		Granoblastic dike	3.014	3.031	0.834	6610	22
335-1256D-Run12-RCJB-RockC-MADC_02	1516.00		Granoblastic dike	3.040	3.054	0.657	6776	26
335-1256D-Run13-RCJB-RockB-MADC_01	1516.00		Granoblastic dike	3.057	3.066	0.473	6907	21
335-1256D-Run13-RCJB-RockB-MADC_02	1516.00		Granoblastic dike	3.058	3.067	0.418	6813	18

The four core samples indicated by Y in the Seawater column were measured with the new seawater bath method for V_P and represent most reliable results. Reported V_P values are the means and 1σ of at least seven measurements. The seven core samples indicated by N were treated according to Expedition 312 protocol. Their velocities are biased toward lower values due to experimental conditions. This table is available in **ASCII** and in Microsoft Excel format (see 103_T12.XLS in CHAPTER_103 in TABLES in **"Supplementary material"**).

Table T12 (continued).

Core, section, interval (cm)/ Sample label ID	V_P y (m/s)		V_P z (m/s)		Mean V_P (m/s)		Seawater bath	Text ID
	Value	±1σ	Value	±1σ	Value	±1σ		
335(312)-1256D-								
222R-1W, 12–15	6186	57	6487	44	6298	166	Y	CUBE3215391
223R-2W, 5–7	6707	46	6732	40	6694	51	Y	CUBE3215421
231R-3W, 52–54	6695	23	6762	36	6737	41	Y	CUBE3215471
231R-3W, 54–56	6798	26	6714	24	6759	48	Y	CUBE3215481
222R-2W, 43–45	5668	257	5474	86	5355	401	N	CUBE3215401
222R-2W, 46–48	5785	116	5734	100	5592	301	N	CUBE3215411
231R-1W, 40–42	5343	202	5773	211	5594	252	N	CUBE3215431
231R-1W, 42–44	5309	173	5607	108	5594	290	N	CUBE3215441
231R-1W, 114–116	5582	150	5742	154	5689	137	N	CUBE3215451
231R-3W, 42–44	6017	108	5699	57	5862	169	N	CUBE3215461
231R-3W, 113–115	5948	256	5819	121	5890	144	N	CUBE3215491
335-1256D-Run12-RCJB-Rock C			6123	20	6123	20	N	SPCM3224611
335-1256D-Run12-RCJB-RockC-MADC_01	6802	23	6788	19	6733	108	Y	CUBE3225531
335-1256D-Run12-RCJB-RockC-MADC_02	6899	20	6882	32	6852	68	Y	CUBE3225541
335-1256D-Run13-RCJB-RockB-MADC_01	6898	18	6861	18	6889	27	Y	CUBE3225771
335-1256D-Run13-RCJB-RockB-MADC_02	6753	15	6755	14	6774	35	Y	CUBE3225781

Table T13. Chronology of logging operations in Hole 1256D during Expedition 335 .

Activity	Date	Time (h)	Tool depth (mbrf)	Comments
Rig floor preparation	26 May	2000		
Run 1: triple combo				
Start tool string rig up		2030		
Tool string check		2200		
RIH		2250	0	
Start downlog	27 May	0050	3800	
Tool string at end of pipe		0055	3865	
WHC testing		0105	4000	Heave was 1–2 m peak to peak; chosen configuration reduced tool motion by 50%
Resume downlog		0150	4000	
End downlog		0245	5100	Downlog interrupted to fully calibrate resistivity tool (HRLA) to ambient temperature
Reach total depth		0255	5165	
Begin first pass up		0300	5165	Problem opening caliper; decided not to run repeat to avoid trouble
Speed up		0405	4850	Priority was lower ~300 m; continue mostly for caliper
Turn off WHC		0455	3950	
Pull into pipe		0505	3864	
End first pass up		0505		
Tools out; start rig down		0700		
Tools rigged down		0900		Bowsprings of upper centralizer appear worn out and need to be replaced
Run 2: FMS-sonic				
Start tool string rig up		0915		Upper centralizer bowsprings replaced while rigging up
Tool string check		1020		
RIH		1050	0	
Tool string at end of pipe		1240	3865	
Pull tool to surface		1250	3885	Could not pass below 3885 mbrf; assumed trouble with new springs
Tool string at surface		1410	0	
RIH		1455	0	Inspection showed no damage; assumed springs too stiff and try again
Tool string at end of pipe		1625	3865	
Tool declared stuck		1800	3885	Tried for >1 h to move, pump…
Tool recovery				
Drop Kinley crimper		2140		Based on depth, count 1 h to work tool down
Drop Kinley hammer		2240		2300 h, lost connection with cable head
Drop Kinley cutter	28 May	0015		
Drop Kinley hammer		0120		0140 h, wireline cut
Wireline on deck		0330		
Tool string at surface		0940		DSI receiver array sticking out of bit
All tools rigged down		1130		

RIH = run into hole, WHC = wireline heave compensator, HRLA = High-Resolution Laterolog Array, FMS = Formation MicroScanner, DSI = Dipole Sonic Imager. This table is available in **ASCII** and in Microsoft Excel format (see 103_T13.XLS in CHAPTER_103 in TABLES in **"Supplementary material"**).